

SPIN-ELECTRIC COUPLING IN QUANTUM DOTS AND MOLECULAR MAGNETS

INAUGURALDISSERTATION

zur

Erlangung der Würde eines Doktors der Philosophie

vorgelegt der

Philosophisch-Naturwissenschaftlichen Fakultät

der Universität Basel

von

Mircea Trif

aus Baia Sprie (Romania)

Basel, 2011

Genehmigt von der Philosophisch-Naturwissenschaftlichen Fakultät auf Antrag von

Prof. Dr. Daniel Loss

Prof. Dr. Yaroslav Tserkovnyak

Basel, den 8. Dezember 2009

Prof. Dr. Eberhard Parlow
Dekan

Acknowledgments

It is a pleasure to thank the many people who made this thesis possible.

First of all, I wish to thank Prof. Daniel Loss for giving me the unique opportunity to pursue my PhD in his group. During this time, I have profited enormously from both his physical intuition and his creative mind.

My special thanks goes to Dr. Vitaly Golovach, Dr. Dimitrije Stepanenko, Dr. Filippo Troiani and Prof. Pascal Simon, with whom I had the chance to collaborate during my PhD. The first two years of my PhD Vitaly was as a 'second' supervisor for me. Not only he had an open ear for my ever so frequent questions, but his explanations were always extremely pedagogical and original. I am very grateful to him. Dimitrije and I were only sharing the same office in the beginning, but the infinite number of discussions, both physics and non-physics related, lead in the end not only to a very fruitful collaboration, but also to close friendship, which I hope will last over the years. Working with Filippo and Pascal was an extraordinary experience for me. I learned that collaborations go beyond the borders of you own group, that teaming is more important than competing. I thank them both for this.

During my time in the Condensed Matter Theory Group at the University of Basel I experienced not only a stimulating scientific environment but also an active social life. I really think is one of the best places to be! My thanks go to Luca Chirolli, Charles Doiron, Mathias Duckheim, Jan Fischer, Kevin van Hoogdalem, Jelena Klinovaja, Fabio Pedrocchi, Beat Röthlisberger, Robert Andrzej Zak, Oded Zilberberg, Robert Zielke, Andreas Wagner, Dr. Audrius Alkauskas, Dr. Dan Bohr, Dr. Bernd Braunecker, Dr. Denis Bulaev, Dr. Oleg Chalaev, Dr. Stefano Chesi, Dr. Bill Coish, Dr. Sigurdur Erlingsson, Dr. Daniel Klauser, Dr. Verena Koerting, Dr. Jörg Lehmann, Dr. Minchul Lee, Dr. Andriy Lyakhov, Dr. Joël Peguiron, Dr. Daniel Saraga, Dr. Manuel Schmidt, Dr. Thomas Schmidt, Dr. Maximilian Schultz, Dr. Dimitrije Stepanenko, Dr. Vladimir M. Stojanovic, Dr. Filippo Troiani, Dr. Oleksandr Tsyplyatyev, Dr. Mihajlo Vanevic, Prof. Christoph Bruder, Prof. Guido Burkard, Prof. Mahn-Soo Choi, Prof. Jose Carlos Egues, Prof. Björn Trauzettel.

Last but not least I would like to thank Prof. Yaroslav Tserkovnyak for co-refereeing this thesis.

Summary

In this thesis we study several aspects related to the dynamics of electrons and holes in quantum dots, as well as dynamics of electron spins in molecular magnets.

Magnetic materials and spin systems are usually probed and controlled by magnetic fields. The techniques of spin manipulation via magnetic fields were developed in the ESR and NMR studies. These techniques allow for detailed study and manipulation of *large* collection of spins.

Reducing the size of a device improves its properties. In case of a prototypical magnetic device, a memory element, the smaller devices will have shorter access times and larger capacity per unit volume, and a smaller power absorption. Another important reason to study even smaller devices is that a plethora of intriguing quantum effects become manifest only when the size of a device is small enough. Typically, the quantum effects start to be important at the nanometer scale. At these scale, the control via magnetic fields of individual devices becomes problematic.

Obtaining electric fields instead, that can be locally controlled and fast switched, is a routine nowadays. The ability to move around molecules with STM tips is just one example of for control of quantum systems at the nanoscale with electric fields. The missing ingredient is a mechanism that would make spins couple to electric fields. In this work I investigated precisely this issue, namely the coupling of electric fields, either classical or quantum, to different spin systems, like spins in quantum dots or molecular magnets.

The thesis is divided in four parts. In the first part, we investigate a new type of spin-spin interaction, which arises due to the presence of both Coulomb repulsion between two electrons localized in quantum dots, and the spin-orbit interaction in the host material (GaAs). We show that this type of coupling is long-range and resembles the interaction of two electric dipoles that depend on spin. For this interaction to arise direct coupling between electrons is not necessary (no tunneling assumed). In the second part we investigate the interaction between spins localized in quantum dots mediated by the electromagnetic modes of a one dimensional microwave cavity and spin-orbit interaction. We show that this interaction can be strong and long range (\sim mm), and can be controlled (switched on and off) either magnetically or electrically. The third part is devoted to hole-spin dynamics in quantum dots. We analyze the weak magnetic field regime of the relaxation of a heavy-hole spin localized in a quantum dot. Driven by recent experiments, we show that two-phonon processes give a good explanation for the saturation of the relaxation time at intermediate temperatures. In the fourth part we show, by several methods, that spin transitions in (some) molecular magnets can be induced by electric fields. We identify a spin-electric coupling caused by an interplay between spin exchange, spin-orbit interaction, and the chirality of the underlying spin texture of the molecular magnet. This coupling allows for the electric

control of the spin (qubit) states, e.g. by using an STM tip or a microwave cavity. We propose an experimental test for identifying molecular magnets exhibiting spin-electric effects.

Contents

Acknowledgments	iii
Summary	v
1 Introduction	1
1.1 Quantum dots and spin qubits	1
1.2 Single molecular magnets as qubits	5
1.3 Outline	7
2 Electrostatically coupled spins	9
2.1 Introduction	9
2.2 The Model	11
2.3 Spin-Spin Coupling	12
2.3.1 Weak Coulomb coupling - $\delta \ll 1$	14
2.3.2 Elliptical dots with $\delta \ll 1$	19
2.3.3 Strong Coulomb coupling - $\delta \geq 1$	20
2.4 Measurement Scheme	26
2.5 Discussions and conclusions	30
3 Spin dynamics in a transmission line	33
3.1 Introduction	33
3.2 Model Hamiltonian	36
3.3 General Spin-photon dynamics	37
3.3.1 Spin-photon interaction	37
3.3.2 Effective spin-spin interaction	39
3.4 Strong longitudinal confinement	40
3.5 Strong transverse confinement	42
3.6 Numerical Estimates	43
3.7 Coherent manipulation	45
3.8 Spin relaxation and decoherence	46
3.8.1 Spin-relaxation in longitudinal confined QDs	47
3.8.2 Spin relaxation in transverse confined QDs	49
3.8.3 Decoherence due to hyperfine interaction	52
3.9 Conclusions	52

4	Hole-Spin Relaxation	55
4.1	Introduction	55
4.2	Heavy-hole Hamiltonian	56
4.3	Spin-phonon interaction	57
4.4	Hole-spin relaxation	58
4.5	Conclusions	62
5	Spin electric effects in molecular antiferromagnets	63
5.1	Introduction	63
5.2	Symmetry analysis of antiferromagnetic spin rings	67
5.2.1	Triangle of $s = 1/2$ spins	67
5.2.2	Spin $s = 3/2$ triangle	71
5.2.3	Spin $s = 1/2$ pentagon	74
5.3	Hubbard model of a molecular nanomagnet	77
5.3.1	Parameters of the Hubbard model of molecular nanomagnets	78
5.3.2	Hubbard model of the spin triangle: direct exchange	79
5.3.3	Superexchange in molecular bonds	83
5.3.4	Electric field along y	86
5.3.5	Bond modification and symmetries	91
5.4	Experimental signatures of the spin-electric coupling	92
5.4.1	Electron spin resonance	93
5.4.2	Nuclear magnetic resonance	97
5.4.3	Magnetization, Polarization, and Susceptibilities	103
5.4.4	Heat capacity	113
5.5	Conclusions	114
A	$J_{\tilde{x},\tilde{y}}$ for arbitrary B-fields	117
B	Displacement and stress tensor	119
C	Spin states in terms of the c_{Γ}^{\dagger} operators	121
D	H_{SO}, H_{e-d}^0 and H_{e-d}^1 matrix elements	123

Chapter 1

Introduction

In this thesis we study several aspects related to the dynamics of electrons and holes in quantum dots, as well as dynamics of electron spins in molecular magnets.

Magnetic materials and spin systems are usually probed and controlled by magnetic fields. The techniques of spin manipulation via magnetic fields were developed in the ESR and NMR studies. These techniques allow for detailed study and manipulation of *large* collection of spins.

Reducing the size of a device improves its properties. In case of a prototypical magnetic device, a memory element, the smaller devices will have shorter access times and larger capacity per unit volume, and a smaller power absorption. Another important reason to study even smaller devices is that a plethora of intriguing quantum effects become manifest only when the size of a device is small enough. Typically, the quantum effects start to be important at the nanometer scale. At these scale, the control via magnetic fields of individual devices becomes problematic.

Obtaining electric fields instead, that can be locally controlled and fast switched, is a routine nowadays. The ability to move around molecules with STM tips is just one example of for control of quantum systems at the nanoscale with electric fields. The missing ingredient is a mechanism that would make spins couple to electric fields. In this work we investigate precisely this issue, namely the coupling of electric fields, either classical or quantum, to different spin systems, like spins in quantum dots or molecular magnets.

1.1 Quantum dots and spin qubits

Quantum dots, also known as artificial molecules, are semiconductor nanostructures that can accommodate several charge carriers, and show discrete level structure. In gate-defined quantum dots, the localization of carriers to small regions is achieved with the help of external gates, by fine-tuning their electrostatic potential. In self-assembled quantum dots instead, the confinement of the carriers appears naturally, for example due to lattice mismatch of two different materials.

While in the first realized quantum dots, the control over the number of electrons was quite poor (several hundreds) and pretty unstable with respect to variation of the external parameters (like gate-potentials, magnetic fields, currents), today's state-of-art quantum dots are stunning: full control over the number of electrons, down to the single electron per

quantum dot have been realized [1, 2].

In addition to the control over the number of electrons, the control over the quantum state of the electrons is really impressive. In particular, the spin of an electron in a quantum dot can be by now easily manipulated in a coherent fashion. Besides the technological progress achieved in designing and controlling them, the quantum dots have been the playground for testing important physical questions. It allowed to probe in a continuous manner the transitions from classical to quantum world, in the same time providing strong tests of quantum mechanical behavior at the nanoscale. The ability to engineer the quantum world is the source of fascination with quantum dots. It opens new opportunities to use the quantum properties of matter for different technological applications. Solid state electronics industry build up its huge success on the constant miniaturization of the on-chip integrated circuits. However, this approach on increasing the performance of electronics has its limits, which are not only of technological nature but, more importantly, of physical nature. Reducing the size further leads to crossing between classical and quantum regimes, where the functionality of the devices is ruled by the laws of quantum mechanics instead of the classical ones. However, this is not at all a drawback, but more of a challenge. It opens the possibility for a new kind of devices that use quantum mechanics as an essential ingredient for their operation, e.g. quantum computers, single-electron transistors, etc.

Information processing using quantum mechanics, or quantum computing, is among the most prominent fields of science in the last fifteen years. The motivation behind this effort comes both from the technological appeal of new and better computers and from the fundamental scientific questions about the nature of information and the physical limits on our ability to process it. Quantum mechanics enters this discussion with understanding that an abstract information is always embedded in some real world objects and therefore it is governed by the laws of nature which are quantum. From the point of view of technology, the appeal of quantum computers comes from the fact that there are problems that are tractable on quantum computers which are believed to be intractable on classical ones. The most famous such problem is factoring of integers into their prime factors [3], suggesting that quantum computers may be intrinsically more powerful than classical ones.

Powerful computers that cannot be built are useless, and it is crucial to know whether the model of a quantum computer describes a machine that can be built, and how such a machine can be built. Based on our current knowledge of quantum mechanics it is possible to build a quantum computer. However, the realization of such a machine seems to be a hard task.

One of the seminal ideas that for implementing a quantum computer was to use the spin of electron as quantum bit (or qubit) for storing and processing quantum information [4]. By now, this program for implementing qubits is called the Loss-DiVincenzo proposal. There are a few basic requirements that a good qubit have to fulfill, called the DiVincenzo criteria:

1. Initialization in a given state with high fidelity;
2. Coherent control of single qubits (one-qubit gates) and controlled interaction between pairs of qubits (two-qubit gates);

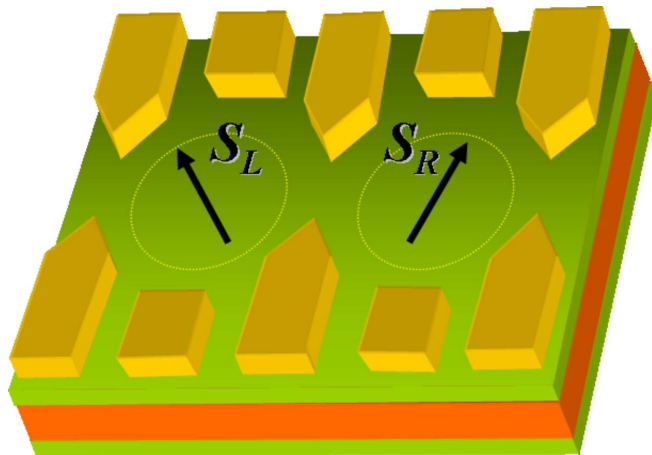


Figure 1.1: Schematics of the double-dot configuration in the Loss-DiVincenzo proposal. In each of the two sites (quantum dots) sits exactly one electron, whose confinement is provided by the gates depicted in yellow. The coupling between the spins is controlled by the middle gates.

3. Long relaxation and decoherence times (much longer than the operation times);
4. Ability to measure the final states of the qubits;
5. Scalable qubits, if one wants to use them in future technologies.

The spin of an electron is a natural quantum system to encode a qubit, since the Hilbert space is by nature only two-dimensional. A general spin states can be obtained by a superposition of the spin 'up' and spin 'down'

$$|\psi\rangle = \alpha|\uparrow\rangle + \beta|\downarrow\rangle, \quad (1.1)$$

with $|\alpha|^2 + |\beta|^2 = 1$. In the Loss-DiVincenzo proposal each of the spins is carried by an electron which is trapped in a quantum dot, like in the sketch showed in Fig. 1.1. The initialization of the qubit is defined by an external applied magnetic field. The spins are supposedly manipulated individually, by local time-dependent magnetic fields which are due either to currents flowing in nearby wires, the modification of the local g -factor by gates, spin-orbit interaction, etc. The interaction between the spins can be controlled in an all-electrical fashion by tuning the exchange interaction between spins. This is accomplished by changing the potential barrier between the two dots. The coupling Hamiltonian between two spins can be mapped to the isotropic exchange spin Hamiltonian $H(t) = J(t)\mathbf{S}_1 \cdot \mathbf{S}_2$, with the exchange coupling $J(t)$ being time-dependent. Finally, the measurement of the spin state at the end of the operation can be made, for example, by spin-to-charge conversion methods.

Most of the experimental setups are based on quantum dots fabricated in a GaAs two-dimensional electron gases (2DEGs). Rapid progress in GaAs nanostructures started once few-electron QDs became available (for a review, see e.g., Ref. [1]), which opened the door

to control the number of electrons in a single QD down to one in vertical [5] and lateral [6] dots, as well as in double QDs. [7–9] Further important experimental progress came with the advent of charge sensors which, quite remarkably, enabled the measurement of the relaxation time of one single spin. [10] The longest spin relaxation times in single GaAs QDs extend up to several seconds [11] and were measured in lateral dots at relatively small magnetic fields ($B \sim 1$ T).

The spin decoherence time in GaAs was measured also in double QDs by studying the hyperfine-induced mixing of singlet and triplet states. [12, 13] In the same set-up, a universal entanglement operation was implemented, [13] enabling a square-root-of-swap operation [4] between two spin-1/2 qubits on a time scale of 180 ps. Resonant and coherent manipulation of a single spin-1/2 has recently been implemented in a GaAs double QD, making use of electron spin resonance (ESR) [14, 15] as well as electric dipole induced spin resonance (EDSR) [?, 16] techniques. Resonant but incoherent (hyperfine-mediated) spin manipulation in double dots was also recently demonstrated. [17]

In the past years though, a new candidate for a qubit state has been attracting growing interest: the spin of a heavy hole (HH) confined in a flat QD. In a bulk semiconductor the HH ($J_z = \pm 3/2$) and light hole (LH) ($J_z = \pm 1/2$) bands are degenerate giving rise to strong mixing and thus to strong HH-spin relaxation. However, in a 2D system the HH and LH bands are split due to the strong confinement along the growth direction [18] implying a significant reduction of the HH spin relaxation via HH-LH mixing.

Holes have several advantages over the electron for qubit implementation. First of all, they interact weaker than the electron with the collection of nuclei in quantum dots due to their p-symmetry of the Bloch functions [19–23]. Even more interesting, this coupling to the nuclei is anisotropic, namely of Ising type, with the Ising direction along the growth direction. This implies very long relaxation times when the spin is initialized along the z direction, even for weak or vanishing magnetic fields, as opposed to electron spin which decays on time scales on the order of ns in weak fields. As for electrons, the spin relaxation time for holes is set by the coupling of the spin to the phonon bath. In bulk GaAs material, the heavy-holes spin life time is as short as picoseconds. However, confinement prolongs this time scale to microseconds, and even milliseconds in weak magnetic fields [20, 24]. It was showed theoretically that the hole-spin relaxation time in quantum dots is the result of the coupling to phonons via the spin-orbit interaction in the host material [25, 26]. In strong magnetic fields, the behavior of the relaxation time have been well described by one-phonon processes. However, as opposed to electrons, the relaxation time show saturation in weak magnetic fields, in the millisecond range. This cannot result from one-phonon processes [25, 26], but instead can be the result of two-phonon processes [27].

Most of the studies of holes in quantum dots were performed optically, in self-assembled quantum dots. However, gate-defined quantum dots are way more controllable and suitable to implement the Loss-DiVincenzo idea. The day one single hole will sit in a gate defined in a quantum dot is around the corner, at present the state-of-art gate defined quantum dots containing only a few holes [28]. Also, detection schemes involving quantum point contacts in p-doped semiconductors are now developed [29].

1.2 Single molecular magnets as qubits

Although the original proposal of using spins as qubits focused on electron localized in quantum dots [4], the basic ideas are quite general. Other systems, like molecular magnets, magnetic ions, electron spins in carbon nanotubes, NV-centers, etc, are as good candidates for storing an electron spin. Each of these systems have advantages and disadvantages. For example, as stated before, electron spins in quantum dots (gate-defined mostly) are extremely controllable, with switching times that can be as fast as hundreds of picoseconds. However, the main drawback of these systems is that it is very hard to wire them up in a large number. Even though there are no fundamental reasons why wiring up a large number of quantum dots should be impossible, it requires precise patterning of conductors in semiconductors, and appears to be very hard with the current technology.

As an alternative to the design and fabrication of connections between many quantum dots, the supra-molecular chemistry allows for a synthesis of large clusters of magnetic centers. In these complex molecules, the interaction between the centers is set by the molecules themselves, and it is perfectly reproducible. The single-molecule magnets (SMMs) [30, 31] represent a class of quantum systems that show rich quantum behavior. At low energies, the SMMs behave as either a large spins or a systems of few interacting spins. The structure of this spin system is tunable by altering the chemical structure of the molecules, and ranges from a single large spin with high anisotropy barrier, to small collections of ferro- or antiferromagnetically coupled spins with various anisotropies. This versatility of available effective spin systems makes the SMMs promising carriers of quantum information. The classical magnetic fields readily interact with the spins in SMMs, and offer the most straightforward control mechanism through the electron spin resonance (ESR) techniques [32].

Quantum behavior of SMMs is clearly manifested in the quantum tunneling of magnetization [33–39]. A prototypical example of quantum tunneling of magnetization is the hysteresis loop of a SMM with a large spin and high anisotropy barrier. The height of the barrier separating the degenerate states of different magnetization leads to long-lived spin configurations with nonzero magnetic moment in the absence of external fields. The transitions between magnetization states in the SMM driven through a hysteresis loop occur in tunneling events that involve coherent change of a many-spin state. These transitions have been observed as step-wise changes in magnetization in single-molecule magnets [36, 37, 40–42]. Similar tunneling between spin configurations are predicted in antiferromagnetic molecules [43, 44], and the observed hysteresis was explained in terms of the photon bottleneck and Landau-Zener transitions [45–48]. The transitions between spin states are coherent processes, and show the signatures of interference between transition paths [49, 50]. It has been argued that they show the effects of Berry phase [51–53].

These features make them, just like quantum dots, objects that are witnesses of the crossover between the classical and quantum worlds. Like in quantum dots, one can chemically engineer the coupling between molecules, but for a much larger number of them. This means wiring up the magnetic molecules, a step forward to the scalability of spin-qubit systems. The drawback here is the control over these couplings. Chemistry alone is not enough for this purpose, but combined with the methods used for the control of spins in quantum dots, can provide full control over the magnetic molecules. There are already plenty of ideas for using molecular magnets for quantum information processing. To give just an example,

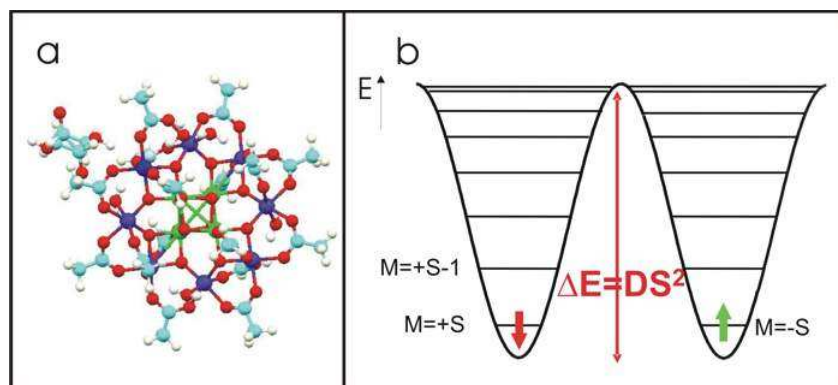


Figure 1.2: The Mn_{12} molecular magnet. a) the schematics of the distribution of the Mn ions in the molecular magnet. b) the level structure of the lowest spin multiplet $S = 10$.

it was showed that Grover algorithm [54] could be efficiently implemented in in such tiny structures [55]. Grover algorithm, or 'searching the needle in the hay-stack' is one of the problems that has been showed it can be solved much faster on a quantum computer than on a classical one. Even though the special resource of quantum mechanics, i.e. entanglement, does not play a role for this algorithm, it still makes use of interference. In figure Fig.1.2 we show one of the most widespread molecular magnets, namely the so called Mn_{12} . This molecule is composed of 12 Mn magnetic ions, 8 of them carrying a spin $3/2$, while $S = 4$ of them a spin $S = 2$. Due to exchange coupling between the magnetic ions, the molecule has a ground state with $S = 10$. For all purposes, this molecule behaves as a large spin individual object, and not as a collection of magnetic ions that interact.

Molecular magnets are probed and controlled usually with magnetic fields, either static or time-dependent. ESR and NMR are by far the most used methods for this purpose, providing information on the parameters of the spin systems (spin-Hamiltonian). However, magnetic fields probe a large number of molecules, and not one in particular. For implementing the spin-qubit program though, access on the single molecule level is needed. Magnetic fields that act locally, on a single molecule, are very hard to obtain. An even harder task is to produce both local and strong magnetic fields. Usually, strong magnetic fields are provided by superconducting coils. These are pretty big in size and thus the magnetic fields they create are not at all local. Electric fields instead can be made both strong and local by using, for example, STM tips or electrostatic gates as done for quantum dots.

Most of the molecular magnets are grown in crystal structures. They form the basis of some bulk materials and usually they are not interacting with each other. The only common feature they share are the lattice vibrations that cause decoherence, in the same time providing means for coupling different magnets. The bulky structure of these materials can be quite a problem if one is to address them individually. The goal would be to isolate single molecular magnets on, for example, surfaces of different materials, in the same time keeping them isolated from the surface itself. This obvious task was a hard one though, and it required a lot of effort and innovation from the experimentalist. In the end, this was worthwhile, by now more and more materials being synthesized on surfaces. The next step now is to control them individually and, preferably, to implement some of the existing

quantum algorithms.

1.3 Outline

In the first Chapter we investigate a new type of spin-spin interaction, which arises due to the presence of both Coulomb repulsion between two electrons localized in quantum dots, and the spin-orbit interaction in the host material (GaAs). We show that this type of coupling is long-range and resembles the interaction of two electric dipoles that depend on spin. For this interaction to arise direct coupling between electrons is not necessary (no tunneling assumed).

In the second Chapter we investigate the interaction between spins localized in quantum dots mediated by the electromagnetic modes of a one dimensional microwave cavity and spin-orbit interaction. We show that this interaction can be strong and long range (\sim mm), and can be controlled (switched on and off) either magnetically or electrically.

In the third Chapter we analyze the weak magnetic field regime for the relaxation of a heavy-hole spin localized in a quantum dot. Driven by recent experiments, we show that two-phonon processes give a good explanation for the saturation of the relaxation time at intermediate temperatures.

In the fourth Chapter we show, by several methods, that spin transitions in (some) molecular magnets can be induced by electric fields. We identify a spin-electric coupling caused by an interplay between spin exchange, spin-orbit interaction, and the chirality of the underlying spin texture of the molecular magnet. This coupling allows for the electric control of the spin (qubit) states, e.g. by using an STM tip or a microwave cavity. We propose an experimental test for identifying molecular magnets exhibiting spin-electric effects.

Chapter 2

Electrostatically coupled spins

We study the spin-spin coupling between two single-electron quantum dots due to the Coulomb and spin-orbit interactions, in the absence of tunneling between the dots. We find an anisotropic XY spin-spin interaction that is proportional to the Zeeman splitting produced by the external magnetic field. This interaction is studied both in the limit of weak and strong Coulomb repulsion with respect to the level spacing of the dot. The interaction is found to be a non-monotonic function of inter-dot distance a_0 and external magnetic field, and, moreover, vanishes for some special values of a_0 and/or magnetic field orientation. This mechanism thus provides a new way to generate and tune spin interaction between quantum dots. We propose a scheme to measure this spin-spin interaction based on the spin-relaxation-measurement technique.

2.1 Introduction

Electron spins in semiconductor nanostructures are not decoupled from the charge degree of freedom, one of the primary reasons for this coupling being the spin-orbit interaction. This coupling leads to many interesting phenomena in the physics of semiconductors [56, 57], an important one being the ability to control the spin of the electron with electric fields acting on its charge degrees of freedom [?, 58–62]. In GaAs quantum dots the spin-orbit interaction manifests itself as a weak perturbation when compared with the confinement energy. The measure of smallness is given by the ratio between the dot radius λ and the spin-orbit length, λ_{SO} —the distance over which an electron travels and thereby precesses by an angle π about the intrinsic 'magnetic' field induced by the spin-orbit interaction. We mention that there are also materials which possess large spin-orbit couplings, with the spin-orbit length on the same order as the dot size, *e.g.* InAs, InP quantum dots. Despite its smallness the spin-orbit interaction is very important for the coherence of the spin dynamics. For example, spin-orbit interaction allows for coupling of the electron spin to (bosonic) environments, such as phonons [63, 64] or particle-hole excitations in quantum point contacts [65], which in turn causes relaxation and decoherence of the spins. Moreover, electrons being charged particles interact via the long range Coulomb forces with each other, even if they are confined to well-separated quantum dots with no overlap of their wave functions. Through this electrostatic coupling and in combination with the spin orbit interaction, the spins of two electrons located in different dots become coupled even in the absence of tunneling between the dots.

In this section we provide a detailed analysis of such an effective spin-spin interaction for lateral quantum dots in a configuration as shown in Fig. 1. We will see that the origin of this interaction is the “tidal” effect each of the electrons produces on the charge distribution of the other electron via electrostatic forces. Because of the spin-orbit interaction, the electric dipole moment (as well as higher moments) in each dot couples to its electron spin. As a result, the two spins experience an interaction resembling a magnetic dipole-dipole interaction [66] with effective magnetic moments which can be strongly enhanced by up to a factor of 10^3 compared to the Bohr magneton. The magnitude of the spin-spin coupling obtained via this spin-electric effect can be efficiently controlled and even completely suppressed by adjusting external parameters such as the magnetic field direction, strength, and inter-dot distance.

The spin-spin interaction can, in principle, be used to perform two-qubit operations as required in the spin-based quantum computing scheme [4], because it entangles spins and can easily be switched on and off. We note that a similar mechanism for spin interaction based on electrostatic coupling was studied very recently in Ref. [67] for vertically coupled quantum dots, and in Ref. [68] for the special case of one-dimensional quantum dots formed in semiconducting nanowires. Besides the differences in geometry and dimensionality, both of these works treat only the case of weak Coulomb interaction (compared to the level spacing), while we treat here also the opposite limit of strong Coulomb interaction where new and interesting features emerge. In the limiting case of strongly elliptical dots we recover the one-dimensional results obtained in Ref. [68].

We emphasize again that in the present study we exclude tunneling and thus the type of spin interaction studied in the following is fundamentally different from the Heisenberg exchange interaction for which the presence of electron tunneling between the dots is crucial¹ [69–71]. Similarly, the combined effect of Heisenberg exchange interaction and spin-orbit coupling [72–76] is also based on tunneling and should be carefully distinguished from the spin-orbit effect studied here. We also note that the Heisenberg exchange coupling allows typically for much stronger spin-spin coupling than the electrostatically induced one. For instance, in GaAs dots the Heisenberg exchange can reach values on the order of 0.1 meV – 1 meV, which, as we shall see, exceeds the electrostatically induced spin coupling by three to four orders of magnitude. Nevertheless, the electrostatic spin coupling can prove useful for cases where it is difficult to get sufficient wave function overlap (needed for large Heisenberg exchange), and, moreover, it is also important to understand the electrostatic spin-effects in detail in order to get control over possible interference effects between different types of spin coupling. This will be for example of importance for spin qubit applications in order to minimize spin decoherence and gate errors.

Finally, in view of experimental tests we propose a scheme to measure the spin-spin interaction in a double dot setup with a nearby charge detector. We propose to combine the spin-measurement technique of Ref. [10] with the entangling property of the spin-spin interaction and present a gate pulsing sequence that enables one to access the coupling constant in the time domain by measuring the occupation probability of a Zeeman sublevel.

¹To distinguish between the two mechanisms we refer to the coupling studied in this work as ‘spin-spin coupling’ as opposed to the Heisenberg exchange coupling.

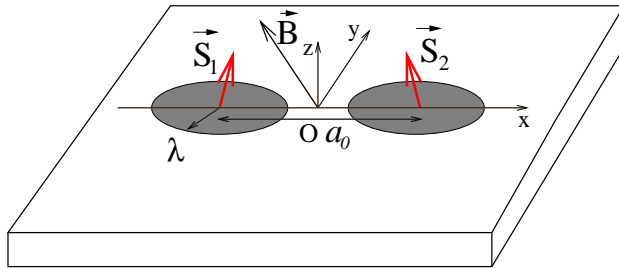


Figure 2.1: The figure shows a sketch of the model system which consists of two identical quantum dots in the xy -plane, separated by distance a_0 (measured from dot-center to dot-center). \vec{S}_i denotes the spin of electron $i = 1, 2$, λ is the dot radius, and \vec{B} is the external magnetic field. The respective orbital wave functions of electron 1 and 2 are assumed to have no overlap (i.e. tunneling between the dots is excluded). The remaining purely electrostatic Coulomb interaction between the electron charges leads, via spin-orbit interaction, to an effective coupling between their spins. This spin-spin interaction depends sensitively on the orientation of \vec{B} , with no component along it, and is proportional to \vec{B}^2 .

2.2 The Model

Our system consists of two electrons each of which is localized in a quantum dot, and the two dots are separated from each other, without tunneling between them. The system is composed of two gate-defined quantum dots in a two-dimensional semiconductor layer (*e.g.* GaAs or InAs). A schematics of the system we consider is shown in Fig 1.

We model the system by a harmonic confinement potential, which, for simplicity is assumed to be the same for both dots. Each dot is assumed to contain one electron with charge $-e$ and spin $\mathbf{S} = (\hbar/2)\boldsymbol{\sigma}$, with $\boldsymbol{\sigma} = (\sigma_x, \sigma_y, \sigma_z)$ being the Pauli matrices. The model Hamiltonian consisting of several terms reads

$$H = H_0 + H_Z + H_C + H_{SO}, \quad (2.1)$$

where H_0 is the energy of the two electrons in the confinement potentials

$$H_0 = \sum_{i=1,2} \left(\frac{p_i^2}{2m^*} + U(\mathbf{r}_i) \right). \quad (2.2)$$

Here, $\mathbf{p}_i = -i\hbar\partial/\partial\mathbf{r}_i + (e/c)\mathbf{A}(\mathbf{r}_i)$ is the 2D kinetic momentum of the i -th electron at position \mathbf{r}_i , m^* the effective mass, c the speed of light, $U(\mathbf{r}_i) = (m^*/2)\omega_0^2 r_i^2$ the confinement potential for the i -th electron which is assumed to be harmonic and isotropic, and $\mathbf{A}(\mathbf{r}_i)$ is the electromagnetic vector potential. The strength of the confinement energy is given by the frequency ω_0 . The second term on the right-hand side of Eq. (3.5) is the Zeeman energy of the two electrons,

$$H_Z = \frac{1}{2}g\mu_B\mathbf{B} \cdot (\boldsymbol{\sigma}_1 + \boldsymbol{\sigma}_2). \quad (2.3)$$

The third term in Eq. (3.5) is the unscreened Coulomb interaction between the two electrons,

$$H_C = \frac{e^2}{\kappa|\mathbf{r}_1 - \mathbf{r}_2 + \mathbf{a}_0|}, \quad (2.4)$$

where κ is the dielectric constant of the material and a_0 is the geometric distance between the two dots, namely between the potential minima ('center') of the dots. With this choice, we measure the distance for each electron from its own dot center. The last term in Eq. (3.5) is the spin-orbit coupling which for strong z -confinement is given by

$$H_{SO} = \sum_{i=1,2} [\beta(-p_x^i \sigma_x^i + p_y^i \sigma_y^i) + \alpha(p_x^i \sigma_y^i - p_y^i \sigma_x^i)], \quad (2.5)$$

being the sum of the Dresselhaus term [77] (β) coming from bulk inversion asymmetry and the Rashba term [78] (α) coming from structure inversion asymmetry. We assume the same coefficients β and α for both dots. It is convenient to work with center-of-mass and relative coordinates [79], as the Coulomb interaction couples only to the relative ones and the solution of the center-of-mass part is straightforward [80, 81]. This then involves the standard substitutions $M = 2m^*$, $m = m^*/2$, $\mathbf{R} = (\mathbf{r}_1 + \mathbf{r}_2)/2$, $\mathbf{r} = \mathbf{r}_1 - \mathbf{r}_2$, and $\mathbf{P} = \mathbf{p}_1 + \mathbf{p}_2$ and $\mathbf{p} = (\mathbf{p}_1 - \mathbf{p}_2)/2$.

2.3 Spin-Spin Coupling

We now turn our attention to the spin-orbit interaction. As was shown in Ref. [64], the spin-orbit coupling gives non-zero first order effects only if a magnetic field is present, as a consequence of the Kramers degeneracy. In order to describe the effective first order spin-orbit term in the presence of a magnetic field we make use of the Schrieffer-Wolff (unitary) transformation [?, 64]

$$\begin{aligned} \tilde{H} &= e^S (H_d + H_Z + H_{SO}) e^{-S} \\ &= H_d + \Delta H + e^S H_Z e^{-S}, \end{aligned} \quad (2.6)$$

where $S = -S^\dagger$ is chosen such that $\mathcal{P}\Delta H = \Delta H$, with the projector operator \mathcal{P} satisfying $\mathcal{P}A = \sum_n A_{nn}|n\rangle\langle n| \forall A$, and $H_d|n\rangle = E_n|n\rangle$. The Hamiltonian $H_d = H_0 + H_C$ (or $H_d = H_R + H_r + H_C$ in center-of-mass and relative coordinates). The Hamiltonian $\tilde{H} = H_d + \Delta H$ is diagonal in the basis of H_d and has the same energy spectrum as the Hamiltonian $H = H_d + H_{SO}$. In first order of the spin-orbit interaction H_{SO} the transformation generator becomes $S = (1 - \mathcal{P})L_d^{-1}H_{SO}$, where L_d is the dot Liouvillean, $L_d A = [H_R + H_r + H_C, A]$, $\forall A$. Evaluating this expression explicitly we obtain

$$S = (1 - \mathcal{P})i \sum_{i=1,2} \boldsymbol{\xi}_i \cdot \boldsymbol{\sigma}_i, \quad (2.7)$$

with $\boldsymbol{\xi}_{1,2} = (y_{1,2}/\lambda_+, x_{1,2}/\lambda_-, 0)$. In second order in spin-orbit coupling the transformed Hamiltonian \tilde{H} becomes

$$\tilde{H} = H_R + H_r + H_Z + H_C + H_{SO}^Z + \Delta H_{SO}, \quad (2.8)$$

with $H_{SO}^Z = H_{SO}^{Z1} + H_{SO}^{Z2}$ and $\Delta H_{SO} = 1/2[S, H_{SO}] + [S, [S, H_Z]]$ where

$$H_{SO}^{Z1,2} = [S, H_Z^{1,2}] = E_Z(1 - \mathcal{P})[\mathbf{l} \times (\boldsymbol{\xi}_R \pm \boldsymbol{\xi}_r/2)] \cdot \boldsymbol{\sigma}_{1,2} \quad (2.9)$$

$$\begin{aligned} \Delta H_{SO} = & \frac{\hbar}{m^* \lambda_- \lambda_+} (1 - \mathcal{P}) \sum_{i=1,2} (x_i p_{iy} - y_i p_{ix}) \sigma_{iz} \\ & + E_Z \frac{1}{\lambda_- \lambda_+} (1 - \mathcal{P}) \sum_{i=1,2} [(\mathbf{l} \times \boldsymbol{\xi}_i) \times \boldsymbol{\xi}_i] \sigma_i. \end{aligned} \quad (2.10)$$

In Eqs. (2.9) and (2.10) $\mathbf{l} = \mathbf{B}/B$ is the magnetic field direction vector, $E_Z = g\mu_B B$ is the Zeeman energy and the vectors $\boldsymbol{\xi}_R$ and $\boldsymbol{\xi}_r$ are given by $\boldsymbol{\xi}_R = (Y'/\lambda_-, X'/\lambda_+, 0)$ and $\boldsymbol{\xi}_r = (y'/\lambda_-, x'/\lambda_+, 0)$, respectively. The new coordinates correspond to a rotation by an angle $\pi/4 - \gamma$ with respect to the coordinate frame in which the direction of the \mathbf{a}_0 -vector is associated with the x -axis in the $XY(xy)$ plane so that the final expressions have the simplest form [64]. Here, γ is the angle between the xy frame in Fig. 1 and the normal axes of the crystal. The spin-orbit lengths λ_{\pm} are given in the form $1/\lambda_{\pm} = m^*(\beta \pm \alpha)$. The terms which are of second order in spin-orbit coupling in Eq. (2.10) (which are also zero and first order respectively in Zeeman splitting) are single-spin terms and no coupling between spins take place in this order. In fact, they are just second order terms which are present in perturbation theory for an isolated spin in a QD, but now renormalized by the Coulomb interaction between the two electrons. We neglect these terms in the following analysis since they only change the on-site Zeeman interaction by a small amount. We are now in a position to derive the coupling between the two spins. This is achieved by performing a second Schrieffer-Wolff (SW2) transformation which excludes the first order contribution in spin-orbit interaction with no diagonal matrix elements. The new transformed Hamiltonian has the form $H_{eff} = e^T \tilde{H} e^{-T}$, with T given by

$$T = (1 - \mathcal{P}) i(L_d + L_Z)^{-1} H_{SO}^Z. \quad (2.11)$$

We assume now that the Zeeman energy is smaller than the orbital confining energy, $E_Z \ll \hbar\omega_0$, which is usually the case for electrons in quantum dots, such that we can neglect in Eq. (2.11) the Zeeman Liouvillean L_Z (for spin-orbit effects due to level crossing see Ref. [25]). In second-order in spin-orbit coupling the effective Hamiltonian H_{eff} becomes

$$H_{eff} = H_d + H_Z + \frac{1}{2} [L_d^{-1} H_{SO}^Z, H_{SO}^Z]. \quad (2.12)$$

The last term in Eq. (2.12) contains the desired spin-spin coupling between the two spins. However, besides this interaction it also contains some self-interaction terms which renormalizes only the Zeeman splitting. We will not study those terms since they are of no practical interest in the case of identical dots. We consider a general magnetic field $\mathbf{B} = (\cos \Phi \sin \theta, \sin \Phi \sin \theta, \cos \theta)$, where θ is the angle between the magnetic field and the z -axis perpendicular to the 2DEG plane and Φ the angle between the in-plane component of the magnetic field and the x -direction (Fig. 1). The interaction between the two spins has the most general form

$$\tilde{H}_s = \frac{1}{2} \sum_{i \neq j} [L_d^{-1} H_{SO}^{Zi}, H_{SO}^{Zj}], \quad i, j = 1, 2. \quad (2.13)$$

The spin Hamiltonian is obtained by averaging over the orbital ground state, $H_s = \langle 0 | \tilde{H}_s | 0 \rangle$. We then obtain

$$H_s = \boldsymbol{\sigma}_1 \cdot \overline{\mathbf{M}} \boldsymbol{\sigma}_2, \quad (2.14)$$

where

$$\overline{\overline{M}}_{ab} = E_Z^2 \langle 0 | [(\mathbf{l} \times L_d^{-1} \boldsymbol{\xi}_1)_a, (\mathbf{l} \times \boldsymbol{\xi}_2)_b] | 0 \rangle, \quad a, b = x, y, z. \quad (2.15)$$

We note that there is no component of the spin along the magnetic field direction as a consequence of the vector product in the tensor $\overline{\overline{M}}$. By diagonalizing the above tensor, we obtain for the Hamiltonian H_s the reduced expression

$$H_s = J_{\tilde{x}} \sigma_{\tilde{x}}^1 \sigma_{\tilde{x}}^2 + J_{\tilde{y}} \sigma_{\tilde{y}}^1 \sigma_{\tilde{y}}^2, \quad (2.16)$$

where the couplings $J_{\tilde{x}, \tilde{y}}$ depend on the magnetic field orientation and on the functions $C_{a_1 b_2} = \langle 0 | [L_d^{-1} a_1, b_2] | 0 \rangle$, with $a, b = x, y$ (for explicit expressions see the Appendix A). Thus, the effective spin-spin interaction is highly anisotropic, and, in general, of the *XY*-type. We note in particular that for an in-plane magnetic field ($\theta = \pi/2$), the spin Hamiltonian reduces to the Ising Hamiltonian, $H_s = J_{\tilde{y}} \sigma_{\tilde{y}}^1 \sigma_{\tilde{y}}^2$ (in a transverse magnetic field). Next, we rewrite H_s in terms of raising/lowering spin operators $\sigma_{\pm} = \sigma_{\tilde{x}} \pm i\sigma_{\tilde{y}}$

$$H_s = J_{eff} (\sigma_+^1 \sigma_-^2 + \sigma_-^1 \sigma_+^2) + J'_{eff} (\sigma_-^1 \sigma_-^2 + \sigma_+^1 \sigma_+^2), \quad (2.17)$$

with $J_{eff} = (1/2)(J_{\tilde{x}} + J_{\tilde{y}})$ and $J'_{eff} = (1/2)(J_{\tilde{x}} - J_{\tilde{y}})$. We recall now that the *full* spin Hamiltonian includes the Zeeman energy, given in Eq. (2.3), which leads to a large energy gap with $2E_Z \gg J_{\tilde{x}, \tilde{y}}$. We will find below that typically

$$\frac{J_{\tilde{x}, \tilde{y}}}{E_Z} \sim \frac{E_Z}{\hbar\omega_0} \left(\frac{\lambda}{\lambda_{SO}} \right)^2 \ll 1 \quad (2.18)$$

under our assumption that $E_Z \ll \hbar\omega_0$ and $\lambda \ll \lambda_{SO}$. As a consequence, we can neglect in Eq. (2.17) the terms proportional to J'_{eff} since they cause transitions between different Zeeman levels of the total spin. The relevant spin-spin interaction, H_s^{eff} , which acts only within the $S - T_0$ subspace, becomes then

$$H_s^{eff} = J_{eff} (\sigma_+^1 \sigma_-^2 + \sigma_-^1 \sigma_+^2). \quad (2.19)$$

Thus, we are left with the task of calculating the coupling strengths $J_{\tilde{x}, \tilde{y}}$ and J_{eff} . Because of the Coulomb term, Eq. (2.4), this cannot be done exactly and some approximations are required. They will depend on the ratio δ between the Coulomb interaction strength, $e^2/\kappa a_0$, and the orbital level spacing, $\hbar\omega_0$, giving $\delta = (e^2/\kappa a_0)/\hbar\omega_0 = (\lambda/a_B) \cdot (\lambda/a_0)$, with $\lambda = \sqrt{\hbar/m^* \omega_0}$ being the dot radius and $a_B = \hbar^2 \kappa / m^* e^2$ - the Bohr radius in the material. In other words, the parameter δ will dictate the physics of the system, and from now on we will speak of the ratio λ/a_B as being the Coulomb interaction strength (representing in fact the 'true' Coulomb strength for touching dots). For making the following analysis more transparent we focus on the case with only Rashba spin-orbit coupling ($\lambda_- = \lambda_+ \equiv \lambda_{SO}$). The generalization to the case with both Rashba and Dresselhaus terms present is straightforward, but at the cost of more complicated expressions (see Appendix A).

2.3.1 Weak Coulomb coupling - $\delta \ll 1$

One interesting case is met when $\delta \ll 1$, such that the Coulomb interaction can be treated as a perturbation compared to the orbital level spacing. In this case, one can retain only the first

order contribution from the Coulomb interaction, which translates into the approximation $L_d^{-1} \approx L_0^{-1} - L_0^{-1} L_C L_0^{-1}$. Making use of this and after some algebra we obtain for the spin-spin coupling the following expression

$$H_s = \int d\mathbf{r}_1 d\mathbf{r}_2 \frac{\delta\rho_1 \delta\rho_2}{\kappa |\mathbf{r}_1 - \mathbf{r}_2 + \mathbf{a}_0|}, \quad (2.20)$$

where the operators $\delta\rho_i$, $i=1,2$, are the charge density distribution modifications in each dot as a consequence of the spin-orbit interaction. They are defined as

$$\delta\rho_i = \rho_i - \rho_i^0, \quad i = 1, 2, \quad (2.21)$$

with ρ_i^0 being the charge density operator in the absence of spin-orbit interaction and $\rho_i = e^{T_0} \rho_i^0 e^{-T_0}$ the one in the presence of spin-orbit interaction, with $T_0 = L_0^{-1} H_{SO}^Z$ for the present approximation. From Eq. (2.20) we see that the spin interaction results from a Coulomb-type of coupling between two charge density distributions which themselves depend on spin.

Let us now analyze in more detail Eq. (2.20). The first task is to find $\delta\rho_i$, for $i = 1, 2$, namely the spin-orbit induced charge distribution or the spin-dependent charge distributions for each dot. In order to do this, we give first some important relations valid in the case of harmonic confining potential, relations which are used in the following for the derivation of the main results

$$L_0^{-1} x_i = -\frac{i}{\hbar m^* \omega_0^2} \left(p_x^i + \frac{e B_z}{c} y_i \right) \quad (2.22)$$

$$L_0^{-1} y_i = -\frac{i}{\hbar m^* \omega_0^2} \left(p_y^i - \frac{e B_z}{c} x_i \right) \quad (2.23)$$

$$L_0^{-1} \mathbf{p}_i = \frac{i m^*}{\hbar} \mathbf{r}_i. \quad (2.24)$$

Making use of the relations Eqs. (2.22–2.24) and within the first order of spin-orbit coupling, *i.e.* $\delta\rho_i \approx [T_0, \rho_i^0]$, we obtain

$$\begin{aligned} \delta\rho_i(\mathbf{r}) = \frac{2E_Z e}{m^* \lambda^2 \omega_0^2 \lambda_{SO}} \rho_{0i} & \left[\cos\theta (y_i \cos\Phi + x_i \sin\Phi) \sigma_x^i \right. \\ & \left. + (y_i \sin\Phi - x_i \cos\Phi) \sigma_y^i \right], \end{aligned} \quad (2.25)$$

with ρ_i^0 being the bare charge density in the dot corresponding to the ground state and which assumes the well-known form for harmonic potentials

$$\rho_i^0(\mathbf{r}) = \frac{1}{\pi \lambda^2} e^{-\frac{(x_i^2 + y_i^2)}{\lambda^2}}. \quad (2.26)$$

We note that when there exist a perpendicular component of the magnetic field, the dot radius is renormalized due to the orbital effect of the magnetic field $\lambda \rightarrow \lambda(1 + r^2)^{-1/4}$, with $r = \omega_0/2\omega_c$ ($\omega_c = eB_z/m^*c$, $B_z = B \cos\theta$). However, we will still refer to λ as being the dot radius, with the appropriate expression depending on the magnetic field orientation. We could now insert the expression Eq. (2.25) for $\delta\rho_i$ in Eq. (2.20) and compute directly the spin Hamiltonian. However, working with the Coulomb potential, it is more convenient to

work with the center-of-mass and relative coordinates and for simplicity the x -axis along the inter-dot direction \mathbf{a}_0 . Assuming for simplicity a perpendicular magnetic field, the spin Hamiltonian H_s takes the form

$$H_s = \frac{4E_Z^2 e^2}{m^{*2} \lambda^4 \omega_0^4 \lambda_{SO}^2} \iint d\mathbf{r} d\mathbf{R} \rho_0(r) \rho_0(R) \times \frac{(X^2 - x^2/4) \sigma_x^1 \sigma_x^2 + (Y^2 - y^2/4) \sigma_y^1 \sigma_y^2}{\kappa \sqrt{y^2 + (x + a_0)^2}}, \quad (2.27)$$

with the electronic densities $\rho_0(r) = (2/\pi\lambda^2) \exp(-r^2/2\lambda^2)$ for the relative coordinates, and $\rho_0(R) = (1/2\pi\lambda^2) \exp(-2R^2/\lambda^2)$ for the center-of-mass coordinates. In Eq. (2.27) there are no mixed terms like $\sigma_x^1 \sigma_y^2$ since those terms vanish because of the odd symmetry of the integrands in the case of harmonic confinement, which reflects inversion symmetry. The limit of in-plane magnetic field is obtained very easy from Eq. (2.27) by substituting the denominator with $[(X^2 - x^2/4) \cos^2 \Phi + (Y^2 - x^2/4) \sin^2 \Phi] \sigma_y^1 \sigma_y^2$. [For general field orientation the expression for H_s is more complicated (see Appendix A).] In order to make the following analysis more transparent, we introduce the dimensionless coordinates $\mathbf{r} \rightarrow \mathbf{r}/\lambda$ and $\mathbf{R} \rightarrow \mathbf{R}/\lambda$. The integration over the center-of-mass coordinates is now straightforward and the reduced expression for the spin Hamiltonian becomes

$$H_s = \frac{E_Z^2}{m^{*2} \lambda \omega_0^4 \lambda_{SO}^2} (\Delta E_C^x \sigma_x^1 \sigma_x^2 + \Delta E_C^y \sigma_y^1 \sigma_y^2), \quad (2.28)$$

for a perpendicular magnetic field and

$$H_s = \frac{E_Z^2}{m^{*2} \lambda \omega_0^4 \lambda_{SO}^2} (\Delta E_C^x \sin^2 \Phi + \Delta E_C^y \cos^2 \Phi) \sigma_y^1 \sigma_y^2, \quad (2.29)$$

for an in-plane magnetic field oriented at an angle Φ with respect to the inter-dot distance vector \mathbf{a}_0 . The energy differences $\Delta E_C^{x,y}$ are given by

$$\Delta E_C^x = \frac{e^2}{\kappa \lambda^2} \int d\mathbf{r} \rho_0(r) \frac{1 - x^2}{\sqrt{y^2 + (x + a_0/\lambda)^2}}, \quad (2.30)$$

$$\Delta E_C^y = \frac{e^2}{\kappa \lambda^2} \int d\mathbf{r} \rho_0(r) \frac{1 - y^2}{\sqrt{y^2 + (x + a_0/\lambda)^2}}. \quad (2.31)$$

The ground state and the first excited states of the dots in relative coordinates give rise to different charge distributions (ρ_0 , ρ_{1x} , and ρ_{1y} , respectively), and thus to different potential energies seen by a test charge at a distance a_0 (along x) away from the center of the charge distribution (in relative coordinates). $\Delta E_C^{x,y}$ are the differences between these potential energies.

Before studying the distance dependence of the spin Hamiltonian H_s (determined by $\Delta E_C^{x,y}$) in the entire range of distances, it is instructive to see how the expression Eq. (2.20) behaves in the large distance limit, $a_0 \gg \lambda$, and to make some comparison with the magnetic dipolar interaction in vacuum [57]. We perform a multipole expansion of the Hamiltonian in Eq. (2.20). The first non-zero contribution takes the form of a dipole-dipole interaction

between two spin-dependent electric dipoles, or phrased differently, the interaction between two charge-induced magnetic dipoles

$$H_s \approx \frac{\mathbf{m}_1 \cdot \mathbf{m}_2 - 3(\mathbf{m}_1 \cdot \mathbf{n}_a)(\mathbf{m}_2 \cdot \mathbf{n}_a)}{\kappa a_0^3}, \quad (2.32)$$

with the dipole moments \mathbf{m}_i given by

$$\mathbf{m}_i = Tr_{orb}[\delta\rho_i \mathbf{r}_i] = \bar{\mu} \boldsymbol{\sigma}_i, i = 1, 2. \quad (2.33)$$

Here, the trace is taken over the orbital degrees of freedom with $\mathbf{n}_a = \mathbf{a}_0/a_0$ and $\bar{\mu}$ being the tensor corresponding to an effective spin-orbit induced magneton

$$\bar{\mu} = \frac{eE_Z}{m^* \omega_0^2 \lambda_{SO}} \begin{pmatrix} -\cos\theta & 0 & 0 \\ 0 & \cos\theta & 0 \\ 0 & \sin\theta & 0 \end{pmatrix}. \quad (2.34)$$

We see from Eq. (2.34) that the tensor $\bar{\mu}$ depends on the magnetic field orientation with respect to the 2DEG and that it is also anisotropic, in contrast to the usual isotropic Bohr magneton $\mu_B = e\hbar/2m_e c$ (m_e is the mass of the free electron and c the speed of light). We note that the z -component of the induced magnetic moment (with $\hat{z} \parallel \mathbf{B}$) vanishes, *i.e.* $\mathbf{m} = (m_x, m_y, 0)$. Let us quantify the strength of $\bar{\mu}$ by the norm $\|\bar{\mu}\| = (1/\sqrt{3})\sqrt{\sum_{i,j} \mu_{ij}^2}$, *i.e.*

$$\|\bar{\mu}\| = \frac{1}{\sqrt{3}} \frac{eE_Z}{m^* \omega_0^2 \lambda_{SO}} \sqrt{1 + \cos^2\theta}. \quad (2.35)$$

We compare now $\|\bar{\mu}\|$ with μ_B . First of all, we note that $\|\bar{\mu}\|$ vanishes when there is no Zeeman splitting. However, for finite magnetic fields, $\|\bar{\mu}\|$ can exceed μ_B by many orders of magnitude in the case of quantum dots. To give an estimate, we assume $\hbar\omega_0 \approx 0.5$ meV, $E_Z \approx 0.05$ meV ($B \approx 2$ T) and $m^* = 0.067m_e$, $\lambda_{SO} \approx 10^{-6}$ m for GaAs quantum dots. With these values, and taking $\theta = 0$ (perpendicular magnetic field) we obtain

$$\frac{\|\bar{\mu}\|}{\mu_B} = \frac{4}{\sqrt{3}} \frac{E_Z}{\hbar\omega_0} \frac{m_e}{m^*} \frac{c}{\omega_0 \lambda_{SO}} \approx 10^3. \quad (2.36)$$

We describe now in more detail the limit of large distance between the dots. From Eqs. (2.28) and (2.27) we find for $a_0 \gg \lambda$

$$H_s = J(\sigma_y^1 \sigma_y^2 - 2\sigma_x^1 \sigma_x^2), \quad (2.37)$$

for a perpendicular magnetic field, and

$$H_s = J(\cos^2 \Phi - 2\sin^2 \Phi) \sigma_y^1 \sigma_y^2 \quad (2.38)$$

for an in-plane magnetic field, with the coupling strength J having the form

$$J = \frac{E_Z^2 e^2}{\kappa m^* \omega_0^4 \lambda_{SO}^2 a_0^3}. \quad (2.39)$$

From Eq. (2.39) we see a large distance decay $\sim a_0^{-3}$, *i.e.* a long range type behavior. We note also that the large distance result in Eq. (2.39) does not depend anymore on the orbital effect of the magnetic field. Working instead with the effective Hamiltonian defined in Eq. (2.19), the effective coupling strength J_{eff} for arbitrary magnetic field is given by

$$J_{eff} = -\frac{J}{2} [1 + \sin^2 \theta (1 - 3 \sin^2 \Phi)]. \quad (2.40)$$

We note that the spin coupling can range from maximally ferromagnetic interaction with $J_{eff} = -J$ at $\theta = \pi/2$ and $\Phi = 0$ to maximally antiferromagnetic interaction with $J_{eff} = J/2$ at $\theta = \pi/2$ and $\Phi = \pi/2$, and with J_{eff} passing through zero for certain angles.

Next, we consider the case of arbitrary distance but still with small Coulomb interaction strength as defined at the beginning of this section. Considering H_s^{eff} defined in Eq. (2.19) we obtain

$$J_{eff} = E_Z \frac{\lambda}{a_B} \frac{E_Z}{\hbar\omega_0} \left(\frac{\lambda}{\lambda_{SO}} \right)^2 G(a_0/\lambda, \theta, \Phi), \quad (2.41)$$

where

$$G(a_0/\lambda, \theta, \Phi) = \frac{\kappa\lambda}{e} [(\cos^2 \theta \cos^2 \Phi + \sin^2 \Phi) \Delta E_C^y + (\cos^2 \theta \sin^2 \Phi + \cos^2 \Phi) \Delta E_C^x]. \quad (2.42)$$

The function $G(a_0/\lambda, \theta, \Phi)$ is plotted in Fig. 2 for different angles θ and Φ . As for the large distance limit in Eq. (2.40), a similar but more complicated ferromagnetic-antiferromagnetic crossover behavior occurs as a function of the field orientation. However, in this case this behavior can also be induced by changing the distance between the dots a_0 (see Fig. 2.2).

Eq. (2.41) suggests that the condition $\delta \ll 1$ is too restrictive. Instead, the weaker condition $(\lambda/a_B)(\lambda/a_0)^3 \ll 1$ is sufficient for the approximation to be valid. Fig. 2 shows a breakdown of the dipolar approximation (*i.e.* of the a_0^{-3} decay), occurring at a dot separation $a_0/\lambda \approx 2$ for perpendicular magnetic fields ($\theta = 0$), and also a cancellation of this interaction for some given distance, which is around $a_0/\lambda \approx 1.8$. This shows that the sum of the two electrostatic energy differences $\Delta E_C^x + \Delta E_C^y$ has a non-monotonic behavior as a function of the distance a_0 . Actually, only ΔE_C^x is non-monotonic, whereas ΔE_C^y has a positive value which decreases with a_0 , as can be seen from Fig. 2. If an in-plane magnetic field is applied along y ($\Phi = 0$) or x ($\Phi = \pi/2$) direction, we obtain a dependence only either on ΔE_C^y or on ΔE_C^x . Accordingly, $G(a_0/\lambda)$ will be larger in some parameter range as compared with the case of perpendicular fields, see Fig. 2. At this point it is instructive to consider numerical estimates for the coupling strength J_{eff} . For this we consider GaAs quantum dots for which we assume $\lambda_{SO} \approx 10^{-6}$ m, $m^* = 0.067 m_e$, $g = -0.44$, $\kappa = 13$, and also consider $\hbar\omega_0 \approx 0.5$ meV, $E_Z = 0.05$ meV ($B \approx 2$ T) and $a_0 = 5 \cdot 10^{-7}$ m. These estimations lead to a coupling strength $J \approx 10^{-10}$ eV, which lead to a time dynamics of the order of 10^{-5} s. If this time scale is longer than the decoherence times in GaAs quantum dots, the system will be insensitive to the coherent dynamics induced by the coupling J_{eff} . Shorter time scales are obtained for materials with larger spin-orbit coupling such as InAs. The spin-orbit length λ_{SO} in this material is comparable with a typical dot size of about 100 nm. Even though our perturbative approach starts to get unreliable in this case, it still can provide a rough estimate for the coupling strength. For InAs we have $m^* = 0.023 m_e$, $g = 14.8$, $\kappa = 13$,

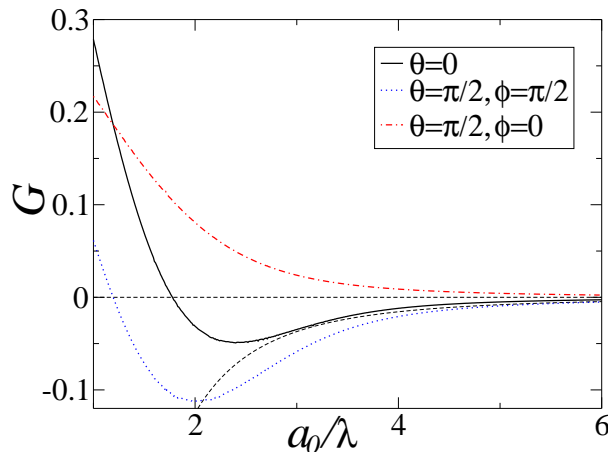


Figure 2.2: The function G occurring in Eq. (2.42) plotted as a function of the geometric distance a_0 between the dot centers scaled by the dot radius λ for different magnetic field orientations. The dashed line represents the dipolar approximation of G for a perpendicular magnetic field ($\theta = 0$) which scales like a_0^{-3} .

$\lambda_{SO} \approx 100\text{nm}$, and we choose $\hbar\omega_0 \approx 1\text{meV}$, $E_Z \approx 0.1\text{meV}$ and $a_0/\lambda \approx 3$. With those values we obtain for the coupling $J_{\text{eff}} \approx 10^{-7}\text{eV}$, which corresponds to a switching time of about $\sim 50\text{ns}$ for a swap of the spin states of electron one and electron two. This time scale for the spin dynamics is shorter than the expected spin decoherence time in such quantum dots. Thus, this interaction mechanism provides a useful way for the dynamical control of the spin-spin coupling. As discussed before, for an in-plane magnetic field the coupling constant could even be higher, depending on the angle of the magnetic field with respect to the inter-dot axis.

2.3.2 Elliptical dots with $\delta \ll 1$

We briefly generalize the previous results to elliptical dot shapes. This will also allow us to study the one-dimensional limit and recover previous results obtained for one-dimensional nanowires [68]. We consider elliptical dots which are characterized by the frequencies ω_{0x} and ω_{0y} corresponding to the x and y directions, respectively. In this case, Eq. (2.39) is replaced by

$$H_s = \frac{e^2 E_Z^2}{m^* \lambda_{SO}^2} \left(\frac{\Delta E_C^x}{\omega_{0x}^4 \lambda_1^2} \sigma_x^2 \sigma_x^2 + \frac{\Delta E_C^y}{\omega_{0y}^4 \lambda_2^2} \sigma_y^1 \sigma_y^2 \right), \quad (2.43)$$

where the electrostatic energies $\Delta E_C^{x,y}$ become now

$$\Delta E_C^x = \frac{1}{\kappa \lambda_1} \int d\mathbf{r} \rho_0(\mathbf{r}) \frac{1 - x^2}{\sqrt{y^2 + (x + a_0/\lambda_1)^2}}, \quad (2.44)$$

$$\Delta E_C^y = \frac{1}{\kappa \lambda_2} \int d\mathbf{r} \rho_0(\mathbf{r}) \frac{1 - y^2}{\sqrt{y^2 + (x + a_0/\lambda_2)^2}}, \quad (2.45)$$

with the charge density distribution function, expressed in relative coordinates,

$$\rho_0(\mathbf{r}) = \frac{2}{\pi\lambda_1\lambda_2} e^{-x^2/2\lambda_1^2 - y^2/2\lambda_2^2}. \quad (2.46)$$

For perpendicular magnetic fields and elliptical dots the lengths $\lambda_{1,2}$ are given by [?]

$$\lambda_{1,2} = \sqrt{\frac{4\hbar(n+1)}{m_{1,2}^*\omega_{1,2}}}, \quad (2.47)$$

where $n = m_1 m_2 \omega_1 \omega_2 \omega_c^2 / B^2$, $\omega_{1,2} = \sqrt{A \pm B} / 2$, $m_{1,2} = 2B / (C \pm \omega_c^2 + B)$, and $m_{1,2}^* = m_{1,2} m^*$ with the explicit expressions for A , B , and C

$$A = \omega_{0x}^2 + \omega_{0y}^2 + \omega_c^2, \quad (2.48)$$

$$B = \sqrt{(\omega_{0x}^2 + \omega_{0y}^2 + \omega_c^2)^2 - 4\omega_{0x}^2 \omega_{0y}^2}, \quad (2.49)$$

$$C = \omega_{0x}^2 - \omega_{0y}^2. \quad (2.50)$$

Taking now also the limit of strongly elliptical dots, *i.e.* $\omega_{0y} \gg \omega_{0x}, \omega_c$, we see that this is equivalent to keeping only one component of the spin interaction, namely the $\sigma_x^1 \sigma_x^2$ part, and that the orbital effect of the magnetic field drops out. The resulting Hamiltonian then becomes

$$H_s = \frac{e^2 E_Z^2 \Delta E_C^x}{m^{*2} \omega_{0x}^4 \lambda^2 \lambda_{SO}^2} \sigma_x^1 \sigma_x^2 + O((\omega_{0x} / \omega_{0y})^4). \quad (2.51)$$

Considering now the large distance limit, $a_0 \gg \lambda$, analogously to Eq. (2.37), our result reduces formally to the one in Ref. [68], *i.e.*

$$H_s = -2 \frac{E_Z^2 e^2}{\kappa m^{*2} \omega_{0x}^4 \lambda_{SO}^2 a_0^3} \sigma_x^1 \sigma_x^2 + O((\omega_{0x} / \omega_{0y})^4). \quad (2.52)$$

The above expression, Eq. (2.52), can be also obtained directly from Eq. (2.37) since within the considered limit there is no orbital effect of the perpendicular magnetic field on the spin-spin interaction. We note that in this limit the resulting spin-spin coupling takes the form of an Ising interaction which, together with single qubit rotations, can be used [4] to efficiently perform CNOT gate operations between two qubits. We finally note that in one dimensions the Rashba interaction can be treated exactly, leading to a renormalization of the g -factor [68], $g \rightarrow g \exp(-\lambda^2 / \lambda_{SO}^2)$. This exact treatment is no longer possible in the 2D case considered here, except for the special case [82] when $\alpha = \pm\beta$ and the problem becomes effectively 1D [82].

2.3.3 Strong Coulomb coupling - $\delta \geq 1$

We turn now to the more involved case of strong Coulomb interaction strength, $\delta \geq 1$, which cannot be treated perturbatively. However, some approximations are still possible and we will explore two of them in the following section. The first approximation consists in reducing the two electron system to two classical point-charge particles. The classical equilibrium

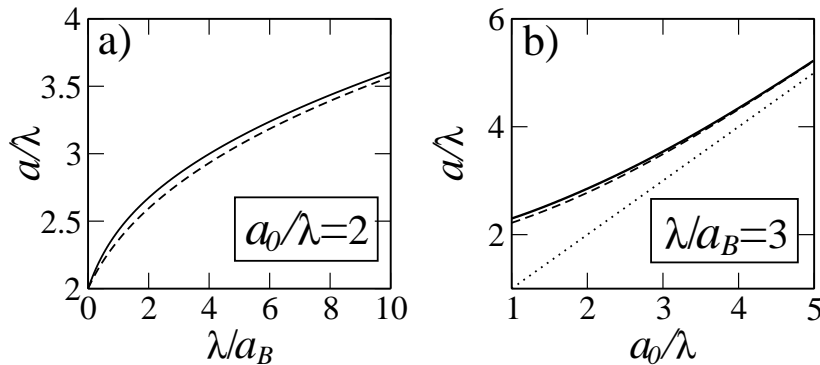


Figure 2.3: a) The effective distance a as a function of the Coulomb interaction strength λ/a_B for $a_0/\lambda = 2$. The full line represents the variational result from Eq. (2.57). The dashed line corresponds to the one obtained from the classical equilibrium solution of Eq. (2.53). b) Effective distance a/λ as a function of the geometrical one a_0/λ for $\lambda/a_B = 3$. All distances are scaled with the dot radius λ . The dotted line is a_0/λ which is shown for comparison.

condition will be obtained by minimizing the total potential energy of the two particles. By doing this, the motion of the electrons will take place around the new equilibrium positions obtained from the equation

$$a^2(a - a_0) = 2\lambda^4/a_B, \quad (2.53)$$

where a_0 is the initial geometric distance and a the effective distance between the electrons in classical equilibrium. However, we are interested in the motion around the equilibrium position, which means that for small deviations, we may substitute the full Coulomb interaction with an effective one, remembering that $\mathbf{r} = \mathbf{r}_1 - \mathbf{r}_2$,

$$\frac{e^2}{\kappa|\mathbf{r} + \mathbf{a}_0|} \rightarrow \frac{e^2}{2\kappa a^3} (3(\mathbf{n}_a \cdot \mathbf{r})^2 - r^2). \quad (2.54)$$

We note that the coordinates are measured now with respect to the new equilibrium position. Within this approximation, the relative Hamiltonian H_r is replaced with the new, renormalized one, \tilde{H}_r

$$\tilde{H}_r = \frac{p^2}{2m} + \frac{1}{2}m\omega_x^2 x^2 + \frac{1}{2}m\omega_y^2 y^2, \quad (2.55)$$

with the definition $\omega_{x,y} = b_{x,y}\omega_0$ and $b_{x,y}$ given by the expressions

$$b_x = \sqrt{1 + 4(\lambda/a_B)(\lambda/a)^3}, \quad b_y = \sqrt{1 - 2(\lambda/a_B)(\lambda/a)^3}. \quad (2.56)$$

We see that this approximation leads only to a renormalization of the orbital frequencies of the relative Hamiltonian. We proceed now to develop a second alternative for treating the Coulomb interaction, namely a variational method based on the same picture of classical equilibrium. This consists in substituting the full Coulomb interaction term with the same type of expression like in Eq. (2.53), but with the effective distance obtained from the variational ansatz. For this we minimize the expectation value of the orbital Hamiltonian, $H_r + H_C$, in the ground state of the effective relative Hamiltonian \tilde{H}_r [Eq. (2.55)] with respect

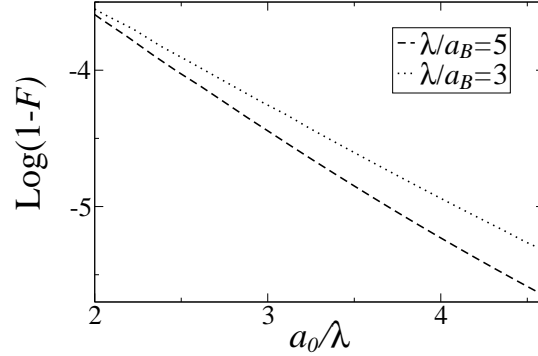


Figure 2.4: The logarithm of infidelity $1 - F$ from Eq. (2.62) as a function of the geometric distance a_0/λ (scaled with the dot radius λ) for two different values of Coulomb interaction strength λ/a_B .

to the effective distance a . This leads to the following equation

$$\frac{\partial}{\partial a} \langle \tilde{\psi}_0 | H_r + H_C | \tilde{\psi}_0 \rangle = 0, \quad (2.57)$$

where $|\tilde{\psi}_0\rangle$ is the ground state belonging to \tilde{H}_r , *i.e.* $\tilde{H}_r |\tilde{\psi}_0\rangle = \tilde{E}_0 |\tilde{\psi}_0\rangle$, with \tilde{E}_0 the ground state energy. Since we are dealing with harmonic oscillators, those wave functions are known. However, Eq. (2.57) for the effective distance a can be solved only numerically. We plot in Fig. 3 the results obtained for the effective distance a as a function of different parameters in both cases, namely the variational result from Eq. (2.57) and also the result obtained from the classical equilibrium condition in Eq. (2.53). We see in Fig. 3 that there is very good agreement between the two approaches in a wide parameter range and moreover, that the effective distance within the variational approach is larger than the one obtained from classical equilibrium, that means a lower ground state energy. We note that a perpendicular magnetic field practically does not change the curves in Fig. 3 (not shown) on a large range of magnetic field strengths ($0 < \omega_c < 3\omega_0$), which means that the effective distance is to a very good approximation independent of the applied magnetic field. In order to verify the accuracy of our variational method, we checked also the numerical fidelity, defined as the overlap of the wave functions in the variational case with the exact (almost, in the sense of perturbation theory) wave function. Although the problem contains no small parameter, we can still define small matrix elements compared with level spacing in a numerical sense. For this we write the full relative Hamiltonian in the following way

$$H_r = \tilde{H}_r + V, \quad (2.58)$$

with the effective Coulomb interaction V (see Eq. (2.54)) expressed now also in terms of the new equilibrium coordinates (introduced after Eq. (2.54)),

$$V = \frac{e^2}{\kappa |\mathbf{r} + \mathbf{a}|} - \frac{e^2}{2\kappa a^3} (3(\mathbf{n}_{a0} \cdot \mathbf{r})^2 - r^2) + \frac{e^2 x}{\kappa a^2}. \quad (2.59)$$

We show now that this term leads to small matrix elements so that indeed $|V_{0n}| \ll |\tilde{E}_n - \tilde{E}_0|$, where the energies \tilde{E}_n and \tilde{E}_0 are the n -eigenvalue and ground-state energy of the

Hamiltonian \tilde{H}_r , respectively. To see this numerically we introduce the fidelity

$$F = \left| \langle \psi_0 | \tilde{\psi}_0 \rangle \right|^2, \quad (2.60)$$

where $|\psi_0\rangle$ and $|\tilde{\psi}_0\rangle$ are the ground state wave functions of the full Hamiltonian H_r and \tilde{H}_r , respectively. We now estimate the fidelity F by using perturbation theory to find the true ground-state wave function $|\psi_0\rangle$ from the effective one $|\tilde{\psi}_0\rangle$

$$|\psi_0\rangle = |\tilde{\psi}_0\rangle + \sum_{n=1}^{\infty} \frac{\langle \tilde{\psi}_n | V | \tilde{\psi}_0 \rangle}{\tilde{E}_n - \tilde{E}_0} |\tilde{\psi}_n\rangle + \dots, \quad (2.61)$$

where we retain only terms to first order in V . Taking into account Eq. (2.61) we obtain the infidelity, $1 - F$, namely the deviation of the true ground state wave function from the effective one

$$1 - F = \sum_{n=1}^{\infty} \left| \frac{\langle \tilde{\psi}_n | V | \tilde{\psi}_0 \rangle}{\tilde{E}_n - \tilde{E}_0} \right|^2. \quad (2.62)$$

We plot in Fig. 4 the infidelity $1 - F$ as a function of the effective distance a for fixed Coulomb strength, λ/a_B . We see that the infidelity takes very small values ($1 - F < 10^{-2}$) on the considered range, for two different Coulomb strengths, which shows that our variational approach is very accurate.

We can now evaluate the spin-spin interaction within this approximation. Since we are now dealing with harmonic potentials only, the problem of finding $J_{\tilde{x},\tilde{y}}$ from Eq. (2.16) becomes straightforward. However, in the derivation of the spin Hamiltonian we need again some relations, similar to Eq. (2.22) and Eq. (2.23), but for the present case with the harmonic oscillator renormalized. These relations read

$$L_R^{-1} X = -\frac{i}{\hbar M \omega_0^2} \left(P_X + \frac{eB_z}{c} Y \right), \quad (2.63)$$

$$L_R^{-1} Y = -\frac{i}{\hbar M \omega_0^2} \left(P_Y - \frac{eB_z}{c} X \right),$$

$$L_r^{-1} x = -\frac{i}{\hbar m \omega_x^2} \left(p_x + \frac{eB_z}{c} y \right), \quad (2.64)$$

$$L_r^{-1} y = -\frac{i}{\hbar m \omega_y^2} \left(p_y - \frac{eB_z}{c} x \right).$$

Making use of the relations Eq. (2.63) and Eq. (2.64), and also with the effective spin-orbit interaction expressed in the center-of-mass and relative coordinates, see Eq. (2.9), the spin-Hamiltonian H_s takes the form

$$H_s = \frac{E_Z^2}{m^{*2} \omega_0^2 \lambda_{SO}^2} \left[\left(\frac{1}{b_x^2} - 1 \right) \sigma_x^1 \sigma_x^2 + \left(\frac{1}{b_y^2} - 1 \right) \sigma_y^1 \sigma_y^2 \right], \quad (2.65)$$

for the case of a perpendicular magnetic field and

$$H_s = \frac{E_Z^2}{m^{*2} \omega_0^2 \lambda_{SO}^2} \left(\frac{\cos^2 \Phi}{b_x^2} + \frac{\sin^2 \Phi}{b_y^2} - 1 \right) \sigma_y^1 \sigma_y^2, \quad (2.66)$$

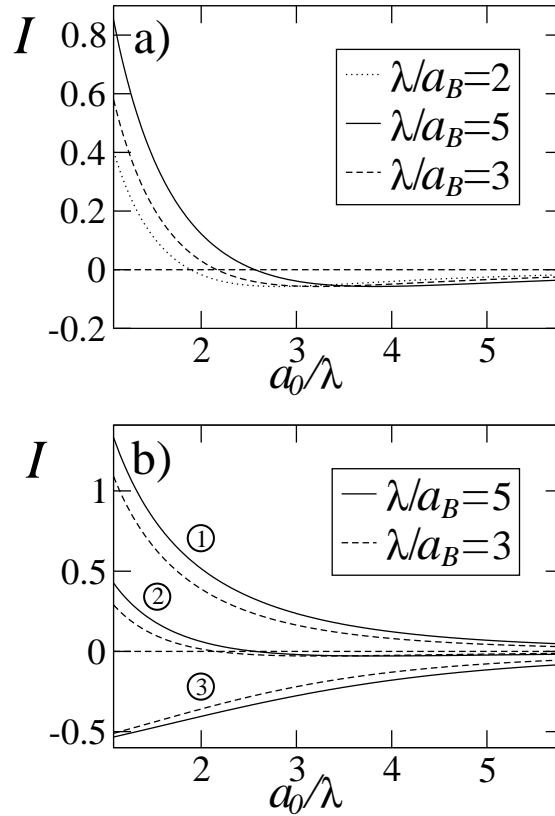


Figure 2.5: The function I from Eq. (2.68) as a function of the dimensionless geometric distance a_0/λ . *a)* The case of perpendicular magnetic ($\theta = 0$) field for three different Coulomb strength parameters λ/a_B . *b)* The case of in-plane magnetic field ($\theta = \pi/2$), for two values of the Coulomb strength λ/a_B , for three angles between the inter-dot distance vector \mathbf{a}_0 and the magnetic field. The groups of lines 1, 2, and 3 correspond to $\Phi = 0$, $\Phi = \pi/4$, and $\Phi = \pi/2$, respectively.

for the case of an in-plane magnetic field which makes an angle Φ with the inter-dot distance direction. The \tilde{y} is along the in-plane direction perpendicular to the in-plane magnetic field. We see that the spin Hamiltonian depends on the Coulomb interaction part via the difference between the inverse of the renormalized frequencies $\omega_{x,y}$ and the bare one ω_0 . As expected, when there is no renormalizations of the bare frequencies (no Coulomb interaction) the interaction vanishes. Referring again to the effective spin Hamiltonian H_s^{eff} from Eq. (2.19), we obtain for the coupling J_{eff} for arbitrary magnetic field orientations

$$J_{eff} = E_z \frac{E_z}{\hbar\omega_0} \left(\frac{\lambda}{\lambda_{SO}} \right)^2 I(a_0/\lambda, a_B/\lambda), \quad (2.67)$$

where

$$I(a_0/\lambda, a_B/\lambda) = \left(\frac{1}{b_x^2} - 1 \right) (\cos^2 \theta \sin^2 \Phi + \cos^2 \Phi) + \left(\frac{1}{b_y^2} - 1 \right) (\cos^2 \theta \cos^2 \Phi + \sin^2 \Phi). \quad (2.68)$$

One can see from Fig. 5b that for in-plane magnetic fields one obtains quite large values for I in the two limiting cases $\Phi = 0$ and $\Phi = \pi/2$. Changing the magnetic field orientation in-plane one can tune the coupling strength J_{eff} from negative to positive values, *i.e.* from ferromagnetic to antiferromagnetic regime, and make it vanish for the angle (for in-plane magnetic field)

$$\Phi = \arcsin \left(b_y \sqrt{(1 - b_x^2)/(b_y^2 - b_x^2)} \right). \quad (2.69)$$

In the case of a perpendicular magnetic field, cf. Fig. 5a, we see that the coupling shows a non-monotonic behavior as a function of distance a_0 , and, moreover, J_{eff} vanishes for some given distance, which for $\lambda/a_B = 5$ is about $a_0/\lambda \approx 2.5$. This could be used to tune J_{eff} on and off by changing the distance between the dots.

Next, we consider the case of very elliptic dots, with the bare oscillator frequencies $\omega_{0x,0y}$ corresponding to the x and y directions, respectively, such that $\omega_{0x} \ll \omega_{0y}$. The spin-spin coupling becomes in this limiting case

$$H_s = \frac{E_Z^2}{m^*2\lambda_{SO}^2\tilde{\omega}_x^2} \left(\frac{1}{b_x^2} - 1 \right) \cos^2 \Phi \sigma_x^1 \sigma_x^2 + O((\omega_{0x}/\omega_{0y})^2), \quad (2.70)$$

where both perpendicular ($\Phi = 0$) and in-plane magnetic fields are contained. We see that the problem becomes effectively 1D with an Ising-type spin-spin coupling, similar to the case of small Coulomb coupling studied in the previous section. We mention that for finite ratio of the two bare frequencies, ω_{0x}/ω_{0y} , the interaction can be varied by changing this ratio, the angle of cancellation defined in Eq. (2.69) varying as well.

The behavior displayed in Fig. 5 can be understood as follows. The spin-spin coupling is directly related to the deformation of the charge distributions in the two dots as a consequence of the strong Coulomb interaction ($\delta \gg 1$). Thus, the stronger the deformation is, the stronger the spin-spin coupling becomes. Or, in our case, the stronger the deviation of the renormalized orbital frequencies $\omega_{x,y}$ from the bare one ω_0 is, the stronger the coupling becomes, see Eqs. (2.65) and (2.66). While the x component of the spin-spin

coupling is bounded because the inverse of ω_x tends to zero as the Coulomb interaction strength δ increases, the y component of this coupling is unbounded since the inverse of ω_y can grow indefinitely. Consequently, the y component will dominate the x component for large Coulomb strength and small inter-dot distance a_0 . However, the situation is reversed in the large distance limit, since ω_x increases faster than ω_y decreases as seen from Eq. (2.56). These opposite limits lead to the non-monotonic behavior depicted in Fig. 5a (perpendicular magnetic field).

We mention that the large distance limit of Eq.(2.67) converges to the large distance result obtained in the previous section, Eq. (2.39). However, it does not converge to the results of the previous section in the case of small distance [Eq.(2.41)], when going from $\delta \gg 1$ to $\delta \ll 1$, a crossover description ($\delta \sim 1$) being needed in this situation. Phrased differently, tuning the spin-spin coupling J_{eff} from strong ($\delta \gg 1$) to small ($\delta \ll 1$) Coulomb interaction regime by varying the inter-dot distance reproduces the corresponding $\delta \ll 1$ result in Eq. (2.39), while by varying the ratio λ/a_B does not reproduce the corresponding $\delta \ll 1$ limit, *i.e.* Eq. (2.41).

Let us give now some estimates for the coupling J_{eff} when an in-plane magnetic field is applied along, say, the x -direction. Assuming now GaAs quantum dots, and $E_Z = 0.1$ meV ($B = 4$ T), $\hbar\omega_0 = 0.5$ meV ($\lambda/a_B \approx 5$), $\lambda/\lambda_{SO} \approx 10^{-1}$. Using these numbers and taking for the geometric inter-dot distance $a_0/\lambda \approx 2$, we obtain $J_{eff} \approx 10^{-7}$ eV. It is worth mentioning that the hyperfine interaction between the electron and the collection of nuclei in a quantum dot ($\approx 10^5$) leads to similar energy scales [83, 84]. This shows that the spin-spin coupling derived here can be very relevant for the spin dynamics in the case of electrostatically coupled quantum dots and that it can also compete with other types of interactions. Considering now the case of InAs quantum dots in a magnetic field along the x direction, with $\lambda_{SO} \approx 2\lambda \approx 100$ nm and $E_Z/\hbar\omega_0 = 0.1$ and taking also $a_0/\lambda \approx 2$, a value of $J_{eff} \approx 10^{-6}$ eV it is obtained. However, this is just a rough estimate since the spin-orbit coupling cannot be treated as a perturbation anymore and our approximation, being pushed to the limit of its range of validity, starts to break down.

2.4 Measurement Scheme

In this section we propose a measurement scheme for the spin-spin interaction J_{eff} . Similar to the spin relaxation experiments in Ref. [10], the left dot is monitored by a sensitive charge detector, such as a quantum point contact (QPC) or a single electron transistor (SET). We show the main steps of the scheme in Fig. 2.4.

The first step is the initialization step shown in Fig. 2.4(a). At low temperatures, $T \ll E_Z$, a single-electron dot will relax to the ground state after a time larger than the spin relaxation time $T_1 \simeq (0.1 - 100)$ ms. A faster spin relaxation can be induced by cotunneling with the lead, for which the dot can be placed closer to the Fermi surface for some time. In Fig. 2.4(a), the left dot is initialized in the lower Zeeman sublevel $|\uparrow\rangle$, whereas the right dot is empty. Next, the right-dot energy is lowered below the Fermi energy and the dot is quickly filled with an electron in either upper or lower Zeeman sublevel. This is a sequential tunneling process and we denote its rate by Γ . In Fig. 2.4(b), both dots are deep below the Fermi surface and J_{eff} is the energy scale that governs a coherent evolution in the subspace

$\{|\uparrow\downarrow\rangle, |\downarrow\uparrow\rangle\}$. The two spin density matrix reads

$$\varrho(t) = \frac{1}{2}|\uparrow\uparrow\rangle\langle\uparrow\uparrow| + \frac{1}{2}|\Psi(t)\rangle\langle\Psi(t)|, \quad (2.71)$$

where $|\Psi(t)\rangle$ is the wave function that describes the occurrence of the state $|\uparrow\downarrow\rangle$ in the initialization step. In the ideal case, $|\Psi(t)\rangle$ evolves coherently due to the spin-spin interaction, Eq. (2.19)

$$|\Psi(t)\rangle = \cos(4J_{eff}t/\hbar)|\uparrow\downarrow\rangle - i\sin(4J_{eff}t/\hbar)|\downarrow\uparrow\rangle. \quad (2.72)$$

Here, we neglect the cotunneling and other spin relaxation processes. In particular, the cotunneling rate Γ^2/U_{\pm} should be much smaller than the spin-spin coupling J_{eff} . Here, U_{\pm} is the addition/extraction energy of the single-electron quantum dot in the Coulomb blockade valley. On the other hand the sequential tunneling rate Γ should be large enough, so that the spins have no time to evolve during the initialization and measurement steps. We summarize the required regime by the inequality

$$\frac{\Gamma^2}{U_{\pm}} \ll J_{eff} \ll \Gamma. \quad (2.73)$$

After a waiting time τ , the probability of the left-dot electron to be in the upper Zeeman sublevel reads,

$$P_{L\downarrow}(\tau) = \frac{1}{4}[1 - \cos(8J_{eff}\tau/\hbar)]. \quad (2.74)$$

Form the period of this function ($\tau_0 = \pi\hbar/4J_{eff}$) one can extract the value of the coupling constant J_{eff} .

The measurement of the probability $P_{L\downarrow}(\tau)$ can be performed in the same fashion as in Ref. [10]. After the waiting time τ , the left dot is brought up to the Fermi level and placed such that the electron can tunnel into the lead only from the upper Zeeman sublevel. This configuration is shown in Fig. 2.4(c). Tunneling of the electron out and refilling the quantum dot with an electron of the opposite spin is monitored by the charge detector close to the left dot (not shown). For each value of the waiting time τ , the cycle of initialization, coherent evolution, and measurement has to be repeated many times in order to reach a good accuracy.

Next, we remark that the hyperfine interaction with the lattice nuclei should not impede the measurement of J_{eff} as long as $4J_{eff} \gtrsim A/\sqrt{N}$, where A is the atomic hyperfine coupling constant and N is the number of nuclei in both quantum dots. Note that the ratio of J_{eff} to A/\sqrt{N} for a constant λ/a scales with the dot lateral size as $\propto \lambda^4$, for strong Coulomb interaction, and as $\propto \lambda^6$, for weak Coulomb interaction. Therefore, the regime $4J_{eff} > A/\sqrt{N}$ can be easily achieved by taking a larger quantum dot. Furthermore, the hyperfine interaction with the nuclei has only the effect of reducing the visibility of oscillations of $P_{L\downarrow}(t)$, and even for $A/\sqrt{N} \gg J_{eff}$ a small part of $P_{L\downarrow}(\tau)$ shows oscillatory behavior with unchanged period, $\tau_0 = \pi\hbar/4J_{eff}$.

In Fig. 2.4, we plot the probability $P_{L\downarrow}(\tau)$ averaged over the realizations of the hyperfine field. We choose $A/\sqrt{N} \geq 4J_{eff}$ to show that the measurement scheme is robust against the hyperfine field. The oscillations are well visible even when A/\sqrt{N} is several times larger than $4J_{eff}$. The averaged probability $\bar{P}_{L\downarrow}(\tau)$ is obtained in the following way. For the subspace

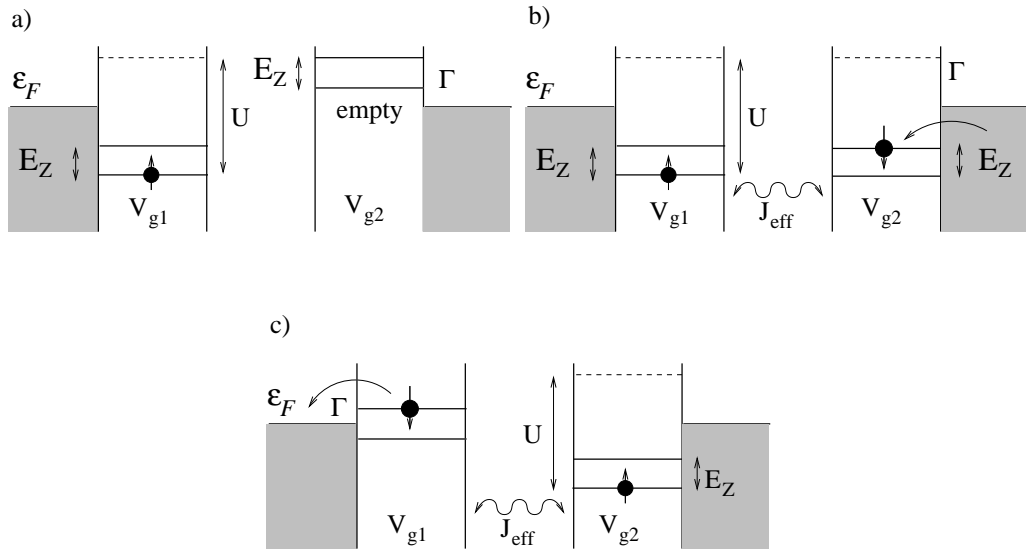


Figure 2.6: Scheme to measure the coupling constant J_{eff} in quantum dots without tunnel coupling. In the initialization step (a), the left dot is at equilibrium with one electron in the lower Zeeman sublevel and the right dot is empty. At the start of the coherent evolution step (b), the right dot is filled with one electron in either upper or lower Zeeman level during a short time $\hbar/\Gamma \ll \hbar/J_{eff}$, and the dots are deep in the Coulomb blockade valley, $\Gamma^2/U_{\pm} \ll J_{eff}$. Further, the two spins evolve coherently due to the spin-spin interaction J_{eff} during a fixed time $\tau \gtrsim \hbar/J_{eff}$. In the read-out step (c), the left dot is brought up to the Fermi surface, so that the electron can tunnel to the lead only if it is in the upper Zeeman sublevel. The latter event is recorded by a charge detector nearby the left dot.

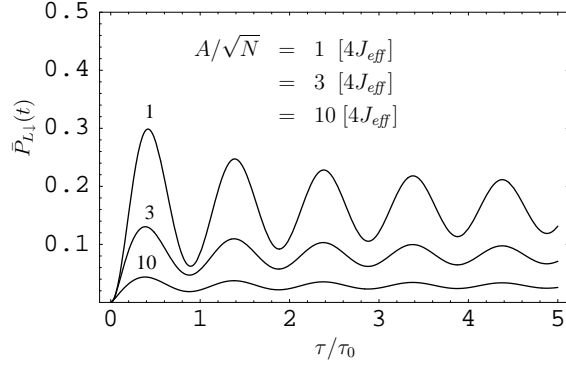


Figure 2.7: Residual oscillations in the averaged probability $\bar{P}_{L\downarrow}(\tau)$ for values of A/\sqrt{N} that exceed the spin-spin interaction strength $4J_{\text{eff}}$. The period of oscillations is not affected by the hyperfine interaction and is given by $\tau_0 = \pi\hbar/4J_{\text{eff}}$. With increasing the hyperfine strength A/\sqrt{N} , the amplitude of oscillations decreases as $\propto \sqrt{N}/A$. As a function of the waiting time τ , the envelope of oscillations decays as $\propto 1/\sqrt{\tau}$.

$\{|\uparrow\downarrow\rangle, |\downarrow\uparrow\rangle\}$ and in the limit $E_Z \gg A/\sqrt{N}$, the coupling of spins to the hyperfine field is given by $H_{\delta h_z} = \frac{1}{2}\delta h_z(\sigma_1^z - \sigma_2^z)$, where the hyperfine field δh_z has a Gaussian distribution with zero average and a variance $\sigma = A/\sqrt{N}$, which we take to be a measurable parameter that defines N^2 . For more detail on the derivation of $H_{\delta h_z}$ we refer the reader to Ref. [85].

For our description to be accurate, the time between subsequent cycles of initialization, coherent evolution, and measurement should be larger than the nuclear spin relaxation time. Considering the sum of $H_{\delta h_z}$ and H_s^{eff} in Eq. (2.19), we find that the probability $P_{L\downarrow}(\tau)$ for a fixed value of δh_z is given by [86]

$$P_{L\downarrow}(\tau) = \frac{1 - \cos\left(2\tau\hbar^{-1}\sqrt{16J_{\text{eff}}^2 + \delta h_z^2}\right)}{4\left(1 + \delta h_z^2/16J_{\text{eff}}^2\right)}. \quad (2.75)$$

The averaged probability $\bar{P}_{L\downarrow}(\tau)$ is then computed by integrating Eq. (2.75) over δh_z with the Gaussian weight factor $P_\sigma(\delta h_z) = \frac{1}{\sigma\sqrt{2\pi}}e^{-\delta h_z^2/2\sigma^2}$, where $\sigma = A/\sqrt{N}$.

Considering $A/\sqrt{N} > 4J_{\text{eff}}$ and $\tau > \pi\hbar/4J_{\text{eff}}$, we find that the visibility of oscillations scales with A/\sqrt{N} and τ as follows

$$v \propto \frac{J_{\text{eff}}\sqrt{N}}{A} \sqrt{\frac{\hbar}{\tau J_{\text{eff}}}}. \quad (2.76)$$

Note that the scaling law $v \propto \sqrt{N}/A$ is weaker than what one might expect naïvely from Eq. (2.75), after substituting there δh_z by its typical value A/\sqrt{N} , which gives $v \propto N/A^2$. The reason for the weaker scaling law is the fact that δh_z is centered around zero and the denominator in Eq. (2.75) has nearly no effect. We find that the numerical results in

²More rigorously, $\sigma = IA/\sqrt{2N_0}$, where $I^2 = \langle I_z^2 \rangle$ is the variance of the z -component of a single nuclear spin (assuming $\langle I_z \rangle = 0$) and $1/N_0 = v_0 \int d^3r |\psi(\mathbf{r})|^4$, with $\psi(\mathbf{r})$ being the electron wave function and v_0 the unit cell volume per nuclear spin.

Fig. 2.4 can be reproduced fairly accurately, if we approximate the argument of the cosine in Eq. (2.75) as follows

$$\sqrt{16J_{eff}^2 + \delta h_z^2} \approx 4J_{eff} \left(1 + \frac{\delta h_z^2}{32J_{eff}^2} + \dots \right). \quad (2.77)$$

This approximation is justified in the regime $\tau \gg \tau_0$ by the the minimal phase requirement, despite the fact that $\delta h_z/J_{eff}$ may be large. With Eq. (2.77), it is easy to average $P_{L\downarrow}(\tau)$ and obtain an approximate expression, which is fairly accurate for $\tau \gtrsim \tau_0$ and asymptotically exact in the limit $\tau \gg \tau_0$. We thus obtain

$$\bar{P}_{L\downarrow}(\tau) = \frac{1}{4} [\bar{p} - \delta p(\tau)], \quad (2.78)$$

$$\bar{p} = \sqrt{\frac{\pi}{2}} \zeta \exp\left(\frac{\zeta^2}{2}\right) \operatorname{erfc}\left(\frac{\zeta}{\sqrt{2}}\right), \quad (2.79)$$

$$\delta p(\tau) = \frac{\zeta \cos[2\pi\tau/\tau_0 + \varphi_0(\tau)]}{[\zeta^4 + (2\pi\tau/\tau_0)^2]^{1/4}}, \quad (2.80)$$

where $\zeta = 4J_{eff}\sqrt{N}/A$, $\operatorname{erfc}(\zeta)$ is the complementary error function, and the running phase shift $\varphi_0(\tau)$ is given by

$$\varphi_0(\tau) = \frac{1}{2} \arctan\left(\frac{2\pi\tau}{\tau_0\zeta^2}\right). \quad (2.81)$$

We note that Eq. (2.78) is exact in two limiting cases: $\zeta \gg 1$ and $\tau \gg \tau_0$. In particular, in the limit $\zeta \rightarrow \infty$, we recover $P_{L\downarrow}(\tau)$ in Eq. (2.75) for all values of τ . In the opposite limit, $\zeta \ll 1$, Eqs. (2.78)–(2.81) can be significantly simplified, yielding

$$\bar{P}_{L\downarrow}(\tau) = \frac{\zeta}{4} \left[\sqrt{\frac{\pi}{2}} - \sqrt{\frac{\tau_0}{2\pi\tau}} \cos(2\pi\tau/\tau_0 + \pi/4) \right]. \quad (2.82)$$

2.5 Discussions and conclusions

In the entire derivation we assumed no tunneling between the dots. Even in the presence of tunneling, when direct Coulomb repulsion, U_{12} (which is just the classical interaction between two charge distributions) is larger than the exchange interaction, J_{exc} ($U_{12} \gg J_{exc}$), the theory presented here is expected to remain still valid. The reason is that this type of spin-spin coupling is a direct consequence of the deformation of the electronic charge distribution due to Coulomb repulsion between the two electrons. Since this is given by the sum of the direct Coulomb part U_{12} , and the exchange part J_{exc} , the spin coupling J_{eff} will be insensitive to exchange in the limit $U_{12} \gg J_{exc}$. The point now is that with finite tunneling, even with the assumption that the coupling strength J_{eff} is not modified by the exchange Coulomb interaction, the resulting Heisenberg exchange coupling J_{exc} ($H_{exc} = J_{exc}\mathbf{S}_1 \cdot \mathbf{S}_2$) will start to compete with the electrostatically induced spin interaction. As a consequence, the spin coupling J_{eff} will be washed out in the limit $J_{exc} \gg J_{eff}$. However, since the Heisenberg exchange coupling decays with the inter-dot distance like [69] $J_{exc} \sim \exp(-2a_0^2)$ while $J_{eff} \sim a_0^{-3}$, the electrostatic spin coupling will start to dominate at not very large distances.

We recall that when having exchange, another type of spin coupling, J_{exc}^{SO} , induced by spin-orbit interaction comes into play, and which is proportional to the Heisenberg coupling J_{exc} , i.e. $J_{exc}^{SO} \propto (0.1 - 0.01)J_{exc}$ for typical GaAs dots [69, 72–76]. Thus, J_{exc}^{SO} can be much larger than J_{eff} for large enough Heisenberg coupling, with a crossover from this exchange-type to the direct Coulomb-type coupling taking place at some inter-dot distance. This crossover, however, occurs before we get $J_{exc} \sim J_{eff}$, since J_{exc}^{SO} is typically 100 times smaller than J_{exc} . To give an estimate, we assume $J_{exc} \approx 10^{-5}\text{eV}$ for $a_0 = 1$, which gives $J_{exc} \approx 3.5 \cdot 10^{-8}\text{eV}$ for $a_0 = 2$, implying that $J_{exc} < J_{eff}$.

Another important issue is the effect of screening induced by the surrounding electrons in the 2DEG and the metallic gates. As is well-known, the screening effect between two charges becomes important for distances exceeding the screening length $\lambda_{scr} \sim \lambda_{Fermi}$ (Fermi liquids). However, the screening of bare Coulomb interaction depends strongly on the dimensionality. In 3D the effect of screening is to induce an exponential decay of the bare Coulomb interaction [87], with the decay parameter λ_{scr} , while in 2D the decay follows a power law ($\sim r^{-3}$ in the large distance limit) [88–91], with λ_{scr} being the relevant length scale. For GaAs, the screening length is around $\lambda_{scr} \sim \lambda_{Fermi} \approx 50\text{ nm}$. Moreover, additional screening is introduced by the electrodes to gate the dots, due to their metallic character. The finite screening implies then that our theory in fact overestimates the strength of the electrostatically induced spin coupling J_{eff} for distances exceeding this screening length and the results obtained here become just an upper bound on J_{eff} for this limit.

Being highly controllable, the coupling J_{eff} could be used to perform two qubit gates for the realization of quantum computers with electron spins, like proposed in Ref. [4]. The switching times range between rather slow ($\sim 10\ \mu\text{s}$ in GaAs) and reasonably fast ($\sim 50\ \text{ns}$ in InAs). When making use of the standard exchange coupling [4] for switching (with typical switching times of 100 ps in GaAs) the electrostatically induced spin-coupling found here can lead to gate errors. However, this effect can be controlled by choosing the magnetic field direction or strength and/or the inter-dot distance such that J_{eff} becomes negligibly small (see Eq. (2.68)).

Here we assume perfect harmonic confinement potentials only. In reality the dot potential is not harmonic, although quantum dots with potentials close harmonic have been reported. Our spin-spin interaction by no means relies on the harmonicity of the quantum dot potential. We have used the harmonic confinement potential in our model to give analytical expressions which can be used to estimate the magnitude of the effect for realistic structures. We believe that deviations of the confinement from harmonic will lead to corrections to our results, but will not change (i) the a^{-3} scaling at large distances ($a \gg \lambda$) and (ii) the magnitude of the coupling constant.

Finally, an important question is how orbital fluctuations (for example of the confining energy $\hbar\omega_0$) or in the interdot distance, measured by variation in the electrostatic energy $e^2/\kappa a_0 \equiv E_{el}$) mediated via spin-orbit coupling lead to fluctuations in the coupling J_{eff} and thus eventually to spin decoherence. The relation between the orbital dephasing time (which is assumed to be known) and the decoherence induced by the spin coupling J_{eff} reads [85]

$$\frac{\tau_\phi^o}{\tau_\phi^s} \sim \left| \frac{\delta J_{eff}}{\delta(\hbar\omega_0)} \right|^2 + \left| \frac{\delta J_{eff}}{\delta E_{el}} \right|^2, \quad (2.83)$$

where τ_ϕ^o is the orbital dephasing time and τ_ϕ^s the corresponding spin decoherence time.

Assuming an orbital dephasing time $\tau_\phi^o \approx 1$ ns and also the limiting case of touching dots with the same GaAs parameters as before we obtain a spin decoherence time (lower bound) $\tau_\phi^s \approx 10^{-3}$ s. We mention that these two channels, *i.e.* fluctuations in the size and in the distance between the dots are the most dominant ones for dephasing through J_{eff} . We can conclude then that the incoherent part due to this type of coupling is negligible compared with other types of decoherence mechanisms, *e.g.* induced by the hyperfine interaction [83–85].

To conclude, we have derived an effective spin-spin interaction between two electrons localized in two quantum dots, spatially separated, induced by the direct Coulomb interaction and mediated by the spin-orbit coupling. This interaction was found to have the form of an anisotropic XY interaction and to be proportional to the Zeeman energy. The spin-spin coupling was studied both in the weak and strong Coulomb interaction limits and for different magnetic field orientations and strengths. The important features are the non-monotonic behavior of this spin interaction for some magnetic field orientations, together with a vanishing of this interaction for particular inter-dot distances. This effect can be used to manipulate the spin-spin interaction in electrostatically coupled quantum dots by tuning the inter-dot distance. We proposed a measurement setup which allows one to access this spin-spin coupling experimentally.

Chapter 3

Spin dynamics in InAs-nanowire quantum-dots coupled to a transmission line

We study theoretically electron spins in nanowire quantum dots placed inside a transmission line resonator. Because of the spin-orbit interaction, the spins couple to the electric component of the resonator electromagnetic field and enable coherent manipulation, storage, and read-out of quantum information in an all-electrical fashion. Coupling between distant quantum-dot spins, in one and the same or different nanowires, can be efficiently performed via the resonator mode either in real time or through virtual processes. For the latter case we derive an effective spin-entangling interaction and suggest means to turn it on and off. We consider both transverse and longitudinal types of nanowire quantum-dots and compare their manipulation timescales against the spin relaxation times. For this, we evaluate the rates for spin relaxation induced by the nanowire vibrations (phonons) and show that, as a result of phonon confinement in the nanowire, this rate is a strongly varying function of the spin operation frequency and thus can be drastically reduced compared to lateral quantum dots in GaAs. Our scheme is a step forward to the formation of hybrid structures where qubits of different nature can be integrated in a single device.

3.1 Introduction

Although lateral QDs have been most successfully used until now to demonstrate spin coherence and usability for quantum computing, [2, 57] novel quantum systems have emerged in recent years, providing a number of new ways to implement the basic ideas of quantum computing. [92] Among such systems are the QDs formed inside semiconductor nanowires. [93, 94]

The use of different semiconductors, other than GaAs, has since long been pursued with the goal to create nanostructures with novel properties. Particular examples are InAs and InP nanowires, where both gate defined and 'barrier' defined QDs could be fabricated. [95–98] The advantage of these materials is that both optical and transport measurements can be carried out on the same type of structure. The number of electrons can equally well be controlled down to one electron per dot, [96] which shows that QDs created in nanowires can serve as alternative candidates for spin-qubits.

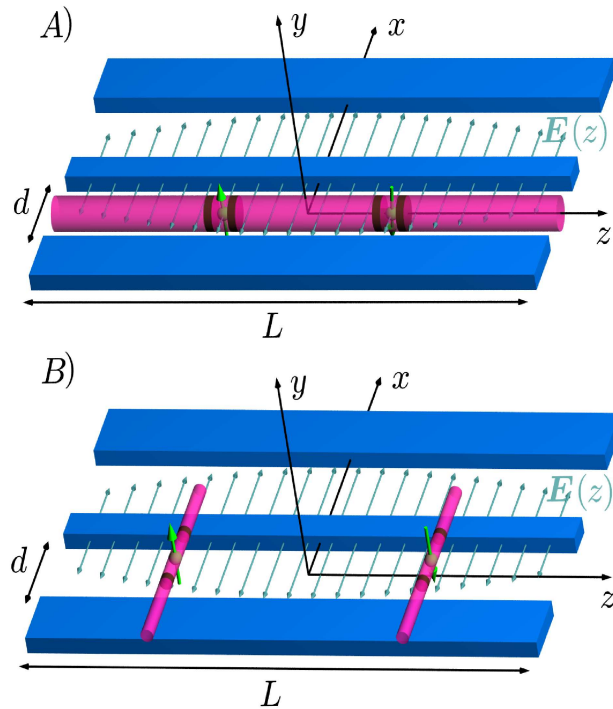


Figure 3.1: Schematics of the two configurations considered in this work. A) Large-diameter InAs nanowire (pink-gray cylinder) positioned inside and parallel to the transmission line (blue-gray). The disk-shaped quantum dots (QD) are located in the nanowire and are formed by two InP-boundaries (brown-dark-gray). Each QD contains only one electron with spin $1/2$ (green-arrows). B) Two small-diameter InAs nanowires (pink-gray) positioned perpendicularly to the transmission line (blue-gray). The elongated QDs are oriented along the nanowire with one electron in each dot. The QD confinement can be achieved by barrier materials (as shown in brown-dark-gray) or by external gates (not shown).

One particular difference between GaAs and InAs semiconductors is the strength of the spin-orbit interaction (SOI), which is much larger for the latter material. This fact, however, is a double-edge sword; on one hand it opens up the possibility to efficiently manipulate the electron spin with *electric* fields only, [?, 62, 99–101] while on the other hand it implies stronger coupling of the spin to charge environments, like phonons, particle-hole excitations, gate voltage fluctuation, etc. However, due to the quasi-1D structure of the nanowires, the spin relaxation times due to phonons and SOI turn out to be longer than one might expect from QDs created in InAs bulk material. Indeed, the time scales obtained in this work are on the order of microseconds to milliseconds for sufficiently large Zeeman splittings. At the same time, the relaxation rate exhibits peaks as a function of a static applied magnetic field due to the quantization of the phonon spectrum. The long relaxation time and the presence of a sizable SOI permits then an efficient control of coherent spin states by making use of EDSR. [?, 62, 99, 100, 102]

One of the main ingredients in the spin-qubit scheme [4] is the electrical control of two-qubit gates to generate entanglement. While the original proposal involved only local interactions between neighboring spins, it is desirable to couple spins directly over large distances, since this produces a better threshold for fault tolerant quantum computation. [103] A solution to this problem was first proposed in Ref. [104] and involves optical cavities whose photon modes mediate interaction between distant spins. The coupling of the spin to optical cavities in semiconductors was also the subject of some recent experiments. [105, 106]

Very recently, 1D electromagnetic cavities (or transmission lines) were shown to be very suitable for reaching the strong coupling regime between superconducting qubits and photons. [107–109] Theoretical extension to QDs were proposed subsequently, including charge and spin qubits. [110, 111] The direct coupling of the spin to the cavity modes via the magnetic dipole transitions is usually weak and one has to use electric dipole transitions together with correlations between spin and charge degrees of freedom in order to obtain a sizable effective coupling. This can be achieved in several ways, e.g. by making use of the Pauli exclusion principle and Coulomb repulsion, [111] or of Raman transitions. [110]

In this section we propose another mechanism to achieve long-distance coupling between spins inside a cavity, namely via SOI which leads to an effective coupling of spin to the electric field component of the cavity photon, and thus eventually to a coupling between distant spins mediated by this photon. In order to reach a sizable coupling strength, it is desirable to use nanostructures with large SOI such as InAs QDs. Two such proposed configurations, which define the two model systems to be studied in this chapter, are sketched in Figs. 3.1 A and B. They consist of nanowire QDs embedded in a transmission line. In particular, in Fig. 3.1A a nanowire positioned *parallel* to the transmission line axis is shown. In this case, the QDs are realized by confining the electrons in the longitudinal direction (i.e. along the nanowire axis) much stronger than in the transverse one. This corresponds to a nanowire with a large diameter, on the order of 80 – 100 nm. Such longitudinal confinement can be achieved by applying metallic gates or by using other materials as barriers (InP for example, which is depicted in Fig. 3.1 in brown) which have a larger band gap than the host material such as e.g. InAs. [94, 96] In Fig 3.1B a small-diameter ($D < 40$ nm) InAs nanowire is shown, being positioned perpendicularly to the transmission line and containing QDs that are elongated along the nanowire. That means that in this case we assume that the electronic confinement along the nanowire is much weaker than in the transverse direction. Then, to a very good

approximation, the electrons can be considered as behaving one-dimensionally, which will allow us to treat the SOI exactly, while this is not possible for the configuration Fig. 3.1A. However, in order to prevent a current flow, the nanowire and the transmission line need to be separated by some insulating coating material, obtained, for example, by atomic layer deposition.

The goal of this work is now to analyze these configurations in detail and, in the first part, to derive an effective spin-spin coupling Hamiltonian. In the second part, we study the spin decay in this system, induced by phonons and SOI, and calculate explicitly the spin relaxation and decoherence times due to this mechanism. We will show that these times are much longer than the switching times needed to manipulate and couple the spins coherently. Thus, our findings provide theoretical evidence that nanowire QDs embedded into transmission lines are promising candidates for spin-qubits with tunable long-range coupling. This scheme also opens the door to hybrid configurations where qubits of different nature (e.g. superconducting and spin qubits) can be coupled via the transmission line.

3.2 Model Hamiltonian

The Hamiltonian of the system composed of the single-electron QD and the cavity reads

$$H = \frac{p^2}{2m^{*2}} + V(\mathbf{r}) + \frac{1}{2}g\mu_B\mathbf{B} \cdot \boldsymbol{\sigma} + H_{SO} + H_{e-\gamma} + H_\gamma, \quad (3.1)$$

where the first two terms represent the bare orbital part of the Hamiltonian, m^* is the effective mass of the electron, g is the g -factor of the electron in the material, and $V(\mathbf{r})$ is the confinement potential, both in the longitudinal and transverse directions. We can obtain an effective Hamiltonian H_{eff} by averaging over the ground-state $|0\rangle$ in the longitudinal or in the transverse directions depending on which case in Fig. 3.1 is considered. Then, for the system in Fig. 3.1A(B) we obtain an effective 2D (1D) Hamiltonian.

The third term stands for the Zeeman interaction, while the fourth term in Eq. (4.1) represents the SOI. For wurtzite InAs nanowires grown along the c -axis, with the longitudinal confinement much stronger than the transverse one (see Fig. 3.1A) the SOI takes the form of a Rashba type, [93] $H_{SO} \equiv H_{SO}^t = \alpha(\mathbf{p} \times \mathbf{c}) \cdot \boldsymbol{\sigma}$, with \mathbf{c} being the unit-vector corresponding to the direction of the c -axis of the crystal. This expression when written in components, becomes

$$H_{SO}^t = \alpha(p_x\sigma_y - p_y\sigma_x). \quad (3.2)$$

We mention that our present study is quite general and can be easily adapted to other types of SOIs (such as Dresselhaus type). In the opposite case, when the transverse confinement is much stronger than the longitudinal one (see Fig. 3.1B), the SOI Hamiltonian H_{SO} takes the form $H_{SO} \equiv H_{SO}^l = (\mathbf{k} \cdot \mathbf{c})(\boldsymbol{\eta} \cdot \boldsymbol{\sigma})$ which, when written in components, becomes

$$H_{SO}^l = \eta p_x \sigma_\eta, \quad (3.3)$$

with $\boldsymbol{\eta} = (\eta_x, \eta_y, \eta_z)$ being a vector of coupling constants and σ_η being the spin component along $\boldsymbol{\eta}$. [93]

The fifth term represents the interaction between the photons in the cavity, labeled γ , and the electron in the QD. This term is given by

$$H_{e-\gamma} = e\mathbf{E}(z) \cdot \mathbf{r}. \quad (3.4)$$

The electric field $\mathbf{E}(z)$ acting on the electron is $\mathbf{E}(z) = \mathbf{e}_x V(z)/d$, with \mathbf{e}_x being the unit vector along x , $V(z)$ represents the fluctuating potential within the transmission line and d is the distance between the transmission line and the center conductor. The voltage fluctuation $V(z)$ has the following form [108]:

$$V(z) = \sum_{p=1}^{\infty} V_p \sin\left(\frac{p\pi z}{L}\right) [a_p + a_p^\dagger], \quad (3.5)$$

where $V_p = \sqrt{\hbar\omega_p/Lc}$, $a_p^\dagger(a_p)$ are the creation (annihilation) operators for the excitations (photons), c the capacitance per unit length, L the length of the resonator, and ω_p the eigenmodes of the resonator. The last term in the Hamiltonian represents the free photons $H_\gamma = \sum_p \hbar\omega_p a_p^\dagger a_p$.

From Eq. (4.1) we see that there exists an infinite number of frequencies in the transmission line, implying a coupling of the electron charge to an infinite number of modes. However, from all these modes, the relevant ones are those close to resonance with the Zeeman splitting of the spin. In the following we disregard all other modes from the problem and we assume also that the QD is in the center of the transmission line, so that the interaction between the electron charge and the photons becomes maximal. Having now defined all the ingredients, we can proceed to study the dynamics of the system.

3.3 General Spin-photon dynamics

3.3.1 Spin-photon interaction

In the following we derive an effective spin-photon Hamiltonian, assuming for both cases in Fig. 3.1 a SOI of arbitrary strength (to be restricted later on). In the case of time-reversal symmetry, the ground state of the dot ($H_d \equiv H_0 + H_{SO} + H_Z$) is two-fold degenerate (Kramers doublet), while this degeneracy is lifted in the presence of a magnetic field. If the magnetic field is such that the doublet splitting and also the electron-photon coupling strength are smaller than the level spacing of the QD, we can restrict our considerations to the dynamics of the lowest doublet only. We label this doublet by $\{|\uparrow\rangle, |\downarrow\rangle\}$, which is now different from the 'true' electron spin. In the absence of SOI interaction the 'true' electron spin will not couple to electric fields by any means, while in the presence of SOI the lowest Kramers doublet will contain orbital part to some amount, allowing coupling to electric fields (quantum or classical). Of course, the amount of orbital part contained will depend on the strength of the SOI compared, for example, to the bare orbital level spacing in the QD. It is of major importance to quantify the amount of orbital degrees of freedom contained in this Kramers doublet by taking as a reference the Kramers doublet free of SOI, i.e. the lowest bare spin state (being the direct product of orbital state and spin state). Assuming for simplicity that the free-of-SOI Hamiltonian has no degenerate levels (beside the Kramers

doublets), we could, in principle, obtain the states in the presence SOI (arbitrarily strong) from the ones in the absence of SOI by switching adiabatically the SOI, i.e. a continuous mapping of states.

Assuming the above mentioned adiabatic switching of SOI, we can connect formally the states in the presence of the SOI to the ones in the absence of the SOI with the help of a unitary transformation or Schrieffer-Wolff (SW) transformation

$$|n_\tau\rangle = e^{-S}|n\rangle|\sigma\rangle, \quad (3.6)$$

where the states $|n\rangle$ are the eigenstates of the Hamiltonian H_0 ($H_0|n\rangle = E_n^0|n\rangle$), $|n_\tau\rangle$ are the Kramers doublets with SOI, $|\sigma\rangle = |\uparrow, \downarrow\rangle$ are the bare spin states, and $S = -S^\dagger$. Also, the relation $H_d|n_\tau\rangle = E_d^{n_\tau}|n_\tau\rangle$ holds from our definition of the transformed state. For notational convenience we denote the lowest Kramers doublet as $|0_\tau\rangle$. This is written simply as $|0_\tau\rangle \equiv |\tau\rangle$, with the identification $|\tau\rangle = \{|\uparrow\rangle, |\downarrow\rangle\}$. The above transformation can be performed on the level of the Hamiltonian, implying diagonalization of the Hamiltonian H_d in the basis of the 'bare' Hamiltonian H_0

$$\bar{H} \equiv e^{-S} H e^S. \quad (3.7)$$

The advantage of transforming the Hamiltonian H_d so that it becomes diagonal in the basis of the bare Hamiltonian H_0 is now obvious. Within this transformation one can in principle proceed to calculate the effect of SOI to arbitrary order in perturbation theory, together with the SOI induced spin-photon coupling. We can now derive an effective spin-photon Hamiltonian within the lowest doublet $|\tau\rangle$ by averaging \bar{H} over the orbital ground state $|0\rangle$. This leaves us with the following effective spin-photon Hamiltonian $H_{s-\gamma} \equiv \langle 0|\bar{H}|0\rangle$ given by

$$H_{s-\gamma} = \frac{1}{2}g\mu_B B_{\text{eff}}\sigma_z + \mathcal{M}_\gamma \cdot \boldsymbol{\sigma}(a^\dagger + a) + \hbar\omega a^\dagger a, \quad (3.8)$$

where

$$\frac{1}{2}g\mu_B B_{\text{eff}}\sigma_z = \langle 0|e^{-S} H_d e^S|0\rangle \quad (3.9)$$

stands for the renormalized magnetic field,

$$\mathcal{M}_\gamma \cdot \boldsymbol{\sigma} = \frac{eV_1}{d} \langle 0|e^{-S} y e^S|0\rangle. \quad (3.10)$$

stands for the spin-photon coupling. Above we made also the substitutions $\omega_1 \equiv \omega$ and $a_1^\dagger \equiv a^\dagger$ ($a_1 \equiv a$). We mention that in order to have a finite coupling of the spin $\boldsymbol{\sigma}$ to the photons, the vector \mathcal{M}_γ must contain some time-reversal breaking parameter, such as the external magnetic field B . In the absence of the magnetic field there is no coupling between the lowest doublet and the photons ($\mathcal{M}_\gamma = 0$) to all orders in SOI.

We now define the spin-photon coupling strength $\nu = \sqrt{(\mathcal{M}_\gamma^x)^2 + (\mathcal{M}_\gamma^y)^2}$ and the detuning of the qubit from the cavity by $\Delta \equiv E_Z^{\text{eff}} - \hbar\omega$, where $E_Z^{\text{eff}} \equiv g\mu_B B_{\text{eff}}$. Close to the resonance between the qubit and the cavity mode ($\Delta \ll E_Z^{\text{eff}}, \hbar\omega$) one can simplify Eq. (3.8) by using the so called rotating wave approximation (RWA). [112] This implies to switch first

to the interaction picture, so that the operators $a(a^\dagger)$ and σ_\mp , where $\sigma_\mp = \sigma_x \mp i\sigma_y$ become time-dependent

$$\sigma_\mp(t) = \sigma_\mp(0)e^{\mp i\omega_Z^{eff}t} \quad (3.11)$$

$$a(t) = a(0)e^{-i\omega t} \quad (3.12)$$

$$\sigma_z(t) = \sigma_z(0). \quad (3.13)$$

where $\omega_Z^{eff} = E_Z^{eff}/\hbar$. Then, we neglect the terms in the time-dependent resulting Hamiltonian which oscillate fast on the time scale \hbar/Δ . This means neglecting counter-rotating terms such as $a^\dagger\sigma_+ \sim e^{i(\omega_Z^{eff}+\omega)t}$, $a\sigma_- \sim e^{-i(\omega_Z^{eff}+\omega)t}$, $a^\dagger\sigma_z \sim e^{i\omega t}$, and $a\sigma_z \sim e^{-i\omega t}$, which average to zero for large times. Within this approximation the Hamiltonian in Eq. (3.8) within the interaction picture becomes static and of the form

$$H_{s-\gamma}^{eff} = \frac{1}{2}g\mu_B B_{eff}\sigma_z + \nu(a^\dagger\sigma_- + \sigma_+a) + \hbar\omega a^\dagger a. \quad (3.14)$$

As expected, the above expression agrees with the Jaynes-Cummings Hamiltonian. [113]

3.3.2 Effective spin-spin interaction

We now investigate the case of two QDs in the cavity in the limit of finite detunings $\Delta_{1,2}$. The Hamiltonian $H_{s-\gamma}^{(2)}$ corresponding to the two spins in the cavity can be found by just extending Eq. (3.14) to two spins

$$H_{s-\gamma}^{(2)} = \sum_{i=1,2} \left(\frac{1}{2}g_i\mu_B B_{eff}^i\sigma_z^i + \nu_i(a^\dagger\sigma_-^i + \sigma_+^i a) \right) + \hbar\omega a^\dagger a. \quad (3.15)$$

For $\nu_i/\Delta_i < 1$ ($i = 1, 2$), the spin-photon interaction can be treated within the second order perturbation theory in ν_i . We use again the SW transformation, similar to the previous section. Here, this implies finding an operator T so that

$$\tilde{H}_{s-\gamma}^{(2)} = e^T H_{s-\gamma}^{(2)} e^{-T} \quad (3.16)$$

is diagonal in the basis of the spin-photon Hamiltonian without spin-photon interaction (the Hamiltonian $H_{s-\gamma}^{(2)}$ with $\nu_{1,2} \equiv 0$). Within first order in spin-photon couplings $\nu_{1,2}$, the transformation operator T reads

$$T = \sum_{i=1,2} \frac{\nu_i}{\Delta_i} (\sigma_+^i a - a^\dagger \sigma_-^i), \quad (3.17)$$

under the assumption that the condition $\nu_i/\Delta_i < 1$, $i = 1, 2$, is satisfied for both dots. The transformed Hamiltonian $\tilde{H}_{s-\gamma}^{(2)}$ becomes

$$\begin{aligned} \tilde{H}_{s-\gamma}^{(2)} &= \left(\hbar\omega + \frac{2\nu_1^2}{\Delta_1}\sigma_z^1 + \frac{2\nu_2^2}{\Delta_2}\sigma_z^2 \right) a^\dagger a \\ &+ \left(E_{1Z}^{eff} + \frac{\nu_1^2}{\Delta_1} \right) \sigma_z^1 + \left(E_{2Z}^{eff} + \frac{\nu_2^2}{\Delta_2} \right) \sigma_z^2 \\ &+ \nu_1\nu_2 \left(\frac{1}{\Delta_1} + \frac{1}{\Delta_2} \right) (\sigma_+^1\sigma_-^2 + \sigma_+^2\sigma_-^1), \end{aligned} \quad (3.18)$$

where $E_{iZ}^{eff} = g\mu_B B_{eff}^i$. We can obtain a pure spin Hamiltonian by neglecting the fluctuations of the photon number $a^\dagger a \rightarrow \langle a^\dagger a \rangle \equiv \bar{n}$, with \bar{n} the average number of photons in the lowest cavity mode. The resulting Hamiltonian $H_s \equiv \tilde{H}_{s-\gamma}^{(2)}|_{a^\dagger a \rightarrow \bar{n}}$ reads

$$H_s = \tilde{E}_Z^1 \sigma_z^1 + \tilde{E}_Z^2 \sigma_z^2 + J(\sigma_+^1 \sigma_-^2 + \sigma_+^2 \sigma_-^1), \quad (3.19)$$

where

$$\tilde{E}_Z^i = E_{iZ}^{eff} + 2 \left(\bar{n} + \frac{1}{2} \right) \frac{\nu_i^2}{\Delta_i}, \quad i = 1, 2, \quad (3.20)$$

$$J = \nu_1 \nu_2 \left(\frac{1}{\Delta_1} + \frac{1}{\Delta_2} \right). \quad (3.21)$$

In Eq. (3.20) we see that the effective Zeeman splitting \tilde{E}_Z^i is quite different from the bare one, $E_{iZ} \equiv g_i \mu_B B$. Besides the SOI renormalization of the Zeeman splitting, there is also a contribution from the spin-photon coupling, which consists of the Lamb shift (the term independent of the average photon number \bar{n}) and the ac Stark shift (the term proportional to the average photon number \bar{n}).

The expression Eq. (3.19) is one of our main results: in the presence of SOI and cavity modes one can achieve an effective spin-spin coupling with the exchange coupling J between two spins that are spatially well-separated. Indeed, this interaction can act over the entire length of the cavity, which can be as large as a few millimeters. Also, the spin-spin interaction is of XY-type (transverse spin-spin coupling), which together with single spin rotations have been shown to be universal for quantum computing. [104, 114] We mention that in order to obtain a maximal effect, one should be able to tune the two qubits into resonance, so that $\tilde{E}_Z^1 = \tilde{E}_Z^2$. [104]

3.4 Strong longitudinal confinement

So far we have taken the SOI into account exactly, regardless of the system under consideration, but under the assumption that the lowest Kramers doublet is well separated from the higher states compared to Zeeman energy and electron-photon coupling. We analyze here the spin-photon coupling for the case shown in Fig. 3.1A. As stated in Section II, in this case we can derive an effective transverse Hamiltonian $H_{eff} \equiv H_t = \langle 0_l | H | 0_l \rangle$, where $|0_l\rangle$ stands for the ground-state wave-function in the longitudinal direction z . The effective Hamiltonian H_t reads

$$H_t = \frac{p_x^2 + p_y^2}{2m^*} + V(x, y) + H_Z + H_{SO}^t + H_{e-\gamma} + H_\gamma, \quad (3.22)$$

with $V(x, y) = \langle 0_l | V(\mathbf{r}) | 0_l \rangle$, while all the other terms stay the same since they do not act in the z -direction. In the above expression we disregarded the term $\langle 0_l | (p_z^2/2m^*) | 0_l \rangle$, as it gives a constant shift of the levels.

We can start in principle to derive the spin-photon interaction from the effective Hamiltonian H_t by making use of the transformation (3.6). However, this cannot be done exactly and we have to proceed in perturbation theory. In order to give some numerical estimates

for the strength of the coupling ν , we assume the limit of weak SOI, quantified by the condition $R/\lambda_{SO} \ll 1$, with R being the dot (wire) radius and $\lambda_{SO} = \hbar/m^*\alpha$ the spin-orbit length. [64, 101, 115] Then, we can treat the SOI within perturbation theory. We assume in the following hard-wall boundary conditions for the electrons confined in the QDs, namely circular hard-wall boundaries in the transverse direction. In the longitudinal direction the electron is also confined by a hard-wall type of potential, but much stronger than in the transverse direction, as stated before. We compute the operator S from Eq. (3.6) within the first order in SOI, $S \approx (L_0 + L_Z)^{-1}H_{SO}$, which gives explicitly

$$S \approx i\boldsymbol{\xi} \cdot \boldsymbol{\sigma} - E_Z L_0^{-1}(\mathbf{b} \times \boldsymbol{\xi}) \cdot \boldsymbol{\sigma}, \quad (3.23)$$

in the limit of $E_Z \ll \Delta E_0$ with $\Delta E_0 = E_1 - E_0$ being the energy difference between the first excited state $|1\rangle$ and the ground state $|0\rangle$. In the above formulas the Liouvilleans $L_{0,Z}$ are defined as $L_{0,Z}A = [H_{0,Z}, A] \forall A$ and $\boldsymbol{\xi} = \lambda_{SO}^{-1}(-y, x, 0)$, $\mathbf{b} = \mathbf{B}/B$. We can obtain an effective Hamiltonian up to second-order in SOI and first order in Zeeman splitting for the lowest Kramers doublet by averaging over the orbital ground state $|0\rangle$,

$$\begin{aligned} H_{s-\gamma} &= \frac{1}{2}g\mu_B\mathbf{B} \cdot \boldsymbol{\sigma} + \langle 0|[S, H_{SO}]|0\rangle + \langle 0|[S, H_{e-\gamma}]|0\rangle \\ &+ \frac{1}{2}\langle 0|[S, [S, H_{e-\gamma}]]|0\rangle + H_\gamma. \end{aligned} \quad (3.24)$$

The orbital wave-functions have the form (for circular hard-wall boundary conditions)

$$\psi_{mp}(r) = \frac{1}{\sqrt{\pi}R} \frac{e^{im\phi}}{J_{|m|+1}(k_{mp}R)} J_{|m|}(k_{mp}r), \quad (3.25)$$

where $J_{|m|}(k_{mp}r)$ are the Bessel functions of the first kind, r is the electron radial coordinate in the transverse direction, and k_{mp} are the solutions of the equation $J_{|m|}(k_{mp}R) = 0$. The appropriate energies are given by $E_{mp} = \hbar^2 k_{mp}^2 / 2m^*$. Also, we assume that the magnetic field \mathbf{B} and the fluctuating electric field \mathbf{E} are both along the x direction, such that $H_{e-\gamma} = eE x$ and $S = i\boldsymbol{\xi} \cdot \boldsymbol{\sigma} - (E_Z/\lambda_{SO})L_0^{-1}x\sigma_z$. After performing the integrations, we are left with the following effective Hamiltonian

$$H_{s-\gamma} = \frac{1}{2}E_Z^{\text{eff}}\sigma_z + \mathcal{M}_\gamma^x(a^\dagger + a)\sigma_y + H_\gamma, \quad (3.26)$$

with

$$E_Z^{\text{eff}} \simeq E_Z \left(1 - 0.25 \left(\frac{R}{\lambda_{SO}} \right)^2 \right), \quad (3.27)$$

$$\mathcal{M}_\gamma^x \simeq 0.25eER \frac{E_Z}{\Delta E_0} \frac{R}{\lambda_{SO}}. \quad (3.28)$$

We see that there is no second order contribution in SOI to the spin-photon interaction, this contribution vanishes identically for cylindrical wires in the ground state. We mention that within the RWA the Jaynes-Cummings coupling ν becomes $\nu = \mathcal{M}_\gamma^x$.

In the case of two spins present in the cavity, one obtains the same expression as in Eq. (3.19), where $\nu_{1,2}$ is given by Eq. (3.28). Since our coupling is proportional to the bare

Zeeman splitting E_Z , we need large magnetic fields in order to obtain a sizable coupling. Then, we can in principle neglect the Lamb and the ac Stark shifts in the expressions for \tilde{E}_Z^i , since they give negligible renormalizations, so that $\tilde{E}_Z^i \approx E_{iZ}^{eff}$. However, as can be seen from Eq. (3.27), the Zeeman splitting can be strongly reduced for large SOI. This feature will turn out to be very important in order to have a long-lived qubit (see below).

3.5 Strong transverse confinement

In this section we analyze the case shown in Fig. 3.1B, i.e. when the transverse confinement in the $y-z$ plane is much stronger than the longitudinal one along \hat{x} . As in the previous case, we can derive an effective longitudinal Hamiltonian by averaging the full Hamiltonian H over the transverse orbital ground-state $|0_t\rangle$. The effective Hamiltonian $H_{eff} \equiv H_l = \langle 0_t | H | 0_t \rangle$ reads

$$H_l = \frac{p_x^2}{2m^*} + V(x) + H_Z + H_{SO}^l + H_{e-\gamma} + H_\gamma, \quad (3.29)$$

with $V(x) = \langle 0_t | V(\mathbf{r}) | 0_t \rangle$, while all other terms remain the same, since they have no action along the x -direction. Again, like in the previous case, we disregard the term $\langle 0_t | (p_y^2 + p_z^2) / 2m^* | 0_t \rangle$, since it gives a constant shift of the levels.

We now derive the spin-photon interaction from the effective Hamiltonian (3.29). As can be seen from Eq. (3.3), the SOI contains only one spin-component, σ_η along the $\boldsymbol{\eta}$ -direction. In this case and in the absence of an external magnetic field the SW transformation (3.6) can be performed exactly, since the SOI appears as an Abelian gauge-potential. [68, 116] In the presence of an external magnetic field, however, this cannot be done exactly anymore. We now apply the transformation (3.6) to the Hamiltonian H_l so that we obtain $\bar{H}_l = e^{-S} H_l e^S$, with the operator S corresponding to the zero-field case. This operator S reads

$$S = -i \frac{x}{\lambda_{SO}} \sigma_\eta, \quad (3.30)$$

with $\lambda_{SO} = \hbar / m^* \eta$. The effect of this transformation can be evaluated exactly and we obtain

$$\bar{H}_l = \frac{p_x^2}{2m^*} + V(x) + H_Z(x) + eEx + \hbar\omega a^\dagger a, \quad (3.31)$$

with

$$H_Z(x) = \frac{1}{2} g \mu_B \left(\cos \left(\frac{2x}{\lambda_{SO}} \right) \mathbf{B}_{\eta\perp} \cdot \boldsymbol{\sigma} + B_\eta \sigma_\eta - \sin \left(\frac{2x}{\lambda_{SO}} \right) (\mathbf{e}_\eta \times \mathbf{B}) \cdot \boldsymbol{\sigma} \right),$$

where $\mathbf{B}_{\eta\perp}$ is the component of the magnetic field \mathbf{B} perpendicular to the vector $\boldsymbol{\eta}$, B_η is the magnetic field component along $\boldsymbol{\eta}$, and $\mathbf{e}_\eta = \boldsymbol{\eta} / \eta$. We now assume, as before, that the Zeeman splitting $E_Z = g \mu_B B$ is much smaller than the orbital level spacing ΔE_0 given by the first two terms in the above Hamiltonian. Also, we assume harmonic confinement potential along the x -direction $V(x) = m^* \omega_0^2 x^2 / 2$ which gives a dot size $l = \sqrt{\hbar / m^* \omega_0}$. This is usually the case for gate-defined QDs. Then, the above condition translates in having $E_Z \ll \hbar \omega_0$. We are now in position to derive an effective spin-photon Hamiltonian by treating $H_Z(x)$ within perturbation theory. We perform a new SW transformation and transform the above

Hamiltonian into a diagonal one in the basis of H_0 to obtain $H_{s-\gamma} = \langle 0|e^{-S'}\bar{H}e^{S'}|0\rangle$. We averaged also over the orbital ground state $|0\rangle$ to obtain a pure spin-photon Hamiltonian. Within lowest order in $E_Z/\hbar\omega_0$ the transformation is given by $S' = (1 - \mathcal{P})L_0^{-1}H_Z(x)$. After inserting the operator S' in the expression for $H_{s-\gamma}$ and keeping only the lowest order corrections, we obtain

$$H_{s-\gamma} = \frac{1}{2}g\mu_B\mathbf{B}_{\text{eff}} \cdot \boldsymbol{\sigma} + \mathcal{M}_\gamma \cdot \boldsymbol{\sigma}(a^\dagger + a) + \hbar\omega a^\dagger a, \quad (3.32)$$

with

$$\mathbf{B}_{\text{eff}} \cdot \boldsymbol{\sigma} = e^{-(l/\lambda_{SO})^2}\mathbf{B}_{\eta\perp} \cdot \boldsymbol{\sigma} + B_\eta\sigma_\eta, \quad (3.33)$$

$$\mathcal{M}_\gamma \cdot \boldsymbol{\sigma} = eV_1\frac{l}{d}\frac{l}{\lambda_{SO}}\frac{E_Z}{\hbar\omega_0}e^{-(l/\lambda_{SO})^2}(\mathbf{e}_\eta \times \mathbf{b}) \cdot \boldsymbol{\sigma}. \quad (3.34)$$

We see that the spin-photon interaction is maximal when the magnetic field is perpendicular to $\boldsymbol{\eta}$, like in the perturbative calculation of the previous section. This is expected since, as in the previous section, the SOI manifest itself as an Abelian gauge potential within lowest order, although there are two spin-components. From now on, we assume a magnetic field perpendicular to $\boldsymbol{\eta}$ so that $B_\eta = 0$, $\mathbf{B} \cdot \boldsymbol{\sigma}_{\eta\perp} = B\sigma_z$ and $(\mathbf{e}_\eta \times \mathbf{b}) \cdot \boldsymbol{\sigma} = \sigma_{\eta\perp, \mathbf{b}} \equiv \sigma_{\hat{x}}$. Then, the spin-photon Hamiltonian reads

$$H_{s-\gamma} = \frac{1}{2}E_Z^{\text{eff}}\sigma_z + \mathcal{M}_\gamma\sigma_{\hat{x}}(a^\dagger + a) + \hbar\omega a^\dagger a, \quad (3.35)$$

with

$$\mathcal{M}_\gamma = eV_1\frac{l}{d}\frac{l}{\lambda_{SO}}\frac{E_Z^{\text{eff}}}{\hbar\omega_0}, \quad (3.36)$$

where $E_Z^{\text{eff}} = E_Z e^{-(l/\lambda_{SO})^2}$ is the effective Zeeman splitting.

We see that the SOI reduces strongly the Zeeman splitting for large values of the ratio l/λ_{SO} . This over-screening of the Zeeman interaction can be understood as follows. After performing the transformation (3.30) there is no SOI present in the system, but the magnetic field in the new 'frame' has an oscillatory behavior, as shown in Eq. (3.32). This means that the magnetic field precesses around the x -direction, the speed of precession being given by the strength of the SOI measured through the SO length λ_{SO} . If the bare Zeeman splitting E_Z is much smaller than the orbital level spacing, $E_Z \ll \hbar\omega_0$, the electron find itself in the orbital ground state $|0\rangle$ given by H_0 . Then, if the SOI strength is increased, the precession frequency increases also, so that there are many precessions of the magnetic field over small distances. Since this implies also small changes of the orbital wave-function, this leads to an average reduction of the effective Zeeman splitting, as obtained above.

3.6 Numerical Estimates

We give now some estimates for the coupling $\nu \equiv \mathcal{M}_\gamma^x$ for QDs in InAs nanowires for both geometries shown in Fig. 3.1. In the first case, we assume the dots to have a width of 5 – 10 nm ($E_w \approx 10$ meV—the transverse confining energy) and a radius $R \approx 50$ nm ($\Delta E_0 \approx 5$ meV). The electron in the QD is characterized by $m^* = 0.023 m_e$, $g \approx 2.5$ and $\lambda_{SO} \approx 100$ nm. [93] We assume also that the 1D cavity is 2 nm long and 100 nm wide,

$c \approx 2 \cdot 10^{-10} \text{ C/V} \cdot \text{m}$ [108] which implies for the fundamental mode $\hbar\omega \simeq 0.5 \text{ meV}$ and an rms electric field $E = V_1/d \simeq 100 \text{ V/m}$. The Zeeman splitting is assumed to be on the same order with the lowest cavity mode, i.e. $E_Z^{\text{eff}} \approx 0.5 \text{ meV}$ ($B \approx 1.75 \text{ T}$). Plugging in all the numbers in the formula for ν , Eq. (3.28) we obtain $\nu \approx 10^{-5} \text{ meV}$ which, in the degenerate case $E_Z^{\text{eff}} = \hbar\omega$, corresponds to a dynamics of the spin-photon system of about 60ns (Rabi oscillations between the spin and the cavity). In the second case there is more control on the orbital level spacing since the dots are obtained in principle by external gating. We now assume a dot radius $R \approx 10 \text{ nm}$ ($E_{0t} \simeq 30 \text{ meV}$), a dot length $l \simeq 40 \text{ nm}$ ($\hbar\omega_0 \simeq 2 \text{ meV}$) and $g \approx 10$. [94] For $E_Z^{\text{eff}} \approx 0.5 \text{ meV}$ we need a magnetic field $B \approx 0.45 \text{ T}$. Also, we assume the same lengths for the cavity as for the first case so that we obtain $\nu \approx 4 \cdot 10^{-4} \text{ meV}$. This gives rise to a dynamics of the spin-photon system of about 2 ns in the degenerate limit $E_Z^{\text{eff}} = \hbar\omega$. We mention that in both cases the renormalized Zeeman splitting is quite different from the bare one, i.e. $E_Z^{\text{eff}} = 0.93E_Z$ in the first case and $E_Z^{\text{eff}} = 0.84E_Z$ in the second case.

For the exchange coupling J between two spins one can achieve values as large as $J \approx 10^{-6} \text{ meV}$ in the limit of quite small detunings ($\Delta \approx 10^{-4} \text{ meV}$) for the case in Fig. 3.1A, which eventually translates into a time dynamics of about 500 ns for coherently swapping the two spins. In the geometry shown in Fig. 3.1B the exchange coupling J can be much larger, on the order of $J \approx 4 \cdot 10^{-5} \text{ meV}$ for detunings on the order of $\Delta \approx 4 \cdot 10^{-3} \text{ meV}$, which implies a time dynamics of about 20 ns for swapping the two spins coherently.

In order to control the exchange coupling J , one should be able in principle to change the Zeeman splitting or the orbital level spacing. In InAs QDs the Zeeman splitting can be changed very efficiently by changing the dot size along the wire direction, [94] in both cases in Fig. 3.1 Considering the case of two QDs in the cavity, one way to decouple them is by tuning the g -factors so that $\Delta_1 = -\Delta_2$, as can be seen from Eq. (3.18). However, in the case of many QDs inside the cavity this will be rather difficult to achieve.

Another possibility is to change the g -factors locally so that the coupling between the spins reduces due to the reduction of the Zeeman splitting E_Z . Assuming that a reduction of J by one order of magnitude is a good measure for the decoupling, one obtains a corresponding change in the g -factor of the order of 15% in the first geometry shown in Fig. (3.1). The rather drastic change of g -factor was already experimentally demonstrated for InAs QDs by Björk *et al.* [94]. They achieved a change in the g -factor from $|g| = 3.5$ to $|g| = 2.3$ when the dot size along the nanowire was reduced from 10 nm to 8 nm, i.e. a variation of about 30%, which shows to be sufficient for our scheme in the geometry shown in Fig. 3.1. The same can be done efficiently for the second geometry, since the dots being gate-defined can be modified strongly along the wire axis.

Yet another way to change the exchange coupling J is by changing the orbital confining energy ΔE_0 . In the first geometry $\nu \sim R^4$, and $J \sim \nu^2$ (assuming two equal spin-photon couplings for simplicity) one obtains a dependence $J \sim R^8$. Then, by using top gates, for example, one can strongly modify the exchange coupling J by a small change of the orbital energy ΔE_0 . This can be done equally, and maybe more efficiently, for the second geometry since, as explained above, the dots can be modified easily along the wire axis. The spin-photon coupling $\nu \sim l^4$, which implies then a scaling of the exchange coupling $J \sim l^8$.

3.7 Coherent manipulation

One way to coherently manipulate and to read-out (measurement) the qubits is by applying an external driving field to the cavity with a varying frequency $H_{ex} = \epsilon(t)(a^\dagger e^{-i\omega_{ex}t} + ae^{i\omega_{ex}t})$, where $\epsilon(t)$ is the amplitude. In the dispersive limit ($\nu_i/\Delta_i \ll 1$) $H_{ex} \rightarrow H_{ex} + [T, H_{ex}]$ so that

$$H_{ex} \simeq \epsilon(t)a^\dagger e^{-i\omega_{ex}t} + \sum_{i=1,2} \frac{\nu_i \epsilon(t)}{\Delta_i} \sigma_i^+ e^{-i\omega_{ex}t} + \text{h.c.} \quad (3.37)$$

The control of the i -th qubit can now be realized by tuning the frequency of the driving field to $\omega_{ex} = E_{iZ}^{\text{eff}} + \nu_i^2/\Delta_i$, while this condition is not satisfied for the other qubits. This gives rise to an electric-dipole spin resonance (EDSR) for the i -th qubit, similar to that studied by Golovach et al. [?] The measurement can be performed by tuning the frequency of the driving close to the cavity mode so that we can observe peaks in transmission at the positions $\hbar\omega + \sum_i (\nu_i^2/\Delta_i) \sigma_z^i$. If detunings are chosen so that all combinations can be distinguished, one can measure all the spins from one shot (or at least group of spins). [108]

A more efficient way to manipulate the spin is to make use of the EDSR-scheme proposed in Ref. [?], namely to apply an alternating electric field $\mathcal{E}(t)$ to the QD, which, via the electric dipole transitions and the SOI, gives rise to an effective alternating magnetic field. Briefly, if only the dipolar coupling to the alternating electric field $\mathcal{E}(t)$ is considered, we get $H_{e-el}(t) = e\mathcal{E}(t)y$, with the electric field $\mathcal{E}(t)$ along y -direction. If the system in Fig. 3.1A is considered, the effective spin-electric field coupling within first order in SOI becomes $H_{s-el} = \langle 0|[S, H_{e-el}(t)]|0\rangle \equiv \delta B(t)\sigma_y$, with the fluctuating magnetic field $\delta B(t)$ having the form

$$\delta B(t) \sim e\mathcal{E}(t)R \frac{E_Z}{\Delta E_0} \frac{R}{\lambda_{SO}}. \quad (3.38)$$

For the case shown in Fig. 3.1B we obtain a similar expression for $\delta B(t)$, but with the bare Zeeman splitting E_Z substituted with the effective Zeeman splitting E_Z^{eff} defined after Eq. (3.36), and the radius R substituted with the dot length l . The electric field $\mathcal{E}(t)$ is assumed to have an oscillatory behavior, $\mathcal{E}(t) = \mathcal{E}_0 \cos \omega_{ac}t$ with ω_{ac} being the frequency of the ac electric field. By tuning the frequency of the oscillatory electric field ω_{ac} in resonance with the qubit splitting E_Z^{eff} one can achieve arbitrary rotations of the spin on the Bloch sphere on time scales given by the Rabi frequency $\omega_R = \delta B(0)/\hbar$. [?] We mention that within lowest order in SOI the induced fluctuating magnetic field $\delta \mathbf{B}(t)$ is always perpendicular to the applied field \mathbf{B} and reaches the maximum when the applied electric field $\mathcal{E}(t)$ points into the same direction as \mathbf{B} . [?] This is the reason for choosing the electric field along the y -direction.

We give here also some estimates for the Rabi frequency ω_R . For this we assume the same parameters as in the previous section and we choose for the amplitude of the electric field $\mathcal{E}_0 \approx 10$ eV/cm. With this values we obtain for the strength of the Rabi frequency $\omega_R \approx 10$ GHz, which gives a time dynamics for the electron spin control on the order of $\omega_R^{-1} \approx 0.1$ ns. This time scale must be much shorter than the usual relaxation and decoherence times for the spin in the QD. Finding the relaxation and decoherence time scales is the subject of the next section.

3.8 Spin relaxation and decoherence

We address now the issue of relaxation and decoherence of the spin in the cavity. There are two types of contributions to the relaxation processes, one arising from the finite decay rate of the cavity, κ , and the other one from the intrinsic relaxation and decoherence of the spin, labeled by $T_{1,2}^{-1}$. To reach the strong coupling regime described here, the losses must be smaller than the coupling between the qubits J in the regime of interest ($\nu^2/\Delta > \kappa, T_{1,2}^{-1}$). Very high-Q factor 1D electromagnetic cavities were already built ($Q = \kappa^{-1} \sim 10^4 - 10^6$), [107] so that the intrinsic relaxation and decoherence of the qubit show up as the limiting factors for reaching the strong coupling regime.

The relaxation and decoherence of the spin-qubit arise mainly from the coupling to the bath of phonons and the collection of nuclei in the QD. The phonon contribution was studied microscopically in great detail for the case of gate-defined GaAs QDs in 2DEGs and it was shown that for large B -fields, similar to the present case, the main contribution to relaxation comes from the deformation potential phonons with a decay time $T_1 \sim 10^{-2} - 10^{-4}$ s. [64] As a consequence, a smaller relaxation time is then expected for InAs QDs since the SOI is one order of magnitude larger than in GaAs ($T_1 \propto (\lambda_{SO}/R)^2$). However, different from the bulk case, the phonon spectrum in nanowires becomes highly non-trivial due to the mixing of the branches by the boundaries, [117] leading to a strong modification of the relaxation time.

In cylindrical nanowires there are three types of acoustic modes: torsional, dilatational and flexural. [118] All these modes couple to the electric charge and, in principle, all of them couple also to the spin for a general SOI Hamiltonian. However, as shown later, this is not actually the case for the SOI acting in the two configurations in Fig. 3.1, and only a small part of the entire spectrum gives rise to spin relaxation.

As stated above, within the large Zeeman splitting limit considered in this chapter, we can take into account only the interaction of the electron with the lattice via the deformation potential. The electron-phonon deformation potential interaction is given by $H_{e-ph} = \Xi_0 \nabla \mathbf{u}(\mathbf{r}, t)$, where Ξ_0 is the deformation potential strength and

$$\mathbf{u}(\mathbf{r}, t) = \frac{1}{\sqrt{N}} \sum_{\mathbf{k}} [\mathbf{u}(\mathbf{k}, \mathbf{r}) b_{\mathbf{k}}(t) + \text{h.c.}], \quad (3.39)$$

with the displacement field $\mathbf{u}(\mathbf{k}, \mathbf{r})$ given by [117, 118]

$$\mathbf{u}(\mathbf{k}, \mathbf{r}) = \nabla \Phi_0 + (\nabla \times \mathbf{e}_z) \Phi_1 + (\nabla \times \nabla \times \mathbf{e}_z) \Phi_2. \quad (3.40)$$

The index $\mathbf{k} \equiv \{q, n, s\}$ quantify the relevant quantum numbers, i.e. the wave-vector along the wire, the winding number and the radial number, respectively, $b_{\mathbf{k}}(t)$ is the annihilation operator for phonons, \mathbf{e}_z is the unit vector along the z direction and

$$\Phi_i = \chi_j f_{ns}^j(r) e^{i(n\phi + qz)}, \quad (3.41)$$

with $j = 0, 1, 2$, $n = 0, \pm 1, \pm 2, \dots$. The functions $f_{ns}^j(r)$ depend only on the radius [117, 119] and χ_j are normalization factors. The effective spin-phonon interaction can be found following the same procedure as that used for deriving the spin-photon interaction for both cases in Fig.3.1.

3.8.1 Spin-relaxation in longitudinal confined QDs

We give here the main steps in the derivation of the relaxation rate for the case shown in Fig. 3.1A. Keeping only terms up to first order in SOI, we obtain

$$H_{s-ph} = \langle 0|[S, H_{e-ph}]|0\rangle, \quad (3.42)$$

with S given in Eq. (3.23) and $|0\rangle$ being the orbital ground-state. Due to the circular symmetry, the first order in SOI term couples only to the $n = 1$ phonons. The resulting spin-phonon coupling has the form

$$H_{s-ph} = \frac{1}{2}g\mu_B\delta B_y(t)\sigma_y, \quad (3.43)$$

with

$$\delta B_y(t) = B \frac{\Xi_0}{\Delta E_0} \frac{R}{\lambda_{SO}} \sum_{q,s} \frac{\mathcal{C}(q,s)}{\sqrt{\mathcal{F}(q,s)\rho_c\omega_{q,s}/\hbar}} K_{q,s}^2 b_{\mathbf{k}}^\dagger + \text{h.c.}, \quad (3.44)$$

$$\mathcal{C}(q,s) \approx 0.25 \int_0^1 \frac{dr r J_1(k_{11}r) J_0(k_{10}r) f_{1s}^0(r)}{|J_2(k_{11}) J_1(k_{10})|}, \quad (3.45)$$

where $K_{q,s} = \omega_{q,s}/c_l$ with $\omega_{q,s}$ being the eigen-modes of the phonon field, c_l the longitudinal speed of sound in InAs. The normalization function $\mathcal{F}(q,s)$ is given by

$$\mathcal{F}(q,s) = \frac{\hbar R^2}{4M\chi_0^2\omega_{\mathbf{k}}}, \quad (3.46)$$

where M is the mass of the ions in a unit cell.

The explicit forms for the $\omega_{q,s}$ and $\mathcal{F}(\omega_{q,s})$ depend on the boundary conditions used for the phonon field. The two quantities relevant for the boundary conditions are the displacement vector $\mathbf{u}(\mathbf{r})$ and the stress vector $\mathbf{t}(r) = T\mathbf{e}_r$ at $r = R$, with T being the stress tensor [118] and \mathbf{e}_r being the unit vector along r . One can now write $\mathbf{u}(\mathbf{r}) = \mathcal{U}\boldsymbol{\chi}$ and $\mathbf{t}(\mathbf{r}) = \mathcal{T}\boldsymbol{\chi}$ with $\boldsymbol{\chi} = (\chi_0, \chi_1, \chi_2)$, where the expressions for the matrices \mathcal{U} and \mathcal{T} are given in Appendix B. There are two limiting cases for the boundaries. The first case is met when there is zero stress at the surface, i.e. $\mathbf{t}(R) = 0$, [118] with $\omega_{q,s}$ being the solutions of $|\mathcal{T}(R)| = 0$ (free surface boundary conditions or FSBC), while the second limiting case is met when the surface is rigid, i.e. $\mathbf{u}(R) = 0$, with $\omega_{q,s}$ being the solutions of $|\mathcal{U}(R)| = 0$ (clamped surface boundary conditions or CSBC). The phonon field is normalized according to the following relation [120]

$$\frac{1}{\pi R^2} \int_0^{2\pi} d\phi \int_0^R dr r \mathbf{u}^*(\mathbf{k}, r, \phi) \cdot \mathbf{u}(\mathbf{k}, r, \phi) = \frac{\hbar}{2M\omega_{\mathbf{k}}}. \quad (3.47)$$

From the FSBC or CSBC, together with the normalization of the phonon field, one obtains the spectrum $\omega_{q,s}$ and the normalization function $\mathcal{F}(q,s)$.

We now use the effective spin-phonon Hamiltonian with the fluctuating field given in Eq. (3.43) to find the spin relaxation and decoherence times, T_1 and T_2 , respectively. We mention here that the fluctuating magnetic field $\delta B_y(t)$ is perpendicular to the external one \mathbf{B} such that there is no pure dephasing coming from the interaction of the spin with phonons in lowest order in SOI. In fact, as shown previously, [64] this is valid for any type of baths, be it phonons, particle-hole excitations etc.

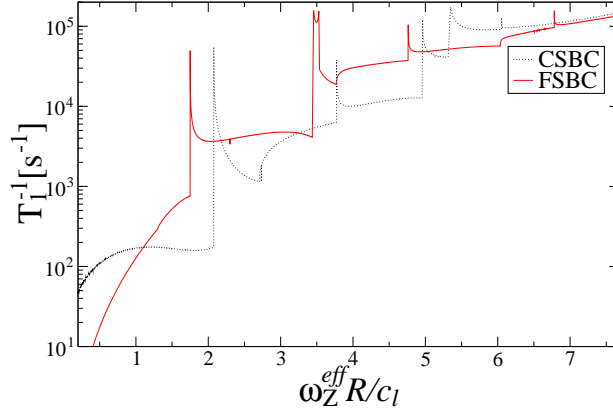


Figure 3.2: The relaxation rate T_1^{-1} as a function of the ratio $\omega_Z^{\text{eff}} R/c_l$, for both FSBC and CSBC (see text for explanations of FSBC and CSBC). Here $\hbar c_l/R \simeq 0.6 \cdot 10^{-4}$ eV ($c_l \simeq 4 \cdot 10^3$ m/s and $R \simeq 50$ nm) corresponding to a magnetic field $B \simeq 0.2$ T, for $g = 2.5$.

In the following we derive the expressions of the T_1 and T_2 times resulting from the fluctuating field $\delta B_y(t)$. For this we need to compute the bath correlator

$$J_{yy}(\omega) = \left(\frac{g\mu_B}{2\hbar} \right)^2 \int_0^\infty dt e^{-i\omega t} \langle \delta B_y(0) \delta B_y(t) \rangle, \quad (3.48)$$

where the brackets $\langle \dots \rangle$ means tracing over the phonon bath being at thermal equilibrium at temperature T . The relaxation time within the Bloch-Redfield approach is given in the present particular case (the B -field along x -direction) by (see Ref. [64, 65])

$$T_1^{-1} = \text{Re}(J_{yy}(\omega_Z^{\text{eff}}) + J_{yy}(-\omega_Z^{\text{eff}})), \quad (3.49)$$

with $\omega_Z^{\text{eff}} = E_Z^{\text{eff}}/\hbar$. Making use of Eq. (3.48) we then finally obtain for the relaxation rate

$$T_1^{-1} = T_{(0)1}^{-1} \left(\frac{\omega_Z^{\text{eff}} R}{c_l} \right)^5 \sum_s \left(\left| \frac{\partial q}{\partial \omega_{q,s}} \right| \frac{\mathcal{C}^2(q,s)}{\mathcal{F}(q,s)} \right)_{\omega_{q,s} \equiv \omega_Z^{\text{eff}}}, \quad (3.50)$$

where

$$T_{(0)1}^{-1} \approx 0.05 \frac{\delta^2 \hbar}{\rho_c R^5} \left(\frac{\Xi_0}{\Delta E_0} \right)^2 \left(\frac{R}{\lambda_{SO}} \right)^2. \quad (3.51)$$

In the above expression $\delta = E_Z/E_Z^{\text{eff}}$, and the functions $\mathcal{C}(q,s)$ and $\mathcal{F}(q,s)$ are defined in Eqs. (3.45,3.46). We mention that within first order in SOI the decoherence time T_2 induced by phonons satisfies $T_2 = 2T_1$ since, as mentioned before, the fluctuating magnetic field induced by phonons $\delta \mathbf{B}$ is perpendicular to the applied one \mathbf{B} . In Fig. 3.8.1 we plot the relaxation time as a function of the ratio $\omega_Z^{\text{eff}} R/c_l$, for $R = 50$ nm and $c_l = 4 \cdot 10^3$ m/s. We see that the relaxation rate exhibits peaks as a function of the effective Zeeman splitting E_Z^{eff} . This is due to the finite size in the transverse direction which gives rise to phonon branches. Each new peak appears when E_Z^{eff} reaches a new energetically higher branch. Note that although the relaxation rate seems to diverge when reaching a new peak, in reality this does not happen

since there are many processes which broaden the phonon DOS at these special points, like phonon-phonon scattering, phonon-substrate scattering, etc. The usual branch splitting is on the order of $\omega_{ph}^R \equiv c_l/R$, which stands for the phonon frequency in bulk material with the wave-length equal to the dot size R . This frequency ω_{ph}^R (or energy, when expressed as $\hbar\omega_{ph}^R$) is the parameter which characterizes the dominant mechanism for the phonon-induced spin relaxation, which can be due to piezoelectric-potential or deformation-potential phonons. In the limit $\omega_Z^{eff} \ll \omega_{ph}^R$ the piezo-phonons give the main contribution to the relaxation rate T_1^{-1} , while in the opposite case, $\omega_Z^{eff} \gg \omega_{ph}^R$, the main contribution to the relaxation rate T_1^{-1} is given by deformation-potential phonons. [64] Here we are in neither of the two limits, but in the range where Zeeman splitting is slightly larger than $\hbar\omega_{ph}^R$, i.e. $\omega_Z^{eff} \geq \omega_{ph}^R$. However, taking into account only the deformation potential mechanism should give the right order of magnitude for the relaxation rate. We mention here that the relaxation rate T_1^{-1} in the low energy limit ($\omega_Z^{eff} R/c_l < 1$) is given predominantly by the longitudinal linear in q mode ($\omega_{long}(q) = c_l q$) and the bending mode, square in q ($\omega_{bend}(q) = Bq^2$, with B being a constant which depends on R). [118]

We see from Fig. 3.8.1 that each new phonon branch gives a strong enhancement of the relaxation rate T_1^{-1} , since it adds more phonon density of states. However, we see also that before the first peak, i.e. before reaching the first new branch, there is little spin relaxation ($T_1 \geq 10^{-3}$ s) for both FSBC and CSBC. This energy scale corresponds to a Zeeman splitting $E_Z^{eff} \approx 10^{-4}$ eV ($E_Z^{eff} \approx 1.2 \cdot 10^{-4}$ eV) for FSBC (CSBC).

If one tunes the *effective* Zeeman splitting E_Z^{eff} below the first peak, the relaxation rate of the qubit becomes very small, and the fact that E_Z^{eff} and *not* E_Z has to be tuned is practically an advantage for reasonably strong SOI since we need quite large E_Z for having large $g \propto E_Z$. In the present case $E_Z^{eff}/E_Z \approx 0.93$, and for larger SOI this ratio will be even smaller.

3.8.2 Spin relaxation in transverse confined QDs

We give here a brief description of the phonon-induced spin relaxation for the case shown in Fig. 3.1B. We first mention that due to the strong confinement in the transverse direction we can average the electron-phonon interaction over the transverse orbital ground state $|0_t\rangle$. Since for the ground state wave function we have $m = 0$ (see Eq. (3.25)), the only modes which couple to the electron, and thus eventually to the spin, are the $n = 0$ modes of the phonon field in Eq. (3.39). Then, the problem of relaxation simplifies considerably.

The transformation $H_{e-ph} \rightarrow e^{-S} H_{e-ph} e^S$, with S given in Eq. (3.30), although exact, does not lead to a coupling of the spin to the phonon field since both the electron-phonon interaction Hamiltonian H_{e-ph} and S contain only coordinate x operator, i.e. they commute. After this transformation, however, we are left with no SOI term, but with the x -dependent Zeeman coupling in Eq. (3.32). We now perform a second transformation $H_{e-ph} \rightarrow e^{-S'} H_{e-ph} e^{S'}$ with S' given before Eq. (3.32), under the assumption $E_Z \ll \hbar\omega_0$. Then, within first order in $E_Z/\hbar\omega_0$ we obtain for the spin-phonon Hamiltonian H_{s-ph} the following expression

$$H_{s-ph} = \langle 0|[S', H_{e-ph}]|0\rangle, \quad (3.52)$$

where we averaged also over the ground-state $|0\rangle$ of the orbital Hamiltonian H_0 . The spin-

phonon Hamiltonian H_{s-ph} reads

$$H_{s-ph} = \frac{1}{2}g\mu_B\delta B_{\tilde{x}}(t)\sigma_{\tilde{x}} + \frac{1}{2}g\mu_B\delta B_{\tilde{z}}(t)\sigma_{\tilde{z}}, \quad (3.53)$$

with

$$\delta B_{\tilde{x},\tilde{z}}(t) = B_{eff} \frac{\Xi_0}{\hbar\omega_0} \sum_{q,s} \frac{M_{s-ph}^{\tilde{x},\tilde{z}}(q)}{\sqrt{2\mathcal{F}(q,s)}\rho_c\omega_{q,s}/\hbar} K_{\mathbf{k}}^2 b_{\mathbf{k}}^\dagger + \text{h.c.}, \quad (3.54)$$

and $\mathbf{k} \equiv \{q, s\}$. The functions $M_{s-ph}^{\tilde{x},\tilde{z}}$ are given by the following expressions

$$M_{s-ph}^{\tilde{x}}(q) = \text{SinhInt} \left(\frac{l^2 q}{\lambda_{SO}} \right) \quad (3.55)$$

$$M_{s-ph}^{\tilde{z}}(q) = \gamma - \text{CoshInt} \left(\frac{l^2 q}{\lambda_{SO}} \right) + \text{Log} \left(\frac{l^2 q}{\lambda_{SO}} \right), \quad (3.56)$$

where $\gamma = 0.577$ is the Euler constant, $\text{Log}(x)$ is the natural logarithm, while the special functions $\text{SinhInt}(x)$ and $\text{CoshInt}(x)$ are defined as

$$\text{SinhInt}(x) = \int_0^x dt \frac{\sinh(t)}{t} \quad (3.57)$$

$$\text{CoshInt}(x) = \gamma + \text{Log}(x) + \int_0^x dt \frac{\cosh(t) - 1}{t}. \quad (3.58)$$

We see that, there is both relaxation and pure dephasing of the spin due to spin-phonon interaction. However, since the deformation-potential phonons is superohmic (even in 1D case for deformation-potential phonons), the pure dephasing rate vanishes [121] so that we retain in the following only the first term in Eq. (3.53). The relaxation rate T_1^{-1} can be found by the same procedure as in the previous case and reads

$$T_1^{-1} = \text{Re}(J_{\tilde{x}\tilde{x}}(\omega_Z^{eff}) + J_{\tilde{x}\tilde{x}}(-\omega_Z^{eff})), \quad (3.59)$$

where the correlation function $J_{\tilde{x}\tilde{x}}$ is defined in Eq. (3.48) with $y \rightarrow \tilde{x}$, and $\omega_Z^{eff} = E_Z^{eff}/\hbar$, as before. The expression for the relaxation rate T_1^{-1} becomes

$$T_1^{-1} = T_{(0)1}^{-1} \left(\frac{\omega_Z^{eff} l}{c_l} \right)^5 \sum_s \left(\left| \frac{\partial q}{\partial \omega_{q,s}} \right| \frac{\widetilde{\mathcal{M}}_{s-ph}^{2\tilde{x}}(q)}{\mathcal{F}(q,s)} \right)_{\omega_{q,s}=\omega_Z^{eff}}, \quad (3.60)$$

where

$$T_{(0)1}^{-1} = \frac{\hbar}{2\pi\rho_c R^2 l^3} \left(\frac{\Xi_0}{\hbar\omega_0} \right)^2 \quad (3.61)$$

and

$$\widetilde{\mathcal{M}}_{s-ph}^{\tilde{x}}(q) = \mathcal{M}_{s-ph}^{\tilde{x}}(q) e^{-q^2 l^2 / 8}. \quad (3.62)$$

In order to find now the dependence of the relaxation rate T_1^{-1} on the effective Zeeman splitting ω_Z^{eff} , we have to find first the phonon eigen-frequencies $\omega_{q,s}$. This can be done following the same steps as in the previous section, depending which kind of boundary

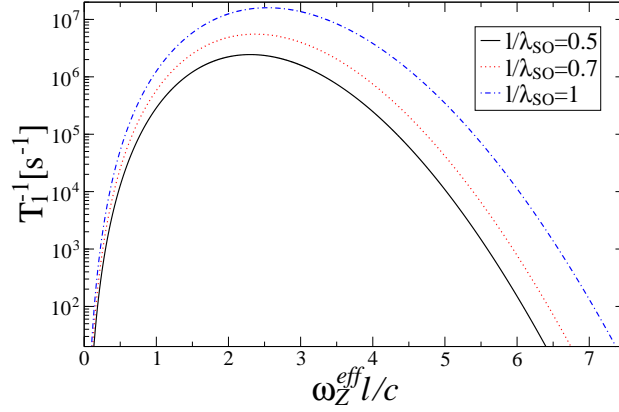


Figure 3.3: The relaxation rate T_1^{-1} as a function of the ratio $\omega_Z^{eff} l / c_s$ for three different ratios l / λ_{SO} and with FSBC (see text).

conditions are used, i.e. FSBC or CSBC. As mentioned earlier, the average distance between the branches s is on the order of $\omega_{ph}^R = c_l / R$. Then, since $R \ll l$, and also due to the gaussian suppression in Eq. (3.62), it is enough to consider in Eq. (3.60) only the lower branch $s = 1$. If we now assume FSBC and the limit $qR \ll 1$, the phonon eigen-frequency becomes linear in q , i.e. $\omega_{q,1} \equiv \omega(q) = c_s q$, with [118]

$$c_s = c_t \sqrt{\frac{3c_l^2 - 4c_t^2}{c_l^2 - c_t^2}}. \quad (3.63)$$

The normalization function χ_0 acquires also a simple form in this limit, and reads

$$\chi_0 = \frac{c_l^2}{3c_l^2 - 4c_t^2} \frac{R}{q} \sqrt{\frac{\hbar}{2M c_s q}}. \quad (3.64)$$

After inserting in Eq. (3.60) the expressions for $\omega(q)$ and χ_0 , we obtain for the relaxation rate T_1^{-1} (FSBC) the final expression

$$T_1^{-1} = \frac{T_{(0)1}^{-1}}{2} \left(\frac{c^2}{3c_l^2 - 4c_t^2} \right)^2 \left(\frac{\omega_Z^{eff} l}{c_s} \right)^3 \widetilde{\mathcal{M}}_{s-ph}^{\tilde{x}^2}(\omega_Z^{eff} l / c_s). \quad (3.65)$$

In Fig. 3.8.2 we plot the relaxation rate T_1^{-1} as a function of the dimensionless parameter $\omega_Z^{eff} l / c_s$ for different SOI strengths measured through the ratio l / λ_{SO} . We assumed here $R = 10$ nm and $l = 50$ nm, which gives $\hbar c_s / l \equiv \hbar \omega_{ph}^l = 0.05$ meV and $\hbar c_l / R \equiv \hbar \omega_{ph}^R = 0.25$ meV. We see in Fig. 3.8.2 that the relaxation rate T_1^{-1} is quite large ($T_1^{-1} \sim 10^5 - 10^7$ s $^{-1}$) for $\omega_Z^{eff} / \omega_{ph}^l \sim 1 - 5$, i.e. when these energies are comparable. However, there is need for a large effective Zeeman splitting $E_Z^{eff} \gg \hbar \omega_{ph}^l$ to achieve a large spin-phonon coupling \mathcal{M}_γ . At the same time, one should stay still below the next phonon branch since above it we find a substantial increase for the relaxation rate. Since this next phonon branch lies somewhere around $2\hbar \omega_{ph}^R \approx 0.5$ meV, the condition for efficient spin-phonon coupling and

weak relaxation becomes $\hbar\omega_{ph}^l \ll E_Z^{eff} < 2\hbar\omega_{ph}^R$. In this regime we are actually satisfying also the necessary condition that $E_Z/\hbar\omega_0 \ll 1$, since for $l = 50$ nm we have $\hbar\omega_0 = 1.3$ meV. We mention that for CSBC the phonon spectrum is gapped, and, in consequence, there is no phonon-induced relaxation of the spin for Zeeman splittings E_Z^{eff} smaller than this gap Δ_{ph} . This energy (gap) is on the order of $\Delta_{ph} \sim 2\hbar\omega_{ph}^R = 0.5$ meV. Note the non-monotonic behavior of the relaxation rate as a function of the effective Zeeman splitting (see Fig. 3.8.2). This non-monotonicity has the same origin as in GaAs QDs, [64] and comes from the fact that for increasing Zeeman splitting the wave-length of the phonon decreases, and when this becomes less than the dot length the phonons decouple from the electron (i.e. the electron-phonon coupling averages to zero). A similar non-monotonic effect has been recently observed in GaAs double QDs. [122]

3.8.3 Decoherence due to hyperfine interaction

The spin decoherence time due to single-phonon processes is given by $T_2 = 2T_1$ so that the main source for decoherence comes from the hyperfine interaction between the electron and the surrounding nuclei. This time scale, T_2^* , is given by [83, 84]

$$T_2^* = 2 \frac{\hbar\sqrt{N}}{A}, \quad (3.66)$$

where N is the number of nuclei in the sample and A is the hyperfine constant. The number of nuclei N can be found as

$$\frac{1}{N} = v_0 \int d^3\mathbf{r} |\psi(\mathbf{r})|^4, \quad (3.67)$$

where v_0 is the unit cell volume per nuclear spin and $\psi(\mathbf{r})$ is the wave function of the electron in the QDs. We see that the larger the number of nuclei, i.e. the bigger the dot, the longer is the pure decoherence time T_2^* for the electron. In a typical GaAs QDs ($R = 30$ nm and $l = 5$ nm, $A_{GaAs} = 90 \mu\text{eV}$, $N \approx 10^5$) this time scale is on the order of $T_2^* \sim 10^{-8}$ s. [83, 84] In InAs material the hyperfine constant $A_{InAs} \approx 300 \mu\text{eV}$ [123], i.e. more than three times larger than in GaAs. However, the number of nuclei found from Eq. (3.67) is on the order $N \approx 10^6$ for both geometries so that the dephasing time $T_2^* \approx 4 \cdot 10^{-9}$ s. However, again like in GaAs, we expect that coherently driving the qubit will prolong the T_2^* time up to 10^{-6} s and with echo up to 10^{-5} s. [13] Moreover, like in GaAs QDs, one can make use of state narrowing procedures, [86, 124] which should lead to a further substantial enhancement of T_2^* due to nuclear spins, and possibly reach the SOI induced limit of $10^{-1} - 10^{-4}$ s calculated above for large magnetic field strengths.

3.9 Conclusions

We have proposed and studied an efficient way to implement spin qubits localized in InAs nanowires coupled to a 1D electromagnetic transmission line (cavity) via SOI. We have analyzed two experimentally achievable configurations of the system. In the first case the electronic confinement is much stronger along the nanowire axis than in the transverse direction (large-radius nanowires), while the other case corresponds to the opposite limit (small-radius

nanowires). We have found an efficient coupling between the spin and the cavity modes due to strong vacuum fluctuations in the cavity and a sizable SOI in InAs. We also have shown that this spin-photon coupling can allow for coupling between two (or several) distant spins, depending on the detuning of the Zeeman splittings E_{iZ}^{eff} from the cavity mode $\hbar\omega$. The SOI-induced exchange coupling J between two spins can be controlled by electrical fields only, e.g. by changing the g -factor and/or orbital level spacing. Also, single-spin rotations can be performed efficiently by electric fields only, through the EDSR mechanism. Exploiting a stronger SOI in InAs nanowires than typically in GaAs structures might seemingly compromise the use of spin for quantum memory, because the orbital environment couples also stronger to the spin. However, we have studied the relaxation of the spin due to the lattice vibrations in the InAs nanowires for both configurations, and shown that the time scale for the spin-decay is on the order of milliseconds for relatively strong magnetic fields ($B \sim 0.5 - 1$ T), much larger than the times associated with the spin-photon dynamics, which takes place on times scales on the order of $10^{-8} - 10^{-7}$ s. This fact is due to the quasi 1D structure of the system where the phonon spectrum shows discrete branches, very different from the bulk limit.

We stress here also that the coupling of the quantized modes of the transmission line to the spin degree of freedom via SOI is not restricted to QDs in semiconductor nanostructures. In principle, this coupling should be possible in other spin-orbit coupled systems too, like nitrogen-vacancy centers (NV-centers), [125, 126] molecular magnets, [127–129] magnetic nanorings, [130] etc. In these systems there is usually a large zero-field splitting (ZFS) of the lowest spin-multiplet attributed to SOI or to dipole-dipole interaction. This would allow for an efficient coupling of the electric fields, quantum or classical, to the spin degree of freedom and finally providing a mechanism for an all-electrical implementation of spin-based quantum information processing.

As a final remark, we mention that the present scheme can be also used to form hybrid structures where spin-qubits are integrated together with other types of qubits in the same 1D transmission line. For example, one can envision a setup where a spin-qubit is coupled via the cavity modes to superconducting qubit as the one studied in Ref. [108] so that one can transfer arbitrary states between the two qubit-systems.

Chapter 4

Relaxation of hole spins in quantum dots via two-phonon processes

We investigate theoretically spin relaxation in heavy hole quantum dots in low external magnetic fields. We demonstrate that two-phonon processes and spin-orbit interaction are experimentally relevant and provide an explanation for the recently observed saturation of the spin relaxation rate in heavy hole quantum dots with vanishing magnetic fields. We propose further experiments to identify the relevant spin relaxation mechanisms in low magnetic fields.

4.1 Introduction

In the past years, a new candidate for a qubit state has been attracting growing interest: the spin of a heavy hole (HH) confined in a flat QD. In a bulk semiconductor the HH ($J_z = \pm 3/2$) and light hole (LH) ($J_z = \pm 1/2$) bands are degenerate giving rise to strong mixing and thus to strong HH-spin relaxation. However, in a 2D system the HH and LH bands are split due to the strong confinement along the growth direction [18] implying a significant reduction of the HH spin relaxation via HH-LH mixing.

A basic requirement for a good qubit is that it can be initialized in a given state (say, spin up) and that the relaxation and decoherence times be much longer when compared to the switching times for single- and two-qubit operations. The spin of a HH localized in a quantum dot has been successfully initialized [20], and the relaxation time has been measured [20, 24], and found to be on the order of 100 microsecs. The relaxation (T_1) and decoherence (T_2) times of a HH-spin localized in a flat QD are, like for electrons, determined by the interaction of the HH with the nuclear spin bath in the QD and the lattice vibrations (phonons). The former interaction is weaker for HHs than for electrons (due to the p-symmetry of the hole) [19, 22]. More importantly, it is of Ising type, making it ineffective for HH-spins initialized along the growth direction [19], as typically done in experiments [20, 21], thus implying very long dephasing times. This is in contrast to electrons, where the hyperfine interaction is isotropic and dominates the spin dynamics at low B-fields [13, 83, 131, 132].

4.2 Heavy-hole Hamiltonian

Phonons couple to the HH spin through the spin-orbit interaction (SOI) [25]. The predicted values [25] for the one-phonon induced relaxation time T_1 agree quite well with data obtained in high B-fields [24]. However, for low B-fields ($B \sim 1.5 - 3\text{T}$) and high temperatures ($T > 2\text{K}$), a clear deviation from the one-phonon theory has been observed [24]. Furthermore, recent experiments on optical pumping of HH-spins in QDs showed saturation of T_1 for very low or even vanishing B-field [20]. The relaxation time was found to be unusually long, $T_1 \approx 0.1 - 1\text{ms}$, like previously observed in high B-fields [24]. Both observations suggest other sources of relaxation, and the question arises what are they and what are their observable consequences? The answer to this question is not only interesting by itself but also relevant for using HHs as qubits. In the following, we show that two-phonon processes are good candidates and even provide a quantitative explanation of the mentioned measurements at low B-fields [20, 24]. The importance of such two-phonon processes was noticed a long time ago for electron spins in silicon-donors [133] and rare-earth ions [134], while for electrons in QDs it was shown that these processes are negligible compared to nuclear spin effects [135, 136].

To describe a HH confined to a QD and interacting with the surrounding phonon bath, we start with the following Hamiltonian

$$H_h = H_0 + H_Z + H_{SO} + H_{h-ph} + H_{ph}, \quad (4.1)$$

where $H_0 = p^2/2m^* + V(\mathbf{r})$, is the dot Hamiltonian, $V(\mathbf{r}) \equiv m^*\omega_0^2 r^2/2$ is the confinement potential which is assumed to be harmonic, with m^* being the HH mass. The second term in Eq. (4.1) is the Zeeman energy of the HH (pseudo-) spin

$$H_Z = g\mu_B \mathbf{B} \cdot \boldsymbol{\sigma}/2, \quad (4.2)$$

with \mathbf{B} being the magnetic field and $\boldsymbol{\sigma}$ the Pauli matrices for the HH spin defined in the $J_z = \pm 3/2$ subspace. The third term represents the spin-orbit Hamiltonian, which, for well separated HH-LH bands (flat dots), reads [25]

$$H_{SO} = \beta p_- p_+ p_- \sigma_+ + h.c. \quad (4.3)$$

This Hamiltonian represents the effective Dresselhaus SOI (restricted to the HH subspace) due to bulk inversion asymmetry of the crystal [25], where $p_{\pm} = p_x \pm ip_y$, $\mathbf{p} = -i\hbar\nabla - e\mathbf{A}(\mathbf{r})$, $\mathbf{A}(\mathbf{r}) = (-y, x, 0)B/2$, and $\sigma_{\pm} = \sigma_x \pm i\sigma_y$. We note that in Eq. (4.3) we have neglected the Rashba SOI and other possibly linear-in-k but small SOI terms [25]. The fourth term in Eq. (4.1) represents the interaction of the HH charge with the phonon field, *i.e.*

$$H_{h-ph} = \sum_{\mathbf{q}j} M_{\mathbf{q}j} X_{\mathbf{q}j}, \quad (4.4)$$

with

$$M_{\mathbf{q}j} = \frac{F(q_z)e^{i\mathbf{q}\cdot\mathbf{r}}}{\sqrt{2\rho_c\omega_{\mathbf{q}j}}} [e\beta_{\mathbf{q}j} - i(\Xi_0 \mathbf{q} \cdot \mathbf{d}_{\mathbf{q}j} - \Xi_z q_z d_{\mathbf{q}j}^z)], \quad (4.5)$$

and $X_{\mathbf{q}j} = \sqrt{\hbar/\omega_{\mathbf{q}j}}(a_{-\mathbf{q}j}^\dagger + a_{\mathbf{q}j})$, where \mathbf{q} is the phonon wave-vector, with j denoting the acoustic branch, $\omega_{\mathbf{q}j} = c_j q$ the phonon energy, with c_j the speed of sound in the j -th branch, $\mathbf{d}_{\mathbf{q}j}$ the polarization unit vector, ρ_c the sample density (per unit volume), and $e\beta_{\mathbf{q}j}$ the piezoelectric electron-phonon coupling and $\Xi_{0,z}$ the deformation potential constants [25]. The form factor $F(q_z)$ in Eq. (4.5) equals unity for $|q_z| \ll d^{-1}$ and zero for $|q_z| \gg d^{-1}$, with d being the dot size in the (transverse) z -direction. The last term in Eq. (4.1) describes the free phonon bath.

4.3 Spin-phonon interaction

In the following, we analyze the effect of the phonons on the HH spin. The phonons do not couple directly to the spin, but the SOI plays the role of the mediator of an effective spin-phonon interaction. Let us define the dot Hamiltonian $H_d \equiv H_0 + H_Z + H_{SO}$. These eigenstates $|n\sigma\rangle$ of H_d are formally connected to the eigenstates $|n\rangle|\sigma\rangle$ of $H_0 + H_Z$ by an exact Schrieffer-Wolff (SW) transformation [64, 137], i.e., $|n\sigma\rangle = e^S|n\rangle|\sigma\rangle$, where $S = -S^\dagger$ is the SW generator and can be found in perturbation theory in SOI. After this transformation, any operator A in the old basis transforms as $A \rightarrow \tilde{A} = e^S A e^{-S}$ in the new basis (e.g., $H_d \rightarrow \tilde{H}_d$, $H_{h-ph} \rightarrow \tilde{H}_{h-ph}$, etc.).

In order to derive the effective spin-phonon interaction, we perform another SW transformation of the total HH Hamiltonian \tilde{H}_h . We get an effective Hamiltonian $H_{eff} = e^T \tilde{H}_h e^{-T}$, where $T = -T^\dagger$ is chosen such that it diagonalizes \tilde{H}_{h-ph} in the eigenbasis of H_d . In lowest order in H_{h-ph} , we obtain $T \approx \tilde{L}_d^{-1} \tilde{H}_{h-ph}$, where the Liouvillean is defined as $\tilde{L}_d A = [\tilde{H}_d, A]$, $\forall A$, and diagonal terms of H_{h-ph} are to be excluded. In 2nd order in H_{h-ph} , we obtain then the effective spin-phonon Hamiltonian

$$\begin{aligned} H_{s-ph} &= \boldsymbol{\sigma} \cdot \sum_{\mathbf{q}j, \mathbf{q}'j'} [\delta_{\mathbf{q}j, \mathbf{q}'j'} \mathbf{C}_{\mathbf{q}j}^{(1)} X_{\mathbf{q}j} + \mathbf{C}_{\mathbf{q}j, \mathbf{q}'j'}^{(2)} X_{\mathbf{q}j} X_{\mathbf{q}'j'} \\ &+ \mathbf{C}_{\mathbf{q}j, \mathbf{q}'j'}^{(3)} (P_{\mathbf{q}j} X_{\mathbf{q}'j'} - P_{\mathbf{q}'j'} X_{\mathbf{q}j})], \end{aligned} \quad (4.6)$$

with

$$\boldsymbol{\sigma} \cdot \mathbf{C}_{\mathbf{q}j}^{(1)} = \langle 0 | \tilde{M}_{\mathbf{q}j} | 0 \rangle, \quad (4.7)$$

$$\boldsymbol{\sigma} \cdot \mathbf{C}_{\mathbf{q}j, \mathbf{q}'j'}^{(2)} = \langle 0 | [\tilde{L}_d^{-1} \tilde{M}_{\mathbf{q}j}, \tilde{M}_{\mathbf{q}'j'}] | 0 \rangle \quad (4.8)$$

$$\boldsymbol{\sigma} \cdot \mathbf{C}_{\mathbf{q}j, \mathbf{q}'j'}^{(3)} = \langle 0 | [\tilde{L}_d^{-1} \tilde{M}_{\mathbf{q}j}, \tilde{L}_d^{-1} \tilde{M}_{\mathbf{q}'j'}] | 0 \rangle. \quad (4.9)$$

Above, $P_{\mathbf{q}j} = i\sqrt{\hbar\omega_{\mathbf{q}j}}(a_{-\mathbf{q}j}^\dagger - a_{\mathbf{q}j})$ is the phonon field momentum operator, and $|0\rangle$ is the orbital ground state. In Eq. (4.6) we have neglected 2nd order corrections in SOI to the energy levels. Note that for vanishing magnetic field $\mathbf{B} \rightarrow 0$ only the last term in H_{s-ph} is non-zero, since only this one preserves time-reversal invariance and thus gives rise to zero field relaxation (ZFR) [133–135].

We now assume the orbital confinement energy $\hbar\omega_0$ much larger than the SOI, i.e. $\|H_0\| \gg \|H_{SO}\|$, and treat the SOI to leading order in perturbation theory. We consider also the \mathbf{B} -field to be applied perpendicularly to the dot plane (as in Refs. [20, 24]). The

SW-generator S can be written as $S = S_+ \sigma_- - h.c.$, and we then find

$$\begin{aligned} S_+ &= A_1 p_+ p_- p_+ + A_2 [p_+ p_- P_+ - (p_+ P_- - P_+ p_-) p_+] \\ &+ A_4 P_+ P_- P_+ + A_3 [(p_+ P_- - P_+ p_-) P_+ + P_+ P_- p_+]. \end{aligned} \quad (4.10)$$

Here, $A_i \equiv A_i(\omega_Z, \omega_c)$ with $\omega_Z = g\mu_B B/\hbar$ and $\omega_c = eB/2c$. For $\omega_Z, \omega_c \ll \omega_0$, we obtain

$$A_1 \approx -\frac{7\beta}{9\hbar} \frac{(\omega_Z + \omega_c)}{\omega_0^2}, \quad (4.11)$$

$$A_2 \approx -\frac{\beta}{3\hbar} \frac{\omega_c}{\omega_0^2}, \quad (4.12)$$

$$A_3 \approx -\frac{2\beta}{9\hbar} \frac{\omega_c^2(\omega_c + \omega_Z)}{\omega_0^4}, \quad (4.13)$$

$$A_4 \approx \frac{2\beta}{3\hbar} \frac{\omega_c^3}{\omega_0^4}, \quad (4.14)$$

while $P_\pm = P_x \pm iP_y$ with $P_{x(y)} = -i\hbar\nabla_{x(y)} \pm (m^*\omega_0^2/\omega_c)y(x)$. After somewhat tedious calculations, we obtain analytic expressions for $\mathbf{C}^{(i)} = (C^{(i,x)}, C^{(i,y)}, 0)$ occurring in Eq. (4.6). We give below only the exact expression for $i = 3$, the rest being too lengthy to be displayed here:

$$\begin{aligned} C_{\mathbf{q}j, \mathbf{q}'j'}^{(3,x/y)} &= \pm M_{\mathbf{q}j}^{\mathbf{q}'j'} m^* \lambda_d^2 \beta e^{-q^2 \lambda_d^2/4} \mathcal{F}(\mathbf{q} \cdot \mathbf{q}') \\ &\times \left(q_y^2 q'_x - q_y'^2 q_x \pm (q_x - q'_x)(2q_y q'_y + 3q_x q'_x) \right), \end{aligned} \quad (4.15)$$

where

$$\begin{aligned} \mathcal{F}(\mathbf{q} \cdot \mathbf{q}') &= \frac{1}{\lambda_d^2 (\mathbf{q} \cdot \mathbf{q}')^2} \left(e^{-\lambda_d^2 \mathbf{q} \cdot \mathbf{q}'/2} - \lambda_d^2 \mathbf{q} \cdot \mathbf{q}'/2 \right) \\ &\times \left(\gamma + \log(\lambda_d^2 \mathbf{q} \cdot \mathbf{q}'/2) + \Gamma(0, \lambda_d^2 \mathbf{q} \cdot \mathbf{q}'/2) \right), \\ M_{\mathbf{q}j}^{\mathbf{q}'j'} &= \frac{\hbar F(q_z) F(q'_z)}{2\rho_c \sqrt{\omega_{\mathbf{q}j} \omega_{\mathbf{q}'j'}}} (\Xi_0 \mathbf{q} \cdot \mathbf{d}_{\mathbf{q}j} - \Xi_z q_z d_{\mathbf{q}j}^z) (\Xi_0 \mathbf{q}' \cdot \mathbf{d}_{\mathbf{q}'j'} - \Xi_z q'_z d_{\mathbf{q}'j'}^z), \end{aligned} \quad (4.16)$$

with λ_d is the dot-diameter. We have also introduced $\gamma \approx 2.17$ the Euler constant and $\Gamma(s, x)$ the incomplete gamma function. We note that $C^{(1,2)} \propto B$, so that these two terms vanish with vanishing B-field.

4.4 Hole-spin relaxation

Let us now analyze the relaxation of the spin induced by all the phonon processes in the spin-phonon Hamiltonian in Eq. (4.6). We first mention that all terms in Eq. (4.6) can be cast in a general spin-boson type of Hamiltonian $H_{s-b}^p = (1/2)g\mu_B \delta \mathbf{B}^p(t) \cdot \boldsymbol{\sigma}$, $p = 1, 2, 3$, with the corresponding identification of the fluctuating magnetic field terms $\delta B_j(t)$ from Eq. (4.6) (e.g. $\delta \mathbf{B}^1(t) \sim \mathbf{C}_{\mathbf{q}j}^{(1)} X_{\mathbf{q}j}$).

Within the Bloch-Redfield approach, the relaxation rate $\Gamma \equiv 1/T_1$ can be expressed as

$$\Gamma = \sum_{i=x,y} [J_{ii}(E_Z/\hbar) + J_{ii}(-E_Z/\hbar)]. \quad (4.17)$$

The correlation functions J_{ij} are defined by

$$J_{ij}(\omega) = (g\mu_B/2\hbar)^2 \int_0^\infty dt e^{-i\omega t} \langle \delta B_i(0) \delta B_j(t) \rangle, \quad (4.18)$$

where $\langle \dots \rangle$ denotes the average over the phonon bath, assumed to be in thermal equilibrium at temperature T . The relaxation time associated with the three types of spin-phonon processes in Eq. (4.6) is $\Gamma = \sum_{i=1,2,3} \Gamma^{(i)}$ with

$$\begin{aligned} \Gamma^{(1)} &= \frac{4\pi}{\hbar} \sum_{\mathbf{qj}} |\mathbf{C}_{\mathbf{qj}}^{(1)}|^2 \left(n(\omega_{\mathbf{qj}}) + \frac{1}{2} \right) \delta(E_Z - \hbar\omega_{\mathbf{qj}}), \\ \Gamma^{(m)} &\simeq \frac{8\pi}{\hbar} \sum_{\mathbf{qj}, \mathbf{q}'j'} |\mathbf{C}_{\mathbf{qj}, \mathbf{q}'j'}^{(m)}|^2 (\omega_{\mathbf{qj}} \omega_{\mathbf{q}'j'})^{m-2} n(\omega_{\mathbf{qj}}) \\ &\quad \times (n(\omega_{\mathbf{q}'j'}) + 1) \delta(\hbar\omega_{\mathbf{qj}} - \hbar\omega_{\mathbf{q}'j'}), \end{aligned} \quad (4.19)$$

where $n(\omega) = 1/(\exp(\omega/k_B T) - 1)$ is the Bose factor and $m = 2, 3$ correspond to B-dependent and B-independent two-phonon rates, *resp.* We remark that in Eq. (4.19) we have neglected some irrelevant processes in the limit of low-B field [63]. Also, for B -fields perpendicular to the dot plane the decoherence time satisfies $T_2 = 2T_1$ for one- and two-phonon processes since the spin-phonon fluctuations $\delta \mathbf{B}_j \perp \mathbf{B}$ [25, 64].

Note that for two-phonon processes the single phonon-energies do not need to match the Zeeman energy separately (as opposed to one-phonon processes), so that there is only a weak dependence on the B-field left which comes from the effective spin-phonon coupling itself.

In Figs. 4.4 and 4.4, we plot the phonon spin-relaxation rate Γ as a function of the B-field and of temperature, *resp.*, for InAs and GaAs quantum dots. Fig. 4.4 shows a clear saturation of Γ at low magnetic fields which is due to two-phonon processes, while Fig. 4.4 shows the known saturation at low temperatures due to one-phonon processes [25].

For these plots, we used the following HH InAs QDs (labeled by A) [138, 139] and GaAs QDs (labeled by B) parameters [25]: $\Xi_0 = 1.9$ eV, $\Xi_z = 2.7$ eV, $c_t^A = 2.64 \cdot 10^3$ m/s ($c_t^B = 3.35 \cdot 10^3$ m/s), $c_l^A = 3.83 \cdot 10^3$ m/s ($c_l^B = 4.73 \cdot 10^3$ m/s), $\rho_c^A = 5.68 \cdot 10^3$ kg/m³ ($\rho_c^B = 5.3 \cdot 10^3$ kg/m³), $m_A^* = 0.25m_e$ ($m_B^* = 0.14m_e$), $g^A = 1.4$ ($g^B = 2.5$), and we assume $\lambda_d = 3$ nm ($\hbar\omega_0^A = 35$ meV, $\hbar\omega_0^B = 60$ meV) and $d = 3$ nm (dot height). Also, $\beta_A \approx 2.1 \cdot 10^5$ m/s and $\beta_B \approx 4.6 \cdot 10^4$ m/s. From Fig. 4.4 we can infer that the two-phonon processes become dominant for magnetic fields $B < 2$ T ($B < 0.5$ T) and for temperatures $T > 2$ K ($T > 3$ K) for InAs (GaAs) QDs. These estimates for the relaxation rates due to one- and two-phonon processes are comparable to the ones recently measured in Refs. [20, 24], thus providing a reasonable explanation for these measurements. Note that, in contrast to the HH case, the relaxation time for electrons shows no deviation from the one-phonon time (or saturation) with decreasing B -field [11].

Next, we provide explicit expressions of the relaxation rates for low and high temperature limits. The rates $\Gamma^{(i)}$ can be written as

$$\Gamma^{(i)} = \delta_i \sum_{m=0}^{r_i} \frac{\omega_Z^{r_i-m} \omega_c^m}{\omega_0^{r_i}} F_i^{(m)}(t), \quad (4.20)$$

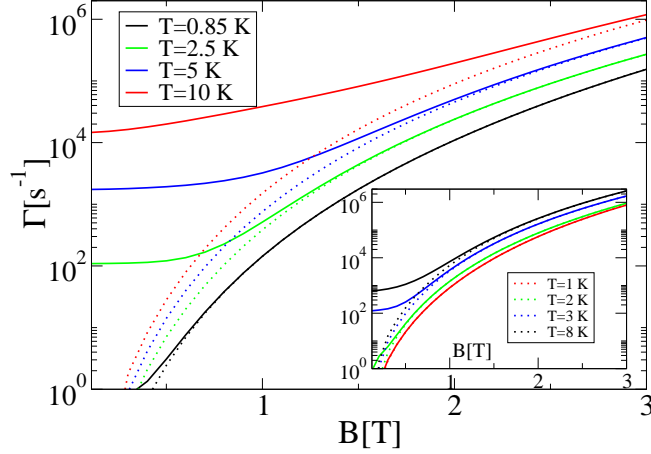


Figure 4.1: The heavy-hole spin relaxation rate Γ for InAs QDs (GaAs QDs in the inset) as a function of magnetic field B for different temperatures T . The full curves represent the rate due to one- and two-phonon processes, *i.e.* $\Gamma = \sum_{i=1}^3 \Gamma^{(i)}$ as defined in Eq. (4.19) for different temperatures T , while the dotted lines present the one-phonon rate $\Gamma^{(1)}$.

where

$$\delta_1 \approx \frac{2\pi \hbar^4 e h_{14}^2 \beta^2}{\kappa^2 m_h \lambda_d^6 \rho_c c_l^5}, \quad (4.21)$$

$$\delta_2 \approx \frac{\pi m_h^4 \beta^2 \Xi_0^4}{\hbar^2 \lambda_d^5 \rho_c^2 c_l^3}, \quad (4.22)$$

$$\delta_3 \approx \frac{\pi m_h^6 \beta^2 \Xi_0^4}{\hbar^4 c_l \lambda_d^3 \rho_c^2}, \quad (4.23)$$

with $r_1 = 5$, $r_2 = 2$, $r_3 = 0$, and $t = k_B T / E_{ph}$ with $E_{ph} \equiv \hbar c_l / \lambda_d$. The functions $F_i^{(m)}(t)$

	$F_1^{(0)}$	$F_1^{(1)}$	$F_2^{(0)}(t)$	$F_2^{(1)}(t)$	$F_2^{(2)}(t)$	$F_3(t)$
$t \ll 1$	0.004	0.015	$10^8 t^{13}$	$10^7 t^{13}$	$5 \cdot 10^6 t^{13}$	$10^9 t^{15}$
$t \gg 1$	$0.08 \frac{t}{\omega_Z}$	$0.03 \frac{t}{\omega_Z}$	$10^2 t^2$	$10^2 t^2$	$30 t^2$	$0.3 t^2$

Table 4.1: The asymptotic values for $F_i^{(m)}(t)$.

depend on the ratios $t = k_B T / E_{ph}$, d/λ , and c_l/c_t . In Table 4.1 we list the asymptotic (scaling) expressions for $F_i^{(m)}(t)$ in low B-fields $\omega_{c,Z} \ll \omega_0$ for low ($t \ll 1$) and high ($t \gg 1$) temperatures. We note that $F_1^{(1)}(t) \approx F_1^{(2)}(t)$ in both regimes, and $F_1^{(3,4,5)} \equiv 0$.

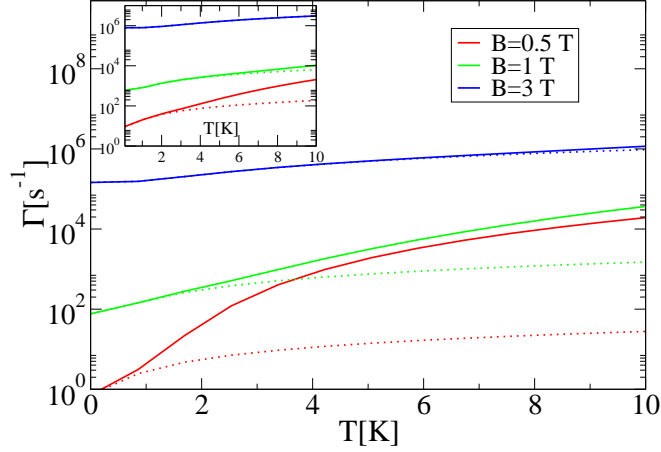


Figure 4.2: The heavy-hole spin relaxation rate Γ in Eq. (4.19) for InAs QDs (GaAs QDs in the inset) as a function of temperature T for different B -field values. For finite B -field, Γ saturates at low temperatures due to one-phonon processes.

Using Eq. (4.20) and Table 4.1 we can write for the two-phonon rates, say, for InAs QDs

$$\Gamma^{(2)} = \delta_2 \begin{cases} 10^7 \left(10 \frac{\omega_Z^2}{\omega_0^2} + \frac{\omega_Z \omega_c}{\omega_0^2} + 0.5 \frac{\omega_c^2}{\omega_0^2} \right) t^{13}, & t \ll 1 \\ 10^2 \left(\frac{\omega_Z^2}{\omega_0^2} + \frac{\omega_Z \omega_c}{\omega_0^2} + 0.3 \frac{\omega_c^2}{\omega_0^2} \right) t^2, & t \gg 1 \end{cases} \quad (4.24)$$

$$\Gamma^{(3)} = \delta_3 \begin{cases} 10^9 t^{15}, & t \ll 1 \\ 0.3 t^2, & t \gg 1. \end{cases} \quad (4.25)$$

From Eqs. (4.25) we find that for $T < 2\text{K}$ and for $B > 0.5\text{T}$ the one-phonon processes dominate the relaxation rate Γ . On the other hand, for low B -fields ($0.1\text{T} < B < 1\text{T}$) and finite temperatures ($T > 2\text{K}$) the two-phonon processes will give the main contribution to Γ , see Fig. 4.4. The main phonon processes could be identified experimentally by analyzing the temperature dependence of Γ , scaling as $\Gamma \sim T$ for one-phonon processes and as $\Gamma \sim T^2$ for two-phonon processes. Also, the saturation of Γ in vanishing B -field is a clear indication of two-phonon processes. Note that the strong enhancement of the two-phonon HH spin relaxation arises because (i) the rate is 2nd order in SOI (whereas for electrons it is 4th order) and (ii) the effective mass for HHs is much larger than that for electrons. Even more, the coupling of the phonon field to the HH spin is qualitatively different compared to electrons (in-plane coupling vs. perpendicular-to-the-plane coupling) allowing for a clear distinction between linear (electrons) and cubic (holes) in momentum SOI via two-phonon relaxation processes.

In order to compute $\Gamma^{(2,3)}$, we took into account only the contribution from the deformation potential since this dominates the two-phonon relaxation for $T/E_{ph} > 0.1$ and

$\omega_Z, \omega_c \ll \omega_0$. For the evaluation of $\Gamma^{(1)}$ instead, we considered both the piezoelectric and deformation potential contributions, both of them being important for B and T considered here. Surprisingly, we found that the ZFR rate $\Gamma^{(3)}$ increases when decreasing the dot size as $\Gamma^{(3)} \sim \lambda_d^{-1}$, while the other two rates decrease with decreasing the dot size as $\Gamma^{(1)} \sim \lambda_d^4$ and $\Gamma^{(2)} \sim \lambda_d$. This behavior strongly differs from the electronic case where the ZFR mechanism is efficient for rather large dots [135].

Interestingly, the present results do not change much if the B -field is tilted with respect to the QD plane. The g -factor for HHs is strongly anisotropic with $g_{\parallel} \ll g_{\perp}$ so that one can neglect the in-plane Zeeman splitting. This implies performing the substitution $\omega_{c,Z} \rightarrow \omega_{c,Z} \cos \theta$ in above results, with θ being the angle between the B -field and the z -direction. This will lead to a reduction of the B -dependent rates ($\Gamma^{(1,2)}$), while the ZFR ($\Gamma^{(3)}$) being independent of B remains the same.

4.5 Conclusions

In conclusion, we have shown that two-phonon processes give rise to a strong relaxation of the HH spin in a flat quantum dot. This time is predicted to be in the millisecond range, comparable to the one measured in recent experiments on optical pumping of a HH spin in QDs [20]. Though other sources of relaxation are not excluded, a careful scaling analysis of the measured relaxation time with the magnetic field and/or the temperature should allow one to identify the two-phonon process as the leading relaxation mechanism for the heavy-hole spin localized in small QDs.

Chapter 5

Spin electric effects in molecular antiferromagnets

Molecular nanomagnets show clear signatures of coherent behavior and have a wide variety of effective low-energy spin Hamiltonians suitable for encoding qubits and implementing spin-based quantum information processing. At the nanoscale, the preferred mechanism for control of quantum systems is through application of electric fields, which are strong, can be locally applied, and rapidly switched. In this work, we provide the theoretical tools for the search for single molecule magnets suitable for electric control. By group-theoretical symmetry analysis we find that the spin-electric coupling in triangular molecules is governed by the modification of the exchange interaction, and is possible even in the absence of spin-orbit coupling. In pentagonal molecules the spin-electric coupling can exist only in the presence of spin-orbit interaction. This kind of coupling is allowed for both $s = 1/2$ and $s = 3/2$ spins at the magnetic centers. Within the Hubbard model, we find a relation between the spin-electric coupling and the properties of the chemical bonds in a molecule, suggesting that the best candidates for strong spin-electric coupling are molecules with nearly degenerate bond orbitals. We also investigate the possible experimental signatures of spin-electric coupling in nuclear magnetic resonance and electron spin resonance spectroscopy, as well as in the thermodynamic measurements of magnetization, electric polarization, and specific heat of the molecules.

5.1 Introduction

The control of coherent quantum dynamics is a necessary prerequisite for quantum information processing. This kind of control is achieved through coupling of the internal quantum degrees of freedom of a suitable micro- or mesoscopic system to an external classical or quantum field that can readily be manipulated on the characteristic spatial and temporal scales of the quantum system.

The molecular nanomagnets (MNs) [30, 31] represent a class of systems that show rich quantum behavior. At low energies, the MNs behave as a large spin or a system of only few interacting spins. The behavior of this spin system can be designed to some degree by altering the chemical structure of the molecules, and ranges from a single large spin with high anisotropy barrier, to small collections of ferro- or antiferromagnetically coupled spins

with various geometries and magnetic anisotropies. This versatility of available effective spin systems makes the MNs promising carriers of quantum information [55]. While the interaction with magnetic fields provides a straightforward access to the spins in an MN, it is preferable to use electric fields for the quantum control of spins, since the electric fields are easier to control on the required short spatial and temporal scales. In this work, we explore the mechanisms of spin-electric coupling and study the ways in which an MN with strong spin-electric coupling can be identified.

Quantum behavior of MNs is clearly manifested in the quantum tunneling of magnetization [33–39, 140]. A prototypical example of quantum tunneling of magnetization is the hysteresis loop of an MN with a large spin and high anisotropy barrier. The height of the barrier separating the degenerate states of different magnetization leads to long-lived spin configurations with nonzero magnetic moment in the absence of external fields. The transitions between magnetization states in the MN driven through a hysteresis loop occur in tunneling events that involve coherent change of a many-spin state. These transitions have been observed as step-wise changes in magnetization in single-molecule ferromagnets [36, 37, 40–42]. Similar tunneling between spin configurations are predicted in antiferromagnetic molecules [43, 44], and the observed hysteresis was explained in terms of the photon bottleneck and Landau-Zener transitions [45–48]. The transitions between spin states are coherent processes and show the signatures of interference between transition paths [49, 50, 141], as well as the effects of Berry phase in tunneling [50–53, 141, 142].

Spin systems within molecular nanomagnets offer a number of attractive features for studying the quantum coherence and for the applications in quantum information processing [55]. A wide variety of spin states and couplings between them allows for encoding qubits. Chemical manipulation offers a way to modify the structure of low-energy spin states [143]. Coherence times of up to $\sim 3 \mu\text{s}$ [144] which can persist up to relatively high temperatures of the order of few Kelvin are sensitive to the isotopic composition of the molecule. A universal set of quantum gates can be applied in a system of coupled antiferromagnetic ring molecules, without the need for local manipulation [145]. The presence of many magnetic centers with the coupled spins allows for the construction of spin cluster qubits that can be manipulated by relatively simple means [146]. In polyoxometalates, the spin structure of the molecule is sensitive to the addition of charge, and controlled delivery and removal of charges via an STM tip can produce useful quantum gates [147]. Chemical bonds between the molecules can be engineered to produce the permanent coupling between the molecular spins and allow for interaction between the qubits [148].

Sensitivity of molecular state to the addition of charge was demonstrated in the tunneling through single molecules [149], and used to control the spin state of a MN [150]. Transport studies of the MNs can provide a sensitive probe of their spin structure [53, 151–154].

The most straightforward and traditional way of controlling magnetic molecules is by applying an external magnetic field. With carefully crafted ESR pulses, it is possible to perform the Grover algorithm, or use the low-energy sector of the molecular nanomagnet as a dense classical memory [55]. Unfortunately the approaches based on magnetic fields face a significant drawback in the large-scale quantum control application. Typically, the quantum manipulation has to be performed on the very short spatial and temporal scales, while the local application of rapidly varying magnetic field presents a challenging experimental problem. For that reason, the schemes for quantum computing tend to rely on modifying

the spin dynamics that is caused by intramolecular interaction, rather than on the direct manipulation of spins [155].

For the applications that require quantum control, the electric fields offer an attractive alternative for spin manipulation in the molecular nanomagnets [156]. One major advantage is that they can be applied to a very small volume via an STM tip [157, 158], and rapidly turned on and off by applying voltage pulses to the electrodes placed close to the molecules that are being manipulated. Switchable coupling between different nanomagnets is essential for qubit implementation. At present, this can be implemented only locally, and the interaction is practically untunable. The use of microwave cavities can offer a solution to this problem. By placing the nanomagnets inside a microwave cavity, one can obtain a fully controllable, long-range interaction between them [156]. This coupling relies on the presence of a quantum electric field inside such a cavity, which mediates the interaction between distant nanomagnets. The interaction can be tuned by tuning each molecule in- or out-of-resonance with the cavity field using local electric or magnetic fields [156]. The spins, however, do not couple directly to the electric fields, classical or quantum, and therefore any electric spin manipulation is indirect, and involves the modification of molecular orbitals or the spin-orbit interaction.

The description of the molecular nanomagnets in terms of spins is an effective low-energy theory that does not carry information about the orbital states. However, it is still possible to predict the form of spin-electric coupling from symmetry considerations and single out the molecules in which such a coupling is possible. In particular, the molecules with the triangular arrangement of antiferromagnetically coupled spin-1/2 magnetic centers interact with external electric field through chirality of their spin structure [156, 159]. The same coupling of chirality to the external electric field was derived for the triangular Mott insulators [160].

While the symmetry of a molecule sets the form of spin-electric coupling, no symmetry analysis can predict the size of the corresponding coupling constant. The coupling strength will depend on the underlying mechanism that correlates the spin and orbital states, and on the detailed structure of low-energy molecular orbitals. To identify molecules that can be efficiently manipulated by electric fields, it is necessary to perform an extensive search among the molecules with the right symmetries and look for the ones that also have a large coupling constant. Unfortunately, this search has to proceed by ab-initio calculations of the coupling constants for a class of molecules of a given symmetry, or by an indiscriminate experimental scanning of all of the available molecules.

In this paper, we contribute to the search for molecules that exhibit strong spin-electric coupling. Based on the symmetry analysis, we identify the parameters of the spin Hamiltonian that can change in the magnetic field, and cause spin-electric coupling. We study the mechanisms that lead to this coupling and describe the experiments that can detect it.

We will consider the spin electric coupling in the language of effective model, namely either the spin Hamiltonian, or the Hubbard model. In reality the mechanism behind the spin-electric coupling involves either the modification of the electronic orbitals in an external field and the Coulomb repulsion of electrons, or the much weaker direct spin-orbit coupling to the external fields. A derivation of spin-electric coupling from this realistic picture would require the knowledge of electronic orbitals from an ab-initio calculation, and the distribution of electric field within the molecule. Both of these problems require substantial

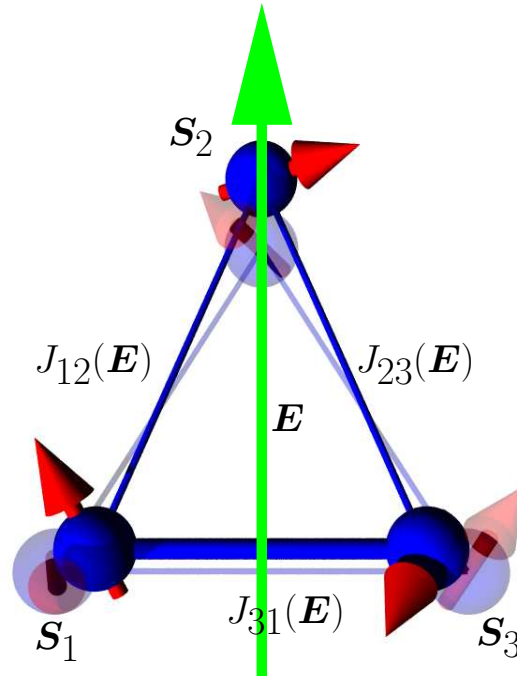


Figure 5.1: (Color online) Schematics of the $s_i = 1/2$ triangular molecule in electric field. The antiferromagnetic exchange couplings, represented by the bonds with thickness proportional to J_{ii+1} , are modified in electric field. In the absence of electric field, exchange couplings are equal $J_{ii+1} = J_{jj+1}$, fade colors (grey online). The full color (blue online) triangle represents the exchange interaction strengths in electric field.

computational power, and can not be performed routinely. Since the electric field acts primarily on the orbital degrees of freedom, and the spin Hamiltonian carries no information about the orbital states, we provide a description in terms of a Hubbard model that still contains some information about the orbital states. We can then describe the properties of the molecule that allow for strong spin-electric coupling in the language of orbitals that offers some intuitive understanding of the underlying mechanisms of interaction.

We identify the response of an MN with spin-electric coupling in the standard measurements of ESR, nuclear magnetic resonance (NMR), magnetization, polarization, linear magnetoelectric effect, and specific heat measurements.

In Sec. II we present a symmetry analysis of the spin-electric coupling in the ring-shaped molecules with antiferromagnetic coupling of spins. In Sec. IV, we describe the MNs using the Hubbard model, and relate the symmetry-based conclusions to the structure of molecular orbitals. In Sec V, we analyze the experimental signatures of spin-electric coupling, and present our conclusions in Sec. VI.

5.2 Symmetry analysis of antiferromagnetic spin rings

Spin chains whose ground state multiplet consists of two quasi-degenerate $S = 1/2$ doublets represent suitable candidates for the manipulation of the spin state by pulsed electric fields. Such a ground-state multiplet characterizes a number of frustrated spin rings, consisting of an odd number of half-integer spins. In the following we consider prototypical examples of such systems.

5.2.1 Triangle of $s = 1/2$ spins

The low-energy properties of most molecular nanomagnets (MNs) are well described in terms of spin degrees of freedom alone. Within the spin-Hamiltonian approach, the coupling of external electric fields to the molecule can be accounted for by suitably renormalizing the physical parameters. In the following, we use the symmetry of the molecules to calculate the changes of spin-Hamiltonian parameters, to identify the system's eigenstates, and to deduce the allowed transitions. Quantitative estimates of the parameters entering the spin Hamiltonian require the use of ab-initio calculations [161], or the comparison with experiments. The simplest example of a spin system which may couple to an external electric field in a non-trivial way is a triangle of $s = 1/2$ spins, like, for example, the Cu_3 MN [162]. The schematics of such a spin system in the presence of an electric field is shown in Fig. 5.1. Its spin Hamiltonian, for the moment in the absence of any external fields (magnetic or electric), reads:

$$H_{\text{spin}} = \sum_{i=1}^N J_{ii+1} \mathbf{s}_i \cdot \mathbf{s}_{i+1} + \sum_{i=1}^N \mathbf{D}_{ii+1} \cdot (\mathbf{s}_i \times \mathbf{s}_{i+1}), \quad (5.1)$$

with $N = 3$ and $\mathbf{s}_4 \equiv \mathbf{s}_1$ in the summation over i . The first term in Eq. (5.1) represents the isotropic Heisenberg exchange Hamiltonian with the exchange couplings J_{ii+1} between the spins \mathbf{s}_i and \mathbf{s}_{i+1} , and the second term represents the Dzyalozhinsky-Moriya (DM) interaction due to the presence of spin-orbit interaction (SOI) in the molecule, with the DM vectors \mathbf{D}_{ii+1} . The states of the spin $S = 1/2$ triangle can be found by forming the direct product of the $SU(2)$ representations of three spins $S = 1/2$: $D_{\text{tot}} = D^{(1/2) \otimes 3} = 2D^{(1/2)} \oplus D^{(3/2)}$, meaning there are eight states in total. The point group symmetry of the molecule is D_{3h} [162], i.e. the triangle is assumed to be equilateral. The D_{3h} symmetry imposes the following restrictions on the spin Hamiltonian parameters: $J_{ii+1} \equiv J$ and $D_{ii+1}^{x,y} \equiv 0$, and $D_{ii+1}^z \equiv D_z$. However, if lower symmetry is considered these restrictions will be relaxed. The spin states in a form adapted to the rotational symmetry C_3 of the system are

$$|\psi_{M=1/2}^{(k)}\rangle = \frac{1}{\sqrt{3}} \sum_{j=0}^2 \epsilon_j^k C_3^j |\downarrow\uparrow\uparrow\rangle \quad (5.2)$$

$$|\psi_{M=3/2}\rangle = |\uparrow\uparrow\uparrow\rangle, \quad (5.3)$$

where $\epsilon_j = \exp(2i\pi/3j)$ and $j = 0, 1, 2$. The states with opposite spin projection $M' = -M$, i.e. with all spins flipped can be written in an identical way (not shown). These states are already the symmetry adapted basis functions of the point group D_{3h} . Moreover, these are

eigenstates of the chirality operator

$$C_z = \frac{1}{4\sqrt{3}} \mathbf{s}_1 \cdot (\mathbf{s}_2 \times \mathbf{s}_3), \quad (5.4)$$

with $C_z |\psi_{M=\pm 1/2}^{(1,2)}\rangle = \pm |\psi_{M=\pm 1/2}^{(1,2)}\rangle$, $C_z |\psi_{M=\pm 1/2}^{(0)}\rangle = 0$ and $C_z |\psi_{M=\pm 3/2}\rangle = 0$. The above states in Eq. (5.3) carry different total spin. There are two spin $S = 1/2$ states, corresponding to $k = 1, 2$, and a spin $S = 3/2$ state corresponding to $k = 0$. Obviously, the states $|\psi_{M=\pm 3/2}\rangle$ have $S = 3/2$.

In an even-spin system, double valued point groups, instead of single valued groups, are usually used in order to describe the states, the splittings and the allowed transitions (magnetic or electric) [163]. In the presence of spin-orbit interaction the splittings can be accounted for either by single group analysis (perturbatively), or by double group analysis (exact). In the following, we analyze the spectrum and the allowed transitions by both single valued point group analysis and double valued point group analysis.

Single valued group analysis of the $s = 1/2$ spin triangle

In the single valued point group D_{3h} , the states $|\psi_{M=\pm 1/2}^{(k)}\rangle$ with $k = 1, 2$ form the basis of the two dimensional irreducible representation E' , while the states $|\psi_{M=\pm 1/2}^{(0)}\rangle$, and the $|\psi_{M=\pm 3/2}\rangle$ transform as A'_2 . The allowed electric transitions in the system are determined by the transformation properties of the basis states.

The simplest and possibly the dominant dependence of the spin Hamiltonian on the applied electric field comes via the modification of the exchange interactions, like depicted in Fig. 5.1. This gives rise to the following term in the spin Hamiltonian

$$\delta H_0(\mathbf{E}) = \sum_{i=1}^3 \delta J_{ii+1}(\mathbf{E}) \mathbf{s}_i \cdot \mathbf{s}_{i+1}, \quad (5.5)$$

where $\delta J_{ii+1}(\mathbf{E}) \approx \mathbf{d}_{ii+1} \cdot \mathbf{E}$, with \mathbf{d}_{ii+1} being vectors that describe the electric-dipole coupling of the bond $\mathbf{s}_i - \mathbf{s}_{i+1}$ to the electric field \mathbf{E} in leading order. There are three such vector parameters and thus nine scalar parameters in total. However, symmetry will allow to drastically reduce the number of free parameters by providing relations between them. The $S = 3/2$ states of the unperturbed spin Hamiltonian form the multiplet ${}^4A'_2$, while the $S = 1/2$ states form two multiplets ${}^2E'$. The electric dipole Hamiltonian is $H_{e-d} = -e \sum_i \mathbf{E} \cdot \mathbf{r}_i \equiv -e \mathbf{E} \cdot \mathbf{R}$, with e standing for the electron charge, \mathbf{r}_i being the coordinates of the i -th electron and $\mathbf{R} = \sum_i \mathbf{r}_i$. The non-zero electric dipole matrix elements of H_{e-d} in the D_{3h} symmetric molecule are

$$\langle \psi_M^{(1,2)} | -ex | \psi_{M'}^{(2,1)} \rangle = i \langle \psi_M^{(1,2)} | -ey | \psi_{M'}^{(2,1)} \rangle \equiv d \delta_{MM'}, \quad (5.6)$$

proportional to the effective electric dipole parameter d . The value of d is not determined by symmetry, and has to be found by some other means (ab-initio, Hubbard modeling, experiments, etc). We mention that all the other matrix elements are zero, e.g. $\langle \psi_M^{(1,2)} | -ex | \psi_{M'}^{(1,2)} \rangle = i \langle \psi_M^{(1,2)} | -ey | \psi_{M'}^{(1,2)} \rangle = 0$, etc. We see that the electric field acts only in the low-energy sector, which allows us to write the effective spin-electric coupling Hamiltonian acting in the lowest quadruplet as

$$H_{e-d}^{\text{eff}} = d \mathbf{E}' \cdot \mathbf{C}_{\parallel}, \quad (5.7)$$

where $\mathbf{E}' = \mathcal{R}_z(7\pi/6 - 2\theta)\mathbf{E}$, with $\mathcal{R}_z(\phi)$ describing the rotation with an angle ϕ about the z axis, and θ is the angle between in-plane component \mathbf{E}_{\parallel} of the electric field \mathbf{E} and the bond $s_1 - s_2$. For $\mathbf{C}_{\parallel} = (C_x, C_y, 0)$ we have

$$C_x = \sum_M \left(|\psi_M^{(1)}\rangle\langle\psi_M^{(2)}| + |\psi_M^{(2)}\rangle\langle\psi_M^{(1)}| \right), \quad (5.8)$$

$$C_y = i \sum_M \left(|\psi_M^{(1)}\rangle\langle\psi_M^{(2)}| - |\psi_M^{(2)}\rangle\langle\psi_M^{(1)}| \right). \quad (5.9)$$

The low-energy spectrum in the presence of electric field and the related states can be expressed in terms of the spin Hamiltonian Eq. (5.5), so that we find anisotropic variations of the exchange coupling constants:

$$\delta J_{ii+1}(\mathbf{E}) = \frac{4d}{3} |\mathbf{E}_{\parallel}| \cos \left(\frac{2\pi}{3}i + \theta \right), \quad (5.10)$$

which depend on the angle θ and the projection of the electric field \mathbf{E} on the plane of the triangle. In the $s_i = 1/2$ triangle the \mathbf{C} -operators can be written as

$$C_x = -\frac{2}{3}(\mathbf{s}_1 \cdot \mathbf{s}_2 - 2\mathbf{s}_2 \cdot \mathbf{s}_3 + \mathbf{s}_3 \cdot \mathbf{s}_1), \quad (5.11)$$

$$C_y = \frac{2}{\sqrt{3}}(\mathbf{s}_1 \cdot \mathbf{s}_2 - \mathbf{s}_3 \cdot \mathbf{s}_1), \quad (5.12)$$

with $[C_i, C_j] = 2i\epsilon_{ijk}C_k$ (ϵ_{ijk} are the Levi-Civita symbols) [156,160]. From the above relations we can conclude that (i) only the electric field component perpendicular to the bond and lying in the plane of the molecule gives rise to spin-electric coupling and (ii) there is only one free parameter d describing the coupling of the spin system to electric fields and $\mathbf{d}_{ii+1} = 4d/3 (\sin(2i\pi/3), \cos(2i\pi/3), 0)$, where $i = 1, 2, 3$ labels the triangle sites and $4 \equiv 1$.

The SOI in a D_{3h} symmetric MN is constrained by the transformation properties of the localized orbitals. It reads

$$H_{\text{SO}} = \lambda_{\text{SO}}^{\parallel} T_{A_2} S_z + \lambda_{\text{SO}}^{\perp} (T_{E''} S_- + T_{E''} S_+), \quad (5.13)$$

with T_{Γ} being tensor operators transforming according to the irreducible representation Γ [163]. The non-zero matrix elements of this SOI Hamiltonian in the low-energy quadruplet read $\langle\psi_M^{(1,2)}|H_{\text{SO}}|\psi_{M'}^{(1,2)}\rangle = \pm M\lambda_{\text{SO}}^{\parallel}\delta_{MM'}$ so that the SOI takes the following effective form

$$H_{\text{SO}} = \Delta_{\text{SO}} C_z S_z, \quad (5.14)$$

with $\Delta_{\text{SO}} = \lambda_{\text{SO}}^{\parallel}$ and $S_z = \sum_i^3 s_i^z$. An effective SOI Hamiltonian is obtained also from the DM SOI Hamiltonian in Eq. (5.1). The constraints $D_{ii+1}^{x,y} = 0$ and $D_{ii+1}^z \equiv D_z$ on the DM vectors due to D_{3h} symmetry of the molecule, give rise to the same effective SOI in Eq. (5.14), with $D_z = \lambda_{\text{SO}}^{\parallel}$. Thus, as expected, the molecular SOI and the DM SOI give rise to the same effective SOI Hamiltonian acting in the low energy quadruplet. Like in the case of the electric dipole parameter d , finding $D_z(\lambda_{\text{SO}}^{\parallel})$ requires more than symmetry, like ab-initio methods or experiments. The transverse SOI, with interaction strength $\lambda_{\text{SO}}^{\perp}$ does not act

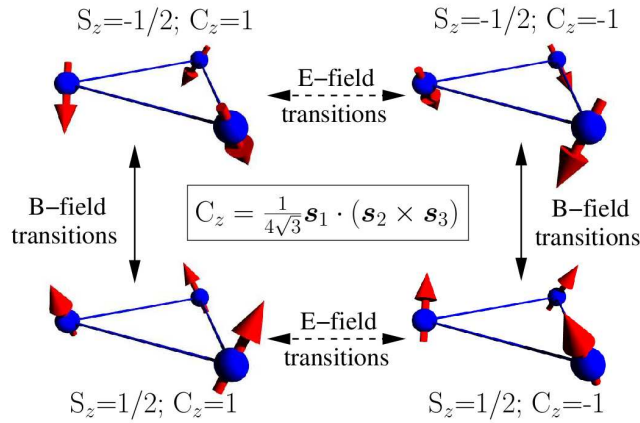


Figure 5.2: The spin transitions in the $s_i = 1/2$ triangle induced by electric and magnetic fields. The electric field causes transitions between the states of opposite chiralities C_z and equal spin projections S_z (horizontal arrows), while the magnetic field instead causes transitions between the states of opposite spin projections S_z and equal chiralities C_z (vertical arrows).

within the low-energy space, and its effect will appear only in higher orders of perturbation theory in $1/J$.

An external magnetic field couples to the spin via the Zeeman term $H_Z = \mathbf{B} \cdot \bar{g}\mathbf{S}$, with $\bar{g} = \text{diag}\{g_{\parallel}, g_{\parallel}, g_{\perp}\}$ being the g -factor tensor in D_{3h} . The full effective Hamiltonian describing the low-energy quadruplet in the presence of SOI, electric field and magnetic field read

$$H_{\text{eff}} = \Delta_{\text{SO}} C_z S_z + \mathbf{B} \cdot \bar{g}\mathbf{S} + d\mathbf{E}' \cdot \mathbf{C}_{\parallel}. \quad (5.15)$$

Note that $[\mathbf{C}, \mathbf{S}] = 0$, and chirality and spin act as independent spin $1/2$ degrees of freedom. Furthermore, in the absence of SOI the chirality \mathbf{C} and the spin \mathbf{S} evolve independently. However, the SOI couples the two and provides with means for electric control of both spin and chirality. Vice-versa, magnetic fields can also couple to chirality due to SOI. Also, while magnetic fields (time-dependent) cause transitions between states of opposite spin projection M but with the same chirality C_z , the electric field does the opposite: it causes transitions between states of opposite chirality C_z , but carrying the same M . Full control of the lowest quadruplet is thus realized in the presence of both electric and magnetic fields, as can be seen in Fig. 5.2.

Double valued group states of the $s = 1/2$ spin triangle

The double group representations allow to non-perturbatively describe the magnetic and electric transitions in the presence of spin-orbit interaction. The lowest quadruplet consists of two Kramers doublets, one of them transforming like $\bar{E}' \sim (|-1/2\rangle, |1/2\rangle)$, and the other one according to $\bar{E}'' \sim (|-3/2\rangle, |3/2\rangle)$. Here $(|M\rangle, |-M\rangle)$ represent pairs of eigenstates of a given angular momentum $J \geq M$, with spin projection $\pm M$. For example, if $M = 1/2$, then $J = 1/2, 3/2, \dots$. The higher energy states instead ($S = 3/2$ states), transform now not as A'_2 , but as \bar{E}' ($M = \pm 1/2$) and as \bar{E}'' ($M = \pm 3/2$). Thus, the $S = 1/2$ states mix with the

$S = 3/2$ states, but only the ones transforming according to the same representations, i.e. there is no mixing between \bar{E}' and \bar{E}'' due to spin-orbit interaction. The magnetic dipole transitions take place between \bar{E}' and \bar{E}'' , and within \bar{E}' and \bar{E}'' , respectively, while electric dipole transitions take place only between \bar{E}' and \bar{E}'' . The selection rules for the electric transitions are $\Delta M = \pm 2$, while for the magnetic transitions these are $\Delta M = 0 \pm 1$. We see that within the double group analysis, i.e. in the presence of SOI, there are allowed electric dipole transitions also within the $S = 3/2$ subspace.

Using both the single group and double group analysis we can pinpoint to the transitions that arise in the absence or only in the presence of SOI. Therefore, the electric dipole transitions present in the single-group are a consequence of the modified exchange interaction, and can arise even in the absence of SOI, while the ones that show up only in the double group analysis are a consequence of the SOI (or modification of SOI in electric field).

We now can establish several selection rules for the SOI, electric field and magnetic field induced transitions. Note that the above analysis was exact in SOI. However, it is instructive to treat electric field, magnetic fields and SOI on the same footing. First, we find that the electric dipole transitions fulfill the selection rules $\Delta C_z = \pm 1$ and $\Delta S_z = 0$, meaning that electric field only couples states within the lowest quadruplet. The SOI transitions show a richer structure. We can separate the SOI interaction in two parts: the perpendicular SOI, quantified by D_z in the DM interaction Hamiltonian, and the in-plane SOI, quantified by $D_{x,y}$ in the DM interaction Hamiltonian, respectively. By doing so, we find that the D_z SOI terms obey the selection rules $\Delta C_z = 0$ and $\Delta S_z = 0$, while for the $D_{x,y}$ terms we get the selection rules $\Delta C_z = \pm 1$ and $\Delta S_z = \pm 1$. We see in-plane SOI ($D_{x,y}$ terms) do not cause any splitting in the ground state and can lead to observable effects only in second order in perturbation theory in $D_{x,y}/J$. Also, note that if σ_h symmetry is present, $D_{x,y} \equiv 0$ and thus there are no in-plane SOI effects at all. Modification of these terms due to an in-plane external electric field \mathbf{E} , however, lead to different selection rules: changes of D_z terms lead to $\Delta C_z = \pm 1$ and $\Delta S_z = 0$, while modification of $D_{x,y}$ lead to $\Delta C_z = 0, \pm 2$ and $\Delta S_z = \pm 1$. The magnetic field transitions obey the selection rules $\Delta S_z = 0, \pm 1$ and $\Delta C_z = 0$. Thus, we can make clear distinction between pure electric field transitions, SOI-mediated electric transitions and magnetic transitions. This distinction between the electric and magnetic field induced transitions could be used to extract the spin-electric coupling strength parameter d from spectroscopic measurements.

5.2.2 Spin $s = 3/2$ triangle

The spin $s = 3/2$ triangle has a more complex level structure than the $s = 1/2$ triangle due to its higher spin. The spin Hamiltonian, however, is similar to the one in Eq. (5.1) for $s = 1/2$, and the reduction of the representation of three spins $S = 3/2$ is $D_{tot} = D^{(3/2) \otimes 3} = 2D^{(1/2)} \oplus 4D^{(3/2)} \oplus 3D^{(5/2)} \oplus 2D^{(7/2)} \oplus D^{(9/2)}$, a total of 64 spin states. The total number of irreducible representations is the same as in the $s = 1/2$ case, and we need only to identify these basis states in terms of the spin states. The $s = 3/2$ triangle states can be defined according to their transformation properties under three-fold rotations C_3 in D_{3h} and are of

the following form

$$|\psi_M^{(k,i)}\rangle = P_k^3 |M, i\rangle, \quad (5.16)$$

$$P_k^3 = \frac{1}{\sqrt{3}} \sum_{j=0}^2 \epsilon_j^k C_3^j, \quad (5.17)$$

where $\epsilon_j^k = \exp(2i\pi jk/3)$, C_3^j are the 3-fold rotation of order j , and $j, k = 0, 1, 2$. The states $|M, i\rangle \equiv |\sigma_1 \sigma_2 \sigma_3\rangle$ represent all possible states (i states in total) with a given spin projection $M (\equiv \sum_k \sigma_k)$ that cannot be transformed into each other by application of the rotation operator C_3^j . These states are showed in Table 5.1.

M \ i	1	2	3	4
1/2	$ \downarrow\uparrow\uparrow\rangle$	$ \uparrow\downarrow\downarrow\rangle$	$ \downarrow\uparrow\uparrow\rangle$	$ \downarrow\uparrow\uparrow\rangle$
3/2	$ \downarrow\uparrow\uparrow\rangle$	$ \downarrow\uparrow\uparrow\rangle$	$ \downarrow\uparrow\uparrow\rangle$	$ \uparrow\uparrow\uparrow\rangle$
5/2	$ \uparrow\uparrow\uparrow\rangle$	$ \downarrow\uparrow\uparrow\rangle$	0	0
7/2	$ \uparrow\uparrow\uparrow\rangle$	0	0	0
9/2	$ \uparrow\uparrow\uparrow\rangle$	0	0	0

Table 5.1: Non-symmetry adapted states of the $s = 3/2$ spin triangle. We use $|\uparrow (\downarrow)\rangle = |\pm 3/2\rangle$.

The corresponding states with all spins flipped, namely with $M' = -M$, can be written in a similar form (not shown). Having identified the symmetric states in terms of the spin states, we proceed to analyze the allowed transitions induced in the spin systems by magnetic and electric field, both within the single valued group and double valued group representations.

Single valued group states of the $s = 3/2$ triangle

The above states are basis of the point group D_{3h} , but not eigenstates of the total spin operator \mathbf{S}^2 , i.e. they do not have definite total spin. However, linear combinations of states of a given total spin projection M and a given 'chiral' numbers k become eigenstates of \mathbf{S}^2 . The total spin eigenstates can be written as $|\psi_{S,M}^{(k)}\rangle = \sum_{l(M)} a_{k,l}^S |\psi_M^{(k,l)}\rangle$, where $l(M)$ is the number of different states with a given M . The coefficients $a_{k,l}$ are to be identified so that these states satisfy $\mathbf{S}^2 |\psi_{S,M}^{(k)}\rangle = S(S+1) |\psi_{S,M}^{(k)}\rangle$, with $S = 1/2, 3/2, 5/2, 7/2, 9/2$. The states with $k = 0$ are all transforming according to the A'_2 representation, while the states with $k = 1, 2$ are organized in doublets, being the bases of the two dimensional representation E' . However, as mentioned above, different combinations of symmetry adapted states carry different total spin S . The magnetic and electric transitions are similar to the ones in the

$s = 1/2$ triangle, in the absence of SOI. The electric field causes transitions only between states with the same M and S , but opposite chirality $C_z = \frac{1}{2\sqrt{3}}\mathbf{s}_1 \cdot (\mathbf{s}_2 \times \mathbf{s}_3)$ (this is different from the triangle with $s_i = 1/2$ spins in each of the vertices). As for the $s = 1/2$ spin triangle, there are electric dipole transitions within the spin system even in the absence of SOI. The ground states is four-fold degenerate consisting of two $S = 1/2$ eigenstates

$$|\psi_{M=1/2}^{(1)}\rangle = \frac{1}{\sqrt{10}} \left(|\psi_{M=1/2}^{(1,1)}\rangle + \sqrt{3}|\psi_{M=1/2}^{(1,2)}\rangle - (\epsilon_1 - \epsilon_2)(|\psi_{M=1/2}^{(1,3)}\rangle - |\psi_{M=1/2}^{(1,4)}\rangle) \right), \quad (5.18)$$

$$|\psi_{M=1/2}^{(2)}\rangle = \frac{1}{\sqrt{10}} \left(|\psi_{M=1/2}^{(2,1)}\rangle + \sqrt{3}|\psi_{M=1/2}^{(2,2)}\rangle + (\epsilon_1 - \epsilon_2)(|\psi_{M=1/2}^{(2,3)}\rangle - |\psi_{M=1/2}^{(2,4)}\rangle) \right). \quad (5.19)$$

We see that, as opposed to the $s = 1/2$ triangle, the lowest states are given by linear combinations of the several $M = 1/2$ symmetry adapted states (the $M = -1/2$ states are obtained by flipping the spins in the states in Eqs. (5.18), (5.19)). This, however, does not modify the conclusions regarding the electric and magnetic transitions in the absence of SOI, these being given by the same rules as in the $S = 1/2$ triangle: electric-field induced transitions between the states of opposite chirality C_z and the same spin projection M . The lowest states are still organized as spin and chirality eigenstates that are split in the presence of SOI as in the previous case.

In the original spin Hamiltonian in Eq. (5.1) the electric field causes modification of the spin Hamiltonian parameters. As for the spin $s = 1/2$ triangle, the strongest effect comes from modification of the isotropic exchange interaction, so that

$$\delta H_0(\mathbf{E}) = \sum_{i=1}^3 \delta J_{i+1}(\mathbf{E}) \mathbf{s}_i \cdot \mathbf{s}_{i+1}, \quad (5.20)$$

with $\delta J_{i+1}(\mathbf{E}) = dE \cos(2\pi i/3 + \theta)$, where θ is the angle between the projection of the external electric field \mathbf{E} to the molecule's plane and the $\mathbf{s}_1 - \mathbf{s}_2$ bond, and $i = 0, 1, 2$. The effect of the electric field on the lowest quadruplet is found to be similar to the spin $s = 1/2$ case. While the SOI splits the two chiral states without mixing them (at least in lowest order), the electric field, on the other hand, mixes the chiral states. The effective Hamiltonian acting in the lowest quadruplet reads

$$H_{\text{eff}} = \Delta_{\text{SO}} C_z S_z + \mathbf{B} \cdot \bar{\mathbf{g}} \mathbf{S} + d' \mathbf{E} \cdot \mathbf{C}_{\parallel}. \quad (5.21)$$

Above, $d' = 3d/2$, $\mathbf{C}_{\parallel} = (C_x, C_y, 0)$, with $C_x = \sum_M |\psi_M^{(1)}\rangle \langle \psi_M^{(2)}| + |\psi_M^{(2)}\rangle \langle \psi_M^{(1)}|$ and $C_x = i \sum_M (|\psi_M^{(1)}\rangle \langle \psi_M^{(2)}| - |\psi_M^{(2)}\rangle \langle \psi_M^{(1)}|)$, and Δ_{SO} stands for the SO splitting. However, in this situation the in-plane chirality operators $C_{x,y}$ cannot be written in a simple form as a function of the individual spin operators, as opposed to the $s = 1/2$ triangle.

Double valued group states of the $s = 3/2$ triangle

The double group representation allows to identify the couplings between different spin states induced by the SOI and to identify the allowed magnetic dipole transitions. Due to SOI, the electric field induced spin transitions will take place also outside the spin quadruplet. In the absence of extra degeneracies (induced, for example, by external magnetic fields), however, these transitions are strongly reduced due the gap of the order J . We can then focus, as for the $S = 1/2$ triangle, only on the lowest quadruplet. These states are organized in two Kramer doublets of the form $(|M\rangle, |-M\rangle)$, one transforming as $\bar{E}' \sim (|1/2\rangle, |-1/2\rangle)$ and the other one as $\bar{E}'' \sim (|-3/2\rangle, |3/2\rangle)$. Here again, $(|M\rangle, |-M\rangle)$ represent angular momentum $J \leq M$ eigenstates with spin projection $\pm M$.

As in the case of the $s = 1/2$ triangle, the electric field induced transitions take place between \bar{E}' and \bar{E}'' , with the selection rules $\Delta M = \pm 2$. Magnetic transitions instead take place both within and between \bar{E}' and \bar{E}'' , satisfying the selection rules $\Delta M = 0, \pm 1$.

If we now treat the SOI, electric field and magnetic fields on the same footing, we arrive at the same selection rules as for the $s = 1/2$ triangle, namely $\Delta C_z = \pm 1$ and $\Delta S_z = 0$ for electric transitions, $\Delta C_z = 0, \pm 1$ and $\Delta S_z = 0, \pm 1$ for SOI transitions, and $\Delta C_z = 0$ and $\Delta S_z = 0, \pm 1$ for magnetic transitions, respectively.

5.2.3 Spin $s = 1/2$ pentagon

We now analyze the spin-electric coupling in a pentagonal molecule with a spin $s = 1/2$ in each of the vertices, like depicted schematically in Fig. 5.3. As in the case of the spin triangle, an external electric field \mathbf{E} gives rise to modification of exchange interaction J_{i+1} in Eq. (5.1). However, the net spin-electric coupling in the lowest spin sector can only be mediated by SOI. i.e. via the DM interaction (which can be also modified in the presence of the \mathbf{E} -field).

To make the analysis simpler, we assume in the following that the pentagonal spin molecule possesses a D_5 point group symmetry, thus no horizontal reflection plane σ_h . However, no generality is lost, since lower symmetry implies more allowed transitions in the spin system. If, for example, in the lower symmetric situation some transitions are forbidden, these transitions will be forbidden in the higher symmetry case. The Hamiltonian is given in Eq. (5.1) with $N = 5$. The states of the pentagon are found from the product of the individual spin representations $D_{tot} = D^{(1/2)\otimes 5} = 5D^{(1/2)} \oplus 4D^{(3/2)} \oplus D^{(5/2)}$, meaning there are 32 spin states in total. As before, these states can be organized in a symmetry adapted basis in the following way

$$|\psi_M^{(k,i)}\rangle = P_5^k |M, i\rangle, \quad (5.22)$$

$$P_5^k = \frac{1}{\sqrt{5}} \sum_{j=0}^4 \epsilon_j^k C_5^j, \quad (5.23)$$

where $\epsilon_j^k = \exp(2i\pi jk/5)$ with $k, j = 0, \dots, 5$, C_5^j are the 5-fold rotations of order j . The states $|M, i\rangle \equiv |\sigma_1\sigma_2\sigma_3\sigma_4\sigma_5\rangle$ represent all possible states (i states in total) with a given spin projection $M (\equiv \sum_k \sigma_k)$ that cannot be transformed into each other by application of the rotation operator C_5^j . These states are showed in in Table 5.2 and the corresponding states

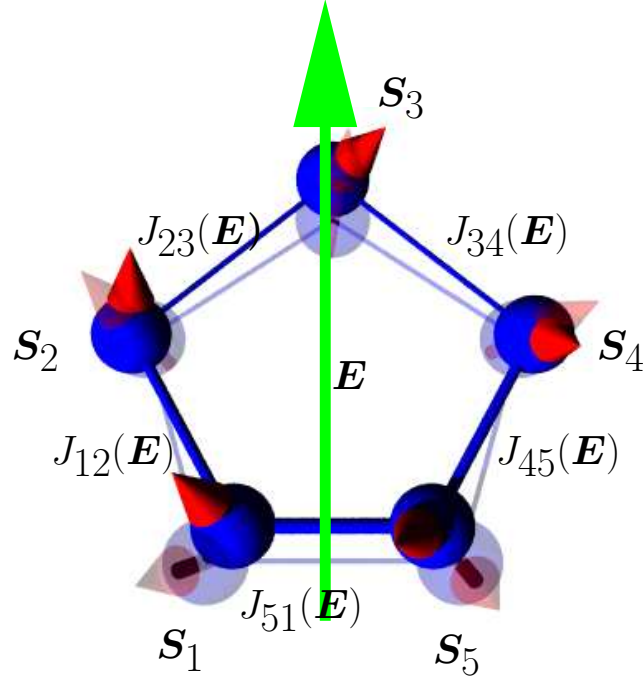


Figure 5.3: (Color online) Schematics of a pentagonal spin ring molecule in electric field \mathbf{E} , light (green) arrow. The molecule in the absence of electric field is depicted in fade colors, while the full colors represent the molecules in electric field. Thickness of the bonds represents the strength of antiferromagnetic exchange interaction between the spins. An electric field modifies the strengths of spin exchange couplings J_{ii+1} .

with all spins flipped, i.e. $M \rightarrow -M$ states (not shown). In the absence of SOI there is no mixing of different k states, i.e. the chirality is a good quantum number. In this case the chirality is quantified by the operator $C_z = 1/(2\sqrt{5} + 2\sqrt{5}) \sum_i \mathbf{s}_i \cdot (\mathbf{s}_{i+1} \times \mathbf{s}_{i+2})$ (the prefactor is chosen for convenience; see below). As in the $s = 1/2, 3/2$ spin triangles, the above states are not yet the eigenstates of the Hamiltonian and we have to solve the equation $S^2 |\psi_S^{(i)}\rangle = S(S+1) |\psi_S^{(i)}\rangle$, with $|\psi_S^{(i)}\rangle = \sum_{k(M)} a_{k,i}^S |\psi_M^{(k,i)}\rangle$. The ground state is spanned, again, by four states, two Kramers doublets with spin $S = 1/2$. In the following we inspect the level structure of these four states in terms of the above symmetry adapted states.

Single valued group $s = 1/2$ pentagon

We focus here only on the four lowest energy states, which are two pairs of $S = 1/2$ states. The first (second) pair is given by linear combination of states with chirality $k = 1$ ($k = 4$)

M \ i	1	2
1/2	$ \uparrow\downarrow\uparrow\downarrow\uparrow\rangle$	$ \uparrow\downarrow\uparrow\uparrow\rangle$
3/2	$ \downarrow\uparrow\uparrow\uparrow\rangle$	0
5/2	$ \uparrow\uparrow\uparrow\uparrow\rangle$	0

Table 5.2: Spin $s = 1/2$ pentagon non-symmetry adapted states.

and spin projection $M = \pm 1/2$. We obtain

$$\begin{aligned}
|\psi_{S=1/2, M=\pm 1/2}^{(k)}\rangle &= \frac{1}{\sqrt{3}} \left(\frac{1}{2 \cos\left(\frac{2k\pi}{5}\right)} |\psi_{M=\pm 1/2}^{(k,1)}\rangle \right. \\
&+ \left. 2\epsilon_2^k \cos\left(\frac{2k\pi}{5}\right) |\psi_{M=\pm 1/2}^{(k,2)}\rangle \right), \tag{5.24}
\end{aligned}$$

so that $C_z |\psi_{M=\pm 1/2}^{(k)}\rangle = (-1)^k |\psi_{M=\pm 1/2}^{(k)}\rangle$. These states (for a given M projection) form the basis of the two dimensional irreducible representation E_1 . We are now in positions to investigate the allowed electric dipole transitions within this lowest subspace. The in-plane electric dipole $\mathbf{d} = (d_x, d_y)$ forms a basis of the irreducible representation E_1 in D_5 . By calculating the product $E_1 \otimes E_1 \otimes E_1 = 2E_1 \oplus 2E_2$ we see that the totally symmetric representation A_1 of D_5 is absent. Therefore, there are *no* electric dipole transitions within the four dimensional subspace in the absence of SOI.

As in the previous two cases, the coupling of the spin Hamiltonian to electric field comes via modification of the spin Hamiltonian parameters. If only the modification of the isotropic exchange Hamiltonian is taken into account, the spin-electric Hamiltonian takes the same form as in Eq. (5.7), with $\delta J_{i+1}(\mathbf{E}) = dE \cos(2i\pi/5 + \theta)$, $i = 1 \dots 5$. The parameter d quantifies the electric dipole coupling of each of the bonds and θ is the angle between the electric field \mathbf{E} and the bond $\mathbf{s}_1 - \mathbf{s}_2$. Note that d is in principle non zero in D_5 point group symmetry. However, the matrix elements of the spin-electric Hamiltonian within the lowest quadruplet are all zero, i.e. $\langle \psi_{S=1/2, M}^{(k)} | \delta H_{e-d}(\mathbf{E}) | \psi_{S=1/2, M'}^{(k')} \rangle \equiv 0$. This means that electric field has no effect on the lowest quadruplet, as found out also by purely symmetry arguments. Therefore, we may expect that the spin-electric coupling in pentagonal spin molecule is caused by SO effects.

Double valued group $s = 1/2$ pentagon

Double valued group analysis allows identifying of the level structure and the allowed transitions in the presence of SOI and magnetic fields. The lowest four states in the double group D_5' are described by the two dimensional irreducible representations $\bar{E}_1' \sim (|-1/2\rangle, |1/2\rangle)$ and $\bar{E}_1'' \sim (|-3/2\rangle, |3/2\rangle)$, respectively. Since both the magnetic μ and electric \mathbf{d} dipoles transform as E_1 in D_5' , both electric and electric transitions will take place between the

same pair of states. The products of the irreducible representations that labels the states in the low-energy quadruplet read: $\bar{E}'_1 \otimes \bar{E}''_2 = E_1 \oplus E_2$, $\bar{E}'_1 \otimes \bar{E}'_1 = A_1 \oplus A_2 \oplus E_1$ and $\bar{E}'_2 \otimes \bar{E}'_2 = A_1 \oplus A_2 \oplus E_2$. These equalities imply the same selection rules in the lowest subspace as for the spin triangle case: $\Delta M = \pm 2$ ($|\pm 1/2\rangle \leftrightarrow |\mp 3/2\rangle$) for electric dipole transitions, and $\Delta M = \pm 1$ ($|\pm 1/2\rangle \leftrightarrow |\mp 1/2\rangle$ and $|\pm 1/2\rangle \leftrightarrow |\pm 3/2\rangle$), for the magnetic ones.

The main feature of pentagonal spin ring is the absence of electric dipole transitions in the lowest quadruplet in the absence of SOI. This is to be contrasted to the spin triangle case, where spin-electric coupling exists in the ground state even in the absence of SOI. This feature finds its explanation from the interplay between the selection rules for electric field transitions and the ones for the SOI. In fact, these selection rules are by no means different from the triangular spin rings. Since the ground state is spanned by four states with chirality $C_z = 1, 4$ and spin $S_z = \pm 1/2$, we see that the condition $\Delta C_z = \pm 1$ for the electric field transitions implies no electric field coupling within the ground state! In the presence of SOI though, spin electric coupling is still possible, but it will be $(D_{x,y}/J)$ times smaller than in triangles. Spin-electric coupling can arise also via modification of the DM vectors $D_{x,y,z}$ in electric field. However, the selection rules for this transitions are, like for the triangle, $\Delta C_z = 0, \pm 2$ and $\Delta S_z = 0, \pm 1$. This means direct splitting in the ground state, and thus we expect that for pentagon spin ring the electric dipole response will be much weaker.

5.3 Hubbard model of a molecular nanomagnet

Spin-Hamiltonian models of molecular nanomagnets are based on the assumption that the spins on magnetic centers are the only relevant degrees of freedom. This assumption of fully quenched and localized orbitals allows for the relatively simple predictions of spin structure in the low-energy states of the molecule. However, since the orbital dynamics plays a crucial role in spin-electric coupling, spin-Hamiltonian models are unable to predict the corresponding coupling constants. In this Section, we relax the assumption of quenched and localized orbitals and treat the orbital degrees of freedom of electrons on magnetic ions within a Hubbard model. This provides an intuitive picture of spin-electric coupling in terms of the deformation of the molecular orbitals induced by the external field. Besides, in the limit of strong quenching of the orbitals, the Hubbard model reproduces a spin Hamiltonian, similar to the results found in the studies of cuprates [164–166] and multiferroics [167, 168]. In particular, we find the relation between modifications of the electronic hopping matrix elements induced by the field and that of the spin-electric coupling in the spin Hamiltonian, thus providing a guide for the estimate of the size of spin-electric coupling in a molecule.

The outline of the present Section is the following. In Subsection 5.3.1, we introduce the Hubbard model of a spin chain with the shape of regular n -targon, and derive the resulting symmetry constraints for the hopping parameters. In Subsection 5.3.2 we assume a direct electron hopping between magnetic sites, and derive the spin Hamiltonian of a spin triangle from the Hubbard model, in the limit of large on-site repulsions; we thus express the coupling to electric fields in terms of the Hubbard-model parameters. In Subsection 5.3.3, we introduce a Hubbard model of a magnetic coupling in the case where this is mediated by a non-magnetic bridge between the magnetic centers; also in this case, we find a connection between the modification of the bridge and spin-electric coupling.

5.3.1 Parameters of the Hubbard model of molecular nanomagnets

Magnetic properties of molecular nanomagnets are governed by the spin state of few electrons in the highest partially occupied atomic orbitals, split by the molecular field. The spin density is localized on the magnetic centers [169], and thus the low-energy magnetic properties are correctly described by quantum models of interacting localized spins [170, 171].

The response of molecular nanomagnets to electric fields, as a matter of principle, does not have to be governed by the electrons occupying the same orbitals that determine the molecule's spin. However, the quantum control of single molecule magnets by electric fields depends on the electrons that both react to electric fields and produce the magnetic response. Therefore, the models of molecular nanomagnets that consider only few orbitals can provide useful information about the electric control of spins.

Hubbard model provides a simplified description of orbital degrees of freedom by including only one or few localized orbitals on each magnetic center. Furthermore, the interaction between electrons is accounted for only by introducing the energies of the atomic configurations with different occupation numbers. The Hubbard model of the MN is given by:

$$H_H = \left[\sum_{i,j} \sum_{\alpha,\beta} c_{i\alpha}^\dagger \left(t\delta_{\alpha\beta} + \frac{i\mathbf{P}_{ij}}{2} \cdot \boldsymbol{\sigma}_{\alpha\beta} \right) c_{j\beta} + \text{h. c.} \right] + \sum_j U_j (n_{j\uparrow}, n_{j\downarrow}). \quad (5.25)$$

where $c_{j\sigma}^\dagger$ ($c_{j\sigma}$) creates (annihilates) an electron with spin $\sigma = \uparrow, \downarrow$ on the orbital localized on j th atom, and $n_{j\sigma} = c_{j\sigma}^\dagger c_{j\sigma}$ is the corresponding number operator. Model parameters U_j , describe the energy of $n_{j\uparrow(\downarrow)}$ spin up(down) electrons on the site j . Hopping parameters t_{ij} , \mathbf{P}_{ij} describe the spin-independent and spin-dependent hopping between sites i and j .

We assume that the largest energy scale is the splitting between the energy of the highest occupied atomic orbital and lowest unoccupied one, induced by the molecular crystal field: this justifies the inclusion of one orbital only for each magnetic center. The on-site repulsion energy is the next largest energy scale in the problem, being U_j larger than the hopping coefficients. Amongst these, processes involving states of different spin, mediated by spin-orbit interaction, are described by the x and y components of \mathbf{P}_{ij} . The parameters $P_{ij;z}$, instead, describe the difference of the hopping matrix elements between spin-up and spin-down electrons. In the following, we shall consider both the case where electron hopping takes place directly between neighboring magnetic ions and that where the magnetic interaction is mediated by bridges of non-magnetic atoms. The Hubbard Hamiltonian can be approximated by a spin Hamiltonian model in the limit $|t_{ij}|, |\mathbf{P}_{ij}| \ll U_j$. The symmetry constraints on the spin Hamiltonian parameters can be deduced from those on the Hubbard model parameters [164]. If the spin-independent hopping dominates ($|t| \gg |\mathbf{P}|$), the resulting spin Hamiltonian will contain the Heisenberg exchange terms and a small additional spin-anisotropic interaction. If $|t| \gtrsim |\mathbf{P}|$, the size of spin-dependent interactions in the spin Hamiltonian will be comparable to the Heisenberg terms. Both these cases appear in the molecule nanomagnets [46, 162, 172, 173].

Symmetry of the molecule imposes constraints to the Hubbard model, thus reducing the number of free parameters. The on-site repulsion parameters U_j are equal for all equivalent

magnetic ions. In the molecules of the form of regular n -tadon, all of the spin-independent hopping parameters are equal, due to the C_n symmetry. The spin-dependent hopping elements are related by both the full symmetry of the molecule and the local symmetry of localized orbitals. For example, in the case of localized orbitals in a regular polygon that are invariant under the local symmetry group of the magnetic center,

$$P_{j,j+1;x} = \exp \left[i \frac{2\pi(j-k)}{n} \right] P_{k,k+1;x}, \quad (5.26)$$

with the convention that site $n+1$ coincides with site 1. In this case, there is only one free parameter that determines all of the P_x matrix elements. Therefore, the regular n -tadon molecule in the absence of external electric and magnetic fields can be described by a Hubbard model, with five independent parameters: U , t , \mathbf{P}_{12} . In addition, the σ_v symmetry, if present will impose $\mathbf{P}_{12} = p\mathbf{e}_z$, thus reducing the number of free parameters to three.

5.3.2 Hubbard model of the spin triangle: direct exchange

In this Subsection we give a brief description of the Hubbard model for a triangular molecule with D_{3h} symmetry. In this model we assume only direct coupling between the magnetic centers, thus no bridge in-between. Even so, this simplified model catches the main features of the effective spin Hamiltonian and gives the microscopic mechanisms for the spin-electric coupling. The Hamiltonian describing the electrons in the triangular molecule reads

$$\begin{aligned} H_H &= \left[\sum_{i,\sigma} c_{i\sigma}^\dagger (t + i\sigma\lambda_{\text{SO}}) c_{i+1,\sigma} + h.c. \right] \\ &+ \sum_{i,\sigma} \left(\epsilon_0 n_{i\sigma} + \frac{1}{2} U n_{i\sigma} n_{i\bar{\sigma}} \right), \end{aligned} \quad (5.27)$$

where $\lambda_{\text{SO}} \equiv p = \mathbf{P}_{ij} \cdot \mathbf{e}_z$ is the spin-orbit parameter (only one), ϵ_0 is the on-site orbital energy, and U is the on-site Coulomb repulsion energy. As stated before, typically $\lambda_{\text{SO}}, |t| \ll U$, which allows for a perturbative treatment of the hopping and spin-orbit Hamiltonians. These assumptions agree well with the numerical calculations performed in [169].

The perturbation theory program involves the unperturbed states of the system. The first set of unperturbed states are the one-electron states

$$|\phi_i^\sigma\rangle = c_{i\sigma}^\dagger |0\rangle, \quad (5.28)$$

while the three-electron states split in two categories: (i) the site singly occupied states

$$|\psi_k^\sigma\rangle = \prod_{j=1}^3 c_{j\sigma_j}^\dagger |0\rangle, \quad (5.29)$$

with $\sigma_j = \sigma$ for $j \neq k$ and $\sigma_j = \bar{\sigma}$, for $j = k$, and (ii) the double-occupied sites

$$|\psi_{kp}^\sigma\rangle = c_{k\uparrow}^\dagger c_{k\downarrow}^\dagger c_{p\sigma}^\dagger |0\rangle, \quad (5.30)$$

with $k = 1, 2, 3$ and $p \neq k$.

The states in Eqs. (5.28), (5.35) and (5.30) are degenerate with energies $E = \epsilon_0$, $E = 3\epsilon_0$ and $E = 3\epsilon_0 + U$, respectively. Note that these states are eigenstates of the Hamiltonian in Eq. (5.27) only in the absence of tunneling and SOI.

The above defined states are not yet adapted to the symmetry of the system, i.e. they are not basis states of the corresponding irreducible representations of D_{3h} point group. Finding these states is required by the fact that the symmetry of the molecule is made visible through the hopping and SOI terms in the Hubbard Hamiltonian. This is accomplished by using projector operators [163]. We obtain for the one-electron symmetry adapted states.

$$|\phi_{A'_1}^\sigma\rangle = \frac{1}{\sqrt{3}} \sum_{i=1}^3 |\psi_i^\sigma\rangle, \quad (5.31)$$

$$|\phi_{E'_\pm}^\sigma\rangle = \frac{1}{\sqrt{3}} \sum_{i=1}^3 \epsilon_{1,2}^{i-1} |\psi_i^\sigma\rangle, \quad (5.32)$$

$$(5.33)$$

where A'_2 and E'_\pm are one-dimensional and two-dimensional irreducible representations in D_{3h} , respectively. Similarly, the symmetry adapted states with the singly-occupied magnetic centers read:

$$|\psi_{A'_2}^{1\sigma}\rangle = \frac{1}{\sqrt{3}} \sum_{i=1}^3 |\psi_i^\sigma\rangle, \quad (5.34)$$

$$|\psi_{E'_\pm}^{1\sigma}\rangle = \frac{1}{\sqrt{3}} \sum_{i=1}^3 \epsilon_{1,2}^{i-1} |\psi_i^\sigma\rangle, \quad (5.35)$$

while the symmetry adapted states of the doubly-occupied magnetic centers read:

$$|\psi_{A'_{1,2}}^{2\sigma}\rangle = \frac{1}{\sqrt{6}} \sum_{i=1}^3 (|\psi_{i1}^\sigma\rangle \pm |\psi_{i2}^\sigma\rangle), \quad (5.36)$$

$$|\psi_{E'_\pm}^{2\sigma}\rangle = \frac{1}{\sqrt{6}} \sum_{i=1}^3 \epsilon_{1,2}^{i-1} (|\psi_{i1}^\sigma\rangle + |\psi_{i2}^\sigma\rangle), \quad (5.37)$$

$$|\psi_{E'_\pm}^{2\sigma}\rangle = \frac{1}{\sqrt{6}} \sum_{i=1}^3 \epsilon_{1,2}^{i-1} (|\psi_{i1}^\sigma\rangle - |\psi_{i2}^\sigma\rangle). \quad (5.38)$$

The tunneling and SOI mixes the singly-occupied and doubly-occupied states. Since both the tunneling and SOI terms in the Hubbard Hamiltonian transform as the totally symmetric irreducible representation A'_1 in D_{3h} , only states transforming according to the same irreducible representations Γ mix. We obtain the perturbed in first order in t/U and λ_{SO} :

$$|\Phi_{A'_2}^{1\sigma}\rangle \equiv |\psi_{A'_2}^{1\sigma}\rangle, \quad (5.39)$$

$$\begin{aligned} |\Phi_{E'_\pm}^{1\sigma}\rangle &\equiv |\psi_{E'_\pm}^{1\sigma}\rangle + \frac{(\bar{\epsilon} - 1)(t \pm \sigma \lambda_{\text{SO}})}{\sqrt{2}U} |\psi_{E'_\pm}^{2\sigma}\rangle \\ &+ \frac{3\epsilon(t \pm \sigma \lambda_{\text{SO}})}{\sqrt{2}U} |\psi_{E'_{\pm 2}}^{2\sigma}\rangle. \end{aligned} \quad (5.40)$$

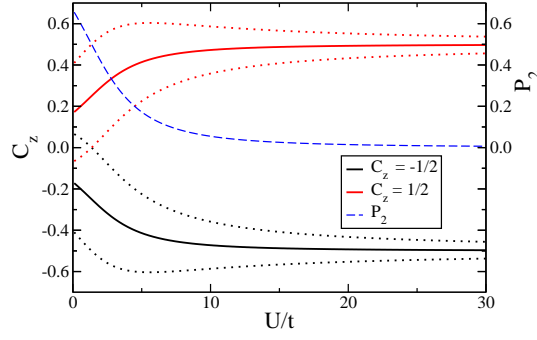


Figure 5.4: Spin-Hamiltonian limit. Expectation values of chirality $\langle C_z \rangle$ (full lines) and their bounds of uncertainty $\langle C_z \rangle \pm \Delta C_z$ (dotted lines), see text, in the low-energy states of the Hubbard model, as a function of the on-site repulsion U , at the fixed hopping matrix element $t = 1$ (left scale). The dashed line shows dependence of the double occupancy probability in the ground state on the right scale. The spin-Hamiltonian description becomes accurate in the $U \rightarrow \infty$ limit. The approach to this limit is slow, and the double occupancy probability is proportional to t/U .

Doubly occupied states become high in energy when $|t|/U, \lambda_{\text{SO}}/U \ll 1$. In this limit, the orbital states are quenched into singly-occupied localized atomic orbitals, and low-energy behavior is determined by spin and described by a spin Hamiltonian. In this limit the states in Eq. (5.35) are exactly the same chiral states in the spin Hamiltonian, i.e. $|\psi_{E_{\pm}}^{1\sigma}\rangle \equiv |\psi_{\sigma}^{(1,2)}\rangle$ and $|\psi_{A_2}^{1\sigma}\rangle \equiv |\psi_{\sigma}^{(0)}\rangle$. The probability of finding two electrons at the same site decays as $1/U$. The lowest energy states have total spin $S = 1/2$ and the chirality $C_z = \pm 1$, and the fluctuations of chirality $\Delta C_z = \sqrt{\langle C_z^2 \rangle - \langle C_z \rangle^2}$ in the eigenstates vanish, see Fig. 5.4. The chiral states emerge as the eigenstates in the large- U limit, when the system is well described by the spin Hamiltonian.

The coupling of the molecule to an external electric field \mathbf{E} takes place via two mechanisms. The first one implies modification of the on-site single particle energies ϵ_0 and leads to the following electric-dipole coupling Hamiltonian

$$\begin{aligned}
 H_{\text{e-d}}^0 &= -e \sum_{\sigma} \frac{E_y a}{\sqrt{3}} c_{1\sigma}^{\dagger} c_{1\sigma} - \frac{a}{2} \left(\frac{E_y}{\sqrt{3}} + E_x \right) c_{2\sigma}^{\dagger} c_{2\sigma} \\
 &+ \frac{a}{2} \left(E_x - \frac{E_y}{\sqrt{3}} \right) c_{3\sigma}^{\dagger} c_{3\sigma},
 \end{aligned} \tag{5.41}$$

with a being the geometrical distance between the magnetic ions and $E_{x,y}$ the in-plane components of the electric field. The second mechanism is due to modification of the hopping parameters t_{ii+1} in electric field and gives

$$H_{\text{e-d}}^1 = \sum_{i,\sigma} t_{ii+1}^{\mathbf{E}} c_{i\sigma}^{\dagger} c_{i+1\sigma}, \tag{5.42}$$

where $t_{ii+1}^{\mathbf{E}} = \langle \Phi_{i\sigma} | -e\mathbf{r} \cdot \mathbf{E} | \Phi_{i+1\sigma} \rangle$ are new hopping parameters induced solely by the electric field \mathbf{E} , and $\Phi_{i\sigma}$ are the Wannier states localized on the magnetic centers. We can write

the \mathbf{E} -induced hoppings as $t_{ii+1}^{\mathbf{E}} = \sum_{q=x,y,z} q_{ii+1} E_q$, with $q_{ii+1} = \langle \Phi_{i\sigma} | -eq | \Phi_{i+1\sigma} \rangle$ being electric dipole matrix elements between the i and $i+1$ ions. These matrix elements are not all independent, symmetry alone reducing drastically the number of independent electric dipole parameters. In order to find suitable independent free parameters, we switch from the description in terms of localized Wannier orbitals $\Phi_{i\sigma}$, to the description in terms of symmetry adapted states, namely from q_{ii+1} to $q_{\Gamma\sigma} = \langle \phi_{\Gamma\sigma} | q | \phi_{\Gamma'\sigma} \rangle$, where $\Gamma = A'_1, E'_\pm$. In the basis of symmetry adapted states, the components $q_{\Gamma\sigma}$ satisfy a number of relations. In particular, we find:

$$\langle \phi_{A'_1}^\sigma | -ex | \phi_{A'_1}^\sigma \rangle = \langle \phi_{A'_1}^\sigma | -ey | \phi_{A'_1}^\sigma \rangle = \langle \phi_{E'_+}^\sigma | -ex | \phi_{E'_+}^\sigma \rangle \equiv 0 \quad (5.43)$$

$$\langle \phi_{E'_-}^\sigma | -ex | \phi_{E'_-}^\sigma \rangle = \langle \phi_{E'_+}^\sigma | -ey | \phi_{E'_+}^\sigma \rangle = \langle \phi_{E'_-}^\sigma | -ey | \phi_{E'_-}^\sigma \rangle \equiv 0, \quad (5.44)$$

$$\langle \phi_{E'_+}^\sigma | -ex | \phi_{E'_-}^\sigma \rangle = -i \langle \phi_{E'_+}^\sigma | -ey | \phi_{E'_-}^\sigma \rangle \equiv d_{EE} \quad (5.45)$$

$$\begin{aligned} \langle \phi_{A'_1}^\sigma | -ex | \phi_{E'_+}^\sigma \rangle &= \langle \phi_{A'_1}^\sigma | -ex | \phi_{E'_-}^\sigma \rangle = -i \langle \phi_{A'_1}^\sigma | -ey | \phi_{E'_+}^\sigma \rangle \\ &= i \langle \phi_{A'_1}^\sigma | -ey | \phi_{E'_-}^\sigma \rangle \equiv d_{AE}. \end{aligned} \quad (5.46)$$

These relations reduce the number of free coupling constants to two, namely d_{EE} and d_{AE} .

It is instructive to write first the relation between the second quantized operators $c_{i\sigma}^\dagger$ ($c_{i\sigma}$) and $c_{\Gamma\sigma}^\dagger$ ($c_{\Gamma\sigma}$), which create (annihilate) electrons in localized and symmetry adapted states, respectively:

$$\begin{pmatrix} c_{1\sigma}^\dagger \\ c_{2\sigma}^\dagger \\ c_{2\sigma}^\dagger \end{pmatrix} = \frac{1}{\sqrt{3}} \begin{pmatrix} 1 & 1 & \epsilon \\ 1 & \bar{\epsilon} & \bar{\epsilon} \\ 1 & \epsilon & 1 \end{pmatrix} \begin{pmatrix} c_{A'_1\sigma}^\dagger \\ c_{E'_+\sigma}^\dagger \\ c_{E'_-\sigma}^\dagger \end{pmatrix}. \quad (5.47)$$

With these expressions at hand, we can write the electric dipole Hamiltonian together with the spin-orbit Hamiltonian in the following form:

$$\begin{aligned} H_{e-d}^0 &= \frac{-iea\sqrt{3}}{2} \sum_{\sigma} (\bar{E} c_{E'_+\sigma}^\dagger c_{A'_1\sigma} - \epsilon E c_{E'_-\sigma}^\dagger c_{A'_1\sigma} \\ &+ \epsilon \bar{E} c_{E'_-\sigma}^\dagger c_{E'_+\sigma}) + H.c., \end{aligned} \quad (5.48)$$

$$\begin{aligned} H_{e-d}^1 &= \sum_{\sigma} d_{AE} (\bar{E} c_{A'_1\sigma}^\dagger c_{E'_+\sigma} - E c_{A'_1\sigma}^\dagger c_{E'_-\sigma}) \\ &+ \bar{E} d_{EE} c_{E'_+\sigma}^\dagger c_{E'_-\sigma} + H.c., \end{aligned} \quad (5.49)$$

$$H_{\text{SO}} = \sqrt{3} \lambda_{\text{SO}} \sum_{\sigma} \sigma (c_{E'_-\uparrow}^\dagger c_{E'_-\uparrow} - c_{E'_+\uparrow}^\dagger c_{E'_+\uparrow}), \quad (5.50)$$

where $E = E_x + iE_y$ ($\bar{E} = E_x - iE_y$). The symmetry adapted states can also be expressed in terms of the symmetry adapted operators c_{Γ}^\dagger . The expressions for these states are shown in Appendix A. Using these states, we can compute all the matrix elements corresponding to the electric dipole and SOI Hamiltonian, respectively. The explicit form of these matrix elements can be found in Appendix B.

We now compute the electric dipole matrix elements between the perturbed chiral states of the E'_{\pm} symmetry. The question is to what order in t/U and/or $eEa(d_{EE}, d_{AE})/U$ we want to do it. We use the relations $|ea| \gg d_{EE}, d_{AE}$, which hold in the case of localized orbitals. This leads us to the following matrix element of the electric dipole in the ground state:

$$|\langle \Phi_{E'_-}^{1\sigma} | H_{e-d}^0 | \Phi_{E'_+}^{1\sigma} \rangle| \propto \left| \frac{t^3}{U^3} eEa \right|, \quad (5.51)$$

$$|\langle \Phi_{E'_-}^{1\sigma} | H_{e-d}^1 | \Phi_{E'_+}^{1\sigma} \rangle| \simeq \left| \frac{4t}{U} Ed_{EE} \right|. \quad (5.52)$$

We now relate the SOI matrix elements to the DM vectors in the effective spin-Hamiltonian. In D_{3h} symmetry, the DM term reads

$$H_{\text{SO}} = \frac{iD_z}{2} \sum_{i=1}^3 (S_+^i S_-^{i+1} - S_-^i S_+^{i+1}), \quad (5.53)$$

which gives rise to the following non-zero matrix elements,

$$\langle \Phi_{E'_{\pm}}^{1\sigma} | H_{\text{SO}} | \Phi_{E'_{\pm}}^{1\sigma} \rangle = \pm \frac{\sqrt{3}D_z}{2} \text{sign}(\sigma), \quad (5.54)$$

and allows us to make the following identification

$$D_z \equiv \frac{5\lambda_{\text{SO}}t}{U}. \quad (5.55)$$

We see that this SOI term acts exactly as the 'microscopic' SOI derived before: it splits the chiral states, but it does not mix them.

The Hubbard model with spin-orbit coupling can reproduce the energy-level structure of the spin Hamiltonian. In the limit of strong on-site repulsion $|t|/U \ll 1$, the atomic orbitals in the triangle vertices are occupied by one electron each. The lowest energy manifold consists of four states with the total spin $S_{\text{tot}} = 1/2$. These states are split from the next four-level $S_{\text{tot}} = 3/2$ manifold by a gap of the order of t^2/U .

5.3.3 Superexchange in molecular bonds

In this Subsection, we use the Hubbard model to deduce the dependence of the spin Hamiltonian of MNs on the external electric fields in the case where the coupling between magnetic sites is mediated by a non-magnetic bridge. In particular, we study how the parameters of the effective spin Hamiltonian depend on the hopping matrix elements that are modified by the presence of an electric field. This method was successfully applied in the studies of strongly correlated electrons, like cuprates [166] and multiferroics [168].

In order to describe the magnetic coupling, we consider a pair of sites corresponding to the magnetic centers and a bridge site. Since the direct overlap of the orbitals localized on the magnetic centers is small, we set the direct hopping between the magnetic centers to zero, but allow for the hopping of electrons between the magnetic sites and the bridge site. This hopping gives rise to superexchange interaction between the spins on the magnetic

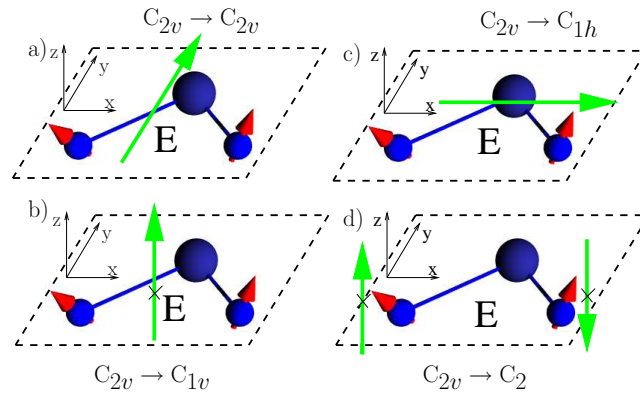


Figure 5.5: Geometry of the bond and reduction of symmetry. (a) Electric field \mathbf{E} in y direction, leaves the C_{2v} symmetry unbroken. (b) An electric field \mathbf{E} in z -direction, normal to the bond plane, reduces the symmetry to $\{E, \sigma_v\}$. (c) An electric field \mathbf{E} in x -direction, along the line connecting the magnetic centers, reduces the symmetry to $\{E, \sigma_h\}$. (d) In an inhomogeneous staggered electric field \mathbf{E} , the reduced symmetry group is $\{E, R_{y,\pi}\}$.

sites [164]. In the limit of strong on-site repulsions, the effective Hamiltonian in the lowest energy sector of the bond corresponds to a spin Hamiltonian where the coupling strengths are determined by the Hubbard model parameters. This correspondence provides an intuitive picture of the mechanism that leads to the interaction between the spins. It also allows us to infer the properties of the molecule that lead to a strong spin-electric coupling, e.g., the delocalization of the orbitals and their local symmetry.

The Hubbard Hamiltonian of the bond is given by

$$H_b = \sum_{i,\alpha\beta} \left[c_{i\alpha}^\dagger \left(t_i \delta_{\alpha\beta} + \frac{i\mathbf{P}_i}{2} \cdot \boldsymbol{\sigma}_{\alpha\beta} \right) b_\beta + \text{h. c.} \right] + U_1(n_1) + U_2(n_2) + U_b(n_b), \quad (5.56)$$

where the indices 1 and 2 refer to the magnetic sites, and b refers to the bridge site. We derive the spin Hamiltonian by fourth-order Schrieffer-Wolff transformation of the Hamiltonian H_b (5.56).

The Schrieffer-Wolff transformation [174] of the bond Hamiltonian $H_b = H_0 + H_{\text{tun}}$ (5.56), where the unperturbed Hamiltonian $H_0 = U_1(n_1) + U_2(n_2) + U_b(n_b)$ produces an effective low energy Hamiltonian H_{12} that approximately describes the low-energy dynamics of the bond. The effective Hamiltonian is

$$H_{12} = \mathcal{P} e^S H_b e^{-S} \mathcal{P}, \quad (5.57)$$

where the antiunitary operator S is chosen so that the low-energy space of H_0 is decoupled from the high-energy space. This operator is found iteratively, $S = S^{(1)} + S^{(2)} + \dots$, so that the n th order transformation $S^{(n)}$ removes the terms that couple the low- and high-energy states up to order n . The projector \mathcal{P} projects to the low-energy states. In our system, the lowest order Schrieffer-Wolff transformation that gives a nontrivial contribution

to the low-energy spin Hamiltonian is of fourth order, and the operator S is approximated as $S \approx \sum_{n=1}^4 S^{(n)}$.

The unperturbed Hamiltonian, $H_0 = U_1 + U_2 + U_b$, describes localized electrons, and the hopping H_{tun} acts as perturbation. The low-energy subspace of the unperturbed Hamiltonian is spanned by the states in which the magnetic ions are singly occupied, and the bridge is doubly occupied. The lowest-order terms that give rise to a nontrivial spin Hamiltonian, in the limit $|t|, |\mathbf{P}| \ll U$, are of the fourth order in t and \mathbf{P} .

The resulting interaction of the spins includes an isotropic exchange of strength J , a Dzyalozhinsky-Moriya interaction described by a vector \mathbf{D} , and an anisotropic exchange term described by a second rank symmetric traceless tensor $\mathbf{\Gamma}$ [175]

$$H_{12} = J\mathbf{S}_1 \cdot \mathbf{S}_2 + \mathbf{D} \cdot (\mathbf{S}_1 \times \mathbf{S}_2) + \mathbf{S}_1 \cdot \mathbf{\Gamma}\mathbf{S}_2. \quad (5.58)$$

Quite generally the interaction between two spins up to second order in \mathbf{P}_{12} can be represented as an isotropic exchange of rotated spins [166]. However, since the frustration in the triangle is strong, it is a good approximation to take only the Dzyalozhinsky-Moriya interaction into account for the weak spin-orbit coupling, $|\mathbf{P}_{12}| \ll |t_{12}|$ when describing a full molecule.

In a bond with a single bridge site, the largest possible symmetry is C_{2v} . We introduce Cartesian coordinates with the x -axis pointing from the magnetic center 1 to 2, y -axis lying in the bond plane and pointing towards the bridge site, and the z -axis normal to the bond plane (Fig. 5.5). The elements of the C_{2v} symmetry group are then rotation $R_{y,\pi}$ by π about the y -axis, reflection σ_v in the yz plane, and reflection σ_h in the xy plane. Each of these symmetry operations present imposes constraints on the parameters of H_b . In the case of localized orbitals that remain invariant under the local symmetries of their respective sites, the constraints resulting from the $R_{y,\pi}$ symmetry are:

$$t_1 = t_2, \quad (5.59)$$

$$P_{x,1} = -P_{x,2}, \quad (5.60)$$

$$P_{y,1} = P_{y,2}, \quad (5.61)$$

$$P_{z,1} = -P_{z,2}. \quad (5.62)$$

The σ_v symmetry implies:

$$t_1 = t_2, \quad (5.63)$$

$$P_{x,1} = P_{x,2}, \quad (5.64)$$

$$P_{y,1} = -P_{y,2}, \quad (5.65)$$

$$P_{z,1} = -P_{z,2}, \quad (5.66)$$

and the σ_h symmetry implies:

$$\mathbf{P}_1 = -\mathbf{P}_2 = p\mathbf{e}_z. \quad (5.67)$$

In the perturbative calculation of the effective spin Hamiltonian parameters, these constraints reproduce the Dzyalozhinsky-Moriya rules. We do not deal with the symmetry of on-site energies $U_{1,2,b}$ in any detail, since they do not affect the spin Hamiltonian at this level of approximation.

5.3.4 Electric field along y

In the electric field pointing along the y axis, the point group symmetry of the bridge remains C_{2v} , and all of the constraints (5.60) – (5.67) hold. The fourth-order Schrieffer-Wolff transformation then gives the interaction between the spins on magnetic centers of the form (5.58) with the parameters

$$J = \frac{1}{12U^3} (48t^4 - 40t^2p_z^2 + 3p_z^4), \quad (5.68)$$

$$\mathbf{D} = \frac{2}{U^3} tp_z (4t^2 - p_z^2) \mathbf{e}_z, \quad (5.69)$$

$$\Gamma_{xx} = \Gamma_{yy} = -\frac{1}{2}\Gamma_{zz} = -\frac{8}{3U^3}t^2p_z^2, \quad (5.70)$$

while all the off-diagonal elements of $\mathbf{\Gamma}$ vanish. Here, the parameters of the Hubbard model satisfy the symmetry constraints of the full C_{2v} , and

$$t_1 = t_2 = t, \quad (5.71)$$

$$\mathbf{P}_1 = -\mathbf{P}_2 = p_z \mathbf{e}_z. \quad (5.72)$$

We have introduced $U^3 = U_{c2}(2U_{c2} - U_{b2})(U_{b1} - U_{b2} + U_{c2})^2/(4U_{c2} - U_{b2})$, where the on-site repulsions are U_{b2} for the doubly occupied bridge, U_{b1} for the singly occupied bridge, and U_{c2} for the doubly occupied magnetic center. The parameter U describes the energy cost of leaving the manifold of states with the minimal energy of Coulomb repulsion. We assume that the lowest energy charge configuration corresponds to a doubly occupied bridge, so that $U_{b2} < U_{b1}$.

In first order, the variations of the spin-Hamiltonian parameters resulting from the modification of the Hubbard model parameters, are:

$$\delta J = \frac{1}{3U^3} [(48t^3 - 20tp_z^2) \delta t + (-20t^2p_z + 3p_z^3) \delta p_z], \quad (5.73)$$

$$\delta D_z = \frac{2}{U^3} [(12t^2p_z - p_z^3) \delta t + (4t^3 - 3tp_z^2) \delta p_z], \quad (5.74)$$

$$\delta \Gamma_{xx} = \delta \Gamma_{yy} = -\frac{\delta \Gamma_{zz}}{2} = -\frac{16tp_z}{3U^3} (p_z \delta t + t \delta p_z). \quad (5.75)$$

Electric field modifies the orbitals and therefore the overlaps between them, that determine the hopping parameters. We consider the case where the variations δt and δp_z are linear in the field intensity E_y : $\delta t = \kappa_t E_y$, $\delta p_z = \kappa_{p_z} E_y$. We will not discuss the effect of variations in the on-site energies U in any details, since their only effect in the fourth order perturbation is a rescaling of all the spin Hamiltonian parameters by $U^3/(U + \delta U)^3$.

We stress that these linear modifications of the hopping parameters are characteristic for the C_{2v} symmetry. If the electric field is oriented differently and thus lowers the system symmetry (see below) first-order increments are not allowed, and the spin-electric coupling is at least a second order effect in the electric field. The modification of the orbitals includes the energy scale of splitting of the atomic orbitals in the molecular field. We have assumed earlier that the splitting of the orbitals localized on the magnetic centers is large, and the dominant source of the spin-electric coupling is the modification of the bridge orbital.

Therefore, the key criterion for strong spin-electric coupling is the presence of bridge orbitals that are weakly split in the molecular field. If, in addition, we assume that the modification is a property of the bond alone, and not of the entire molecule, the κ parameters can be determined in an ab-initio calculations on a smaller collection of atoms.

In the limit of weak spin-orbit coupling, $|t| \gg |p_z|$, the main effect of the electric fields is a change of J , leading to our symmetry-based results, see Eq.5.15. In particular, the d parameter of the symmetry analysis is:

$$d = \frac{4}{U^3} \left[(48t^3 - 20tp_z^2) \kappa_t + (-20t^2p_z + 3p_z^3) \kappa_{pz} \right]. \quad (5.76)$$

In this case, the Dzyalozhinsky-Moriya vector \mathbf{D} is constraint to point in the z direction, $\mathbf{D} = D\mathbf{e}_z$. The model suggests that the dominant effect of the electric field in the molecules with dominant Heisenberg exchange ($J \gg |\mathbf{D}|$) is modification of the isotropic exchange constants J , and

$$\frac{|\delta\mathbf{D}|}{|\delta J|} \sim \frac{|\mathbf{D}|}{|J|}, \quad (5.77)$$

so that the modification of the Dzyalozhinsky-Moriya vector $\mathbf{D} \rightarrow \mathbf{D} + \delta\mathbf{D}$ is weaker. However, in the molecules in which the modifications of J are inefficient in inducing the spin-electric coupling, as for example in the spin-1/2 pentagon, the modifications of \mathbf{D} may eventually provide the main contribution to the spin-electric coupling.

Electric field pointing in a generic direction breaks the C_{2v} symmetry of the bridge, and allows further modification of the Hubbard and spin Hamiltonian parameters, that do not obey all the symmetry constraints in Eqs. (5.59) – (5.67). With the relaxed constraints, both the direction and intensity of $\mathbf{P}_{1,2}$, as well as the spin-independent hoppings $t_{1,2}$ become field-dependent. This observation can be used in the search for molecules that show strong spin-electric coupling. The energy cost of changing the distance between the localized orbitals may be significantly higher than the cost of modifying the shape of the bridge orbital. In order to investigate this dependence, we study the effective spin Hamiltonian description of a bridge with all possible residual symmetries.

Residual σ_v symmetry

An electric field $\mathbf{E} = E\mathbf{e}_z$ normal to the bond's plane reduces the initial C_{2v} symmetry down to $\{E, \sigma_v\}$. This reduction of the symmetry also happens when a molecule is deposited on the surface parallel to the bond plane. While the constraints in Eq. 5.67 hold, this reduction of symmetry implies the appearance of nonzero in-plane components of $\mathbf{P}_{1,2}$. We parameterize the most general Hubbard model parameters $t_{1,2}$, $\mathbf{P}_{1,2}$ consistent with the symmetry as

$$t_1 = t_2 = t, \quad (5.78)$$

$$P_{1,x} = P_{2,x} = p_{xy} \cos \phi, \quad (5.79)$$

$$P_{1,y} = -P_{2,y} = p_{xy} \sin \phi, \quad (5.80)$$

$$P_{1,z} = -P_{2,z} = p_z. \quad (5.81)$$

The effective low energy spin Hamiltonian, derived by Schrieffer-Wolff transformation up to fourth order in t/U , and $|\mathbf{P}|/U$ is given by (5.58), with the non-zero parameters

$$J = \frac{1}{12U^3} [p_{xy}^4 - 2p_{xy}^2 p_z^2 + 3p_z^4 - 8t^2 (p_{xy}^2 + 5p_z^2) + 48t^4 - 8p_{xy}^2 (p_z^2 - 4t^2) \cos 2\phi + 2p_{xy}^4 \cos 4\phi], \quad (5.82)$$

$$D_y = -\frac{p_{xy}}{U^3} (p_z \cos \phi + 2t \sin \phi) (-p_z^2 + 4t^2 + p_{xy}^2 \cos 2\phi), \quad (5.83)$$

$$D_z = -\frac{1}{2U^3} (4tp_z - p_{xy}^2 \sin 2\phi) (p_z^2 - 4t^2 - p_{xy}^2 \cos 2\phi), \quad (5.84)$$

$$\Gamma_{xx} = -\frac{1}{6U^3} [p_{xy}^2 (1 - \cos 2\phi) + 2p_z^2] [8t^2 + p_{xy}^2 (1 + \cos 2\phi)], \quad (5.85)$$

$$\Gamma_{yy} = \frac{1}{12U^3} \left\{ -p_{xy}^4 + 8p_{xy}^2 p_z^2 + 32t^2 (p_{xy}^2 - p_z^2) + p_{xy}^2 [8(p_z^2 - 4t^2) \cos 2\phi + p_{xy}^2 \cos 4\phi + 48tp_z \sin 2\phi] \right\}, \quad (5.86)$$

$$\Gamma_{yz} = \Gamma_{zy} = \frac{p_{xy}}{U^3} (p_z \cos \phi + 2t \sin \phi) (-4tp_z + p_{xy}^2 \sin 2\phi) \quad (5.87)$$

$$\Gamma_{zz} = -\Gamma_{xx} - \Gamma_{yy}. \quad (5.88)$$

In the lowest order in spin-orbit coupling the spin interaction consists of the isotropic exchange with $J \approx 4t^4/U^3$, and the DM interaction with $\mathbf{D} \approx -8t^3(p_{xy} \sin \phi \mathbf{e}_y + p_z \mathbf{e}_z)/U^3$.

As a matter of principle, the spin-orbit coupling mediated hopping \mathbf{P} does not have to be much weaker than the spin-independent hopping t . In this case, all the nonzero terms in Eqs. (5.82) — (5.88) are of comparable size, and the variation of spin Hamiltonian with the angle ϕ becomes significant. Note that the angle ϕ describes the directions of spin-orbit coupling induced hopping parameters $\mathbf{P}_{1,2}$, and that it is not directly connected to the bond angle between the magnetic sites and the bridge site. However, for the bridge orbital without azimuthal symmetry, the angle ϕ does depend on the bond angle. For the molecules in which the full symmetry allows only for the spin-electric coupling mediated by the spin-orbit interaction, this effect is important.

With these assumptions, the dependence of the effective spin Hamiltonian on p_{xy} suggests that the strength of induced in-plane Dzyalozhinsky-Moriya vector will be sensitive to the angle ϕ that is determined by the angular dependence of the bridge- and magnetic center orbitals. In turn, for a fixed symmetry of the bridge orbital, this dependence directly translates into the dependence of the spin-electric coupling constant on the bridge bond angle.

In the presence of electric field $\mathbf{E} = E\mathbf{e}_z$, the hopping parameters will change from their initial values, that satisfy the constraints implied by the C_{2v} symmetry, into a set of values that satisfy those implied by σ_v only. The resulting change in the spin-Hamiltonian

parameters reads:

$$\delta J = \frac{1}{3U^3} [4t_0 (12t_0^2 - 5p_{z0}^2) \delta t + p_{z0} (-20t_0^2 + 3p_{z0}^2) \delta p_z], \quad (5.89)$$

$$\delta D_y = -\frac{1}{U^3} (4t_0^2 - p_{z0}^2) (2t_0 \sin \phi + p_{z0} \cos \phi) \delta p_{xy}, \quad (5.90)$$

$$\delta D_z = \frac{2}{U^3} [p_{z0} (12t_0^2 - p_{z0}^2) \delta t + t_0 (4t_0^2 - 3p_{z0}^2) \delta p_z], \quad (5.91)$$

$$\delta \Gamma_{xx} = \delta \Gamma_{yy} = -\frac{1}{2} \delta \Gamma_{zz} = -\frac{16}{3U^3} t_0 p_{z0} (p_{z0} \delta t + t_0 \delta p_z), \quad (5.92)$$

$$\delta \Gamma_{yz} = \delta \Gamma_{zy} = -\frac{4}{U^3} t_0 p_{z0} (2t_0 \sin \phi + p_{z0} \cos \phi) \delta p_{xy}. \quad (5.93)$$

The σ_v -symmetric variations of Hubbard parameters occur when an external electric field is applied along the z direction to a C_{2v} symmetric bond. Again, the variations of the parameters is generically linear in the field strength, $\delta t = \kappa_{t,\sigma v} E_z$, $\delta p_{xy} = \kappa_{p_{xy},\sigma v} E_z$, $\delta p_z = \kappa_{p_z,\sigma v} E_z$, where the κ parameters depend on the modification of the bridge orbital in the electric field. As opposed to the case of the field along y direction that maintains the bonds C_{2v} symmetry, the κ parameters for the field along z axis vanish in zero field, since the z -component of a vector has no matrix elements between the relevant C_{2v} -symmetric states. The linear expansion is valid when the field is strong enough to distort the bridge orbital. Alternatively, the expansion is valid for a bond with lower symmetry in zero electric field, e. g., when the bond is close to a surface.

Residual σ_h symmetry

In an electric field that lies in plane of the bond, with $\mathbf{E} \parallel \hat{\mathbf{x}}$, the only residual symmetry transformation is the reflection about the xy plane (σ_h). Within this reduced symmetry, the two magnetic sites are no longer equivalent, but the spin-dependent hopping parameters $\mathbf{P}_{1,2}$ still point along the z axis:

$$t_1 \neq t_2, \mathbf{P}_1 = p_1 \mathbf{e}_z \neq p_2 \mathbf{e}_z = \mathbf{P}_2. \quad (5.94)$$

In the fourth order in hopping t , \mathbf{P} , the resulting low energy spin Hamiltonian is again given by Eq. 5.58, with the following non-zero coupling constants:

$$J = \frac{1}{12U^3} [32t_1 t_2 p_{1z} p_{2z} - 4(t_1^2 p_{2z}^2 + t_2^2 p_{1z}^2) + 48t_1^2 t_2^2 + 3p_{1z}^2 p_{2z}^2], \quad (5.95)$$

$$\mathbf{D} = -\frac{1}{U^3} (t_1 p_{2z} - t_2 p_{1z}) (4t_1 t_2 + p_{1z} p_{2z}) \mathbf{e}_z, \quad (5.96)$$

$$\Gamma_{xx} = \Gamma_{yy} = -\frac{\Gamma_{zz}}{2} = -\frac{2}{3U^3} (t_1 p_{2z} - t_2 p_{1z})^2, \quad (5.97)$$

Similarly to the case of full C_{2v} symmetry, the spin Hamiltonian consists of the isotopic exchange J , Dzyalozhinsky-Moriya vector $\mathbf{D} = D_z \hat{\mathbf{z}}$ normal to the bond plane, and diagonal tensor Γ isotropic in the bond plane ($\Gamma_{xx} = \Gamma_{yy}$). We stress that the dependence of the effective spin Hamiltonian parameters on those entering the spin Hubbard Hamiltonian is different for these two symmetries, and so is the response to the applied electric field. On one hand, the C_{2v} preserving electric field induces the transitions in the lowest energy multiplet in the lowest order. On the other hand, the electric field that reduces the bond symmetry to $\{E, \sigma_h\}$ does not alter the coupling of spins in the lowest order, since the deformation of the molecule requires some coupling to the field.

As in previous case, we expand the σ_h symmetric spin Hamiltonian around the C_{2v} symmetric case. We introduce a perturbation of the parameters Hubbard parameters in the electric field consistent with the residual symmetry: $t_1 = t_0 + \delta t_1$, $t_2 = t_0 + \delta t_2$, $p_{1z} = p_{z0} + \delta p_{1z}$, $p_{2z} = -p_{z0} + \delta p_{2z}$. As a consequence, the spin Hamiltonian parameters are incremented by:

$$\delta J = \frac{1}{6U^3} [4t_0 (12t_0^2 - 5p_{z0}^2) (\delta t_1 + \delta t_2) + p_{z0} (-20t_0^2 + 3p_{z0}^2) (\delta p_{1z} - \delta p_{2z})], \quad (5.98)$$

$$\delta D_z = \frac{1}{U^3} [p_{z0} t_0 (12t_0 - p_{z0}) (\delta t_1 + \delta t_2) + t_0 (4t_0^3 - 3p_{z0}^2) (\delta p_{1z} - \delta p_{2z})], \quad (5.99)$$

$$\delta \Gamma_{xx} = \delta \Gamma_{yy} = -\frac{\delta \Gamma_{zz}}{2} = -\frac{8}{3U^3} t_0 p_{z0} [p_{z0} (\delta t_1 + \delta t_2) + t_0 (\delta p_{1z} - \delta p_{2z})]. \quad (5.100)$$

As for the case of σ_v residual symmetry, there is no spin-electric effect of the first order in electric field, and the crucial condition for coupling to the electric field in this direction is weak splitting of the bridge orbitals in the molecular field.

Residual $R_{y,\pi}$ symmetry

Reduction of the symmetry of the bond, from the full C_{2v} to the group $\{E, R_{y,\pi}\}$, does not occur for any vector perturbation. In terms of electric fields, this reduction of the symmetry would correspond to an inhomogeneous electric field that points in the \mathbf{e}_z direction at the position of one of the magnetic centers, and in the $-\mathbf{e}_z$ direction at the position of the other. This symmetry breaking can also happen when the localized orbitals on the magnetic centers have lobes of opposite signs extending in the z -direction, and oriented opposite to each other.

The most general Hubbard model parameters consistent with the residual symmetry are

$$t_1 = t_2 = t, \quad (5.101)$$

$$P_{1x} = -P_{2x} = p_{xy} \cos \phi, \quad (5.102)$$

$$P_{1y} = P_{2y} = p_{xy} \sin \phi, \quad (5.103)$$

$$P_{1z} = P_{2z} = p_z. \quad (5.104)$$

After the fourth-order Schrieffer-Wolff transformation, the effective low-energy spin Hamiltonian has the form (5.58) with nonzero parameters

$$J = \frac{1}{12U^3} (p_{xy}^4 - 2p_{xy}^2 p_z^2 + 3p_z^4 - 8t^2 (p_{xy}^2 + 5p_z^2) + 48t^2 + 8p_{xy}^2 (p_z^2 - 4t^2) \cos 2\phi + 2p_{xy}^4 \cos 4\phi), \quad (5.105)$$

$$D_x = \frac{1}{U^3} p_{xy} (-2t \cos \phi + p_z \sin \phi) (p_z^2 - 4t^2 + p_{xy}^2 \cos 2\phi), \quad (5.106)$$

$$D_z = -\frac{1}{2U^3} (4tp_z + p_{xy}^2 \sin 2\phi) (p_z^2 - 4t^2 + p_{xy}^2 \cos 2\phi), \quad (5.107)$$

$$\Gamma_{xx} = \frac{1}{12U^3} (-p_{xy}^4 + 8p_{xy}^2 p_z^2 + 32t^2 (p_{xy}^2 - p_z^2) + p_{xy}^2 (-8 (p_z^2 - 4t^2) \cos 2\phi + p_{xy}^2 \cos 4\phi - 48tp_z \sin 2\phi)), \quad (5.108)$$

$$\Gamma_{zx} = \Gamma_{xz} = \frac{1}{U^3} p_{xy} (2t \cos \phi - p_z \sin \phi) (4tp_z + p_{xy}^2 \sin 2\phi), \quad (5.109)$$

$$\Gamma_{yy} = \frac{1}{6U^3} (p_{xy}^2 (1 + \cos 2\phi) + 2p_z^2) (p_{xy}^2 (-1 + \cos 2\phi) - 8t^2), \quad (5.110)$$

$$\Gamma_{zz} = -\Gamma_{xx} - \Gamma_{yy} = -\frac{1}{6U^3} (-p_{xy}^4 + 2p_{xy}^2 p_z^2 + 8t^2 (p_{xy}^2 - 4p_z^2) + p_{xy}^2 (-2 (p_z^2 - 4t^2) \cos 2\phi + p_{xy}^2 \cos 4\phi - 24tp_z \sin 2\phi)). \quad (5.111)$$

The expansion from the C_{2v} symmetric case gives (see the discussion of the σ_v residual symmetry in Subsection 5.3.4):

$$\delta J = \frac{1}{3U^3} [4t_0 (12t_0^2 - 5p_{z0}^2) \delta t + p_{z0} (-20t_0^2 + 3p_{z0}^2) \delta p_z], \quad (5.112)$$

$$\delta D_x = \frac{1}{U^3} (4t_0^2 - p_{z0}^2) (2t_0 \cos \phi_0 - p_{z0} \sin \phi_0) \delta p_{xy}, \quad (5.113)$$

$$\delta D_z = \frac{2}{U^3} [p_{z0} (12t_0^2 - p_{z0}^2) \delta t + t_0 (4t_0^2 - 3p_{z0}^2) \delta p_{z0}], \quad (5.114)$$

$$\delta \Gamma_{xx} = \delta \Gamma_{yy} = -\frac{1}{2} \delta \Gamma_{zz} = -\frac{16}{3U^3} p_{z0} t_0 (p_{z0} \delta t + t_0 \delta p_z), \quad (5.115)$$

$$\delta \Gamma_{zx} = \delta \Gamma_{xz} = \frac{4}{U^3} t_0 p_{z0} (2t_0 \cos \phi_0 - p_{z0} \sin \phi_0) \delta p_{xy}. \quad (5.116)$$

As in the case of σ_v symmetry, the resulting interaction of the spins on magnetic centers becomes dependent on the angle ϕ between the two \mathbf{P} parameters. This dependence is pronounced in the case of strong spin-orbit coupling and can lead to the dependence of spin-electric effects on both the geometry of the bond and the shape of the bridge orbital.

5.3.5 Bond modification and symmetries

Spin-electric coupling induced by the superexchange through bridge atoms depends on the symmetry of the bridge and the direction of the electric field. This symmetry reflects on the resulting coupling of spins in an MN. In this subsection, we combine the results of the Hubbard model study of the individual bonds with the previous symmetry considerations, and provide rough estimates of the most promising spin-electric coupling mechanism in the triangular and pentagonal molecules.

The spin-electric coupling via superexchange is most sensitive to the electric fields that does not break the initial C_{2v} local symmetry of the bond. This symmetry corresponds to the electric field that lies in the plane of the molecule and normal to the bond. All the other couplings require modification of the bridge orbitals, and are suppressed by a factor $d|\mathbf{E}|/U_d$, where U_d is on-site repulsion on the bridge. Assuming that this repulsion is strong, we can model the spin electric coupling as a set of modifications of the spin interactions δH_{jj+1} between the neighboring magnetic centers, with $|\delta H_{jj+1}| \propto |E_{\perp}^{\text{bond}}|$, where E_{\perp}^{bond} is the projection of the electric field normal to the bond and lying in the molecule's plane.

In the triangle, the strongest effects of electric field is modification of exchange couplings $\delta J_{jj+1} = \delta J_0 \cos(2j\pi/3 + \theta_0)$, where the angle θ_0 describes the orientation of the in-plane component of the electric field, and δJ_0 is a molecule-dependent constant. This modification leads to a specific coupling of the in-plane components of chirality to the electric field $H_{e-d}^{\text{eff}} = d\mathbf{E}' \cdot \mathbf{C}_{\parallel}$, see (5.7). Other types of coupling are suppressed either due to weaker influence of electric field on the bonds, or due to the symmetry of the molecule. If the spin-electric coupling is mediated by the spin-orbit interaction, the suppression is by a factor of the order $|\mathbf{D}|/J$, and if the coupling is mediated by electric field, the suppression factor is $d|\mathbf{E}|/J$. Assuming the simplest case, the modification of exchange coupling is the most promising mechanism for spin-electric coupling in triangular molecules.

In the pentagons, the modification of spin-spin interaction δH_{jj+1} preferred by the superexchange mechanism is inefficient in inducing the spin-electric coupling of the molecule. The pattern δJ_{jj+1} of exchange coupling constants induced by an external electric field does not couple the states within the lowest energy manifold. In order to couple the spins in the pentagon to an external field, another mechanism is needed. The modification of the Dzyalozhinsky-Moriya vectors $\delta D_{jz} = \delta D_{z0} \cos(2j\pi/5 + \theta_0)$, where δD_{z0} is a molecule-dependent constant, and θ_0 describes the orientation of the in-plane component of the electric field, is preferred by the superexchange bridge model. In the symmetry analysis, we have found that this form of modification of spin-orbit coupling does not induce spin-electric coupling. The same applies to the modifications of in-plane components $\mathbf{D}_{j,xy}$. The main effect that gives rise to spin-electric coupling is the modification of the exchange interactions δJ_{jj+1} in the presence of the original spin-orbit interaction $D_{jj+1,z}$. Compared to a triangle composed out of identical bonds, this interaction will be weaker by a factor of $|\mathbf{D}_{jj+1}|/J_{jj+1}$.

In summary, within our model of the superexchange-mediated spin-electric coupling, the most promising candidates for the spin manipulation via electric field are triangular molecules. In pentagons, the best candidates are molecules with strong spin-orbit interaction, and weakly split bridge orbitals.

5.4 Experimental signatures of the spin-electric coupling

Coherent quantum control of spins in an MN using electric fields can be achieved by resonant driving of the transitions between the chirality eigenstates [156]. At present, however, little is known about the effects of electric fields on the spin states of molecular magnets. As a preliminary step, it is useful to identify possible signatures of such a coupling that are observable in the experiments routinely used to characterize these systems.

In this section, we study the ways in which the spin-electric coupling can be detected in electron spin resonance (ESR), in nuclear magnetic resonance (NMR), and in the thermo-

dynamic measurement of an MN.

5.4.1 Electron spin resonance

Electron spin resonance (ESR) investigates transitions between states belonging to a given S multiplet and having different spin projections M along the magnetic field direction [32]. This technique provides information on the anisotropies of the spin system, as well as on the chemical environment, and the spin dynamics [144]. In the following, we show how the effects of an external electric field can show up in the ESR spectra of antiferromagnetic spin rings by affecting both the frequency and the oscillator strength of the transitions.

Triangle of $s = 1/2$ spins

We start by considering the simplest case of interest, namely that of a triangle of $s = 1/2$ spins with D_{3h} symmetry. The lowest energy eigenstates of the spin triangle, given in Eq. (5.3) form an $S = 1/2$. The effective Hamiltonian H_{eff} of the molecule in the presence of electric and magnetic field, and acting within this quadruplet is given by Eq. (5.15).

We first consider the case of a static magnetic field perpendicular to the molecule's plane ($\mathbf{B} \parallel \hat{\mathbf{z}}$). The eigenvalues of H_{eff} are then given by:

$$\lambda_{\sigma}^{\alpha} = \sigma[\mathcal{B} + \alpha(\Delta_{\text{SO}}^2 + \mathcal{E}^2)^{1/2}], \quad (5.117)$$

where $\mathcal{E} \equiv d|\mathbf{E} \times \hat{\mathbf{z}}|$, $\mathcal{B} = \mu_B \sqrt{g_{\parallel}^2 B_z^2 + g_{\perp}^2 B_{\perp}^2}$, $\sigma = \pm 1/2$ is the eigenvalue of S_z , $\alpha = \pm 1$ is the the eigenstate chirality in the limit of vanishing electric field: $|\lambda_{\sigma}^{\alpha}\rangle_{\mathcal{E}=0} = (-\alpha)^{\sigma-1/2}|\alpha, \sigma\rangle$. In the presence of electric field, the eigenstates read:

$$\begin{aligned} |\lambda_{\sigma}^{\alpha}\rangle &= \{2\sigma[\Delta_{\text{SO}} + \alpha(\mathcal{E}^2 + \Delta_{\text{SO}}^2)^{1/2}]|+1, \sigma\rangle \\ &+ \mathcal{E}e^{-i\theta}|-1, \sigma\rangle\}/D^{\alpha}, \end{aligned} \quad (5.118)$$

where $D^{\alpha} = \{\mathcal{E}^2 + [\Delta_{\text{SO}} + \alpha(\mathcal{E}^2 + \Delta_{\text{SO}}^2)^{1/2}]^2\}^{1/2}$.

Electron spin resonance induces transitions between such eigenstates. The transition amplitudes are given by the absolute values of matrix elements of x -component of the total spin, taken between the states that the transition connects,

$$\langle \lambda_{-1/2}^{\alpha} | S_x | \lambda_{+1/2}^{-\alpha} \rangle = -\mathcal{E}^2 / D^{+1} D^{-1} \quad (5.119)$$

$$\langle \lambda_{-1/2}^{\alpha} | S_x | \lambda_{+1/2}^{\alpha} \rangle = \frac{\Delta_{\text{SO}}[\Delta_{\text{SO}} + \alpha(\mathcal{E}^2 + \Delta_{\text{SO}}^2)^{1/2}]}{(D^{\alpha})^2}. \quad (5.120)$$

The corresponding frequencies are given by:

$$\lambda_{+1/2}^{\alpha} - \lambda_{-1/2}^{-\alpha} = \mathcal{B} \quad (5.121)$$

$$\lambda_{+1/2}^{\alpha} - \lambda_{-1/2}^{\alpha} = \mathcal{B} + \alpha(\mathcal{E}^2 + \Delta_{\text{SO}}^2)^{1/2}. \quad (5.122)$$

As an illustrative example, we plot the frequencies and amplitudes of the ESR transitions as a function of the electric field (Fig. 5.6). While for $\mathcal{E} = 0$, these transitions can only take place between states of equal C_z (red and green symbols online, transitions with the

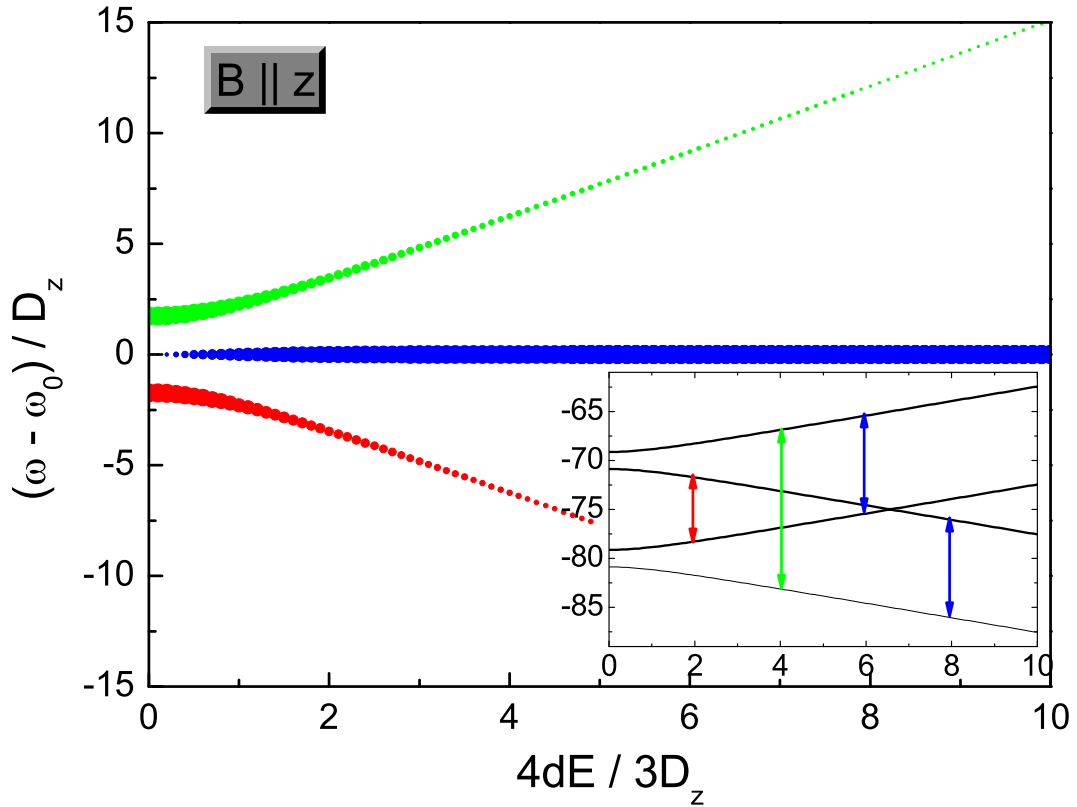


Figure 5.6: (color online) Energy (ω) of the ESR transitions in a triangle of $s = 1/2$ spins as a function of the applied electric field \mathbf{E} that lies in the molecule's plane, so that $d|\mathbf{E}| = dE = \mathcal{E}$. The magnetic field is $\mathbf{B} \parallel \hat{z}$ and $\omega_0 = g\mu_B B$, see Eqs. (5.121) and (5.122). The diameter of the circles is proportional to the transition amplitudes $|\langle \alpha | S_x | \alpha' \rangle|$, Eqs. (5.119) and (5.120). Here, $|\alpha\rangle$ are the eigenstates of H in the lowest energy $S = 1/2$ multiplet. Inset: Eigenvalues (in units of D_z) as a function of $\mathcal{E} = d|\mathbf{E}_{\parallel}|$, in units $3D_z/4$.

larger amplitude at low fields, in the figure and in the inset), the electric field mixes states of opposite chirality, thus transferring oscillator strength to two further transitions, whose frequencies are independent of \mathcal{E} (blue symbols online, constant frequency transition in the figure). In the limit $dE \gg D_z$, the eigenstates of the spin Hamiltonian tend to coincide with those of \mathbf{S}_{12}^2 , and ESR transitions take place between states of equal S_{12} . While the eigenstates depend on the in-plane orientation of the electric field, no such dependence is present in the frequencies and oscillator strength of the ESR transitions. Besides, these quantities are independent of the exchange coupling J , and depend on the value of the applied magnetic field only through an additive constant (ω_0).

The dependence of the ESR spectrum on the applied electric field is qualitatively different if the static magnetic field is applied in-plane (e.g., $\mathbf{B} \parallel \hat{\mathbf{x}}$ and the oscillating field oriented along $\hat{\mathbf{z}}$). In this case, the eigenvalues of H_{eff} are:

$$\mu_\sigma^\alpha = \alpha\sigma[\Delta_{\text{SO}}^2 + (\mathcal{E} + \alpha\mathcal{B})^2]^{1/2}, \quad (5.123)$$

where $\sigma = \pm 1/2$ is the value of $\langle S_x \rangle$ in the limit of large magnetic field ($\mathcal{B} \gg \mathcal{E}, \Delta_{\text{SO}}$) and $\alpha = \pm 1$. The corresponding eigenstates read:

$$\begin{aligned} |\mu_\sigma^\alpha\rangle &= \{e^{i\theta}(\Delta_{\text{SO}} + \mu_\sigma^\alpha)[|+1, +1/2\rangle - |-1, -1/2\rangle] \\ &+ (\mathcal{B} + \alpha\mathcal{E})[|+1, -1/2\rangle - |-1, +1/2\rangle]\}/D_\sigma^\alpha, \end{aligned} \quad (5.124)$$

where

$$D_\sigma^\alpha = \sqrt{2}[(\Delta_{\text{SO}} + \mu_\sigma^\alpha)^2 + (\mathcal{B} + \alpha\mathcal{E})^2]^{1/2}. \quad (5.125)$$

The expectation values of the total spin along the magnetic field for each of the above eigenstates are given by the following expressions

$$\langle \mu_\sigma^\alpha | S_x | \mu_\sigma^\alpha \rangle = 2[(\Delta_{\text{SO}} + \mu_\sigma^\alpha)(\mathcal{B} - \alpha\mathcal{E})]/(D_\sigma^\alpha)^2, \quad (5.126)$$

which are independent of the in-plane direction of the electric field. The ESR transitions between such eigenstates induced by a magnetic field that oscillates along the z direction are given by the expressions:

$$\begin{aligned} \langle \mu_\sigma^\alpha | S_z | \mu_{\sigma'}^{-\alpha} \rangle &= \frac{(\Delta_{\text{SO}} + \mu_\sigma^\alpha)(\Delta_{\text{SO}} + \mu_{\sigma'}^{-\alpha}) + (\mathcal{E}^2 - \mathcal{B}^2)}{D^\alpha D^{-\alpha}}, \\ \langle \mu_\sigma^\alpha | S_z | \mu_{\sigma'}^\alpha \rangle &= 0. \end{aligned} \quad (5.127)$$

Therefore, the application of the electric field shifts the energy of the transitions between states of opposite α , thus removing their degeneracy; however, unlike the case $\mathbf{B} \parallel \hat{\mathbf{z}}$, it does not increase the number of allowed transitions.

In the case of tilted magnetic fields, the dependence of the ESR spectrum on the applied electric field presents qualitatively different features (Fig. 5.7). In particular, the spectrum is dominated by two pairs of degenerate transitions that anticross as a function of the electric field. Away from the anticrossing, the transitions with the largest oscillator strength display frequency dependence on the electric field.

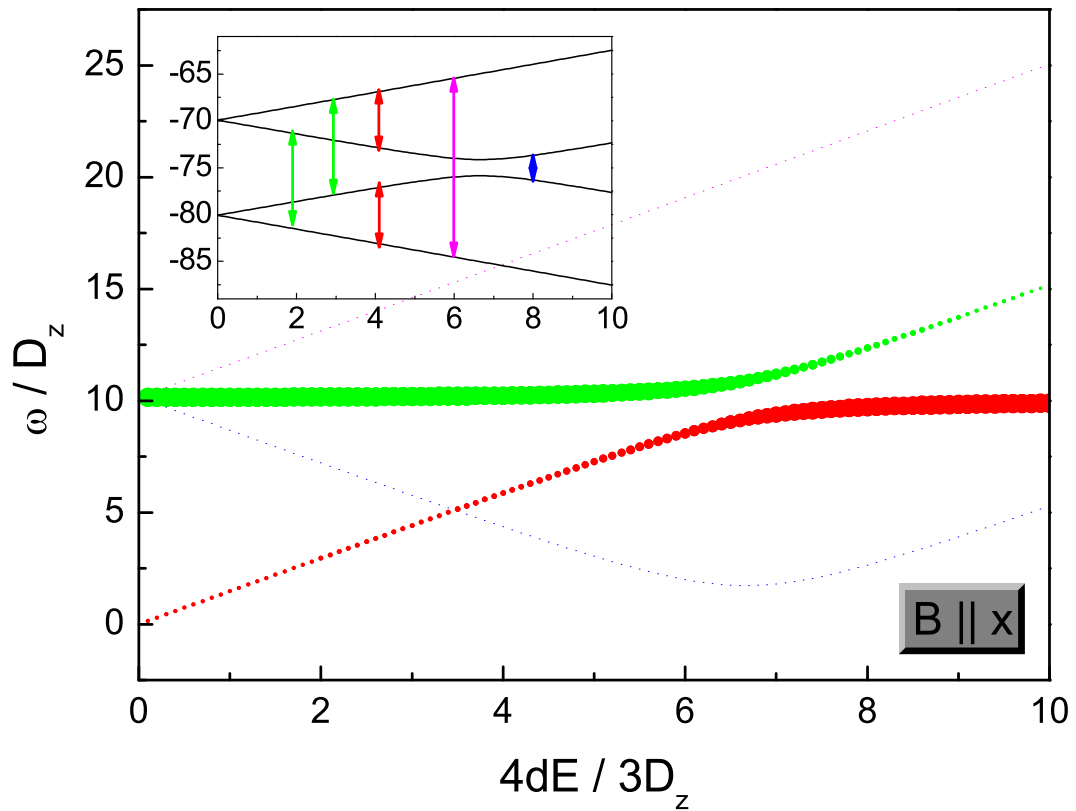


Figure 5.7: Energy (ω) of the ESR transitions in a triangle of $s = 1/2$ spins as a function of the applied in-plane electric field \mathbf{E} , so that $d|\mathbf{E}| = dE = \mathcal{E}$, and in the presence of the in-plane magnetic field $\mathbf{B} \parallel \hat{\mathbf{x}}$. The diameter of the circles is proportional to $|\langle \alpha | S_z | \alpha' \rangle|$, Eqs. (5.121) and (5.122). The states $|\alpha\rangle$ are the eigenstates of H in the lowest $S = 1/2$ multiplet. Inset: Eigenvalues (in units of D_z) as a function of $d|\mathbf{E}_{\parallel}| = \mathcal{E}$, in units $3D_z/4$.

Pentagons of $s = 1/2$ spins

Triangles of $s = 3/2$ spins (not shown here) display the same qualitative behavior as the one discussed above. In contrast, chains including an odd number $N > 3$ spins behave differently. This is mainly due to the fact that the spin-electric coupling δH does not couple directly the four eigenstates of H belonging to the lowest $S = 1/2$ multiplet: such coupling only takes place through mixing with the higher $S = 1/2$ multiplet. As a consequence, the effects of the spin-electric coupling tend to be weaker as compared to the case of the triangle; besides, unlike the above case of the spin triangle, they depend on the exchange coupling J . Illustrative numerical results are shown in Figs. 5.8 and 5.9 for the cases of a perpendicular and in-plane magnetic field, respectively. In the former case, both the frequencies and amplitude of the ESR transitions are hardly affected by the electric field, in the same range of physical parameters considered in Fig. 5.6. In the case of an in-plane magnetic field, instead, a relatively small shift in the transition energies is accompanied by a strong transfer of the oscillator strength, for values of the spin-electric coupling exceeding the Dzyalozhinsky-Moriya coupling constant.

5.4.2 Nuclear magnetic resonance

The spin-electric Hamiltonian δH_0 modifies non uniformly the super-exchange couplings between neighboring spins. This might not affect the projection of the total spin (as in the case $\mathbf{B} \parallel \hat{\mathbf{z}}$, see above), but it generally affects the moment distribution within the spin chain. Such effect can be investigated through experimental techniques that act as local probes in molecular nanomagnets, such as nuclear magnetic resonance (NMR) [176] or x-ray absorption [177]. In NMR, the expectation value of a given spin within the cluster can be inferred through the frequency shift induced on the transitions of the corresponding nucleus. The shift in the nuclear resonance frequency for the nucleus of the i -th magnetic ion is $\Delta\nu = \gamma A \langle s_{z,i} \rangle$, where A is the contact hyperfine interaction constant at the nuclear site. The constant of proportionality A depends on the spin density at the position of the nucleus, and can be extracted from the experiment by considering the polarized ground state $M = S$ at high magnetic fields [176]. As in the case of ESR, the dependence of the NMR spectra on the applied electric field qualitatively depends on the orientation of the static magnetic field \mathbf{B} with respect to the molecule. Unlike the case of ESR, however, it also depends on the in-plane orientation of the electric field, i.e. on the way in which the \mathbf{E} breaks the symmetry of the molecule.

Spin triangles

Let us start by considering a spin $s = 1/2$ triangle, with a magnetic field applied perpendicular to the molecule plane ($\mathbf{B} \parallel \hat{\mathbf{z}}$). In this case, the distribution of the spin projection along z is given by the following expression:

$$\langle \lambda_\sigma^\alpha | s_{i,z} | \lambda_\sigma^\alpha \rangle = \sigma/3 + f_\sigma^\alpha(\mathcal{E}) \cos[\theta + \pi(5/3 - i)], \quad (5.128)$$

where

$$f_\sigma^\alpha(\mathcal{E}) \equiv \frac{4\sigma\mathcal{E}[\Delta_{\text{SO}} + \alpha(\Delta_{\text{SO}}^2 + \mathcal{E}^2)^{1/2}]}{3(D^\alpha)^2}. \quad (5.129)$$

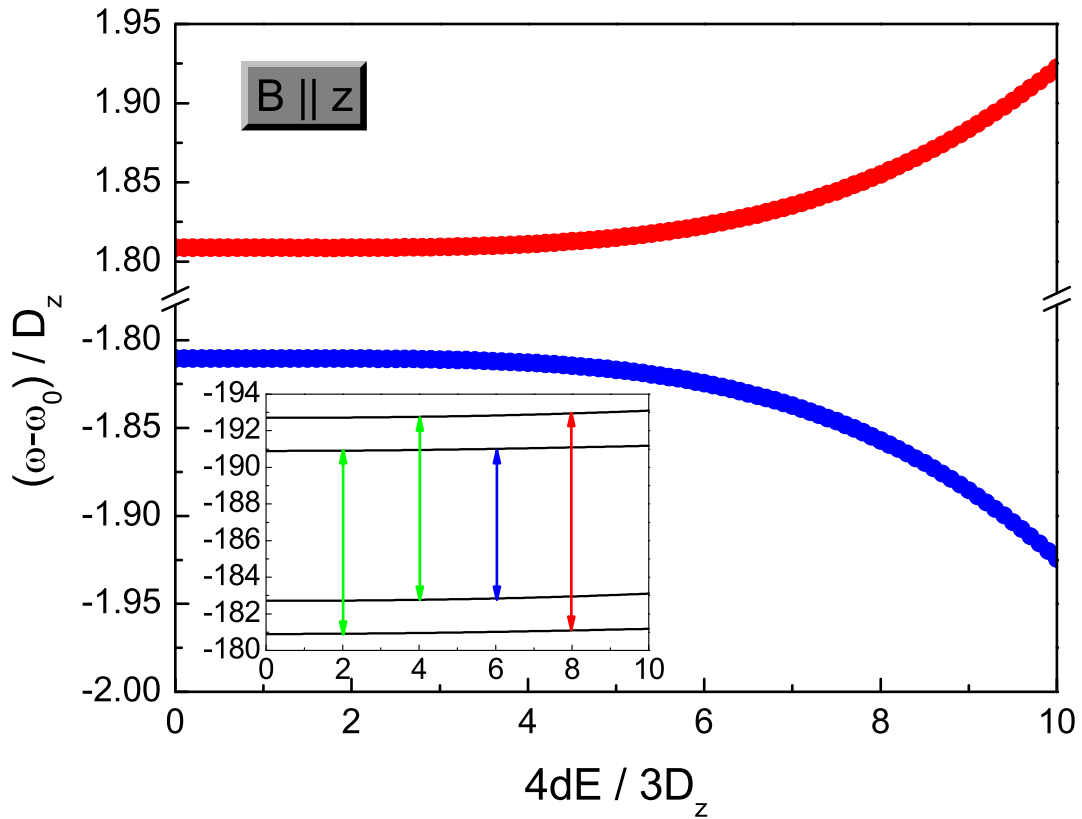


Figure 5.8: Energy (ω) of the ESR transitions in a pentagon of $s = 1/2$ spins as a function of the electric field applied in the molecule's plane $d|\mathbf{E}| = dE = \mathcal{E}$. The Zeeman splitting, $\omega_0 = g\mu_B B$ is set by the magnetic field $\mathbf{B} \parallel \hat{z}$, orthogonal to the molecule's plane. The considered transitions are those between eigenstates ($|\alpha\rangle$) belonging to the $S = 1/2$ multiplet of the spin Hamiltonian (figure inset). Unlike the case of the spin triangle, these are coupled to each other by the electric field via eigenstates belonging to other multiplets, and therefore depends also on the exchange constant J (here $J/\Delta_{SO} = 100$). The diameter of the circles is proportional to $|\langle\alpha|S_x|\alpha'\rangle|$, and therefore to the transition amplitude.

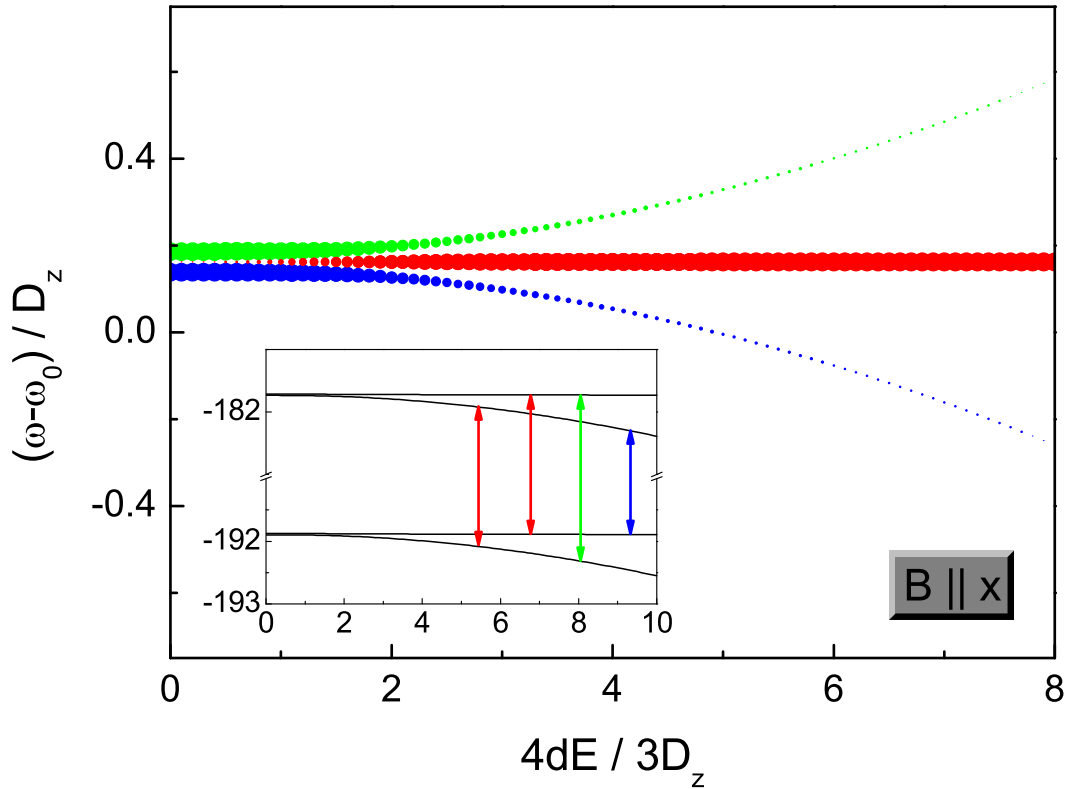


Figure 5.9: Energy (ω) of the ESR transitions in a pentagon of $s = 1/2$ spins as a function of the applied in-plane electric field \mathbf{E} , so that $d|\mathbf{E}| = dE = \mathcal{E}$. The Zeeman splitting is set by an in-plane magnetic field $\mathbf{B} \parallel \hat{\mathbf{x}}$, and $\omega_0 = g\mu_B B$. The considered transitions are those between eigenstates ($|\alpha\rangle$) belonging to the $S = 1/2$ multiplet of the spin Hamiltonian (figure inset). Unlike the case of the spin triangle, these are coupled to each other by the electric field via eigenstates belonging to other multiplets, and therefore depends also on the exchange constant J (here $J/\Delta_{\text{SO}} = 100$). The diameter of the circles is proportional to $|\langle \alpha | S_z | \alpha' \rangle|$, and therefore to the transition amplitude.

Here, the expressions of the eigenstates $|\lambda_\sigma^\alpha\rangle$ and of D^α are given in Subsection 5.4.1. For $E = 0$, the three spins are equivalent and $\langle \lambda_{\pm 1/2}^\alpha | s_{i,z} | \lambda_{\pm 1/2}^\alpha \rangle = \pm 1/6$. If the electric field is finite and oriented along one of the triangle sides (e.g., $\mathbf{E} \parallel \mathbf{r}_{12}$, corresponding to $\theta = 0$), then expectation values along z of spins 1 and 2 undergo opposite shifts, whereas that of spin 3 is left unchanged: $\Delta_{\mathbf{E}} \langle s_{1,z} \rangle = -\Delta_{\mathbf{E}} \langle s_{2,z} \rangle$, where $\Delta_{\mathbf{E}} \langle s_{i,z} \rangle \equiv \langle s_{i,z} \rangle_{\mathbf{E}} - \langle s_{i,z} \rangle_{\mathbf{E}=0}$. This is shown in Fig. 5.10 for the ground state of the spin Hamiltonian, but the above relations hold for any of the four eigenstates $|\lambda_\sigma^\alpha\rangle$ belonging to the $S = 1/2$ quadruplet. If the NMR frequency shifts $\Delta\nu_i$ are larger than the corresponding line widths, the single line at $\mathbf{E} = 0$ splits into three equispaced lines, with intensity ratios 1:1:1. If, instead, the electric field is applied along a symmetry plane of the triangle (e.g., $\mathbf{E} \perp \mathbf{r}_{12}$, corresponding to $\theta = \pi/2$), spins 1 and 2 remain equivalent and their magnetic moments display the same electric field dependence, while the shift of the third one is opposite in sign and twice as large in absolute value: $\Delta_{\mathbf{E}} \langle s_{1,z} \rangle = \Delta_{\mathbf{E}} \langle s_{2,z} \rangle = -\Delta_{\mathbf{E}} \langle s_{3,z} \rangle / 3$. The intensity ratios of the two NMR lines are, correspondingly, 1:2. The expectation values for the remaining eigenstates can be derived by the following equations: $\Delta_{\mathbf{E}} \langle \lambda_{-1/2}^\alpha | s_{i,z} | \lambda_{-1/2}^\alpha \rangle = -\Delta_{\mathbf{E}} \langle \lambda_{+1/2}^\alpha | s_{i,z} | \lambda_{+1/2}^\alpha \rangle$ and $\langle \lambda_\sigma^1 | s_{i,z} | \lambda_\sigma^1 \rangle = -\Delta_{\mathbf{E}} \langle \lambda_\sigma^{-1} | s_{i,z} | \lambda_\sigma^{-1} \rangle$. Therefore, at finite temperature, the shifts in the expectation values of the three spins are given by:

$$\frac{\Delta_{\mathbf{E}} \langle s_{i,z} \rangle}{\Delta_{\mathbf{E}} \langle \lambda_{-1/2}^{+1} | s_{i,z} | \lambda_{-1/2}^{+1} \rangle} = \frac{\sum_\alpha \alpha \cosh\left(\frac{\lambda_{-1/2}^\alpha}{k_B T}\right)}{\sum_\alpha \cosh\left(\frac{\lambda_{-1/2}^\alpha}{k_B T}\right)}. \quad (5.130)$$

If the field is oriented along the molecule plane ($\mathbf{B} \parallel \hat{\mathbf{x}}$), the expectation value of the three spins corresponding to each of the eigenstates are given by the following expressions:

$$\langle \mu_\sigma^\alpha | s_{i,x} | \mu_\sigma^\alpha \rangle = g_\sigma^\alpha(\mathcal{E}) + (1/3) \cos(\theta - 2i\pi/3), \quad (5.131)$$

where

$$g_\sigma^\alpha(\mathcal{E}) \equiv \frac{2(\Delta_{\text{SO}} + \mu_\sigma^\alpha)(\mathcal{B} + \alpha\mathcal{E})}{(D^\alpha)^2}. \quad (5.132)$$

If the magnetic field is parallel to the triangle plane, the in-plane electric field can modify the total spin expectation value along \mathbf{B} . The changes that \mathbf{E} induces in the magnetization distribution within the triangle at zero temperature are less varied than in the previous case (Fig. 5.10). In fact, the magnitude of the $\Delta_{\mathbf{E}} \langle s_{i,z} \rangle$ is much smaller, and all the spins undergo shifts of equal sign and slope. The NMR line, which is splitted into three lines already for $\mathbf{E} = 0$, is rigidly by the applied electric field.

If the triangle is formed by half-integer spins $s > 1/2$, an analogous dependence of the expectation values $\langle s_{i,z} \rangle$ on the electric field is found. As an illustrative example, we report in Fig. 5.11 the case of $s = 3/2$.

Pentagon of $s = 1/2$ spins

Spin chains consisting of an odd number of half-integer spins present analogous behaviors, but also meaningful differences with respect to the case of the spin triangle. In particular, the spin-electric Hamiltonian δH_0 does not couple states belonging to the lowest $S = 1/2$ quadruplet directly (i.e., matrix elements $\langle i | \delta H_0 | j \rangle = 0$ for $i, j \leq 4$); these couplings are

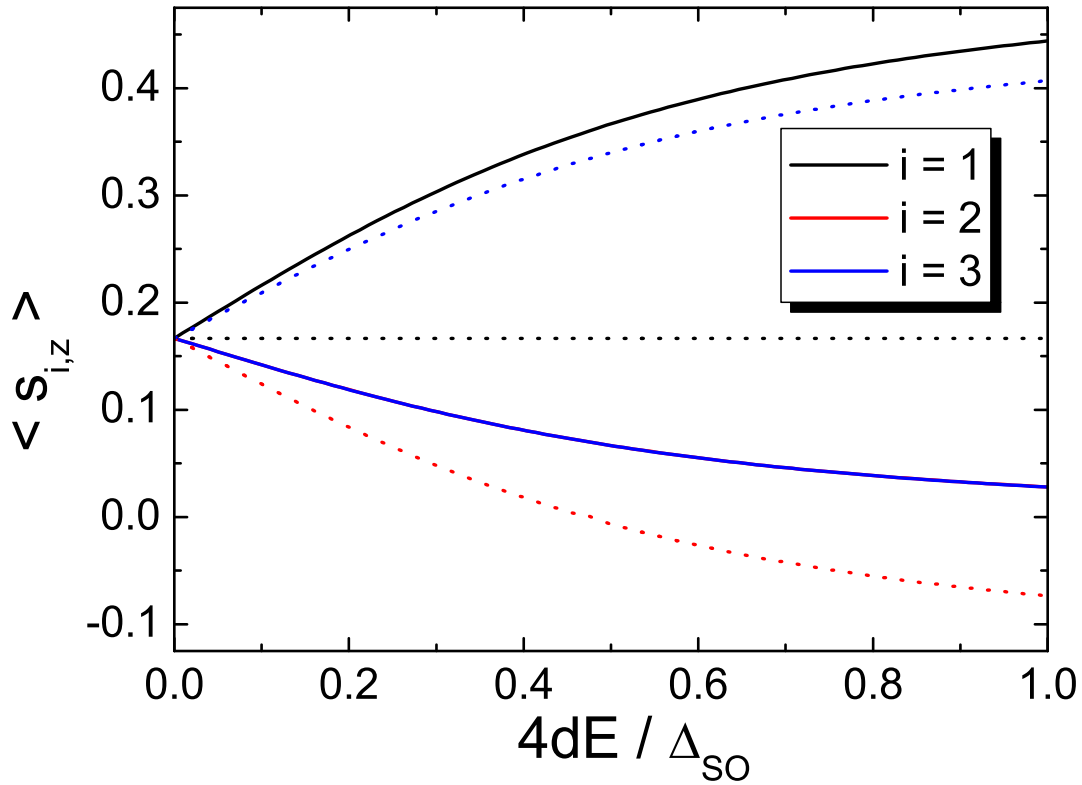


Figure 5.10: (Color online) Expectation values of the z -component of $s = 1/2$ spins in a triangular molecule as a function of applied electric field. The magnetic field is perpendicular to the ring plane ($\mathbf{B} \parallel \hat{\mathbf{z}}$); the electric field is parallel and perpendicular to \mathbf{r}_{12} in the upper and lower panel, respectively. In the electric field along one of the bonds (lower panel), the spins that lie on that bond have the same out-of-plane projections. The shadings (colors online) denote the different spins.

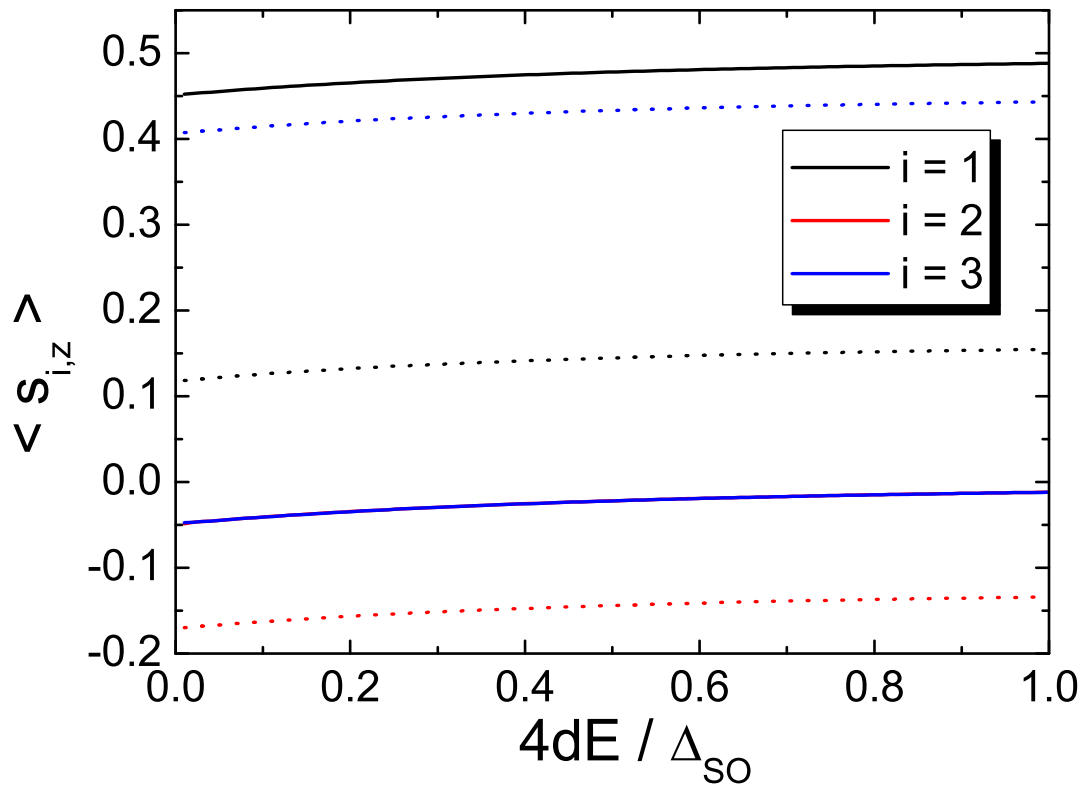


Figure 5.11: (Color online) Expectation values of the z -component of $s = 3/2$ spins in a triangular molecule as a function of applied electric field. The magnetic field is perpendicular to the ring plane ($\mathbf{B} \parallel \hat{\mathbf{z}}$); the electric field is parallel and perpendicular to \mathbf{r}_{12} in the upper and lower panel, respectively. The shadings (colors online) denote the different spins.

mediated by states belonging to higher $S = 1/2$ multiplets, that are higher in energy by a quantity $\sim J$. Therefore, the effect of the electric field tends to be significantly smaller than in the case of a triangle with equal D_z and \mathcal{E} (see Fig. 5.12), and depends also on the exchange coupling J .

5.4.3 Magnetization, Polarization, and Susceptibilities

The spin-electric coupling shifts the energy eigenvalues of the nanomagnet, thus affecting thermodynamic quantities, such as magnetization, polarization and susceptibilities. In the following, we compute these quantities in the case of the $s = 1/2$ spin triangle as a function of the applied magnetic and electric fields. Under the realistic assumption that the exchange splitting J is the largest energy scale in the spin Hamiltonian, and being mainly interested in the low-temperature limit, we restrict ourselves to the $S = 1/2$ quadruplet, and use the effective Hamiltonian H_{eff} in Eq. (5.21).

The eigenenergies of the lowest $S = 1/2$ sector in the presence of electric and magnetic fields are

$$E_{\alpha,\gamma} = \alpha\gamma\sqrt{\mathcal{B}^2 + \Delta_{\text{SO}}^2 + \mathcal{E}^2 + 2\gamma E_0^2}, \quad (5.133)$$

with $\mathcal{B} = \mu_B\sqrt{g_{\parallel}^2 H_{\parallel}^2 + g_{\perp}^2 H_{\perp}^2}$, $E_0 = [(\mathcal{B}_z \Delta_{\text{SO}})^2 + (\mathcal{B}\mathcal{E})^2]^{1/4}$, and $\mathcal{B}_z = \mu_B g_{\parallel} H_{\parallel}$. Note that these energies are the generalization of the ones in the previous section, which were valid for in-plane magnetic field only. The partition function for N identical and non-interacting molecules is $Z = Z_1^N$, with $Z_1 = \sum_{\alpha,\gamma} \exp(-\beta E_{\alpha,\gamma})$ being the partition function for one molecule, and $\beta = 1/(k_B T)$. The free energy reads

$$F \equiv -1/\beta \ln Z = -Nk_B T \ln \left[2 \sum_{\gamma} \cosh(\beta E_{\gamma}) \right], \quad (5.134)$$

with $E_{\gamma} \equiv E_{1/2,\gamma}$. From this, we can derive different thermodynamic quantities like the magnetization $M_i = -\partial F/\partial H_i$, the electric polarization $P_i = -\partial F/\partial E_i$, the heat capacity $C = -\partial/\partial T(\partial \ln(Z)/\partial \beta)$, and the corresponding susceptibilities: $\chi_{E_i E_j} = \partial P_i/\partial E_j = \partial^2 F/\partial E_i \partial E_j$ - the *electric* susceptibility, $\chi_{H_i H_j} = \partial M_i/\partial H_j = \partial^2 F/\partial H_i \partial H_j$ - the *spin* susceptibility, and $\chi_{E_i H_j} = \partial P_i/\partial M_j = \partial^2 F/\partial E_i \partial H_j$ - the *spin-electric* susceptibility. For the electric polarization components P_i we get

$$P_i = \frac{Nd\mathcal{E}_i}{4 \sum_{\gamma=\pm 1} \cosh(\beta E_{\gamma})} \sum_{\gamma=\pm 1} \frac{\sinh(\beta E_{\gamma})}{E_{\gamma}} \times \left(1 + \gamma \frac{\mathcal{B}^2}{E_0^2} \right) (1 - \delta_{i,z}), \quad (5.135)$$

while for the magnetization components M_i we get

$$M_i = \frac{Ng_i \mu_B \mathcal{B}_i}{2 \sum_{\gamma=\pm 1} \cosh(\beta E_{\gamma})} \sum_{\gamma=\pm 1} \frac{\sinh(\beta E_{\gamma})}{E_{\gamma}} \times \left(1 + \gamma \frac{\Delta_{\text{SO}}^2 \delta_{i,z} + \mathcal{E}^2}{E_0^2} \right), \quad (5.136)$$

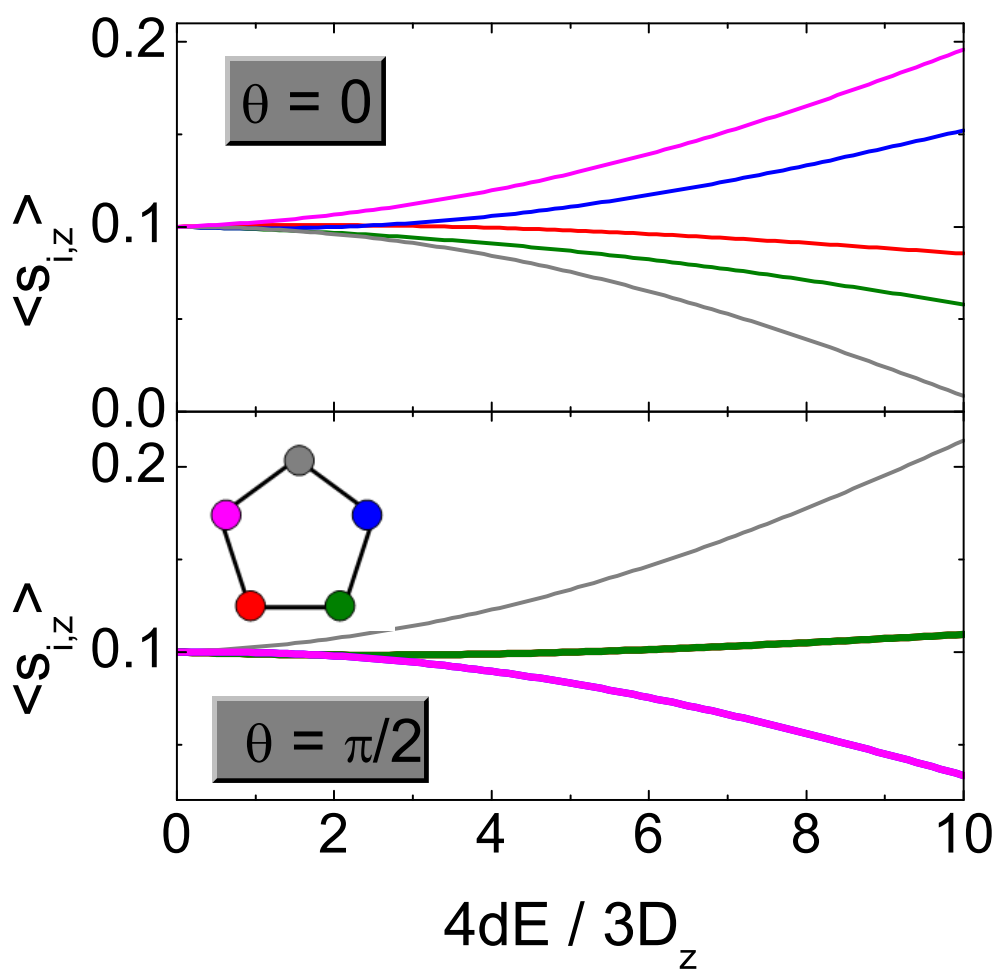


Figure 5.12: (Color online) Expectation values of the z -component of $s = 1/2$ spins in a pentagon as a function of applied electric field. The magnetic field is perpendicular to the ring plane ($\mathbf{B} \parallel \hat{\mathbf{z}}$); the electric field is parallel ($\theta = 0$) and perpendicular ($\theta = \pi/2$) to \mathbf{r}_{12} in the upper and lower panel, respectively. The shadings (colors online) denote the different spins.

where again $i = x, y$. Making use of the above expressions, we can obtain the above defined susceptibilities

$$\begin{aligned} \chi_{E_i E_j} &= \frac{P_i}{E_j} \delta_{ij} - \beta P_i P_j + \frac{N d^4 E_i E_j}{2 \sum_{\gamma=\pm 1} \cosh(\beta E_\gamma)} \left[\sum_{\gamma=\pm 1} \gamma \frac{\mathcal{B}^4 \sinh(\beta E_\gamma)}{E_0^6 E_\gamma} \right. \\ &\quad \left. + \frac{\beta E_\gamma \cosh(\beta E_\gamma) - \sinh(\beta E_\gamma)}{2 E_\gamma^3} \left(1 + \gamma \frac{\mathcal{B}^2}{E_0^2} \right)^2 \right] = \chi_{E_j E_i} \end{aligned} \quad (5.137)$$

$$\begin{aligned} \chi_{B_i B_j} &= \frac{M_i}{B_j} \delta_{ij} - \beta M_i M_j + \frac{N g_i^2 g_j^2 B_i B_j}{2 \sum_{\gamma=\pm 1} \cosh(\beta E_\gamma)} \sum_{\gamma=\pm 1} \left[\frac{\beta E_\gamma \cosh(\beta E_\gamma) - \sinh(\beta E_\gamma)}{2 E_\gamma^3} \right. \\ &\quad \times \left(1 + \gamma \frac{\Delta_{\text{SO}}^2 \delta_{i,z} + \mathcal{E}^2}{E_0^2} \right) \left(1 + \gamma \frac{\Delta_{\text{SO}}^2 \delta_{j,z} + \mathcal{E}^2}{E_0^2} \right) \\ &\quad \left. + \frac{(\Delta_{\text{SO}}^2 \delta_{i,z} + \mathcal{E}^2)(\Delta_{\text{SO}}^2 \delta_{j,z} + \mathcal{E}^2) \sinh(\beta E_\gamma)}{E_0^6 E_\gamma} \right] = \chi_{B_j B_i} \end{aligned} \quad (5.138)$$

$$\begin{aligned} \chi_{B_i E_j} &= -\beta M_i P_j + \frac{N g_i^2 d^2 B_i E_j}{2 \sum_{\gamma=\pm 1} \cosh(\beta E_\gamma)} \sum_{\gamma=\pm 1} \left[\frac{\beta E_\gamma \cosh(\beta E_\gamma) - \sinh(\beta E_\gamma)}{2 E_\gamma^3} \right. \\ &\quad \times \left(1 + \gamma \frac{\Delta_{\text{SO}}^2 \delta_{i,z} + \mathcal{E}^2}{E_0^2} \right) \left(1 + \gamma \frac{\mathcal{B}^2}{E_0^2} \right) \\ &\quad \left. + \gamma \frac{(\Delta_{\text{SO}}^2 \delta_{i,z} + \mathcal{E}^2)(\Delta_{\text{SO}}^2 \delta_{j,z} + \mathcal{E}^2) \sinh(\beta E_\gamma)}{E_0^6 E_\gamma} \right] (1 - \delta_{j,z}) = \chi_{E_j B_i}. \end{aligned} \quad (5.139)$$

The polarization \mathbf{P} , magnetization \mathbf{M} , and susceptibilities χ , Eq. (5.135) – Eq. (5.139), all depend on the spin-electric coupling constant d . In the following, we analyze the details of this dependence and identify the conditions suitable for extracting the value of d from the measurable quantities.

Polarization and magnetization

The in-plane polarization of the molecule as a function of the magnetic field is illustrated in Fig. 5.13 and Fig. 5.14. The polarization is a growing function of the magnetic field strength, and it gets reduced by the normal component of the field.

The low-temperature, $k_B T \ll \Delta_{\text{SO}}$, thermodynamic properties of a molecule with spin-electric coupling show a simple dependence on the strength of external electric and magnetic fields in the special cases of in-plane and out-of plane magnetic field. We focus only on effects in leading orders in electric field under the realistic assumption that the electric dipole splitting is small compared to the SO splitting, i.e. $\mathcal{E} \ll \Delta_{\text{SO}}$. Also, we analyze two limiting cases: (i) $k_B T \ll \mathcal{E}$, i.e. low-temperature regime, and (ii) $k_B T \gg \mathcal{E}$, i.e. high temperature regime. However, we assume all temperatures (in both regimes) to satisfy $k_B T \ll \Delta_{\text{SO}}$ so that the spin-orbit split levels are well resolved. In the first case (i), we

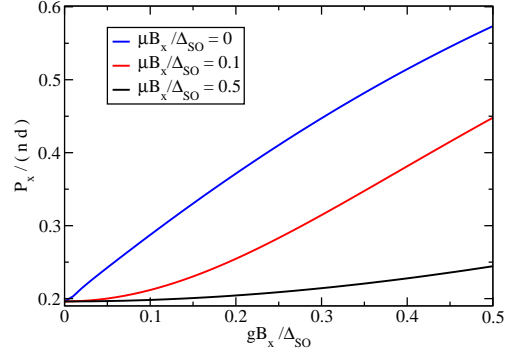


Figure 5.13: Electric polarization P_x (x component) in Eq. (5.135) as a function of the magnetic field in x direction. The three lines correspond to various values of an additional external electric field in the z direction. The plot is for the temperature $k_B T = 0.001 \Delta_{SO}$, and the electric field $dE_x = 0.1 \Delta_{SO}$.

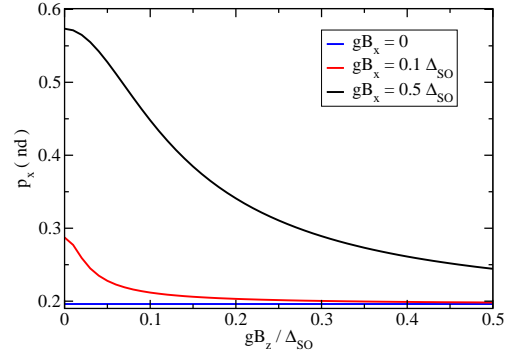


Figure 5.14: Electric polarization P_x (x component) in Eq. (5.135) as a function of the magnetic field in z direction. The three lines correspond to various values of the external magnetic field in the x direction. The plot is for the temperature $k_B T = 0.001 \Delta_{SO}$, and the electric field $dE_x = 0.1 \Delta_{SO}$.

obtain for the polarization

$$P_i \simeq \begin{cases} \frac{nd\mathcal{E}_i\mathcal{B}}{4\mathcal{E}\Delta_{\mathcal{B}}} & \text{for } \mathcal{E} \ll \mathcal{B} \\ \frac{nd\Delta_{SO}^2\mathcal{E}_i}{4\Delta_{\mathcal{B}}^3} & \text{for } \mathcal{E} \gg \mathcal{B}, \end{cases} \quad (5.140)$$

while for the second situation (ii) we obtain

$$P_i \simeq \frac{nd\Delta_{SO}^2\mathcal{E}_i}{4\Delta_{\mathcal{B}}^3} \left(1 + \frac{\mathcal{B}^2}{\Delta_{SO}^2} \beta \Delta_{\mathcal{B}} \right), \quad (5.141)$$

with $\Delta_{\mathcal{B}} = \sqrt{\mathcal{B}^2 + \Delta_{SO}^2}$ and $n = N/V$ the density of molecules in the crystal. We see that, for low temperatures, the electric polarization P_i ranges from being independent of the

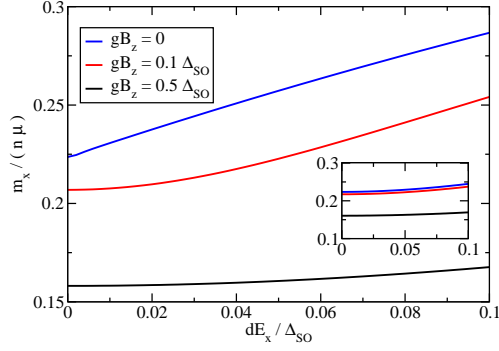


Figure 5.15: In-plane magnetization M_x in x -direction in Eq. (5.136) as a function of the electric field E_x in x -direction. The three lines correspond to a fixed value of an additional magnetic field in the z -direction. The assumed temperature is $k_B T = 0.001 \Delta_{\text{SO}}$, while in the inset it is at higher temperature $k_B T = 0.1 \Delta_{\text{SO}}$.

magnitude of the electric field ($\mathcal{E} \ll \mathcal{B}$), to a linear dependence on the applied electric field E for large fields ($\mathcal{E} \gg \mathcal{B}$). Also, the polarization is strongly dependent on the magnetic field (linear in B) for low E -fields, thus implying strong magneto-electric response.

We now switch to the other special case, namely when the external magnetic field is applied perpendicularly to the spin triangles. The electric polarization now reads

$$P_i = \frac{nd\mathcal{E}_i}{4\Delta_{\mathcal{E}}} \tanh(\beta\Delta_{\mathcal{E}}), \quad (5.142)$$

with $\Delta_{\mathcal{E}} = \sqrt{\Delta_{\text{SO}}^2 + \mathcal{E}^2}$. The polarization P_i does not depend on the magnetic field B , and there are no spin-electric effects present for this particular case.

Our results suggest that the spin-electric coupling can be detected by measuring the polarization of the crystal of triangular single molecule antiferromagnets that lie in parallel planes in the in-plane electric and magnetic fields.

The out-of plane component M_z of the molecule's magnetization is rather insensitive to the electric fields, since any effect of the applied in-plane electric field has to compete with the spin-orbit coupling induced zero-field splitting Δ_{SO} . Since we expect to find weak coupling to electric field and small coupling constant d , it would require very strong electric field to achieve the regime $d|\mathbf{E}| \sim \Delta_{\text{SO}}$. The in-plane components of magnetization M_x, M_y , on the other hand show clear dependence on electric fields, Fig. 5.15. At low magnetic fields the in-plane component of polarization appears and grows with the strength of in-plane electric fields. However, the electric field dependence becomes less pronounced when an additional magnetic field is applied normal to the triangle's plane.

In the dependence of the magnetization on electric fields, and for the case of an in-plane magnetic field, we find the same two main regimes as in the study of the polarization: $\mathcal{E} \gg k_B T$ (i) and $\mathcal{E} \ll k_B T$ (ii). In the first case (i) we obtain

$$M_i \simeq \frac{ng_i\mu_B\mathcal{B}_i}{4\Delta_{\mathcal{B}}} \left(1 + \frac{\mathcal{E}\Delta_{\text{SO}}^2}{\mathcal{B}\Delta_{\mathcal{B}}^2} \right), \quad (5.143)$$

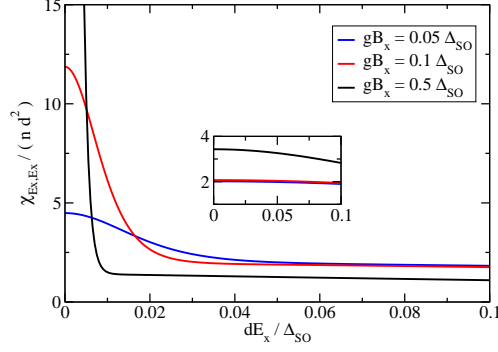


Figure 5.16: Electric susceptibility (xx component), Eq. (5.137), as a function of the electric field in x direction. The three lines correspond to various values of the external magnetic field in the x direction. The plot is for the temperature $k_B T = 0.001 \Delta_{SO}$. In the inset, the same quantity is plotted at a higher temperature, $k_B T = 0.1 \Delta_{SO}$.

while for the second case (ii) we get

$$M_i = \frac{ng_{\perp}\mu_B \mathcal{B}_i}{4\Delta_B} \left[1 - \frac{3\mathcal{E}^2 \Delta_{SO}^2}{2\Delta_B^4} \left(1 - \frac{\beta \Delta_B}{3} \right) \right]. \quad (5.144)$$

The magnetization shows a strong dependence on the electric field E , especially for $\mathcal{E} \gg \mathcal{B}$ where this is linear in E -field. For low electric fields, however, the magnetization shows only a weak dependence on the electric field, both at low and high temperatures.

For the magnetization (along z) in the presence of a perpendicular (also along z) magnetic field we obtain

$$M_z = \frac{ng_z \mu_B}{4} \tanh(\beta \mathcal{B}), \quad (5.145)$$

which is manifestly independent of the spin-electric coupling constant d .

Susceptibilities

The effects of spin-electric coupling on the polarization of a molecule show up in the electric susceptibility and the spin-electric susceptibility. In Fig. 5.16 and Fig. 5.17, we plot the xx and xy component of the electric susceptibility tensor as a function of electric field for various strengths and orientations of an additional magnetic field. Both susceptibilities show a high peak in the region of weak electric fields that is suppressed by in-plane magnetic fields. The peaks are pronounced at low temperatures, and vanish as the temperature exceeds the splitting of the two lowest-energy levels, $k_B T \gg d|\mathbf{E}|_{\parallel}$.

In the case of in-plane magnetic field, and weak coupling to the electric field $d|\mathbf{E}| \ll \Delta_{SO}$, we can calculate the electric $\chi_{E_i E_j}$ and spin-electric $\chi_{E_i H_j}$ susceptibilities in the two limiting cases (i) and (ii) defined above, with $i = x, y$. For the electric susceptibility we obtain:

$$\chi_{E_i E_j} \simeq \begin{cases} \frac{nd^2 \mathcal{B} (\mathcal{E}^2 \delta_{ij} - \mathcal{E}_i \mathcal{E}_j)}{4\mathcal{E}^3 \Delta_B} & \text{for } \mathcal{E} \ll \mathcal{B} \\ \frac{nd^2 \Delta_{SO}^2 \delta_{ij}}{4\Delta_B^3} & \text{for } \mathcal{E} \gg \mathcal{B} \end{cases} \quad (5.146)$$

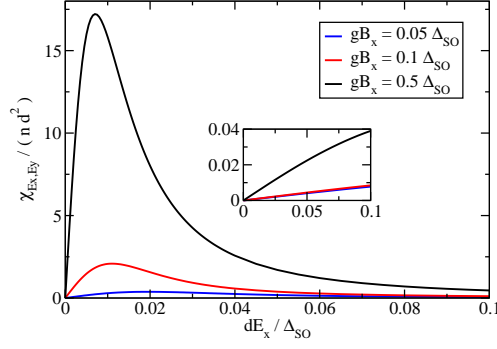


Figure 5.17: Electric susceptibility (xy component), Eq. (5.137), as a function of the electric field in x direction. The three lines correspond to various values of the external magnetic field in the x direction. The plot is for the temperature $k_B T = 0.001 \Delta_{SO}$. In the inset the same quantity is plotted at a higher temperature $k_B T = 0.1 \Delta_{SO}$.

in the first case (i), and

$$\chi_{E_i E_j} \simeq \frac{nd\Delta_{SO}^2 \delta_{ij}}{4\Delta_B^3} \left(1 + \frac{\mathcal{B}^2}{\Delta_{SO}^2} \beta \Delta_B \right). \quad (5.147)$$

in the second case (ii). We see that for low E -fields, the electric susceptibility $\chi_{E_i E_j}$ depends strongly on the applied electric field, and even vanishes if the field is applied, say, along x or y directions. For large E -fields instead, the electric susceptibility becomes independent of the electric field itself and, for low magnetic fields (i.e., for $\mathcal{B} \ll \Delta_{SO}$) this reduces to a constant value $\chi_{E_i E_j} = \delta_{ij} n d^2 / 4$. At finite (large) temperatures the electric susceptibility is still independent of the electric field, but it is enhanced by thermal effects $\sim 1/T$.

For the electric susceptibilities $\chi_{E_i E_j}$ in perpendicular magnetic field, we obtain

$$\chi_{E_i E_j} = \frac{nd^2}{4\Delta_{\mathcal{E}}} \left(\delta_{ij} - \frac{\mathcal{E}_i \mathcal{E}_j}{\Delta_{\mathcal{E}}} \right), \quad (5.148)$$

where we assumed $\Delta_{SO} \gg k_B T$, as in the previous Section. As expected, there is no dependence of $\chi_{E_i E_j}$ on the B -field, and for vanishing electric field the electric susceptibility reduces to a constant $\chi_{E_i E_j} = n d^2 / 4 \Delta_{SO}$.

The quantity of most interest in the present spin system is the spin-electric susceptibility $\chi_{E_i B_j}$, i.e. the magnetic response (electric response) in electric fields (magnetic fields). The nonzero spin-electric susceptibility allows for the electric control of magnetization and magnetic control of polarization in the crystals of triangular MNs, even in the case when the coupling between the molecules is negligible. In addition, $\chi_{E_i B_j}$ is nonzero only in the presence of spin-electric coupling, i.e. when $d \neq 0$.

The spin-electric susceptibility shows a characteristic peak in weak electric fields which vanishes in an external magnetic field, see Figs. 5.18 and 5.19. The peak in the diagonal xx -component, $\chi_{E_x E_x}$, moves towards the higher electric fields and broadens as the magnetic field B_x increases. The peak in the off-diagonal component $\chi_{E_x B_z}$, on the other hand, shifts towards the lower electric fields, and narrows as the in-plane magnetic field increases. Both peaks disappear at high temperatures, $k_B T \gg \Delta_{SO}$.

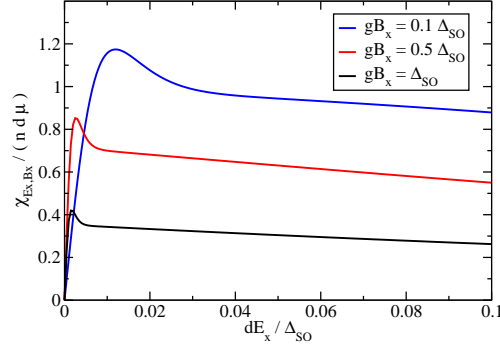


Figure 5.18: Linear magnetoelectric tensor (xx component) in Eq. (5.139) as a function of the electric field in x direction. The three lines correspond to various values of the external magnetic field in the x direction. The plot is for the temperature $k_B T = 0.001 \Delta_{SO}$.

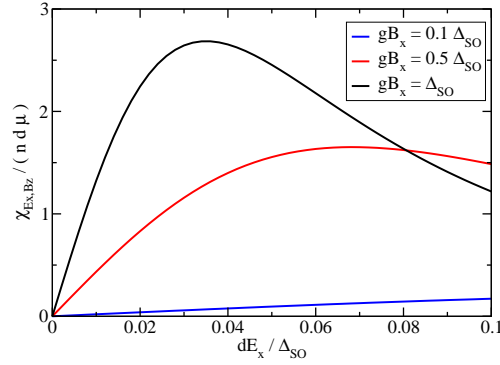


Figure 5.19: Linear magnetoelectric tensor (xz component) in Eq. (5.139) as a function of the electric field in x direction. The three lines correspond to various values of the external magnetic field in the x direction. The plot is for the temperature $k_B T = 0.001 \Delta_{SO}$.

For in-plane magnetic fields and weak spin-electric coupling the spin-electric susceptibility $\chi_{E_i B_j}$ is

$$\chi_{E_i B_j} \simeq \frac{ndg_j \mu_B \mathcal{E}_i \mathcal{B}_j \Delta_{SO}^2}{4\mathcal{E}\mathcal{B}\Delta_B^3} \quad (5.149)$$

for the low temperature case (i), while for the second case (ii) we obtain

$$\chi_{E_i B_j} \simeq -\frac{3n\Delta_{SO}^2 dg_j \mu_B \mathcal{E}_i \mathcal{B}_j}{4\Delta_B^5} \left(1 - \frac{\beta\Delta_B}{3}\right). \quad (5.150)$$

By inspecting the above expression, we can infer that for low temperatures and low E -fields the spin-electric susceptibility shows no dependence on the absolute value of the electric field E and only a weak dependence on the applied magnetic field B . Moreover, when both fields are applied along one special direction, say, along x , and assuming also $\mathcal{B} \ll \Delta_{SO}$, the spin-electric susceptibility becomes $\chi_{E_x B_x} = ndg_i \mu_B / 4\Delta_{SO}$, i.e. it reaches a constant

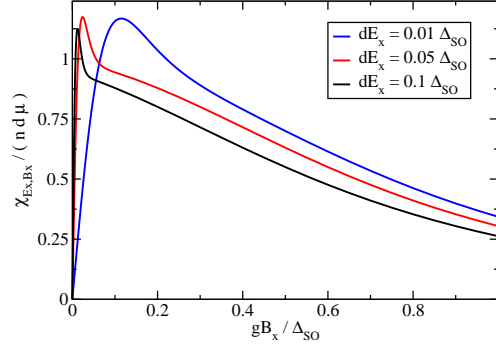


Figure 5.20: Linear magnetoelectric tensor (xx component) in Eq. (5.139) as a function of the magnetic field in x direction. The three lines correspond to various values of the external electric field in the x direction. The plot is for the temperature $k_B T = 0.001 \Delta_{\text{SO}}$.

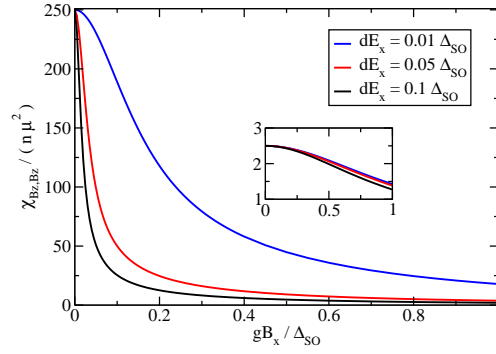


Figure 5.21: Magnetic susceptibility (zz component) in Eq. (5.138) as a function of the magnetic field in x direction. The three lines correspond to various values of the external electric field in the x direction. The plot is for the temperature $k_B T = 0.001 \Delta_{\text{SO}}$. The inset represents the same quantity at a higher temperature $k_B T = 0.1 \Delta_{\text{SO}}$.

value. The finite temperature expression shows that the spin-electric response is reduced, as opposed to the electric response where temperature increases the response. Thus, for strong spin-electric response one should probe the spin system at low temperatures ($k_B T \ll \Delta_{\text{SO}}$).

The diagonal out-of-plane component of the magnetic susceptibility, χ_{B_z, B_z} , in the presence of an external magnetic field in the x direction decays strongly in the applied electric field along the x direction, Fig. 5.21. In electric fields, the χ_{B_x, B_x} component shows a peak that is reduced by the application of the magnetic field in x direction, Fig. 5.22.

We can derive the magnetic susceptibilities in the two regimes. In the first case (i) we obtain (assuming now only linear effects in E -field):

$$\begin{aligned} \chi_{B_i B_j} &= \frac{ng_1^2 \mu_B^2}{2\Delta_B} \left[\delta_{ij} - \frac{\mathcal{B}_i \mathcal{B}_j}{\Delta_B^2} \right. \\ &\quad \left. + \frac{\mathcal{E} \Delta_{\text{SO}}^2}{B \Delta_B^2} \left(\delta_{ij} - \frac{(3B^2 + \Delta_B^2) \mathcal{B}_i \mathcal{B}_j}{B^2 \Delta_B^2} \right) \right], \end{aligned} \quad (5.151)$$

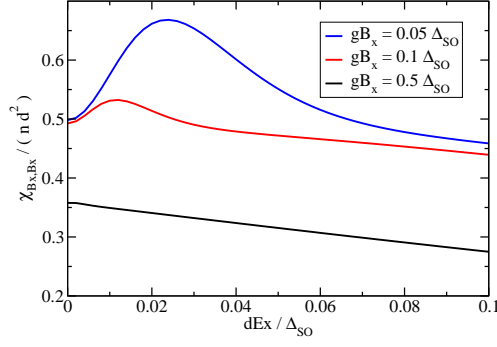


Figure 5.22: Magnetic susceptibility (xx component), Eq. (5.138) as a function of the electric field in x direction. The three lines correspond to various values of the additional magnetic field in the z direction. The plot is for the temperature $k_B T = 0.001 \Delta_{\text{SO}}$.

with $i, j = x, y$, while

$$\chi_{B_z B_z} = \frac{ng_z^2 \mu_B^2 \Delta_{\text{SO}}^2}{2\Delta_B \mathcal{B}\mathcal{E}}, \quad (5.152)$$

for $\mathcal{B}_z \Delta_{\text{SO}} \ll \mathcal{B}\mathcal{E}$. At low temperatures the in-plane magnetic susceptibility shows a linear dependence on the applied electric field E , thus allowing for a simple estimate of the electric dipole parameter d from magnetic measurements. Note that for strong electric fields ($\mathcal{E} \gg \mathcal{B}$), the magnetic susceptibility can vanish, since the magnetization does not depend on the magnetic field anymore. However, such a regime would not help to identify the electric dipole coupling strength d from susceptibility measurements directly. The perpendicular magnetic susceptibility shows a strong electric field dependence $\chi_{B_z B_z} \sim \mathcal{E}^{-1}$ and can be used as an efficient probe for extracting the electric dipole parameter d . In the second case (ii) we obtain

$$\begin{aligned} \chi_{B_i B_j} &= \frac{ng_{\perp}^2 \mu_B^2}{2\Delta_B} \left[\delta_{ij} - \frac{\mathcal{B}_i \mathcal{B}_j}{\Delta_B^2} - \frac{\mathcal{E}^2 \Delta_{\text{SO}}^2}{\Delta_B^4} \right. \\ &\times \left. \left(\frac{3}{2} \left(\delta_{ij} + \frac{\mathcal{B}_i \mathcal{B}_j}{\Delta_B^2} \right) - \beta \Delta_B \left(\delta_{ij} + \frac{4\mathcal{B}_i \mathcal{B}_j}{\Delta_B^2} \right) \right) \right], \end{aligned} \quad (5.153)$$

when $i, j = x, y$, and

$$\chi_{B_z B_z} = \frac{ng_z^2 \mu_B^2 \mathcal{B}^2}{2\Delta_B^3} \left(1 + \beta \Delta_B \frac{\Delta_{\text{SO}}^2}{\mathcal{B}^2} \right). \quad (5.154)$$

The magnetic response increases with temperature. Also, in this limit the dependence of the magnetic susceptibility on the applied electric field is rather weak ($\chi_{B_i B_j}(\mathcal{E}) \sim \mathcal{E}^2$), thus this regime is also not suitable for observing spin-electric effects.

For the magnetic susceptibility in the perpendicular magnetic field we find

$$\chi_{B_z B_z} = \frac{\beta ng_z^2 \mu_B^2}{4} \text{sech}(\beta \mathcal{B}), \quad (5.155)$$

while for the in-plane magnetic susceptibility $\chi_{B_x(y)B_x(y)}$ we obtain

$$\begin{aligned} \chi_{B_x(y)B_x(y)} &= \frac{ng_z^2\mu_B^2\Delta_{\text{SO}}}{2(\mathcal{B}^2 - \Delta_{\text{SO}}^2)} \\ &\times \left[\frac{\mathcal{B}}{\Delta_{\text{SO}}} \left(1 - \frac{\mathcal{E}^2}{\mathcal{B}^2} \right) \tanh(\beta\mathcal{B}) - 1 \right], \end{aligned} \quad (5.156)$$

in the limit $\mathcal{B}, k_B T \ll \Delta_{\text{SO}}$. We mention that for B perpendicular to the molecular plane there is no electric field E (magnetic field B) dependence of the magnetization M_i (electric polarization P_i). Thus, in order to see spin-electric effects one needs to apply magnetic fields which have non-zero in-plane components.

5.4.4 Heat capacity

Next we investigate the dependence of the heat capacity on the applied electric and magnetic fields in different regimes. The heat capacity is defined as $C = -\partial/\partial T(\partial \ln(Z)/\partial\beta)$, so that we obtain

$$C = \frac{Nk_B\beta^2}{4} \sum_{p=\pm 1} \frac{(E_1 + pE_{-1})^2}{\cosh^2 \left[\frac{\beta(E_1 + pE_{-1})}{2} \right]}. \quad (5.157)$$

We consider the cases of perpendicular B-field and in-plane B-field in the limit $\Delta_{\text{SO}} \gg k_B T$. In the first case, i.e. for $B \parallel z$ we obtain

$$C \simeq Nk_B\beta^2 \begin{cases} \Delta_{\mathcal{E}}^2 e^{-2\beta\Delta_{\text{SO}}} + \mathcal{B}^2 e^{-2\beta\mathcal{B}}, & \mathcal{B} \gg k_B T \\ \Delta_{\mathcal{E}}^2 e^{-2\beta\Delta_{\text{SO}}} + \frac{\mathcal{B}^2}{4}, & \mathcal{B} \ll k_B T. \end{cases} \quad (5.158)$$

The heat capacity C shows a quadratic dependence on the applied electric field for the entire range of E-field strengths. On the other hand, the magnetic field dependence of C is non-monotonic, and shows a maximum for some finite B-field strength $\mathcal{B}_{\text{max}} \simeq k_B T$. In the second situation, i.e. for $B \perp z$ we get

$$C \simeq Nk_B\beta^2 \begin{cases} \frac{\mathcal{B}^2 \mathcal{E}^2}{\Delta_{\mathcal{B}}^2} e^{-2\frac{\beta\mathcal{B}\mathcal{E}}{\Delta_{\mathcal{B}}}} + \Delta_{\mathcal{B}}^2 e^{-2\beta\Delta_{\mathcal{B}}}, & \mathcal{E} \gg k_B T \\ \frac{\mathcal{B}^2 \mathcal{E}^2}{4\Delta_{\mathcal{B}}^2}, & \mathcal{E} \ll k_B T. \end{cases} \quad (5.159)$$

As in the previous case, the dependence of the heat-capacity C is linear in E-field for low E-fields. However, for large E-fields the dependence is non-monotonic and thus shows a maximum for some finite electric field strength $\mathcal{E}_{\text{max}} \simeq k_B T$. Note that in this case also the dependence on the magnetic field is non-monotonic, and thus we obtain a second maximum for $\mathcal{B}_{\text{max}} \simeq k_B T$. We can conclude from the above expressions that the strongest dependence of the heat capacity on the electric field is when the magnetic field is applied in-plane, and then it is mostly quadratic.

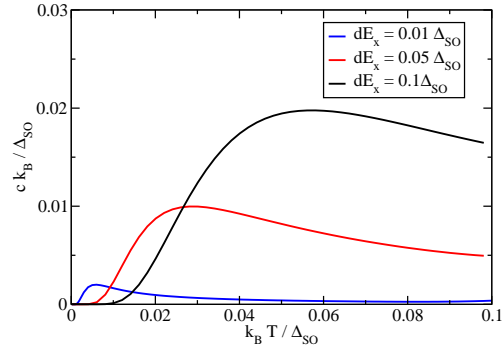


Figure 5.23: Heat capacity, Eq. (5.157), as a function of temperature in various electric fields.

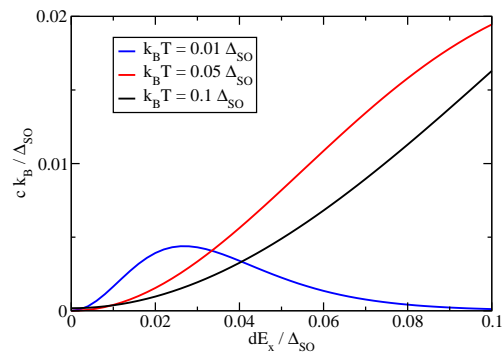


Figure 5.24: Heat capacity, Eq. (5.157), at low temperature as a function of external electric field.

For the derivation of all the thermodynamic quantities presented in the previous sections, we have restricted ourselves to the contributions arising from only the lowest four states, even though the spin system spans eight states in total. This description is valid if the splitting between the energies of $S = 1/2$ and $S = 3/2$ states is much larger than the temperature $k_B T$. This splitting varies strongly with the applied magnetic field, for $\mathcal{B} = 3J/4$ one of the $S = 3/2$ states ($M = -3/2$) crossing the $M = 1/2$ of the $S = 1/2$ states and, even more, for $\mathcal{B} > 3J/2$ the $M = -3/2$ becomes the spin system ground states. Thus, for large magnetic fields our effective description in terms of only the $S = 1/2$ states breaks down and one have to reconsider the previous quantities in this limit.

5.5 Conclusions

Electric fields can be applied at very short spatial and temporal scales which makes them preferable for quantum information processing applications over the more standard magnetic fields. Nanoscale magnets, while displaying rich quantum dynamics, have not yet been shown to respond to electric fields in experiments. We have investigated theoretically the possibility of spin-electric coupling in nanoscale magnets using symmetry analysis, and found

that the spin-electric coupling is possible in antiferromagnetic ground-state manifolds of spin-1/2 and spin-3/2 triangles, as well as in spin-1/2 pentagon. The spin-electric coupling in the triangle can exist even in the absence of spin-orbit coupling, while the coupling in the pentagon requires the spin-orbit interaction in the molecule. We have characterized the form of the spin-electric coupling in all of these molecules and presented the selection rules for the transitions between the spin states induced by electric fields.

While the symmetry can predict the presence or absence of the spin-electric coupling, it can not predict the size of the corresponding coupling constant. In order to find a molecule suitable for electric manipulation, it is necessary to have an estimate of the spin-electric coupling strength. For this purpose, we have described the nanoscale magnets in terms of the Hubbard model, and related the coupling constants of the symmetry-based models to the hopping and on-site energy parameters of the Hubbard model. We have found that the modification of the Hubbard model parameters due to the electric field produces a spin-electric coupling of the same form as predicted by the symmetry analysis. However, within the Hubbard model, the coupling constants have a clear and intuitive meaning in terms of the hopping and on-site energies of the localized electrons. We have also studied the superexchange interaction of the spins on the magnetic centers through the bridge. If we assume that the interaction of the localized spins is a property of the bridge alone, the spin-electric coupling can be calculated by ab-initio analysis of the bridge alone, and not of the entire molecule.

Finally, we analyzed the role of spin-electric coupling in standard experimental setups typically used for the characterization of nanoscale magnets. We find that the spin-electric coupling can be detected in the ESR and NMR spectra that probe the local spins. Also, thermodynamic quantities, like the polarization, magnetization, linear magnetoelectric effect, and the specific heat show signatures of spin-electric coupling in the triangular molecules. Thus, our results set a path toward finding suitable molecules that exhibit spin-electric effects and how they can be identified experimentally.

In this work, we have focused on the spin rings with an odd number of magnetic centers (odd spin rings), whose low-energy spectrum is dominated by frustration effects. The odd spin rings, due to frustration, possess a four-fold degenerate ground state multiplet, which can be split by electric fields. As opposed to the odd spin rings, the ground states of even-spin rings is usually a non-degenerate $S = 0$ state, separated from the higher energy states by a gap of the order of exchange coupling J . Coupling of the electric field to these states can thus proceed only via excited states, and the coupling strength is reduced by $d|\mathbf{E}|/J$. Similarly, in lower-symmetry odd-spin rings, the ground state multiplet consists of an $S = 1/2$ Kramers doublet, which can not be split by electric fields, i.e. there is no spin-electric effect in zero magnetic field. Therefore, the odd spin rings seem to be the most suitable candidates for observing the spin-electric coupling and using it to control the spins.

Appendix A

$J_{\tilde{x},\tilde{y}}$ for arbitrary B -fields

In this Appendix we give explicit formulas for the couplings $J_{\tilde{x},\tilde{y}}$ for an arbitrary magnetic field orientation $\mathbf{B} = B(\cos \Phi \sin \theta, \sin \Phi \sin \theta, \cos \theta)$ and for both Rashba and Dresselhaus spin-orbit couplings present. These are obtained by diagonalizing the tensor $\overline{\overline{M}}$, which leads to

$$J_{\tilde{x},\tilde{y}} = \frac{1}{2} [(C_1 + C_2) \cos^2 \theta + (C_1 \cos^2 \phi + C_2 \sin^2 \phi - C_3 \sin 2\phi) \sin^2 \theta] \pm \frac{\sqrt{((C_1 + C_2) \cos^2 \theta + \sin^2 \theta (C_1 \cos^2 \phi + C_2 \sin^2 \phi - C_3 \sin 2\phi))^2 - 4(C_1 C_2 - C_3^2) \cos^2 \theta}}{-4(C_1 C_2 - C_3^2) \cos^2 \theta}, \quad (\text{A.1})$$

with $\phi = \Phi - \gamma$ (the angle γ is defined after Eq. (2.9)). The functions C_i ($i = 1, 2, 3$) can be expressed in terms of $C_{a_1 b_2} = \langle 0 | [L_d^{-1} a_1, b_2] | 0 \rangle$, $a, b = x, y$, *i.e.*

$$C_1 = \frac{1}{\lambda_-^2} (\sin^2 \gamma C_{x_1 x_2} + \cos^2 \gamma C_{y_1 y_2} + \sin 2\gamma C_{x_1 y_2}) \quad (\text{A.2})$$

$$C_2 = \frac{1}{\lambda_+^2} (\cos^2 \gamma C_{x_1 x_2} + \sin^2 \gamma C_{y_1 y_2} - \sin 2\gamma C_{x_1 y_2}) \quad (\text{A.3})$$

$$C_3 = \frac{1}{2 \lambda_+ \lambda_-} (\sin 2\gamma (C_{x_1 x_2} - C_{y_1 y_2}) - \cos 2\gamma C_{x_1 y_2}). \quad (\text{A.4})$$

These functions can be identified very easily from our formulas derived in the paper. For example, for the case considered in Eq. (2.28) (weak Coulomb coupling regime) we get

$$C_{x_1 x_2} = \frac{\Delta E_C^x}{m^* \lambda^2 \omega_0^4}, \quad C_{y_1 y_2} = \frac{\Delta E_C^y}{m^* \lambda^2 \omega_0^4}, \quad C_{x_1 y_2} = 0. \quad (\text{A.5})$$

Appendix B

Displacement and stress tensor

In this Appendix we give explicit formulas for the displacement $\mathbf{u}(\mathbf{r})$ and stress $\mathbf{t}(\mathbf{r})$ vectors, respectively. We can write the displacement vector $\mathbf{u}(\mathbf{r}) = (u_r, u_\phi, u_z)$ from Eq. (3.40) in components

$$u_k(\mathbf{r}, t) = \sum_j U_{kj}(r) \chi_j e^{i(n\phi + qz - \omega t)}, \quad k = r, \phi, z, \quad (\text{B.1})$$

with $\chi_j = (\chi_0, \chi_1, \chi_2)$ and the matrix $\mathcal{U}(r)$ having the form

$$\mathcal{U}(r) = \begin{pmatrix} \frac{\partial}{\partial r} f_{0n}(r) & i \frac{n}{r} f_{1n}(r) & iq \frac{\partial}{\partial r} f_{2n}(r) \\ i \frac{n}{r} f_{0n}(r) & -\frac{\partial}{\partial r} f_{1n}(r) & -\frac{nq}{r} f_{2n}(r) \\ iq f_{0n}(r) & 0 & k_1^2 f_{2n}(r) \end{pmatrix}. \quad (\text{B.2})$$

The other relevant quantity for the elastic problem is the stress tensor T . [118] In order to obtain T , we first have to find the strain tensor S as a function of displacement $\mathbf{u}(\mathbf{r})$. The independent components of the strain tensor coordinates have expressions (in cylindrical coordinates) [118] of the form

$$\begin{aligned} S_{rr} &= \frac{\partial u_r}{\partial r} \\ S_{\phi\phi} &= \frac{1}{r} \left(\frac{\partial u_\phi}{\partial \phi} + u_r \right) \\ S_{zz} &= \frac{\partial u_z}{\partial z} \\ S_{r\phi} &= \frac{1}{2r} \left(\frac{\partial u_r}{\partial \phi} + r^2 \frac{\partial}{\partial r} \left(\frac{u_r}{r} \right) \right) \\ S_{z\phi} &= \frac{1}{r} \frac{\partial u_z}{\partial \phi} + \frac{\partial u_\phi}{\partial z} \\ S_{rz} &= \frac{1}{2} \left(\frac{\partial u_r}{\partial z} + \frac{\partial u_z}{\partial r} \right). \end{aligned} \quad (\text{B.3})$$

The stress tensor, T , which quantifies the surface forces, is related to the strain tensor S by the elastic modulus constants. [118] Since we are interested in the boundary conditions at

the surface of the cylinder, the relevant part of the stress tensor is given by the stress vector $\mathbf{t} = T\mathbf{e}_r$, with \mathbf{e}_r being the unit vector along the radius. We write here only these relevant parts of the stress tensor T as a function of the strain tensor components

$$\begin{aligned} T_{rr} &= \rho(c_l^2 - 2c_t^2)(S_{rr} + S_{\phi\phi} + S_{zz}) + 2\rho c_t^2 S_{rr} \\ T_{r\phi} &= 2\rho c_t^2 S_{r\phi} \\ T_{rz} &= 2\rho c_t^2 S_{rz}, \end{aligned} \quad (\text{B.4})$$

and $\mathbf{t} = (T_{rr}, T_{r\phi}, T_{rz})$. We write now the relevant stress vector \mathbf{t} , which is given explicitly by the following relation

$$\begin{pmatrix} T_{rr} \\ T_{r\phi} \\ T_{rz} \end{pmatrix} = \rho \begin{pmatrix} c_l^2 \frac{\partial}{\partial r} + (c_l^2 - 2c_t^2) \frac{1}{r} & (c_l^2 - 2c_t^2) \frac{1}{r} \frac{\partial}{\partial \phi} & (c_l^2 - 2c_t^2) \frac{\partial}{\partial z} \\ c_t^2 \frac{1}{r} \frac{\partial}{\partial \phi} & c_t^2 \left(\frac{\partial}{\partial r} - \frac{1}{r} \right) & 0 \\ c_t^2 \frac{\partial}{\partial z} & 0 & c_t^2 \frac{\partial}{\partial r} \end{pmatrix} \begin{pmatrix} u_r \\ u_\phi \\ u_z \end{pmatrix}. \quad (\text{B.5})$$

We can bring the stress matrix to the same form as we did for the displacement, namely $t_k(\mathbf{r}) = \sum_j \mathcal{T}_{kj}(r) \chi_j e^{i(n\phi + qz - \omega t)}$, with the matrix \mathcal{T} having the explicit form

$$\mathcal{T}(r) = \begin{pmatrix} \left(2c_t^2 \frac{\partial^2}{\partial r^2} - (c_l^2 - 2c_t^2) \left(\frac{\omega}{c_l} \right)^2 \right) f_{0n} & 2inc_t^2 \frac{\partial}{\partial r} \left(\frac{f_{1n}}{r} \right) & 2iqc_t^2 \frac{\partial^2}{\partial r^2} f_{2n} \\ 2inc_t^2 \frac{\partial}{\partial r} \left(\frac{f_{0n}}{r} \right) & -c_t^2 \left(2 \frac{\partial^2}{\partial r^2} + k_1^2 \right) f_{1n} & -2qnc_t^2 \frac{\partial}{\partial r} \left(\frac{f_{2n}}{r} \right) \\ 2ic_t^2 q \frac{\partial}{\partial r} f_{0n} & -c_t^2 \frac{nq}{r} f_{1n} & c_t^2 (k_1^2 - q^2) \frac{\partial}{\partial r} f_{2n}. \end{pmatrix} \quad (\text{B.6})$$

Appendix C

Spin states in terms of the c_{Γ}^{\dagger} operators

In this appendix we show the expressions for the three-electron symmetry adapted states $|\psi_{\Gamma}^{i,\sigma}\rangle$ in Eqs. (5.35) and (5.38) in terms of the symmetry adapted creation operators $c_{\Gamma,\sigma}^{\dagger}$. Making use of Eq. (5.47) we obtain

$$|\psi_{A_2}^{1\sigma}\rangle = \frac{i\epsilon}{\sqrt{3}}(c_{A_1\bar{\sigma}}^{\dagger}c_{E'_+\sigma}^{\dagger}c_{E'_-\sigma}^{\dagger} + c_{E'_+\bar{\sigma}}^{\dagger}c_{E'_-\sigma}^{\dagger}c_{A_1\sigma}^{\dagger} - c_{E'_-\bar{\sigma}}^{\dagger}c_{E'_+\sigma}^{\dagger}c_{A_1\sigma}^{\dagger})|0\rangle \quad (\text{C.1})$$

$$|\psi_{E'_+}^{1\sigma}\rangle = \frac{i}{\sqrt{3}}(c_{A_1\bar{\sigma}}^{\dagger}c_{A_1\sigma}^{\dagger}c_{E'_+\sigma}^{\dagger} + \epsilon c_{E'_+\bar{\sigma}}^{\dagger}c_{E'_+\sigma}^{\dagger}c_{E'_-\sigma}^{\dagger} + \bar{\epsilon}c_{E'_-\bar{\sigma}}^{\dagger}c_{E'_-\sigma}^{\dagger}c_{A_1\sigma}^{\dagger})|0\rangle \quad (\text{C.2})$$

$$|\psi_{E'_-}^{1\sigma}\rangle = \frac{i}{\sqrt{3}}(c_{A_1\bar{\sigma}}^{\dagger}c_{A_1\sigma}^{\dagger}c_{E'_-\sigma}^{\dagger} + \epsilon c_{E'_-\bar{\sigma}}^{\dagger}c_{E'_-\sigma}^{\dagger}c_{E'_+\sigma}^{\dagger} + \bar{\epsilon}c_{E'_+\bar{\sigma}}^{\dagger}c_{E'_+\sigma}^{\dagger}c_{A_1\sigma}^{\dagger})|0\rangle \quad (\text{C.3})$$

$$|\psi_{A_1}^{2\sigma}\rangle = \frac{\sigma\epsilon}{\sqrt{2}}(c_{E'_+\bar{\sigma}}^{\dagger}c_{A_1\sigma}^{\dagger}c_{E'_-\sigma}^{\dagger} + c_{E'_-\bar{\sigma}}^{\dagger}c_{A_1\sigma}^{\dagger}c_{E'_+\sigma}^{\dagger})|0\rangle \quad (\text{C.4})$$

$$|\psi_{A_2}^{2\sigma}\rangle = -\frac{i\sigma\epsilon}{\sqrt{6}}(2c_{A_1\bar{\sigma}}^{\dagger}c_{E'_+\sigma}^{\dagger}c_{E'_-\sigma}^{\dagger} + c_{E'_+\bar{\sigma}}^{\dagger}c_{A_1\sigma}^{\dagger}c_{E'_-\sigma}^{\dagger} - c_{E'_-\bar{\sigma}}^{\dagger}c_{A_1\sigma}^{\dagger}c_{E'_+\sigma}^{\dagger})|0\rangle \quad (\text{C.5})$$

$$|\psi_{E'_+}^{2\sigma}\rangle = \frac{\sigma}{\sqrt{2}}(\bar{\epsilon}c_{A_1\bar{\sigma}}^{\dagger}c_{A_1\sigma}^{\dagger}c_{E'_+\sigma}^{\dagger} + \epsilon c_{E'_-\bar{\sigma}}^{\dagger}c_{A_1\sigma}^{\dagger}c_{E'_-\sigma}^{\dagger})|0\rangle \quad (\text{C.6})$$

$$|\psi_{E'_-}^{2\sigma}\rangle = \frac{\sigma}{\sqrt{2}}(\bar{\epsilon}c_{A_1\bar{\sigma}}^{\dagger}c_{A_1\sigma}^{\dagger}c_{E'_-\sigma}^{\dagger} + \epsilon c_{E'_+\bar{\sigma}}^{\dagger}c_{A_1\sigma}^{\dagger}c_{E'_+\sigma}^{\dagger})|0\rangle \quad (\text{C.7})$$

$$|\psi_{E'_+}^{2\sigma}\rangle = \frac{i\sigma\bar{\epsilon}}{\sqrt{6}}(c_{A_1\bar{\sigma}}^{\dagger}c_{A_1\sigma}^{\dagger}c_{E'_+\sigma}^{\dagger} - \bar{\epsilon}c_{E'_-\bar{\sigma}}^{\dagger}c_{A_1\sigma}^{\dagger}c_{E'_-\sigma}^{\dagger} - 2\epsilon c_{E'_+\bar{\sigma}}^{\dagger}c_{E'_+\sigma}^{\dagger}c_{E'_-\sigma}^{\dagger})|0\rangle \quad (\text{C.8})$$

$$|\psi_{E'_-}^{2\sigma}\rangle = \frac{i\sigma\bar{\epsilon}}{\sqrt{6}}(c_{A_1\bar{\sigma}}^{\dagger}c_{A_1\sigma}^{\dagger}c_{E'_-\sigma}^{\dagger} - \bar{\epsilon}c_{E'_+\bar{\sigma}}^{\dagger}c_{A_1\sigma}^{\dagger}c_{E'_+\sigma}^{\dagger} - 2\epsilon c_{E'_-\bar{\sigma}}^{\dagger}c_{E'_-\sigma}^{\dagger}c_{E'_+\sigma}^{\dagger})|0\rangle, \quad (\text{C.9})$$

where σ stands above for $sign(\sigma)$.

Appendix D

H_{SO} , H_{e-d}^0 and H_{e-d}^1 matrix elements

For the SOI matrix elements we obtain

$$\langle \psi_{A'_1}^{2\sigma} | H_{SO} | \psi_{A'_2}^{1\sigma} \rangle = \frac{2i\lambda_{SO}}{\sqrt{2}} \sigma, \quad (D.1)$$

$$\langle \psi_{E'_\pm}^{2\sigma} | H_{SO} | \psi_{E'_\pm}^{1\sigma} \rangle = \pm \frac{i\bar{\epsilon}\lambda_{SO}}{\sqrt{2}} \sigma, \quad (D.2)$$

$$\langle \psi_{E'_\pm}^{2\sigma} | H_{SO} | \psi_{E'_\pm}^{1\sigma} \rangle = \pm \sigma \frac{\sqrt{3}\epsilon\lambda_{SO}}{\sqrt{2}}, \quad (D.3)$$

$$\langle \psi_{A'_1}^{2\sigma} | H_{SO} | \psi_{A'_2}^{2\sigma} \rangle = -\sigma 2\lambda_{SO} \quad (D.4)$$

$$\langle \psi_{E'_\pm}^{2\sigma} | H_{SO} | \psi_{E'_\pm}^{2\sigma} \rangle = \pm \sigma \frac{\sqrt{3}}{2} \lambda_{SO}, \quad (D.5)$$

$$\langle \psi_{E'_\pm}^{2\sigma} | H_{SO} | \psi_{E'_\pm}^{2\sigma} \rangle = \pm \frac{\lambda_{SO}}{2} \sigma, \quad (D.6)$$

$$\langle \psi_{E'_\pm}^{2\sigma} | H_{SO} | \psi_{E'_\pm}^{2\sigma} \rangle = \mp \sigma \frac{\sqrt{3}}{2} \lambda_{SO}, \quad (D.7)$$

while the remaining terms are equal to zero. For the electric dipole matrix elements we obtain

$$\langle \psi_{E'_1}^{2\sigma} | H_{e-d}^0 | \psi_{E'_1}^{2\sigma} \rangle = \frac{a}{2} \left((\bar{\epsilon} - 1)E_x + \epsilon\sqrt{3}E_y \right) \quad (D.8)$$

$$\langle \psi_{E'_2}^{2\sigma} | H_{e-d}^0 | \psi_{E'_2}^{2\sigma} \rangle = \frac{a}{2} \left(\epsilon E_x + \frac{1 - \bar{\epsilon}}{\sqrt{3}} E_y \right) \quad (D.9)$$

$$\langle \psi_{E'_1}^{2\sigma} | H_{e-d}^0 | \psi_{E'_2}^{2\sigma} \rangle = -\frac{a}{2} \left(\epsilon E_x + \frac{1 - \bar{\epsilon}}{\sqrt{3}} E_y \right) \quad (D.10)$$

$$\langle \psi_{E'_2}^{2\sigma} | H_{e-d}^0 | \psi_{E'_1}^{2\sigma} \rangle = -\frac{a}{2} \left((\bar{\epsilon} - 1)E_x + \epsilon\sqrt{3}E_y \right) \quad (D.11)$$

$$\langle \psi_{E'_-}^{1\sigma} | H_{e-d}^1 | \psi_{E'_+}^{2\sigma} \rangle = -\frac{i\epsilon E}{\sqrt{6}} (\epsilon d_{EE}^* - 2\bar{\epsilon} d_{AE}^* - d_{AE}) \quad (D.12)$$

$$\langle \psi_{E'_+}^{1\sigma} | H_{e-d}^1 | \psi_{E'_-}^{2\sigma} \rangle = \frac{i\epsilon \bar{E}}{\sqrt{6}} (\epsilon d_{EE} + 2\bar{\epsilon} d_{AE}^* + d_{AE}), \quad (D.13)$$

$$\langle \psi_{E'_-}^{1\sigma} | H_{e-d}^1 | \psi_{E'_+}^{2\sigma} \rangle = \frac{\epsilon E}{\sqrt{2}} (\epsilon d_{EE}^* + d_{AE}), \quad (D.14)$$

$$\langle \psi_{E'_+}^{1\sigma} | H_{e-d}^1 | \psi_{E'_-}^{2\sigma} \rangle = -\frac{\epsilon \bar{E}}{\sqrt{2}} (\epsilon d_{EE} - d_{AE}) \quad (D.15)$$

$$\langle \psi_{E'_-}^{1\sigma} | H_{e-d}^1 | \psi_{E'_+}^{1\sigma} \rangle = 0. \quad (D.16)$$

Bibliography

- [1] L. P. Kouwenhoven, D. G. Austing, and S. Tarucha *Rep. Prog. Phys.*, vol. 64, p. 701, 2001.
- [2] R. Hanson, L. P. Kouwenhoven, J. R. Petta, S. Tarucha, and L. M. K. Vandersypen *Rev. Mod. Phys.*, vol. 79, p. 1217, 2007.
- [3] P. W. Shor, “Algorithms for quantum computation: discrete log and factoring,” in *Proceedings of the 35th Annual Symposium on the Foundations of Computer Science*, (Los Alamos), p. 124, IEEE Computer Society Press, 1994.
- [4] D. Loss and D. P. DiVincenzo *Phys. Rev. A*, vol. 57, p. 120, 1998.
- [5] S. Tarucha, D. G. Austing, T. Honda, R. J. van der Hage, and L. P. Kouwenhoven *Phys. Rev. Lett.*, vol. 77, p. 3613, 1996.
- [6] A. Ciorga, A. S. Sachrajda, P. Hawrylak, C. Gould, P. Zawadzki, S. Jullian, Y. Feng, and Z. Wasilewski *Phys. Rev. B*, vol. 61, p. R16315, 2000.
- [7] J. M. Elzerman, R. Hanson, J. S. Greidanus, L. H. Willems van Beveren, S. d. Franceschi, L. M. K. Vandersypen, S. Tarucha, and L. P. Kouwenhoven *Phys. Rev. B*, vol. 61, p. 161308, 2003.
- [8] T. Hayashi, T. Fujisawa, H. D. Cheong, Y. H. Jeong, and Y. Hirayama *Phys. Rev. Lett.*, vol. 91, p. 226804, 2003.
- [9] J. R. Petta, A. C. Johnson, C. M. Marcus, M. P. Hanson, and A. C. Gossard *Phys. Rev. Lett.*, vol. 93, p. 186802, 2004.
- [10] J. M. Elzerman, R. Hanson, L. H. Willems van Beveren, B. Witkamp, L. M. K. Vandersypen, and L. P. Kouwenhoven *Nature*, vol. 430, p. 431, 2004.
- [11] A. Amasha, K. MacLean, I. Radu, D. M. Zumbuhl, M. A. Kastner, M. P. Hanson, and A. C. Gossard *Phys. Rev. Lett.*, vol. 100, p. 46803, 2008.
- [12] A. C. Johnson, J. R. Petta, J. M. Taylor, A. Yacoby, M. D. Lukin, C. M. Marcus, M. P. Hanson, and A. C. Gossard *Nature*, vol. 435, p. 925, 2005.
- [13] J. R. Petta, A. C. Johnson, J. M. Taylor, E. A. Laird, A. Yacoby, M. D. Lukin, C. M. Marcus, M. P. Hanson, and A. C. Gossard *Science*, vol. 309, p. 2180, 2005.

- [14] H. A. Engel and D. Loss *Phys. Rev. B*, vol. 65, p. 195321, 2002.
- [15] F. H. L. Koppens, C. Buizert, K. J. Tielrooij, I. T. Vink, K. C. Nowack, T. Meunier, L. P. Kouwenhoven, and L. M. K. Vandersypen *Nature*, vol. 442, p. 766, 2006.
- [16] K. C. Nowack, F. H. L. Koppens, Y. V. Nazarov, and L. M. K. Vandersypen *Science*, vol. 318, p. 1430, 2007.
- [17] E. A. Laird, C. Barthel, E. I. Rashba, C. M. Marcus, M. P. Hanson, and A. C. Gossard *Phys. Rev. Lett.*, vol. 99, p. 246601, 2007.
- [18] R. Winkler, *Spin-Orbit Coupling Effects in Two-Dimensional Electron and Hole Systems*. Berlin: STMP, Springer-Verlag, 2003.
- [19] J. Fischer, W. A. Coish, and D. Loss *Phys. Rev. B*, vol. 78, p. 155329, 2008.
- [20] B. Gerardot, D. Brunner, P. A. Dalgarno, P. Oehberg, S. Seidl, M. Kroner, K. Karrai, N. G. Stoltz, P. M. Petroff, and R. J. Warburton *Nature*, vol. 451, p. 441, 2008.
- [21] D. Brunner, B. D. Gerardot, P. A. Dalgarno, G. Wüst, K. Karrai, N. G. Stoltz, P. M. Petroff, and R. J. Warburton *Science*, vol. 325, p. 70, 2009.
- [22] B. Eble, C. Testelin, P. Desfonds, F. Bernardot, A. Balocchi, T. Amand, A. Miard, A. Lemaitre, X. Marie, and M. Chamarro *Phys. Rev. Lett.*, vol. 102, p. 146601, 2009.
- [23] C. Testelin, F. Bernardot, B. Eble, and M. Chamarro *Phys. Rev. B*, vol. 79, p. 195440, 2009.
- [24] D. Heiss, S. Schaeck, H. Huebl, M. Bichler, G. Abstreiter, J. J. Finley, D. Bulaev, and D. Loss *Phys. Rev. B*, vol. 76, p. 241306(R), 2007.
- [25] D. Bulaev and D. Loss *Phys. Rev. Lett.*, vol. 95, p. 076805, 2005.
- [26] D. Bulaev and D. Loss *Phys. Rev. Lett.*, vol. 98, p. 097202, 2007.
- [27] M. Trif, P. Simon, and D. Loss *Phys. Rev. Lett.*, vol. 103, p. 106601, 2009.
- [28] Y. Komijani, M. Csontos, T. Ihn, K. Ensslin, D. Reuter, and A. D. Wieck *Europhys. Lett.*, vol. 84, p. 57004, 2008.
- [29] Y. Komijani, M. Csontos, I. Shorubalko, T. Ihn, K. Ensslin, Y. Meir, D. Reuter, and A. D. Wieck *arXiv:0908.2360*.
- [30] D. Gatteschi, R. Sessoli, and J. Villain, *Molecular nanomagnets*. Oxford: Oxford University Press, 2006.
- [31] D. Gatteschi and R. Sessoli, "Quantum Tunneling of Magnetization and Related Phenomena in Molecular Materials," *Angew. Chem. Int. Ed.*, vol. 42, p. 268, 2003.
- [32] A. Bencini and D. Gatteschi, *EPR of Exchange Coupled Systems*. Berlin Heidelberg: Springer-Verlag, 1989.

- [33] E. M. Chudnovsky and L. Gunther, "Quantum tunneling of magnetization in small ferromagnetic particles," *Phys. Rev. Lett.*, vol. 60, p. 661, 1988.
- [34] D. D. Awschalom, J. F. Smyth, G. Grinstein, D. P. DiVincenzo, and D. Loss, "Macroscopic quantum tunneling in magnetic proteins," *Phys. Rev. Lett.*, vol. 68, p. 3092, 1992.
- [35] R. Sessoli, D. Gatteschi, A. Caneschi, and M. A. Novak, "Magnetic bistability in a metal-ion cluster," *Nature*, vol. 365, p. 141, 1993.
- [36] L. Thomas, F. Lioni, R. Ballou, D. Gatteschi, R. Sessoli, and B. Barbara, "Macroscopic quantum tunnelling of magnetization in a single crystal of nanomagnets," *Nature*, vol. 383, p. 145, 1996.
- [37] J. R. Friedman, M. P. Sarachik, J. Tejada, and R. Ziolo, "Macroscopic measurement of resonant magnetization tunneling in high-spin molecules," *Phys. Rev. Lett.*, vol. 76, p. 3830, 1996.
- [38] W. Wernsdorfer, E. Bonet Orozco, K. Hasselbach, A. Benoit, D. Mailly, O. Kubo, H. Nakano, and B. Barbara, "Macroscopic quantum tunneling of magnetization of single ferrimagnetic nanoparticles of barium ferrite," *Phys. Rev. Lett.*, vol. 79, p. 4014, 1997.
- [39] J. Tejada, X. X. Zhang, E. del Barco, J. M. Hernández, and E. M. Chudnovsky, "Macroscopic resonant tunneling of magnetization in ferritin," *Phys. Rev. Lett.*, vol. 79, p. 1754, 1997.
- [40] D. Gatteschi, A. Caneschi, L. Pardi, and R. Sessoli, "Large Clusters of Metal Ions: The Transition from Molecular to Bulk Magnets," *Science*, vol. 265, p. 1054, 1994.
- [41] C. Sangregorio, T. Ohm, C. Paulsen, R. Sessoli, and D. Gatteschi, "Quantum tunneling of the magnetization in an iron cluster nanomagnet," *Phys. Rev. Lett.*, vol. 78, p. 4645, 1997.
- [42] D. Gatteschi, R. Sessoli, and A. Cornia, "Single-molecule magnets based on iron(iii) oxo clusters," *Chem. Commun.*, vol. 9, p. 725, 2000.
- [43] A. Chiolero and D. Loss, "Macroscopic quantum coherence in molecular magnets," *Phys. Rev. Lett.*, vol. 80, p. 169, 1998.
- [44] F. Meier and D. Loss, "Electron and nuclear spin dynamics in antiferromagnetic molecular rings," *Phys. Rev. Lett.*, vol. 86, p. 5373, 2001.
- [45] M. N. Leuenberger and D. Loss, "Incoherent zener tunneling and its application to molecular magnets," *Phys. Rev. B*, vol. 61, p. 12200, 2000.
- [46] I. Chiorescu, W. Wernsdorfer, A. Müller, H. Bögge, and B. Barbara, "Butterfly hysteresis loop and dissipative spin reversal in the $s = 1/2$, v_{15} molecular complex," *Phys. Rev. Lett.*, vol. 84, p. 3454, 2000.

- [47] I. Chiorescu, W. Wernsdorfer, A. M \tilde{a} ijller, H. B \tilde{a} ugg \tilde{e} , and B. Barbara, “Non-adiabatic landau-zener transitions in low-spin molecular magnet v15,” *Journal of Magnetism and Magnetic Materials*, vol. 221, no. 1-2, p. 103, 2000.
- [48] O. Waldmann, R. Koch, S. Schromm, P. M \ddot{u} ller, I. Bernt, and R. W. Saalfrank, “Butterfly hysteresis loop at nonzero bias field in antiferromagnetic molecular rings: Cooling by adiabatic magnetization,” *Phys. Rev. Lett.*, vol. 89, p. 246401, 2002.
- [49] M. N. Leuenberger and D. Loss, “Spin tunneling and phonon-assisted relaxation in *mn12*-acetate,” *Phys. Rev. B*, vol. 61, p. 1286, 2000.
- [50] M. N. Leuenberger, F. Meier, and D. Loss, “Quantum spin dynamics in molecular magnets,” *Monatshefte f \ddot{u} r Chemie*, vol. 134, p. 217, 2003.
- [51] W. Wernsdorfer and R. Sessoli, “Quantum phase interference and parity effects in magnetic molecular clusters,” *Science*, vol. 284, p. 133, 1999.
- [52] G. Gonz \acute{a} lez and M. N. Leuenberger, “Berry-phase blockade in single-molecule magnets,” *Phys. Rev. Lett.*, vol. 98, p. 256804, 2007.
- [53] G. Gonz \acute{a} lez, M. N. Leuenberger, and E. R. Mucciolo, “Kondo effect in single-molecule magnet transistors,” *Phys. Rev. B*, vol. 78, p. 054445, 2008.
- [54] L. K. Grover, “Quantum mechanics helps in searching for a needle in a haystack,” *Phys. Rev. Lett.*, vol. 79, p. 325, 1997.
- [55] M. Leuenberger and D. Loss, “Quantum computing in molecular magnets,” *Nature*, vol. 410, p. 789, 2001.
- [56] D. D. Awschalom, D. Loss, and N. Samarth, *Semiconductor spintronics and quantum computation*. Berlin: Springer, 2002.
- [57] V. Cerletti, W. A. Coish, and D. Loss *Nanotechnology*, vol. 16, p. 27R, 2005.
- [58] V. I. Mel’nikov and E. I. Rashba *Sov. Phys. JETP*, vol. 34, p. 1353, 1972.
- [59] M. Dobrowolska, A. Witowski, J. K. Furdyna, T. Ichiguchi, H. D. Drew, and P. A. Wolff *Phys. Rev. B*, vol. 29, p. 6652, 1984.
- [60] G. Salis, Y. Kato, K. Ensslin, D. C. Driscoll, A. C. Gossard, and D. D. Awschalom *Nature*, vol. 414, p. 619, 2001.
- [61] E. I. Rashba and A. L. Efros *App. Phys. Lett.*, vol. 83, p. 5295, 2003.
- [62] M. Duckheim and D. Loss *Nat. Phys.*, vol. 3, p. 195, 2006.
- [63] A. V. Khaetskii and Y. V. Nazarov *Phys. Rev. B*, vol. 64, p. 125316, 2001.
- [64] V. N. Golovach, A. Khaetskii, and D. Loss *Phys. Rev. Lett.*, vol. 93, p. 016601, 2004.
- [65] M. Borhani, V. N. Golovach, and D. Loss *Phys. Rev. B*, vol. 73, p. 155311, 2006.

- [66] A. Abragam, *Principle of Nuclear Magnetism*. Oxford: Oxford University Press, 1961.
- [67] N. Zhao, L. Zhong, J.-L. Zhu, and C. P. Sun *Phys. Rev. B*, vol. 74, p. 075307, 2006.
- [68] C. Flindt, A. S. Sorensen, and K. Flensberg *Phys. Rev. Lett.*, vol. 97, p. 240501, 2006.
- [69] G. Burkard, D. Loss, and D. P. DiVincenzo *Phys. Rev. B*, vol. 59, p. 2070, 1999.
- [70] X. Hu and D. S. Sarma *Phys. Rev. A*, vol. 61, p. 062301, 2000.
- [71] J. Schliemann, D. Loss, and A. H. MacDonald *Phys. Rev. B*, vol. 63, p. 085311, 2001.
- [72] K. K. Kavokin *Phys. Rev. B*, vol. 64, p. 075305, 2001.
- [73] N. E. Bonesteel, D. Stepanenko, and D. P. DiVincenzo *Phys. Rev. Lett.*, vol. 87, p. 207901, 2001.
- [74] D. Stepanenko, N. E. Bonesteel, D. P. DiVincenzo, G. Burkard, and D. Loss *Phys. Rev. B*, vol. 68, p. 115306, 2003.
- [75] D. Stepanenko and N. E. Bonesteel *Phys. Rev. Lett.*, vol. 93, p. 140501, 2004.
- [76] G. Burkard and D. Loss *Phys. Rev. Lett.*, vol. 88, p. 047903, 2002.
- [77] G. Dresselhaus *Phys. Rev.*, vol. 100, p. 580, 1955.
- [78] Y. Bychkov and E. I. Rashba *J. Phys. C*, vol. 17, p. 1039, 1984.
- [79] N. F. Johnson and M. C. Payne *Phys. Rev. Lett.*, vol. 67, p. 1157, 1991.
- [80] V. Fock *Z. Phys.*, vol. 47, p. 446, 1928.
- [81] C. G. Darwin *Math. Proc. Cambridge Philos. Soc.*, vol. 27, p. 86, 1930.
- [82] J. Schliemann, J. C. Egues, and D. Loss *Phys. Rev. Lett.*, vol. 90, p. 146801, 2003.
- [83] A. Khaetskii, D. Loss, and L. Glazman *Phys. Rev. Lett.*, vol. 88, p. 186802, 2002.
- [84] W. A. Coish and D. Loss *Phys. Rev. B*, vol. 70, p. 195340, 2004.
- [85] W. A. Coish and D. Loss *Phys. Rev. B*, vol. 72, p. 125337, 2005.
- [86] D. Klauser, W. A. Coish, and D. Loss *Phys. Rev. B*, vol. 73, p. 205302, 2006.
- [87] D. Pines and P. Nozieres, *The theory of quantum liquids, Vol. 1*. New York: Benjamin, 1966.
- [88] F. Stern *Phys. Rev. Lett.*, vol. 18, p. 546, 1967.
- [89] T. Ando, A. B. Fowler, and F. Stern *Rev. Mod. Phys.*, vol. 54, p. 437, 1982.
- [90] C. W. J. Beenakker and H. van Houten, *Solid State Physics: Advances in Research and Applications*. New York: Academic, 1991.

- [91] D. Saraga and D. Loss *Phys. Rev. B*, vol. 72, p. 195319, 2005.
- [92] M. A. Nielsen and I. L. Chuang, *Quantum Computation and Quantum Information*. New York: Cambridge University Press, 2000.
- [93] C. Fasth, F. A., L. Samuelson, V. N. Golovach, and D. Loss *Phys. Rev. Lett.*, vol. 98, p. 266801, 2007.
- [94] M. T. Börk, A. Fuhrer, A. E. Hansen, M. W. Larsson, L. E. Froberg, and L. Samuelson *Phys. Rev. B*, vol. 72, p. 201307R, 2005.
- [95] M. T. Björk, C. Thelander, A. E. Hansen, L. E. Jensen, M. W. Larsson, L. R. Wallenberg, and L. Samuelson *Nano. Lett.*, vol. 4, p. 1621, 2004.
- [96] C. Fasth, A. Fuhrer, M. T. Börk, and L. Samuelson *Nano. Lett.*, vol. 5, p. 1487, 2005.
- [97] A. Pfund, I. Shorubalko, R. Leturcq, and K. Ensslin *Appl. Phys. Lett.*, vol. 89, p. 252106, 2006.
- [98] I. Shorubalko, A. Pfund, R. Leturcq, M. T. Borgström, F. Gramm, E. Müller, E. Gini, and K. Ensslin *Nanotechnology*, vol. 18, p. 044014, 2007.
- [99] E. I. Rashba and A. L. Efros *Phys. Rev. Lett.*, vol. 91, p. 126405, 2003.
- [100] Y. Kato, R. C. Myers, A. C. Gossard, and D. D. Awschalom *Nature*, vol. 427, p. 50, 2004.
- [101] M. Trif, V. N. Golovach, and D. Loss *Phys. Rev. B*, vol. 75, p. 085307, 2007.
- [102] K. C. Nowack, F. H. L. Koppens, Y. V. Nazarov, and L. M. K. Vandersypen, “Coherent control of a single electron spin with electric fields,” *Science*, vol. 318, p. 1430, 2007.
- [103] K. M. Svore, B. M. Terhal, and D. P. DiVincenzo *Phys. Rev. A*, vol. 72, p. 022317, 2005.
- [104] A. Imamoglu, D. D. Awschalom, G. Burkard, D. P. DiVincenzo, D. Loss, M. Sherwin, and A. Small *Phys. Rev. Lett.*, vol. 83, p. 4204, 1999.
- [105] J. Berezovsky, M. H. Mikkelsen, O. Gywat, N. G. Stoltz, L. A. Coldren, and D. D. Awschalom *Science*, vol. 314, p. 1916, 2006.
- [106] M. Atature, J. Dreiser, A. Badolado, and A. Imamoglu *Nat. Phys.*, vol. 3, p. 101, 2007.
- [107] A. Wallraff, D. I. Schuster, A. Blais, L. Frunzio, R. S. Huang, J. Majer, S. Kumar, S. M. Girvin, and R. J. Schoelkopf *Nature*, vol. 431, p. 162, 2004.
- [108] A. Blais, R. S. Huang, A. Wallraff, S. M. Girvin, and R. J. Schoelkopf *Phys. Rev. A*, vol. 69, p. 062320, 2004.
- [109] O. Gywat, F. Meyer, D. Loss, and D. D. Awschalom *Phys. Rev. B*, vol. 73, p. 125336, 2006.

- [110] L. Childress, A. S. örensen, and M. D. Lukin *Phys. Rev. A*, vol. 69, p. 042302, 2004.
- [111] G. Burkard and A. Imamoglu *Phys. Rev. B*, vol. 74, p. 041307(R), 2006.
- [112] C. Cohen-Tannoudji, J. Dupont-Roc, and G. Grynberg, *Atom-Photon Interactions*. INC: John Wiley and Sons, 1992.
- [113] E. T. Jaynes and F. W. Cummings *Proc. IEEE*, vol. 51, p. 89, 1963.
- [114] A. Blais, J. Gambetta, A. Wallraff, D. I. Schuster, S. M. Girvin, M. H. Devoret, and R. J. Schoelkopf *Phys. Rev. A*, vol. 75, p. 032329, 2007.
- [115] I. L. Aleiner and V. I. Fal'ko *Phys. Rev. Lett.*, vol. 87, p. 256801, 2001.
- [116] L. S. Levitov and E. I. Rashba *Phys. Rev. B*, vol. 67, p. 115324, 2003.
- [117] N. Nishiguchi *Phys. Rev. B*, vol. 50, p. 10970, 1994.
- [118] A. N. Cleland, *Foundations of Nanomechanics. From Solid-State Theory to Device Applications*. Berlin Heidelberg: Springer-Verlag, 2003.
- [119] N. Nishiguchi *Phys. Rev. B*, vol. 52, p. 5279, 1995.
- [120] M. A. Stroschio, K. W. Kim, S. G. Yu, and A. Ballato *J. Appl. Phys.*, vol. 76, p. 4670, 1994.
- [121] U. Weiss, *Quantum Dissipative Systems*. Singapore: World Scientific, 1998.
- [122] T. Meunier, I. T. Vink, L. H. van Beveren, K. J. Tielrooij, R. Hanson, F. H. Koppens, P. Tranitz, H. W. Wegscheider, L. P. Kouwenhoven, and L. M. K. Vandersypen *Phys. Rev. Lett.*, vol. 98, p. 126601, 2007.
- [123] T. Yokoi, S. Adachi, H. Sasakura, S. Muto, H. Z. Song, T. Usuki, and S. Hirose *Phys. Rev. B*, vol. 71, p. 041307, 2005.
- [124] D. Stepanenko, G. Burkard, G. Giedke, and A. Imamoglu *Phys. Rev. Lett.*, vol. 96, p. 136401, 2006.
- [125] T. Gaebel, M. Domhan, I. Popa, C. Wittmann, P. Neumann, F. Jelezko, J. R. Rabeau, N. Stavrias, A. D. Greentree, S. Prawer, J. Meijer, J. Twamley, P. R. Hemmer, and J. Wrachtrup *Nat. Phys.*, vol. 2, p. 408, 2006.
- [126] R. Hanson, F. Mendoza, R. J. Epstein, and D. D. Awschalom *Phys. Rev. Lett.*, vol. 97, p. 087601, 2006.
- [127] M. N. Leuenberger and D. Loss *Nature*, vol. 410, p. 789, 2001.
- [128] M. A. Stroschio, K. W. Kim, S. G. Yu, and A. Ballato *J. Appl. Phys.*, vol. 76, p. 4670, 1994.
- [129] J. Lehmann, A. Gaita-Arinño, E. Coronado, and D. Loss *Nature Nanotech.*, vol. 2, p. 317, 2007.

- [130] F. Troiani, A. Ghirri, M. Afronete, S. Carretta, P. Santini, G. Amoretti, S. Pipigkos, and G. Timco *Phys. Rev. Lett.*, vol. 94, p. 207208, 2005.
- [131] F. H. L. Koppens, J. A. Folk, J. M. Elzerman, R. Hanson, L. H. Willems van Beveren, I. T. Vink, H. P. Tranitz, W. Wegscheider, L. P. Kouwenhoven, and L. M. K. Vandersypen
- [132] C. W. Lai, P. Maletinski, A. Badolado, and A. Imamoglu *Phys. Rev. Lett.*, vol. 96, p. 167403, 2006.
- [133] E. Abrahams *Phys. Rev.*, vol. 107, p. 491, 1957.
- [134] H. Capellmann, S. Lipinski, and K. U. Neumann *Z. Phys. B*, vol. 75, p. 323, 1989.
- [135] P. San-Jose, G. Zarand, A. Shnirman, and Schön *Phys. Rev. Lett.*, vol. 97, p. 076803, 2006.
- [136] P. San-Jose, G. Schön, A. Shnirman, and G. Zarand *Phys. Rev. B*, vol. 77, p. 045305, 2008.
- [137] G. L. Pikus and G. E. Pikus, *Symmetry and Strain-Induced Effects in Semiconductors*. New York: Wiley, 1974.
- [138] M. Kroner, K. M. Weiss, B. Biedermann, S. Seidl, A. W. Holleitner, A. Badolado, P. M. Petroff, P. Ohberg, R. J. Warburton, and K. Karrai
- [139] M. Kroner, K. M. Weiss, B. Biedermann, S. Seidl, S. Manus, A. W. Holleitner, A. Badolado, B. D. Petroff, P. M. and Gerardot, R. J. Warburton, and K. Karrai
- [140] E. del Barco, A. D. Kent, E. M. Rumberger, D. N. Hendrickson, and G. Christou, "Symmetry of magnetic quantum tunneling in single molecule magnet *mn12*-acetate," *Phys. Rev. Lett.*, vol. 91, p. 047203, 2003.
- [141] D. Loss, D. P. DiVincenzo, and G. Grinstein, "Suppression of tunneling by interference in half-integer-spin particles," *Phys. Rev. Lett.*, vol. 69, p. 3232, 1992.
- [142] M. N. Leuenberger and D. Loss, "Spin tunneling and topological selection rules for integer spins," *Phys. Rev. B*, vol. 63, p. 054414, Jan 2001.
- [143] F. Troiani, A. Ghirri, M. Affronete, S. Carretta, P. Santini, G. Amoretti, S. Piligkos, G. Timco, and R. E. P. Winpenny, "Molecular engineering of antiferromagnetic rings for quantum computation," *Phys. Rev. Lett.*, vol. 94, p. 207208, 2005.
- [144] A. Ardavan, O. Rival, J. J. L. Morton, S. J. Blundell, A. M. Tyryshkin, G. A. Timco, and R. E. P. Winpenny, "Will spin-relaxation times in molecular magnets permit quantum information processing?," *Phys. Rev. Lett.*, vol. 98, p. 057201, 2007.
- [145] S. Carretta, P. Santini, G. Amoretti, F. Troiani, and M. Affronete, "Spin triangles as optimal units for molecule-based quantum gates," *Phys. Rev. B*, vol. 76, p. 024408, 2007.

- [146] F. Meier, J. Levy, and D. Loss, "Quantum computing with antiferromagnetic spin clusters," *Phys. Rev. B*, vol. 68, p. 134417, 2003.
- [147] J. Lehmann, A. Gaita-Ariño, E. Coronado, and D. Loss, "Spin qubits with electrically gated polyoxometalate molecules," *Nature Nanotechnology*, vol. 2, p. 312, 2007.
- [148] G. A. Timco, S. Carretta, F. Troiani, F. Tuna, R. J. Pritchard, C. A. Muryn, E. J. L. McInnes, A. Ghirri, A. Candini, P. Santini, G. Amoretti, M. Affronte, and R. E. P. Winpenny, "Engineering the coupling between molecular spin qubits by coordination chemistry," *Nature Nanotechnology*, vol. 4, p. 173, 2008.
- [149] H. B. Heersche, Z. de Groot, J. A. Folk, H. S. J. van der Zant, C. Romeike, M. R. Wegewijs, L. Zobbi, D. Barreca, E. Tondello, and A. Cornia, "Electron transport through single *mn12* molecular magnets," *Phys. Rev. Lett.*, vol. 96, p. 206801, 2006.
- [150] K. Osorio, Edgar A. amd Moth-Poulsen, H. S. J. van der Zant, J. Paaske, P. HedegÅerd, K. Flensberg, J. Bendix, and T. BjÅyrnholm, "Electrical manipulation of spin states in a single electrostatically gated transition-metal complex," *Nano Letters*, vol. 10, p. 105, 2010.
- [151] C. Romeike, M. R. Wegewijs, and H. Schoeller, "Spin Quantum Tunneling in Single Molecular Magnets: Fingerprints in Transport Spectroscopy of Current and Noise," *Phys. Rev. Lett.*, vol. 96, p. 196805, 2006.
- [152] C. Romeike, M. R. Wegewijs, W. Hofstetter, and H. Schoeller, "Quantum-Tunneling-Induced Kondo Effect in Single Molecular Magnets," *Phys. Rev. Lett.*, vol. 96, p. 196601, 2006.
- [153] M. N. Leuenberger and E. R. Mucciolo, "Berry-phase oscillations of the kondo effect in single-molecule magnets," *Phys. Rev. Lett.*, vol. 97, p. 126601, 2006.
- [154] L. Michalak, C. M. Canali, M. R. Pederson, M. Paulsson, and V. G. Benza, "Theory of tunneling spectroscopy in a *mn12* single-electron transistor by density-functional theory methods," *Phys. Rev. Lett.*, vol. 104, p. 017202, 2010.
- [155] F. Troiani, M. Affronte, S. Carretta, P. Santini, and G. Amoretti, "Proposal for Quantum Gates in Permanently Coupled Antiferromagnetic Spin rings without Need of Local Fields," *Phys. Rev. Lett.*, vol. 94, p. 190501, 2005.
- [156] M. Trif, F. Troiani, D. Stepanenko, and D. Loss, "Spin-electric coupling in molecular magnets," *Phys. Rev. Lett.*, vol. 101, p. 217201, 2008.
- [157] C. F. Hirjibehedin, C. P. Lutz, and A. J. Heinrich, "Spin coupling in engineered atomic structures," *Science*, vol. 312, p. 1021, 2006.
- [158] A. C. Bleszynski-Jayich, L. E. Fröberg, M. T. Björk, H. J. Trodahl, L. Samuelson, and R. M. Westervelt, "Imaging a one-electron inas quantum dot in an inas/inp nanowire," *Phys. Rev. B*, vol. 77, p. 245327, 2008.

- [159] A. I. Popov, D. I. Plokhov, and A. K. Zvezdin, "Anapole moment and spin-electric interactions in rare-earth nanoclusters," *EPL (Europhysics Letters)*, vol. 87, p. 67004, 2009.
- [160] L. N. Bulaevskii, C. D. Batista, M. V. Mostovoy, and D. I. Khomskii, "Electronic orbital currents and polarization in mott insulators," *Phys. Rev. B*, vol. 78, p. 024402, 2008.
- [161] V. Bellini, A. Olivieri, and F. Manghi, "Density-functional study of the cr[_{sub} 8] anti-ferromagnetic ring," *Phys. Rev. B*, vol. 73, p. 184431, 2006.
- [162] K.-Y. Choi, Y. H. Matsuda, H. Nojiri, U. Kortz, F. Hussain, A. C. Stowe, C. Ramsey, and N. S. Dalal, "Observation of a half step magnetization in the Cu₃-type triangular spin ring," *Phys. Rev. Lett.*, vol. 96, p. 107202, 2006.
- [163] B. S. Tsukerblat, *Group Theory in Chemistry and Spectroscopy: A Simple Guide to Advanced Usage*. Dover Publications, 2006.
- [164] T. Moriya, "New mechanism of anisotropic superexchange interaction," *Phys. Rev. Lett.*, vol. 4, p. 228, 1960.
- [165] L. Shekhtman, O. Entin-Wohlman, and A. Aharony, "Moriya's anisotropic superexchange interaction, frustration, and dzyaloshinsky's weak ferromagnetism," *Phys. Rev. Lett.*, vol. 69, no. 5, p. 836, 1992.
- [166] T. Yildirim, A. B. Harris, O. Entin-Wohlman, and A. Aharony, "Symmetry, spin-orbit interactions, and spin anisotropies," *Phys. Rev. Lett.*, vol. 73, no. 21, p. 2919, 1994.
- [167] I. A. Sergienko and E. Dagotto, "Role of the dzyaloshinskii-moriya interaction in multiferroic perovskites," *Phys. Rev. B*, vol. 73, p. 094434, 2006.
- [168] S. Dong, K. Yamauchi, S. Yunoki, R. Yu, S. Liang, A. Moreo, J.-M. Liu, S. Picozzi, and E. Dagotto, "Exchange bias driven by the dzyaloshinskii-moriya interaction and ferroelectric polarization at g-type antiferromagnetic perovskite interfaces," *Phys. Rev. Lett.*, vol. 103, p. 127201, 2009.
- [169] A. V. Postnikov, J. Kortus, and M. R. Pederson, "Density functional studies of molecular magnets," *Physica Status Solidi (b)*, vol. 243, p. 2533, 2006.
- [170] M. I. Belinsky, "Spin-frustrated v₃ and cu₃ nanomagnets with dzialoshinsky-moriya exchange. 1. inelastic neutron scattering and epr in scalene, isosceles and equilateral trimers," *Chemical Physics*, vol. 361, p. 137, 2009.
- [171] M. I. Belinsky, "Spin-frustrated v₃ and cu₃ nanomagnets with dzialoshinsky-moriya exchange. 2. spin structure, spin chirality and tunneling gaps," *Chemical Physics*, vol. 361, pp. 152 – 167, 2009.
- [172] J. M. Clemente-Juan, E. Coronado, A. Gaita-Arino, C. Gimenez-Saiz, H.-U. Gudel, A. Sieber, R. Bircher, and H. Mutka, "Magnetic polyoxometalates: Anisotropic exchange interactions in the moiety of [(naoh₂)co₃(h₂o)(p₂w₁₅o₅₆)₂]¹⁷⁻," *Inorganic Chemistry*, vol. 44, p. 3389, 2005.

- [173] J. Luzon, K. Bernot, I. J. Hewitt, C. E. Anson, A. K. Powell, and R. Sessoli, "Spin chirality in a molecular dysprosium triangle: The archetype of the noncollinear ising model," *Phys. Rev. Lett.*, vol. 100, p. 247205, 2008.
- [174] R. Winkler, *Spin-Orbit Coupling Effects in Two-Dimensional Electron and Hole Systems*. Springer-Verlag Berlin, Heidelberg, New York, 2003.
- [175] T. Moriya, "Anisotropic superexchange interaction and weak ferromagnetism," *Phys. Rev.*, vol. 120, p. 91, 1960.
- [176] E. Micotti, Y. Furukawa, K. Kumagai, S. Carretta, A. Lascialfari, F. Borsa, G. A. Timco, and R. E. P. Winpenny, "Local spin moment distribution in antiferromagnetic molecular rings probed by nmr," *Phys. Rev. Lett.*, vol. 97, p. 267204, 2006.
- [177] A. Ghirri, G. Lorusso, F. Moro, F. Troiani, V. Corradini, C. Muryn, F. Tuna, G. Timco, R. E. P. Winpenny, and M. Affronte, "Probing edge magnetization in antiferromagnetic spin segments," *Phys. Rev. B*, vol. 79, p. 224430, 2009.

Curriculum vitae

Name: Mircea Trif
Born: 11 January 1982
Nationality: Romanian

Education

- 1988 - 1992 Elementary School Nr. 2, Baia Sprie, Romania
- 1992 - 1996 Secondary School Nr. 2, Baia Sprie, Romania
- 1996 - 2000 "Gheorghe Sincai" College, Baia Mare, Romania
- 2000 - 2004 Bachelor of Physics, Babes-Bolyai University, Cluj-Napoca, Romania
- 2004 - 2004 Master of Physics, Babes-Bolyai University, Cluj-Napoca, Romania
- 2005 - 2009 Ph.D. of Physics, University of Basel, Basel, Switzerland
- Aug. 2004 B.Sc. in Theoretical Physics
- Bachelor project under the supervision of Prof. I. Grosu
- " Bose-Einstein condensation in layered systems "
- Jul. 2005 M.Sc. in Theoretical Physics
- Master thesis under the supervision of Prof. Dr. I. Tifrea
- " Collective modes in non-identical bilayer semiconductor heterostructures"
- 2005 - 2009 Ph.D. student under the supervision of Prof. Dr. D. Loss

Publications

- Mircea Trif, Filippo Troiani, Dimitrije Stepanenko, Daniel Loss
Spin electric effects in molecular antiferromagnets

arXiv:1001.3584v1.

- Jan Fischer, Mircea Trif, W. A. Coish, and Daniel Loss
Spin interactions, relaxation and decoherence in quantum dots
Solid State Communications **149**, 1443 (2009).
- Mircea Trif, Pascal Simon (Orsay), Daniel Loss
Relaxation of hole spins in quantum dots via two-phonon processes
Phys. Rev. Lett. **103**, 106601 (2009).
- Mircea Trif, Filippo Troiani, Dimitrije Stepanenko, Daniel Loss
Spin-Electric Coupling in Molecular Magnets
Phys. Rev. Lett. **101**, 217201 (2008).
- Mircea Trif, Vitaly N. Golovach, Daniel Loss
Spin dynamics in InAs-nanowire quantum-dots coupled to a transmission line
Phys. Rev. B **77**, 045434 (2008).
- Dimitrije Stepanenko, Mircea Trif and Daniel Loss
Quantum computing with molecular magnets
Inorganica Chimica Acta **361** (2008) 3740.
- Björn Trauzettel, Massoud Borhani, Mircea Trif, Daniel Loss
Theory of Spin Qubits in Nanostructures
JPSJ, Special Topics: Advances in Spintronics.
J. Phys. Soc. Jpn. **77**, 031012 (2008).
- Mircea Trif, Vitaly N. Golovach, Daniel Loss
Spin-spin coupling in electrostatically coupled quantum dots
Phys. Rev. B **75**, 085307 (2007).
- M. Crisan, M. Trif and I. Grosu
Quantum effects in the three-dimensional dilute Bose system at finite temperature: renormalization group approach
Modern Physics Letters B, **20**, 1267 (2006).